Modeling the Dynamic Response of Low-Density, Reticulated, Elastomeric Foam Impregnated with Newtonian and Non-Newtonian Fluids

by

Matthew A. Dawson

B.S., Mechanical Engineering
Colorado School of Mines, 2004

S.M., Mechanical Engineering
Massachusetts Institute of Technology, 2005

Submitted to the Department of Mechanical Engineering in Partial Fulfillment of the Requirements for the Degree of

Doctor of Philosophy in Mechanical Engineering
at the
MASSACHUSETTS INSTITUTE OF TECHNOLOGY
June, 2008

Signature of Author_____
Department of Mechanical Engineering
April 10, 2008

Certified by_____
Lorna J. Gibson
Matoula S. Salapatas Professor of Materials Science and Engineering
Thesis Supervisor

Accepted by___
Lallit Anand
Chairman, Departmental Committee on Graduate Studies

Abstract

Engineering cellular solids, such as honeycombs and foams, are widely used in applications ranging from thermal insulation to energy absorption. Natural cellular materials, such as wood, have been used in structures for millennia. However, despite their extensive use, a comprehensive understanding of the dynamic interaction between the interstitial fluid in the cells of the foam and the foam itself has yet to be developed. In this thesis, we explore the dynamic, compressive response of low-density, reticulated, elastomeric foam impregnated with Newtonian and non-Newtonian fluids. To develop tractable analytical models for this complex, non-linear phenomenon, a study is first undertaken on the permeability of foam under deformation. Using these results, a model is developed for the dynamic, uniaxial compressive response of low-density, reticulated, elastomeric foam filled with a viscous Newtonian fluid. This comprehensive model is found to be well approximated by a simpler model, based on the lubrication approximation. Furthermore, in the lubrication limit, a model for the dynamic, uniaxial compressive response of foam filled with a non-Newtonian fluid is also developed. All of the models presented in this thesis are supported by extensive experimental studies. The experiments also suggest that these models are applicable over a wide-range of parameters, such as strain, strain rate, and pore size. Finally, these models are used in two case studies to assess the feasibility of composite structures containing a layer of liquid-filled foam in dynamic loading applications. The first case study focuses on applications in energy absorption with the experimental design of a motorcycle helmet. The second case study focuses on applications in mitigating the effects of blast waves with a parametric study of the design of a blast wall. These studies provide insight into the usefulness of the models and demonstrate that composite structures with a layer of liquid-filled foam have enormous potential in a wide range of dynamic loading applications.

Doctoral Committee Chair:

Dr. Lorna J. Gibson,
Matoula S. Salapatas Professor of Materials Science and Engineering, M.I.T.

Committee Members:

Dr. Gareth H. McKinley,
SoE Professor of Teaching Innovation, Mechanical Engineering, M.I.T.
Dr. Annette E. Hosoi
Associate Professor of Mechanical Engineering, M.I.T.

Dedication

To The Lord,

My life, my light, my way.

"Because out from Him and through Him and to Him are all things.

To Him be the glory forever. Amen."

Romans 11:36

"To the only God our Savior

through Jesus Christ our Lord

be glory, majesty, might, and authority

before all time and now and unto all eternity. Amen."

Jude 1:25

Acknowledgements

I would like to express my deepest appreciation to my thesis advisor Professor Lorna J. Gibson whose inspiring thoughts and vast experience made the developments in this thesis possible. I have truly developed under her tutelage. Her financial support (through NSF Grant Number CMS-0408259 for which we are grateful) has provided the means necessary to undertake the research for this thesis.

I would also like to thank the Department of Defense for providing the NDSEG Fellowship under which this research was conducted. Their financial support allowed me to focus on research and provided me with the freedom to pursue my goals.

I wish also to thank Professor Gareth H. McKinley and Professor Annette E. Hosoi in the Department of Mechanical Engineering. The ideas in this thesis benefited greatly from their insight, experience, and creativity. Their strong support was invaluable.

Finally, I would like to acknowledge the moral support I received from my wife and family. Their love, guidance, and encouragement have been instrumental in my success.

Biography

Matthew A. Dawson was raised in Englewood, Colorado. Even at a young age he had a passion for innovation. He developed his first of many inventions at the age of twelve, which promoted efficient energy consumption by harvesting energy from vehicles that would otherwise be wasted during deceleration. His diligent and creative nature were manifest further at fifteen when he became captivated by the field of number theory and began to explore relationships between perfect numbers, prime numbers, and irrational numbers. He graduated from Cherry Creek High School ranked first out of 790 students. He continued his academic pursuits at Colorado School of Mines where he worked on a variety of projects, including designing a small scale hydroelectric power plant and creating trigger mechanisms for debris flow warning systems in South America. He graduated with highest honors in only three years with a Bachelor of Science in Mechanical Engineering.

After college he became the co-founder and President of Emeon Technologies, Inc., a company specializing in automated investment algorithms. He filed for his first U.S. Patent on an energy conversion device for space heating at the age of 22. He also invented and implemented the mathematics game *Match Set*, which has demonstrated promise to enhance the cognitive skills of young students. Additionally, his professional experiences include internships among the foremost engineers in the country with ChevronTexaco, ExxonMobil, Lawrence Livermore National Labs, and the MIT Investment Management Co.

He has received numerous honors, becoming a member of the engineering and mathematics honor societies Tau Beta Pi and Kappa Mu Epsilon, a National Defense Science and Engineering Fellow, a Department of Homeland Security Fellow, a National AP scholar with Honors, an American Invitational Mathematics Exam participant, and a Professional Engineer in Training. By the age of 20 he completed his first publication of the Dawsonian Secrets of Mathematics. This was the first of numerous publications, including Biomimetics: extending nature's design of thin-wall shells with cellular cores *(WIT Transactions of Ecology and the Environment, 2006)*, Optimization of cylindrical shells with compliant cores (*International J. of Solids and Structures, 2007*), Permeability of Open-Cell Foams Under Compressive Strain *(International J. of Solids and Structures, 2007)*, The Dynamic Response of Open-Cell Foam Filled with a Newtonian Fluid Under Compression *(J. of Applied Mechanics, 2008)*, The Dynamic Response of Open-Cell Foam Impregnated with a Non-Newtonian Fluid Under Compression *(Under Review by the J. of Applied Mechanics, 2008).*

Table of Contents

List of Tables

Page

List of Figures

Nomenclature

C, C_1	Empirical constants associated with the dynamic response of fluid-filled foam
d	Average cell diameter of porous media
D	The distance between an explosive and the target in meters
E^*	Effective foam modulus
E_S	Modulus of material from which foam is made
h	Height of cylindrical foam specimen in axial compression direction
$\dot{h}$	The rate of change of the height of a cylindrical foam specimen
J_O	Zero order Bessel function of the first kind
k	Intrinsic permeability of porous media
k_{el}^*	Intrinsic permeability of open-cell foam at the elastic buckling strain
k_d	Intrinsic permeability of open-cell foam at the densified strain
m	Consistency index for power-law fluid
n	Power-law exponent for power-law fluid
P	Local pressure in fluid
P_{ro}	Maximum reflected overpressure caused by an explosive blast on a plate
R	Radius of foam specimen
$\underline{V}$	Local velocity vector of fluid
W	Weight of an explosive in kg
z	Scaled blast distance parameter
χ_{el}^*	Volume fraction of cells in at the elastic buckling strain
χ_d	Volume fraction of cells at the densified strain
ε	Strain taken to be positive in compression
$\dot{\varepsilon}$	Strain rate of foam specimen in axial compression
ε_{el}^*	Elastic buckling strain
ε_d	Densified strain
ε_D	Fully densified strain
ϕ	Volume fraction of particles in non-Newtonian dispersion
$\dot{\gamma}$	Shear rate of fluid
$\underline{\dot{\gamma}}$	Strain rate tensor of fluid
η	Dynamic viscosity of non-Newtonian fluid
μ	Dynamic viscosity of Newtonian fluid
ν	Poisson's ratio

ρ	Density of fluid
ρ_o^*	Initial density of foam at 0% strain
ρ_S	Density of solid from which foam is made
ρ_o^*/ρ_S	Relative density of foam
σ^*	Average uniform stress response of dry foam under axial compression
σ_{el}^*	Average uniform elastic buckling stress response of dry foam under axial compression
σ_f	Average uniform stress contribution of fluid in dynamically compressed fluid-filled foam
$\underline{\tau}$	Stress tensor of fluid

1 Introduction

"If I have seen further it is by standing on the shoulders of giants."

Sir Isaac Newton (1676)

Throughout history, cellular materials have been utilized in engineering design (Gibson and Ashby, 1997). From the Egyptians to the Greeks to the Romans, nearly every civilization has utilized cellular materials for their strength to weight ratio and their ability to sustain large elastic deformation. Today, one of the most common types of cellular materials found in engineering structures is foam. **Fig. 1.1** shows a sample of low-density, open-cell (reticulated) polyurethane foam, used throughout this thesis. Foam can be manufactured from nearly any material over a wide range of microstructural configurations. This versatility has resulted in the widespread use of foams in applications ranging from energy absorption to thermal insulation to chemical filtration.

The mechanical behavior of foam has drawn the greatest interest in research, which has resulted in an extensive body of comprehensive literature (Wendlle, 1976; Hilyard, 1982; Suh and Webb, 1985; Hilyard and Collier, 1987; Hilyard and Cunningham, 1994; Weaire and Fortes, 1994; Gibson and Ashby, 1997). One of the unique characteristics of the microstructural behavior of foam under compression is that the stress response is relatively constant over a large range of strain. This characteristic behavior is particularly useful in energy absorption applications. First, the ability to undergo large deformations gives foam the capacity to absorb a substantial amount of energy. Second, the relatively constant stress under deformation ensures the underlying body is not exposed to excessively high loads or accelerations. Numerous studies have explored

applications of foam to energy absorption in vehicles (Fuganti et al., 2000; Chen, 2001), helmets (Shuaeib et al., 2007), and protective equipment (Hager et al., 2001). But this characteristic behavior of foam may also be useful in engineering structures which require a time-delayed response, such as in the case of a structure exposed to a blast wave. Recently, one of the most promising structural designs for blast protection has proven to be sandwich panels, consisting of a low-density, rigid, cellular-core sandwiched between two parallel plates **(Fig. 1.2)**. Numerous analytical and computational studies on the expected performance of various types of sandwich panels under a range of blast loads have been conducted (Xue and Hutchinson, 2003; Fleck and Deshpande, 2004; Xue and Hutchinson, 2004; Qiu, Deshpande, and Fleck, 2005; Hutchinson and Xue, 2005). The advantage of this type of composite structure under blast loading was first recognized by Taylor (1963) and explained in detail by Kambouchev, Noels, and Radovitzky (2005); The fundamental concept is that the motion of the structure, due to the deformation of core, relieves the pressure acting on it, reducing the transmitted impulse.

While foam has shown theoretical potential in a variety of energy absorption and blast protection designs, there are a number of practical scenarios where the thickness of the foam, the weight of the foam, or the rigidity of the foam limits the implementation of a sandwich structure with a standard, rigid foam layer. In these scenarios, we propose the use of a layer of low-density, flexible, reticulated (open-cell) foam, impregnated with a high viscosity Newtonian or non-Newtonian liquid (after Bettin, 2005b). A standard foam is impregnated with air (an extremely low viscosity fluid), which adds a negligible contribution to the response of an open-cell foam (Gibson and Ashby, 1997). However, in the proposed liquid-filled foam design, the viscous contribution of the liquid to the

dynamic response of the structure can be significant. This liquid-filled foam design also allows for more controllable energy dissipation, by means of viscous flow, over a much smaller compressive deformation. Therefore, a thinner, often lighter-weight design can be used to efficiently absorb energy from an impact or mitigate the effect of a blast wave. This liquid-filled structure also has a number of additional potential advantages over a standard design. One of the primary advantages is that liquid-filled, elastic foams are inherently highly reversible under deformation. Even under large deformations, the microstructural damage to elastic, open-cell foam is minimal (Shen et al., 2000). Therefore, the ability of the foam to contain the fluid should not be dramatically affected. In addition, for the case of a non-Newtonian, shear thickening liquid, the shear thickening process is largely reversible, allowing for the fluid to behave consistently under repeated loading (Bender and Wagner, 1996). Standard, inelastic foams, however, dissipate energy through permanent plastic deformation, making them inherently irreversible. Therefore, liquid-filled structures are more capable of efficiently protecting against repeated loading. Furthermore, the liquid-filled composite structure is passive, giving them a tremendous advantage over active systems. These benefits are often realized when technologies are introduced into the field and exposed to adverse operating conditions. Finally, the adaptable and formable nature of liquid-filled, elastic foams makes them highly versatile. Their versatility gives them potential in a variety of commercial applications from impact protection equipment (helmets, pads, vehicles, etc.) to military blast protection equipment (personnel, vehicles, infrastructure, etc.).

There is always a need to improve the efficiency of commercial protective equipment, particularly for protecting the head. The Center for Disease Control estimates there are roughly 1.5 million traumatic brain injuries (TBI's) in the U.S.

each year from transportation accidents and sporting related injuries (Sosin, Sniezek, and Thurman, 1996). Over 50,000 of these brain injuries result in fatalities (Sosin, Sniezek, and Waxweiler, 1995). The total cost to the U.S. economy for TBI's was estimated to be $37.8 Billion for 1985 (Max, Mackenzie, and Rice, 1991). To combat this epidemic, the government has invested substantial funds for research and development of protective equipment for vehicles, giving $86 million to crash worthiness testing in 2007 (DOT, 2007). While a significant amount of research on impact protection of vehicles is being undertaken, there is still a substantial need for research in the field of personal protective equipment, such as in the field of motorcycle helmets. For instance, in 1999, 2,470 motorcyclists were killed and more than 50,000 were injured in traffic accidents in the United States (NHTSA, 1999). The NHTSA found that brain injury is the primary cause of death in motorcycle accidents and that motorcycle helmets are 67% effective in preventing brain injuries (NHTSA, 1996a); however, many motorcyclists avoid wearing helmets because of their excessive size and weight. In 1996, 51% of the motorcyclists between the ages of 15 and 20 who were fatally injured in accidents were not wearing helmets (NHTSA, 1996b). Improving the weight efficiency of motorcycle helmets by incorporating a thin, composite layer of liquid-filled foam may increase the utilization of helmets and dramatically reduce the number of motorcycle fatalities.

While development of protective equipment for energy absorption applications has been ongoing for decades, development of protective equipment designed to mitigate the effects of blast waves has only recently received attention (Gama et al., 2001; Fedorenko et al., 2004; Talaslidis et al., 2004; and Liang et al., 2005). The reason for the increased interest in this field is due to the fact that terrorist bombings have increased dramatically in recent years, becoming one of the most

prominent threats worldwide. According to the U.S. Department of State the frequency of terrorist bombings increased by 30% from 2005 to 2006 with over 19,500 facilities bombed or targeted worldwide in 2006 (U.S. Dept. of State, 2006). The results of these attacks have been devastating with a corresponding increase in fatalities of 39%. The resulting fatalities from terrorist bombings constituted a majority of the total terrorist related fatalities in both 2005 and 2006 (14,618 and 20,498, respectively). Currently, much of the research in the field of blast protection is focused on protection of infrastructure utilizing specially designed barriers or blast walls (Boh et al., 2004; Louca et al., 2004; and Davidson, 2005).

However, the threat of terrorist attacks with improvised explosive devices (IED's) is not only to infrastructure, but also to military personnel. While a number of researchers have explored the design of stand-off, blast walls, very little research has been done on the development of an inexpensive, lightweight armor, which can effectively protect personnel, vehicles, and structures from a blast wave. A recent study of injuries sustained by marines in Iraq, conducted from March through August of 2004, found that 97% of injuries were caused by IED's or mines (Gondusky, 2005). Of these injuries, primary blast injuries, caused entirely by pressure waves, were found to be of greatest concern; these primary blast injuries constituted 33% of injuries indoors and 12% of injuries outdoors (Gondusky, 2005). Fortunately, armor with an integrated layer of liquid-filled foam has the potential to effectively protect against primary blast injuries. By delaying the propagation of the impinging stress wave, the novel armor reduces the peak stress transmitted to the underlying body, and thus, reduces the pressure gradient across critical organs. Preventing these primary blast injuries is crucial since they can be severe, consisting of damage to the lungs, the brain (traumatic brain injury), the central nervous system, the

tympanic membrane, and the intestinal tract (DePalma, 2005; Coppel, 1976; Leibovici, 1999; and Trudeau, 1998). The most immediately life-threatening primary blast injury is typically associated with barotrauma of air-filled organs, such as the lungs, (Mellor et al., 1989 and Haberstroh, 2004) where large pressure gradients across the alveolar-capillary interface can lead to microscopic hemorrhaging and sudden fatality.

Unfortunately, with the increasingly tumultuous political atmosphere and the increasing availability of high power explosives, attacks on personnel, vehicles, and structures are on the rise. **Fig. 1.3** shows the dramatic increase in the number of fatalities of U.S. soldiers in Iraq over the past four years caused by improvised explosive devices. The effectiveness of these terrorist attacks has the potential to encourage further incidences in the future. Therefore, the need to develop a lightweight, inexpensive, blast-resistant armor for personnel, vehicles, and structures only promises to grow.

While existing technologies do very little to resist against multiple impacts in a motorcycle accident or mitigate the effects of primary blast injury caused by an explosive, composite structures, with a layer of liquid-filled foam, demonstrate the potential to protect against these scenarios in a weight-, size-, and cost-efficient manner. However, developing an optimal design for such a structure requires a comprehensive understanding of the dynamic behavior of the liquid-filled foam. Although the mechanical response of open-cell foam under compression is well understood (Gent and Thomas, 1959; Gent and Thomas, 1963; Wendlle, 1976; Hilyard, 1982; Suh and Webb, 1985; Hilyard and Collier, 1987; Hilyard and Cunningham, 1994; Weaire and Fortes, 1994; Gibson and Ashby, 1998), developing a detailed understanding of the dynamic interaction

between the interstitial fluid in the cells of the foam and the foam itself in compression is still on the frontier of research. Outside of a brief computational and experimental analysis by Hilyard (1971), who developed a third order, non-linear equation of motion, nearly all exploration of the dynamic response of liquid-filled foams has been entirely computational (Rehkopf, McNeice, and Brodland, 1996; Mills and Lyn, 2002; and Schraad and Harlow, 2006).

This thesis explores the dynamic, compressive response of fluid-filled foam and its applications. In addition, it delves into methods for using the models, which describe the response of this structure, in practical engineering design. In *Chapter 2*, an extensive literature review is provided on the mechanical behavior of foams as well as the on the interaction of foams with fluids. Moreover, a brief review of non-Newtonian fluids (NNF) is presented along with a discussion of shear thickening fluids (STF) and their properties. Finally, a discussion of applications of liquid-filled foams to energy absorption and blast wave protection is given in conjunction with a detailed review of the motivation for technological improvements in these fields. In *Chapter 3*, a model for the microstructural behavior of low-density, open-cell foam under compressive strain is proposed. Using this model, a tractable relationship between the permeability and the applied compressive strain of open-cell foam filled with a Newtonian liquid is developed. Experimental studies are found to strongly support the resulting deformation behavior model and permeability model for a wide range of parameters. Based on the permeability model, in *Chapter 4*, a model is developed for the complete dynamic response of a cylindrical specimen of low-density, reticulated, elastomeric foam impregnated with a viscous Newtonian fluid under axial compression. This model is compared with experimental results and found to describe the data well for a large range fluid

properties and foam properties. In addition, this comprehensive model is found to converge rapidly toward a simpler lubrication model; where a lubrication model assumes that the characteristic dimension in the radial direction is much greater than that in the axial direction. In *Chapter 5*, a robust lubrication model for the dynamic compressive response of a non-Newtonian-fluid-filled (NNF-filled) foam is presented. Similar to its Newtonian counterpart, the NNF-filled foam model, developed for high rate loading of highly shear thickening fluids impregnated in open-cell foam, is also tested and supported experimentally. In *Chapter 6*, the previous models are used qualitatively in an experimental design processes, exploring the development of motorcycle helmets comprised of composite structures with a composite layer of liquid-filled foam. In particular, a motorcycle helmet design is sought, which reduces the weight and increases the protection to multiple impacts over existing standard designs. *Chapter 7* utilizes the models developed in this thesis in a numerical study of blast protection technologies. An in depth parametric study is performed on a composite blast wall containing a layer of liquid-filled foam. This blast protection technology demonstrates the potential to outperform existing state-of-the-art technologies and dramatically reduce the peak loading on a structure exposed to a blast wave. Finally, conclusions based on the results of this thesis are summarized in *Chapter 8* in along with recommendations for potential extensions of the work presented in this dissertation.

References

Bender, J. and Wagner, N., (1996), "Reverisible Shear Thickening in Monodisperse and Bidisperse Colloidal Dispersions", *J. Rheo.*, **40**, 899-916.

Bettin, G. and McKinley, G.H., (2005), "High Deformation Rate Behavior of Polymeric Foams Filled with Concentrated Silica Suspensions", *Soc. Rheology 77th Annual Meeting.*

Boh, J.W., Louca, L.A., and Choo, Y.S., (2004), "Energy Absorbing Passive Impact Barrier for Profiled Blastwalls", *Int. J. Impact Eng.*, **31**, 976-95.

Chen, W., (2001), "Crashworthiness Optimization of Ultralight Metal Structures", Doctoral Thesis. Massachusetts Institute of Technology, Cambridge, Massachusetts.

Cooper, G., Townend, D., Cater, S., Pearce, B., (1991), "The Role of Stress Waves in Thoracic Visceral Injury from Blast Loading: Modification of Stress Transmissiono by Foams and High-Density Materials", *J. Biomech.* **24**, 273-295.

Davidson, J., Fisher, J., Hammons, M., Porter, J., and Dinan, R., (2005), "Failure Mechanism of Polymer-Reinforced Concrete Masonry Walls Subjected to Blast", *J. Struct. Eng.*, **131**, 8, 1194-1205.

DePalma, R., Burris, D. Champion, H., Hodgson, M., (2005), "Blast Injuries", *New England J. Med..* **352**, 1335-1344.

Fedorenko, A.G., Syrunin, M.A., and Ivanov, A.G., (2005), "Criterion for Selecting Composite Materials for Explosion Containment Structures (Review)", *Comb., Explosion, and Shock Waves,* **41**, 5, 487-95.

Fleck, N.A. and Deshpande, V.S., (2004), "The Resistance of Clamped Sandwich Beams to Shock Loading", *J. Applied Mech.*, **71**, 386-401.

Fuganti, A., (2000), "Aluminum Foams for Automotive Applications", *Adv. Eng. Mat.*, **2**, (4), 200-204.

Gama, B.A., et al., (2001), "Aluminum Foam Integral Armor: A New Dimension in Armor Design", *Comp. Struct.*, **52**, 381-395.

Gent, A. and Thomas, A., (1959), "The Deformation of Foamed Elastic Materials", *J. Applied Poly. Sci.*, **1**, 107.

Gent, A. and Thomas, A., (1963), "Mechanics of Foamed Elastic Material", *Rubber Chem. Tech.*, **36**, 597.

Gibson, L.J. and Ashby, M.F., (1997), *Cellular Solids – Structures and Properties, 2nd Ed.*, Cambridge Univserisy Press, Cambridge.

Gondusky, J. and Reiter, M., (2005), "Protecting Military Convoys in Iraq: An examination of Battle Injuries Sustained by a Mechanized Battalion During Operation Iraqi Freedom II", *Military Medicine.* **170**, 546-549.

Haberstroh, J., (2004), "Focus on Head Injuries", *Newsday.* March 29, 2004

Hager, S., Skorpenske, R., and Triouleyre, S., et al., (2001), "New Technology for Viscoelastic Foam", *J. Cell. Plas.*, **37** (5), 377-99.

Hilyard, N.C., (1971), "Observations on the Impact Behaviour of Polyurethane Foams; II. The Effect of Fluid Flow", *J. Cell. Plastics.* **7**, 84-90.

Hilyard, N., (1982), *Mechanics of Cellular Plastics,* Applied Science, Barking, U.K.

Hilyard, N. and Collier, P., (1987), "A Structural Model Air Flow in Flexible PUR Foams", *Cell. Poly.* **6**, 9-26.

Hilyard, N. and Cunningham, A., (1994), *Low Density Cellular Plastics,* Chapman and Hall, London.

Hutchinson, J.W. and Xue, Z., (2005), "Metal Sandwich Plates Optimized for Pressure Impulses", *Int. J. Mech. Sci.*, **47**, 545-569.

Kambouchev, N., Noels, L., and Radovitzky, R., (2006), "Nonlinear Compressibility Effects in Fluid-Structure Interaction and Their Implications on the Air-Blast Loading of Structures", *J. App. Physics,* **100**, 063519:1-11.

Leibovici, D. Gofrit, O., Shapira, S., (1999), "Eardrum perforation in explosion survivors: is it a marker of pulmonary blast injury?", *Ann. Emerg. Med.* **34**, 168-72.

Liang, C.C. and Tai, Y.S., (2006), "Shock Responses of a Surface Ship Subjected to Noncontact Underwater Explosions", *Ocean Eng.*, **33**, 748-772.

Louca, L.A., Boh, J.W., Choo, Y.S., (2004), "Response of Profiled Barriers Subject to Hydrocarbon Explosions", *Proc. Inst. Civil Eng.*, **157**, 319-331.

Max, W., Mackenzie, E., and Rice, D., (1991), "Head Injuries: Costs and Consequences", *J. Head Trauma Rehab.*, **6**, 76-91.

Mellor, S. and Cooper, G., (1989), "Analysis of 828 Servicemen Killed or Injured by Explosion in Northern Ireland 1970-84 The Hostile Action Caualty System", *Br. J. Surg.* **76**, 1006-10.

Mills, N. and Lyn, G., (2002), "Modelling Air Flow in Impacted Polyurethane Foam", *Cell. Poly.* **21**, 343-65.

National Highway Safety Transportation Administration (NHTSA), (1996a), "Traffic Safety Facts", U.S., ***Motorcycles***, 1-6.

National Highway Safety Transportation Administration (NHTSA), (1996b), "Traffic Safety Facts", U.S., ***Young Drivers***, 1-6.

National Highway Safety Transportation Administration (NHTSA), (1999), "Motorcycle Safety Facts", U.S., ***Young Drivers***, 1-6.

Qiu, X., Deshpande, V.S., and Fleck, N.A., (2005), "A One-Dimensional Response of Sandwich Plates to Underwater Shock Loading", *J. Mech. Phys. Solids*, **53**, 2347-2383.

Rehkopf, J., Brodland, G., and McNeice, G., (1996), "Experimentally Seperating Fluid and Matrix Contributions to Polymeric Foam Behavior", *Experimental Mechanics*. **36**, 1-6.

Schraad, M. and Harlow, F., (2006), "A Multi-Field Approach to Modeling the Dynamic Response of Cellular Materials", *Int. J. Mech. Sci.*, **48**, 85-106.

Shen, Y., Golnaraghi, F., and Plumtree, A., (2001), "Modelling Compressive Cyclic Stress-Strain Behaviour of Structural Foam", *Int. J. Fatigue* **23**, 491-497.

Shuaeib, F., Hamouda, A., Wong, S., Radin, R., Ahmed, M., (2007), "A new motorcycle helmet liner material: The finite element simulation and design of experiment optimization", *Mat. and Design*, **28**, pp. 182-195.

Sosin, D., Sniezek, J., and Thurman, D., (1991), "Incidence of Mild and Moderate Brain Injury in the United States", *Brain Injury*, **10**, 47-54.

Sosin, D., Sniezek, J., and Waxweiler, R., (1995), "Trends in Death Associated with Traumatic Brain Injury", *JAMA*, **273**, 1778-80.

Suh, K. and Webb, D., (1985), "Cellular Materials", *Encyclopedia of Polymer Science*, **3**, 2nd Ed., Wiley, New York.

Talaslidis, D., Manolis, G., Paraskevopoulos, E., Panagiotopoulos, C., Pelekasis, N., Tsamopoulos, J., (2004), "Risk Analysis of Industrial Structures Under Extreme Transient Loads", *Soil Dynamics and Earthquake Eng.*, **24**, 435-48.

Taylor, G.I., (1963), "In Aerodynamics and the Mechanics of Projectiles and Explosions", *The Scientific Papers of Sir Geoffrey Ingram Taylor*, **3**, pp. 287-303.

Trudeau, D., Anderson, J., and Hansen, L., Shaglov, D., Schmoller, J., Nugent, S., Barton, S., (1998), "Findings of Mild Traumatic Brain Injury In Combat Verterans with PTSD and a History of Blast Concussion", *J.Neuro. Clin Neurosci.* **10**, 308-13.

U.S. Department of Defense, (2007), "Fallen Warriors: Operation Iraqi Freedom", *U.S. Department of Defense News about the War on Terrorism.* Operation Iraqi Freedom List of Names.

U.S. Department of State, (2007), "Country Reports on Terrorism", *National Counterterrorism Center: Annex of Statistical Information*, 1.

Weaire, D. and Fortes, M., (1994), "Stress and Strain in Liquid and Solid Foams", *Adv. Phys.*, **43**, 685-738.

Wendle, B., (1976), "*Engineering Guide to Structural Foams*", Technomic Publishing Co., Westport, Connecticut.

Xue, Z. and Hutchinson, J.W., (2003), "Preliminary Assessment of Sandwich Plates Subject to Blast Loads", *Int. J. Mech. Sci.*, **45**, 687-705.

Xue, Z. and Hutchinson, J.W., (2004), "A Comparative Study of Impulse-Resistant Metallic Sandwich Plates", *Int. J. Impact Eng.*, **30**, 1283-1305.

Figures

A) 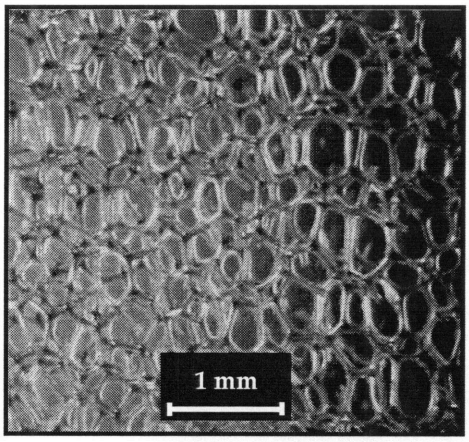

B) 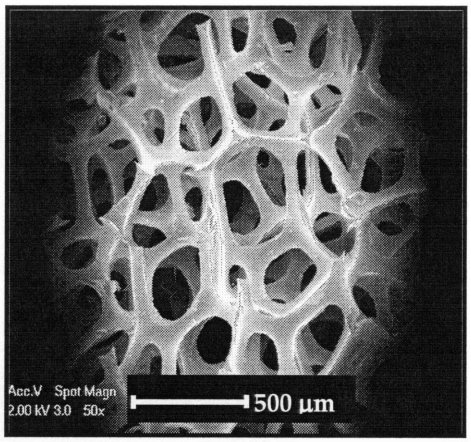

Figure 1.1: Open-cell polyurethane foam (70 pores per inch).
A) Optical micrograph; B) Scanning electron micrograph.

A)

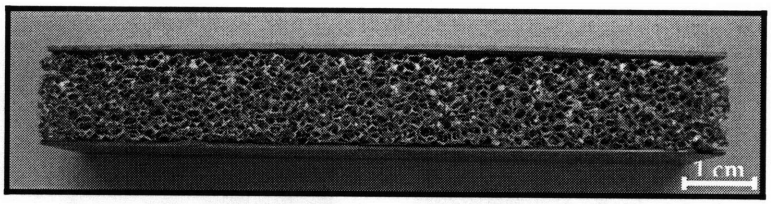

B)

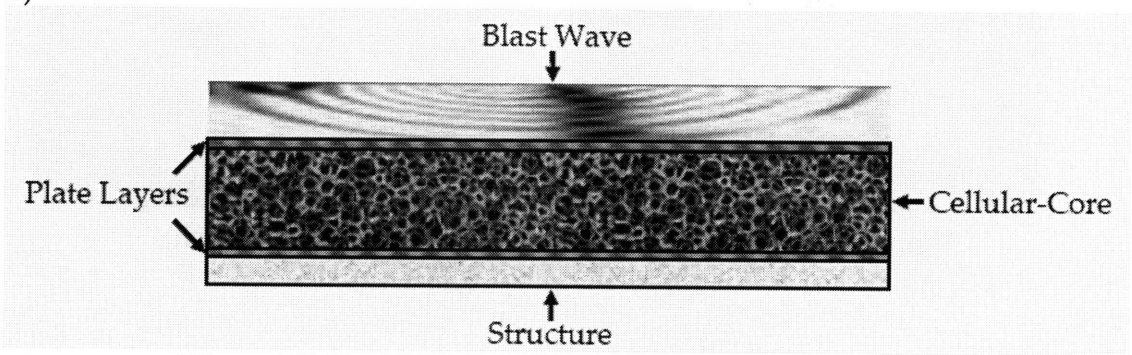

Figure 1.2: Sandwich panel design for blast protection.
A) Actual sample; B) Theoretical schematic.

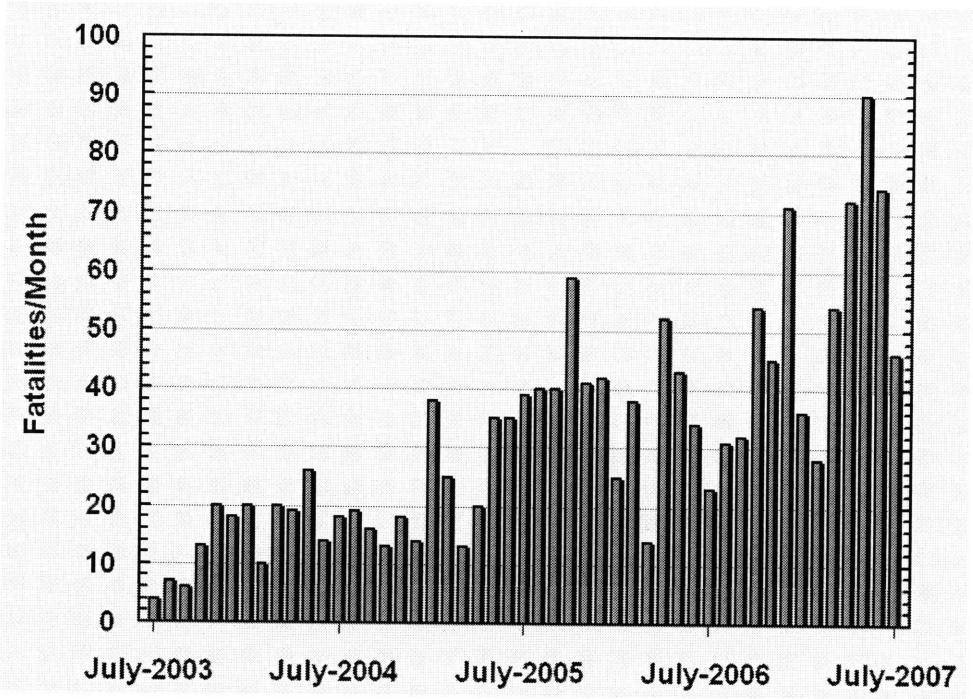

Figure 1.3: Fatalities of U.S. soldiers in Iraq caused by improvised explosive devices. Information supplied by U.S. Department of Defense (2007).

2 Literature Review

2.1 Mechanical Properties of Foam

Although there are many types of cellular materials, foam is one of the most ubiquitous cellular materials in engineering. Because of its widespread use, there is an extensive literature on foams examining everything from their microstructure to their mechanical properties to their response under various loading scenarios. In general, foams have three-dimensional polyhedral cells that can be either closed-cell or open-cell (Gibson and Ashby, 1997). **Fig. 2.1** shows micrographs of both closed- and open-cell foam. Closed-cell foams, as the name describes, have cells that are completely isolated from their neighbors by cell faces, such that no fluid can pass from one cell to another. Open-cell (reticulated) foam is comprised entirely of cell struts (edges), which readily allows for the passage of fluid between cells. Because the interconnected network of cells allows open-cell foams to be impregnated with liquid, open-cell foams are utilized throughout this dissertation.

The properties of open-cell foam are related to its structure, its density, and the material from which the foam is made. The microstructure of the foam governs the initial relative density of the foam ρ_o^*/ρ_s, where ρ_o^* is the initial density of the foam at zero strain, and ρ_s is the density of the solid from which the foam is made (Gibson and Ashby, 1997). At any given strain ε, the current relative density of the foam is given by ρ^*/ρ_s. Another critical property related to the microstructure and relative density of the foam is the pore size, characterized by the grade of the foam, which is often measured by the number of pores per linear inch (ppi). In this thesis, we are concerned with foams which can be readily impregnated with high viscosity fluids; therefore, we primarily consider low-

density, open-cell, elastomeric foams, with relative densities on the order of ρ_o^*/ρ_s = 0.03, and foam grades ranging from 70 to 90 ppi.

2.1.1 Quasi-Static Compressive Response of Open-Cell Foam

The quasi-static, compressive response of open-cell foam has been studied extensively. Numerous authors provide in-depth reviews (Wendle, 1976; Hilyard, 1982; Suh and Webb, 1985; Hilyard and Collier, 1987; Hilyard and Cunningham, 1994; Weaire and Fortes, 1994; Gibson and Ashby, 1997). The unique deformation response of open-cell foam under compression has received a great deal of attention (Bart-Smith, et al., 1997; Gibson and Ashby, 1997; Wang and Cuitino, 2002; Gong and Kyriakides, 2004). For elastic, open-cell foam under compression it has been observed that cells behave linear-elastically up to the elastic buckling strain ε_{el}^*, at which point layers of cells buckle and collapse, generating local densified bands of large deformation in which the average diameter of the cells is reduced substantially as shown in **Fig. 2.2** (Bart-Smith et al., 1997; Gong and Kyriakides, 2004). A detailed discussion of this banding phenomenon, which is widely seen in open-cell polymeric foams, is given by Gioia et al. (2000). As the initial collapse band forms, the rest of the specimen remains in the linear elastic regime, at a strain close to the elastic buckling strain, ε_{el}^*. As the overall strain increases, cells adjacent to the collapsed band also collapse, so that the length of the densified band increases while that of the remainder of the foam in the linear elastic regime decreases **(Fig. 2.3)**.

The compressive stress-strain response of open-cell foam is a direct result of this unique microstructural deformation behavior. The kinematics of deformation lead to the well known quasi-static, stress-strain response of open-cell foam under compression as shown in **Fig. 2.4**. The stress-strain behavior in **Fig. 2.4** is

classified into three distinct regimes (i.e. linear-elastic, plateau, and densified regimes). The elastic buckling strain occurs at the point in which the stress response leaves the linear elastic regime and enters the "plateau-like" response. The characteristic "plateau-like" response is caused by the near constant stress required to initiate buckling and then collapse a layer of cells, resulting in propagation of the densified regime. Early attempts were made to describe the compressive stress-strain response of open-cell foams both through micromechanics perspectives (Gent and Thomas, 1959; Gent and Thomas, 1963) and through phenomenological based methods (Rusch, 1969). Since this early effort, phenomenological models have appeared sparsely (Massimiliano et al., 2007) along with some finite element models (Everett et al., 1998), primarily developed for numerical simulation. However, the continued development of micromechanics models has provided great insight into the compressive response of open-cell foam (Dementev and Tarakanov, 1970; Warren and Kraynik, 1988; Warren and Kraynik, 1997; Zhu et al., 1997; Michalska et al., 2003; Gong et al., 2004).

Much of the micromechanics modeling has been based on the Kelvin foam model of a cell. According to Gibson and Ashby (1997), Lord Kelvin showed in 1887 that space could be partitioned into identical tetrakaidecahedral cells of equal volume and minimal surface area. This tetrakaidecahedral or Kelvin foam model consists of repeating Kelvin cells, comprised of six quadrilateral surfaces and eight non-planar hexagonal surfaces. Although the tetrakaidecahedral unit (with planar faces, sometimes called the Kelvin cell) model of foam has been nearly universally adopted in micromechanics models for quite some time, the complexity of micromechanics models has continued to increase with time. Gent and Thomas (1959) and Lederman (1971) began with models based on simple stretching of cell walls. Gibson and Ashby (1997) identified bending as the primary mode of deformation in low density foams in the linear elastic regime

and used dimensional arguments to deduce the moduli. They also analyzed elastic buckling of the cell edges in open cell foams to obtain an equation for the plateau stress. More recently, Warren and Kraynik (1988) and Zhu et al. (1997) have developed more comprehensive models incorporating stretching, bending, and twisting of cell walls. However, the complexity of the more comprehensive models prevents the analysis of more than a few cells, nearly prohibited their widespread adoption. Gibson and Ashby's (1997) model for the compressive stress-strain response of reticulated foam has become the standard micromechanics model because of its tractable nature. They relate the effective modulus of the foam E^*, and the elastic buckling stress σ^*, to the modulus of solid from which the foam E_s, and the relative density of the foam ρ^*/ρ_s by:

$$E^* = E_s\left(\rho^*/\rho_s\right)^2 \tag{2.1a}$$

$$\sigma_{el}^* = CE_s\left(\rho^*/\rho_s\right)^2 \tag{2.1b}$$

where C is a constant, typically 0.05. They also developed relations governing the quasi-static stress response of the foam where the average, uniform stress response or the axial compressive force divided by the cross-sectional area of the foam is taken to be σ^*. As previously discussed, under axial compression cells begin to buckle and collapse at the elastic buckling strain. The corresponding stress at the elastic buckling strain is the elastic buckling stress σ_{el}^*, which is a critical parameter in the study of open-cell foams. The primary relations governing the compressive response of foams are given by (Gibson and Ashby, 1997):

$$\sigma^* = \varepsilon E^* \qquad 0 < \varepsilon < \varepsilon_{el}^* \tag{2.2}$$

$$\sigma^* = \sigma^*_{el} \qquad \varepsilon^*_{el} < \varepsilon < \varepsilon_D\left(1-\frac{1}{D}\right)+\varepsilon^*_{el} \quad (2.3)$$

$$\sigma^* = \frac{\sigma^*_{el}}{D}\left(\frac{\varepsilon_D}{\varepsilon_D-\varepsilon}\right)^g \qquad \varepsilon > \varepsilon_D\left(1-\frac{1}{D}\right)+\varepsilon^*_{el} \quad (2.4)$$

where ε is the strain, taken to be positive in compression and given by the compression deformation of the foam over the initial height of the foam, ε_{el}^* is the elastic buckling strain, and g and D are constants associated with the microstructure of the foam. For polyurethane foams, Gibson and Ashby (1997) give the constant g as unity. The fully densified strain ε_D, is the strain at which point the cells have collapsed sufficiently that opposing cell walls touch; further deformation beyond this strain compresses the cell wall material itself. The fully densified strain is given by

$$\varepsilon_D = 1-1.4\left(\frac{\rho^*_o}{\rho_s}\right). \quad (2.5)$$

The constant D is given by

$$D = \frac{\varepsilon_D}{\varepsilon_D - \varepsilon^*_p} \quad (2.6)$$

where the strain ε_p^*, corresponds to the strain at which the stress at the end of the plateau region begins to exceed the elastic buckling stress. It is important to note, the model presented by Gibson and Ashby, like all of the continuum models discussed, assumes cells are isotropic, neglecting the inherent anisotropy

associated with the manufacturing of actual open-cell foam. Despite this assumption, this model has demonstrated the ability to accurately represent the response of open-cell foam, and therefore, has gained wide-spread acceptance.

2.1.2 Dynamic Compressive Response of Open-Cell Foam

Similar to the models for the quasi-static response of foam, models for the dynamic response of open-cell foam under compression are prolific. It is well known at high strain rates, inertial effects contribute to the dynamic compressive response of open-cell foam (Gibson and Ashby, 1997). Gibson and Ashby (1997) attribute large contributions in this field to a select group of authors consisting of Reid, Stronge, and Wierzbicki. Gibson and Ashby (1997) have provided a succinct summary of the primary results of their publications, pertinent to the field of inertial effects in dynamic compression of foam (Abramowicz and Wierzbicki, 1988; Shim, Yap, and Stronge, 1992; Reid, Reddy, and Peng, 1993). The contribution to the enhanced strength under dynamic crushing is attributed to three dynamic factors: localization, micro-inertia, and densification (Gibson and Ashby, 1997). Localization is the concentration of deformation, at a given instant, into a thin layer, resulting in strain rates which are much larger than the apparent nominal strain rate. Localization is particularly important when considering the micro-inertia of the cell walls, which is associated with rotation and lateral motion of cell walls when they buckle. This suppresses the more compliant buckling modes, increasing the crushing strength, and diffuses the crushing wavefront. Diffusion of the wavefront leads to densification, which causes the stress to increase dramatically due to contact of the cell walls with one another. The combination of these three effects leads to the rate dependence found in the dynamic compression of open-cell foams.

Various models have been proposed to characterize these phenomena, such as the phenomenological models developed by Zhao and Gary (2002). More recently broad experimental studies have shown promise to aid in the development of models (Lee, et al., 2006; Yu, Li, and Hu, 2006). While inertial effects can be important, the most significant contribution to the enhanced dynamic response of foam under compression is often that from the viscous and inertial effects of fluid flow through the foam. However, the complexity of modeling the contribution of fluid flow to the dynamic response of porous media has resulted in this subject becoming one of the most challenging areas of research in the field of cellular solids, and in particular, in the field of open-cell foam. In essence, the topic of this thesis is the viscous flow contribution to the dynamic response of fluid-filled foam. Prior to exploring the literature on this subject in *Section 2.3*, it is first important to consider the types of fluids which could be impregnated in open-cell foam and their properties.

2.2 The Properties of Newtonian and Non-Newtonian Fluids

The most common fluid found in open-cell foam is air. Because air has a small density and an extremely low viscosity, the contribution of air to the dynamic response of low-density, open-cell foam is often negligible. However, the contribution of some liquids can be much more substantial. There are two types of liquids which are considered for impregnation into an open-cell foam: Newtonian and non-Newtonian. Although the focus of this thesis is on liquids, we will not limit our discussion to merely liquids, but we will also discuss fluids in general. The properties of Newtonian fluids are well-known. The definition of a Newtonian fluid is a fluid where the shear stress exerted by the fluid is linearly proportional to the velocity gradient perpendicular to the direction of shear (shear rate), where μ is the constant of proportionality or the Newtonian dynamic viscosity (White, 1999). The behavior of a non-Newtonian fluid,

however, is much more complex. A thorough review of the vast field of non-Newtonian fluid dynamics is given by Bird et al. (1987). Although there are many types of non-Newtonian fluids, in this thesis, we only consider the "generalized Newtonian fluid". The "generalized Newtonian fluid" captures one of the most important characteristics of a non-Newtonian fluid, in that the viscosity η, can be dependent upon the shear rate. However, it cannot describe normal stress effects or time-dependent, elastic effects, which often occur with this unique class of fluids (Bird et al., 1987). In general, the stress tensor $\underline{\tau}$, can be written in terms of the viscosity η, and the rate of strain tensor $\underline{\dot{\gamma}}$, in the form

$$\underline{\tau} = -\eta \underline{\dot{\gamma}} \tag{2.7}$$

where η, is a function of the scalar invariants of $\underline{\dot{\gamma}}$ (Bird et al., 1987).

It has long been observed in engineering that the viscosity of many non-Newtonian fluids exhibits a unique relationship with respect to the strain rate of the fluid (Bird et al., 1989). It is often found that there is a highly linear correlation between the log of the viscosity and the log of the strain rate. This is characteristic of a power-law model, which is one of the most fundamental empirical models for "generalized Newtonian fluids". Power-law models have been used extensively to describe the behavior of many non-Newtonian fluids (Bird et al., 1987). The viscosity of a power-law fluid is given as

$$\eta = m\left(\dot{\gamma}\right)^{n-1} \tag{2.8}$$

where m is the consistency index, n is the power-law exponent, and $\dot{\gamma}$ is the magnitude of the rate of strain tensor or the shear rate of the fluid. $\dot{\gamma}$ is

calculated by taking the square root of one-half of the dot product of the rate of strain tensor with itself. The power-law exponent n, which effectively describes the slope of the line on a log-log plot, can be used to further characterize the fluid. If n =1 and $m = \mu$, the power-law model reduces to a standard Newtonian fluid. If $n < 1$, the fluid is called a pseudoplastic or shear thinning fluid, and if $n > 1$, the fluid is called a shear thickening fluid. Since this model is tractable and found to accurately describe a broad range of fluids, it has become one of the most widespread empirical models used to describe the behavior of non-Newtonian fluids.

2.2.1 The Behavior of Shear Thickening Fluids

In this thesis we consider a special type of non-Newtonian, field-activated fluid commonly referred to as a shear thickening fluid. The behavior of these fluids has been studied for over half of a century; by 1989, Barnes (1989) already counted over 100 references on the subject of shear thickening fluids. Even more recently, shear thickening fluids have received a great deal of attention for use in novel applications because of their unique ability to transition from a low-viscosity state to a high-viscosity state beyond a critical shear stress (Decker et al., 2007). A sample of this shear thickening phenomenon is given for a 50% volume fraction precipitated calcium carbonate (PCC)/Ethylene Glycol (EG) mixture in **Fig. 2.6**. This transition is marked by a rapid and sometimes discontinuous increase in viscosity with incremental increases in shear stress (or shear rate) (Hoffman, 1974; Barnes 1989). The type of shear thickening fluid which has received the most attention is generally comprised of concentrated suspensions of nonaggregating particles disperse in a carrier fluid (Barnes et al., 1989). This thickening behavior for particle dispersions is only known to occur at high volume fractions where the density of the particles is such that their

separation is less than that of the particle diameter; and therefore, multiple-body interactions and lubrication forces between the particles become important (Stickel and Powell, 2005). Comprehensive reviews of the behavior of shear thickening fluids are given by Barnes (1989), Hoffman (1982; 1998), Laun and Bung (1991), and Stickel and Powel (2005).

Explanations for the mechanism for shear thickening have been proposed, but the literature has not reached a consensus as to the exact mechanism. Numerous studies have concluded shear thickening in colloidal suspensions is due to the formation and jamming of clusters of particles ('hydroclusters') bound together by hydrodynamic lubrication forces between particles (Boissis and Brady, 1989; Farr et al., 1997; Foss and Brady, 2000; Catherall et al., 2000) as shown in **Fig. 2.7**. This critical transition occurs when the hydrodynamic forces driving particles together exceed the repulsive forces due to interparticle (i.e. electrostatic or steric) potentials and Brownian motion (Maranzano and Wagner, 2001a). Detailed reviews and quantitative descriptions of the mechanisms for shear thickening of colloidal suspensions are given by Bender and Wagner (1996), Maranzano and Wagner (2001a), and Maranzano and Wagner (2001b). Hoffman, however, has proposed another mechanism for the shear thickening effect, the 'order-disorder' mechanism. He proposed that as a monodisperse suspension is sheared, particles align in hexagonally packed layers parallel to the plane of shear (Hoffman, 1972). After a critical stress is achieved, instabilities in the flow begin to grow, inducing particles out of their ordered layers; these particles then collide and jam into one another, resulting in a dramatic increase in the viscosity of the fluid (Hoffman, 1972). His most recent work couples the 'order-disorder' theory with the 'hydrocluster' theory in that once the particles have been driven

out of their ordered layers, they may form hydroclusters of particles both with and without particle contact, which then jam into one another (Hoffman, 1998).

2.2.2 Effect of Composition of Shear Thickening Fluids

The behavior of a shear thickening fluid is strongly governed by the composition of the fluid. Many studies have examined the effect of the properties of the suspension on the rheological properties of shear thickening fluids. Some of the properties that have been studied include the particle size, the particle shape, the volume fraction of particles in the fluid, the polydispersity of particles, the particle charge, the particle surface characteristics, the Brownian energy of the particles, and the fluid viscosity (Hoffman, 1972; Bossis and Brady, 1989; Bender and Wagner, 1996; Maranzano and Wagner, 2001a). Comprehensive reviews of the effects of these parameters can be found in Laun et al. (1991), Barnes (1989), and Stickel and Powell (2005). Barnes (1989) considered the following six properties as the most important factors: the volume fraction of particles in the fluid, the particle size, the polydispersity of particles, the particle shape, the particle-particle interaction, and the fluid viscosity. Understanding the effects of these properties is critical in that they allow a shear thickening fluid to be designed according to desired specifications.

Barnes (1989) suggests the rheology of shear thickening fluids depends substantially upon the volume fraction of particles in the dispersion Φ. The shear thickening effect has only been observed to occur at relatively high volume fractions where the particles are within close enough proximity to one another that interparticle forces can play a role. The exact volume fraction, which induces the shear thickening effect, is based upon the properties of the particles and the suspending fluid. The range of volume fractions of particles in dispersions which have exhibited shear thickening characteristics is quite large,

varying from as low as 10% to greater than 60% (Clark, 1967; Hoffman, 1972; Barnes, 1989; Egres et al., 2006). However, most recent studies utilize near hard sphere dispersions, which tend to exhibit shear thickening beyond 40-50% volume fraction at relatively low-strain rates (Bender and Wagner, 1996; Maranzano and Wagner, 2001a; Gopalakrishnan and Zukoski, 2004). These studies also reveal commonly known trends that as the volume fraction is increased, for any given shear thickening fluid, the critical shear stress required for shear thickening decreases, the overall viscosity increases, and the corresponding magnitude of the viscosity jump increases as shown in **Fig. 2.8** by Egres et al., 2005.

The effect of the size of particles and the distribution of the sizes of particles on shear thickening fluids has also been the subject of numerous investigations (Wagstaff and Chaffey, 1977; Barnes, 1989; D'Haene and Mewis, 1994; Chow and Zukoski, 1995; Hoffman, 1998; Maranzano and Wagner, 2001a; Egres and Wagner, 2005). The primary effect of the size of the particles has been shown to be on the transition value of the critical stress (Hoffman, 1972; and Barnes, 1989). Models have been developed by Bender and Wagner (1996), which relate the critical shear stress transition value to the characteristic particle size. In general, for monodisperse spherical particles, the shear stress is expected to scale with the characteristic radius of the particles to the third power for electrostatically stabilized particles and to the second power for Brownian suspensions. The distribution of the characteristic particle sizes also has an effect on the critical shear stress. In general, it is well known that increasing the polydispersity increases the critical shear stress transition value and decreases the overall shear thickening effect (Wagstaff and Chaffey, 1977; Barnes, 1989; D'Haene and Mewis, 1994; Bender and Wagner, 1996).

In addition to the size of particles, the shape of the particles, the particle-particle interactions, and the continuous phase viscosity also have a dramatic effect on the behavior of a shear thickening fluid. As particles become more anisotropic, both Barnes (1989) and Egres and Wagner (2005) found the shear thickening effect occurs at much lower volume fractions and the magnitude of the critical jump in viscosity increases. The interparticle interactions also govern the magnitude of the increase in the viscosity. There are three types of suspensions: Flocculated, neutral, and electrostatically charged particles (Barnes, 1989). Flocculated suspensions do not exhibit shear thickening, but rather shear thinning. Neutral particles (Brownian or hard spheres) exhibit shear thickening and repulsive particles (electrostatically charged particles) demonstrate even more dramatic shear thickening (Barnes, 1989). Barnes proposes an explanation for this observation; as the distance between the particles increases, the effective volume fraction increases, decreasing the critical shear stress. This phenomenon can be more clearly envisioned by realizing increasing the distance between particles is similar to increasing the effective diameter of each particle, which, as previously discussed, results in a larger effective volume fraction. Finally, the continuous phase viscosity also contributes significantly to the behavior of shear thickening fluids. Barnes (1989) noted that for like dispersions, changing the continuous phase viscosity by a factor changes the suspension viscosity by the same factor.

2.2.3 Commonly Studied Shear Thickening Fluids

Knowing the effects and contributions of various characteristic properties of a dispersion has allowed researchers to begin to focus on designing more tailored fluids, which exhibit a behavior that may be advantageous in certain applications. Recent literature has focused heavily on a specific type of colloidal dispersion utilizing monodisperse, spherical nanoparticles (Bender and Wagner,

1996; Maranzano and Wagner, 2001a; Maranzano and Wagner, 2001b; Lee and Wagner, 2003; Gopalakrishnan and Zukoski, 2004). In most of these studies, near hard-sphere, silica nanoparticles with diameters on the order of 100 nm are suspended in ethylene glycol or polyethylene glycol at volume fractions typically ranging from 40% to 60%. There are a number of advantages to this type of fluid. One of the primary reasons this particular shear thickening fluid has received a great deal of attention is that it exhibits reversible shear thickening on very short time scales (Bender and Wagner, 1996; Maranzano and Wagner, 2001a). It also demonstrates dramatic shear thickening with jumps in the magnitude of the viscosity of several orders of magnitude. Moreover, these fluids are practical, being comprised of relatively inexpensive and nonhazardous materials. While much of the attention in this field has been on silica based dispersions, more recently other colloidal suspensions have also been the subject of numerous investigations. Egres and Wagner (2005; 2006) have examined acircular-precipitated calcium carbonate colloidal suspensions. This type of shear thickening fluid is also practical economically, and it has shown potential to have an even more dramatic shear thickening effect. In this thesis we examine the potential for both of these types of shear thickening fluids.

2.2.4 Rheology of Non-Newtonian Fluids

Characterizing the behavior of shear thickening fluids is a complex and challenging area of research. Although there have been some studies on the complex viscosity under dynamic shear (Lee and Wagner, 2003) and on the extensional flow properties (Bettin, 2005a), the majority of research has only consider steady state shear behavior (Bender and Wagner; Maranzano and Wagner, 2001). One of the greatest problems with performing any rheological studies of highly shear thickening fluids is the problem of wall slip (Hu and

Larson, 2002; Yoshimura and Prud'Homme, 1988). Hu and Larson (2002) and Yoshimura and Prud'Homme (1988) provide detailed discussions of slip and methods for mitigating it. Slip between the fluid and the instrument occurs because inhomogeneous fluid properties occur at the solid boundaries. A reduced fluid viscosity is often observed at the boundary, creating a thin layer of fluid having a large velocity gradient that can be treated as a slip layer (Yoshimura and Prud'Homme, 1988). Bettin (2005a) found the effect of slip could be completely eliminated for monodisperse suspensions by roughening the surfaces to a roughness on the order of the characteristic size of the particles. Roughening the surfaces of instrumentation is most readily done with the parallel plate fixtures utilized for steady shear experimental configurations. Thus, the ability to eliminate slip in steady state experiments has resulted in it being one of the most widely used methods for characterizing the rheology of shear thickening fluids.

2.3 Fluid Flow Through Porous Media

Flow through porous media has been studied for over a century, dating back to Henry Darcy in 1856. Darcy (1856) published one of the most noteworthy articles in this field on his study of water flow through sand. In this study, he developed what is now known as Darcy's Law, which is a phenomenological model relating the characteristic properties of the fluid to the characteristic properties of the flow through a factor called the intrinsic permeability k, and given as

$$\Delta P = \frac{-\mu \underline{V}}{k} \tag{2.9}$$

where P is the local pressure in the fluid and $\underline{V}$ is the local velocity vector of the fluid. The permeability is a property of the porous media and is a measure of its porosity and tortuosity or the effective resistance to flow. Although Darcy's work is only applicable to low-Reynolds number flow, where viscous forces dominate inertial forces, much of the field of flow through porous media has been built upon his work. This is primarily because most flows encountered in engineering have sufficiently low Reynolds numbers to be dominated by viscous forces. Over time, modifications to Darcy's law have been made to account for the translational flow between boundaries (Brinkman, 1947) and inertial effects with the Forchheimer equation (Dupuit, 1857); however, the utilization of these more complex equations in permeability studies has been limited.

2.3.1 Intrinsic Permeability of Porous Media

Understanding the intrinsic permeability of porous media is relevant to a vast array of disciplines from chemical engineering to geophysics to fluid mechanics. Because of its importance in many engineering disciplines, this topic has received a great deal of attention over the past century. Even by 1975, a number of extensive reviews had been published in the field (Bear, 1972; Dullien, 1975); however, only recently have more advanced topics on the flow of non-Newtonian fluids through porous media been explored.

A number of studies have been undertaken on non-Newtonian fluid flow through porous media (Kawase and Ulbrecht, 1983; Comiti and Renaud, 1989; Sahimi, 1993; Sabiri and Comiti, 1996; Shah and Yorsos, 1995; Seguin et al., 1996; Comiti et al., 2002; Chen et al., 2005). All of these studies examine similar capillary-type flow models, which directly follow from Darcy's law and are only applicable in the viscous regime where inertial forces can be neglected. These capillary-type models allow for the components of the permeability (porosity

and tortuosity) to be clearly distinguished and studied. Since both the models and the experiments in these papers are designed for high viscosity fluids with low Reynolds number flows through low porosity materials, such as packed granular beds, Darcy's law is highly applicable. The treatment of these analyses is further simplified with the use of power-law based descriptions of the non-Newtonian fluid. Despite the relatively simple treatment, these studies developed comprehensive models for both the mass transfer and the pressure drop, which were shown to describe experimental results remarkably well (Sabiri and Comiti, 1996; Seguin et al., 1996; Comiti et al., 2002).

For over a century one of the greatest challenges has been modeling the transition from the creep regime, where Darcy's law is applicable, to the regime where inertial effects become important. Various experimental studies found characteristic Reynolds numbers marking the transition for open-cell foam (Gent and Rusch, 1966), porous rock (Tek, 1957), and fixed beds of spheres and cylinders (Dybbs and Edwards, 1984). More recently, significant advances have been made by Seguin, who developed models for the case of flow rates applicable to Darcy's law, which describe experimental data well (Seguin et al., 1998a; Seguin et al., 1998b; Seguin et al., 2000).

In addition to developing a better understanding of the flow rates applicable to Darcy's law, considerable advances have also been made in understanding what types of porous materials Darcy's law can be applied to. Although Darcy's law was developed for low porosity media, such as soils, it has also been shown to be applicable to highly porous structures, such as low-density foams by Jones and Fesman (1965) and Gent and Rusch (1966) who examined the flow of air through open-cell foam and described relationships between the cell structure and the permeability of the open-cell foam. Gent and Rusch (1966) also developed a model for the deformation of open-cell foam under compression in the linear

elastic regime. Their hypothesis of the kinematic behavior of open-cell foam was supported by permeability studies. Hilyard and Collier (1987) later extended their work, developing and testing a theoretical capillary-based model for predicting the effect of strain on the permeability of reticulated, flexible foam in the regime where inertial forces cannot be neglected. Innocentini et al. (1999) also successfully examined the applicability of Forchheimer's modified Darcy equation to the more complex flow regime, where inertial effects cannot be neglected. Finally, Sabiri (1996) recently examined the pressure drop of non-Newtonian fluid flow through open-cell foam. He developed a capillary-type model based on Forchheimers' modified Darcy's law with a power-law fluid. While his model was successful in describing the characteristic trends observed experimentally, the models failed to accurately describe the magnitude of the response observed.

Overall, the success of analytical models in providing a comprehensive description of the flow of fluids through highly porous materials, such as low-density, open-cell foam, has been limited. This has resulted in the development of numerous computational methods for modeling the permeability of open-cell foam (Mills and Lyn, 2002; Fitzgerald et al., 2004; Mills, 2005). Although the analytical extension of Darcy's law to highly porous materials and the numerous computational studies have been a substantial contribution to the field of flow through open-cell foam, there is still a need to examine this field further. Despite these extensive studies, a tractable permeability model for open-cell foam, applicable to a wide range of foam grades and a large range of compressive strains, has yet to be developed. Moreover, an understanding of the intrinsic permeability of open-cell foam under deformation has yet to be extended to model the response of fluid-filled foam under dynamic loading.

2.3.2 Dynamic Compressive Response of Fluid-Filled Foam

A logical extension of quasi-static study of flow through porous materials is the study of the response of a fluid-filled, porous material under dynamic loading. Despite the enormous number of applications, this subject has received very little attention in the literature. There could be multiple reasons for this, including the fact that modeling the deformation behavior of porous media is complex, and modeling the effect of the fluid flow on the kinematics of the porous media is even more difficult. To date, there is no in-depth model for the response of fluid-filled foam under dynamic compression; however, a handful of experimental studies of this subject have been carried out.

Hilyard and Kanakkanatt (1969) carried out one of the first studies of the mechanical damping properties of liquid-filled foams. Their experiments examined how temperature changes affect fluid damping in liquid-filled, flexible, open-cell foam. Hilyard (1971) followed this experimental study by developing the first computational model for the response of liquid-filled, open-cell foam under dynamic compression. Hilyard (1971) developed a third-order, non-linear equation of motion describing the contribution of the fluid to the impact behavior of open-cell foam. His study was shown to be in good agreement with experimental results. However, this model is highly intractable and requires multiple empirical constants, which vary strongly with small changes in the parameters of the system. Therefore, the results of this analysis could only be taken as a qualitative description of the dynamic response of fluid-filled foam. Recently, more robust numerical analyses on closed-cell foams have been carried out and verified with comprehensive experimental studies (Rehkopf, McNeice, and Brodland, 1995; Rehkopf, McNeice, and Brodland, 1996). Rehkopf and colleagues successfully developed computational models for the compressive response of fluid-filled, closed-cell foam under cyclic dynamic compression. Their models separated the response of the fluid (air) inside the

cells from that of the foam. Using this model, they demonstrated as foam undergoes cyclic compression, the foam structure degrades and the contribution of the fluid to the response of the fluid-filled foam decreases.

More advanced computational methods for the complete dynamic response of fluid-filled, open-cell foams have been developed by Mills and Lyn (2002) and Schraad and Harlow (2005). In particular, Schraad and Harlow (2005) have a comprehensive code, which can be utilized on a broad range of problems, but the complexity of their code has limited its use. In addition, there is insufficient experimental data to verify their code. The only known experimental studies have been carried out by Tyler and Ashby (Gibson and Ashby, 1997) who examined for a narrow range of experiments. Their studies are compared with a tractable scaling model developed by Gibson and Ashby (1997) for the contribution of a fluid to the dynamic compressive response of fluid-filled foam. This model, based on scaling relations, is considered to be the only known closed-form model describing this phenomenon. Gibson and Ashby considered a simple 2-D axial compression model for fluid-filled foam as shown in **Fig. 2.9**. They assumed viscous flow where Darcy's law governs the flow. Furthermore, they described the kinematics of deformation by extending the Gent and Rusch model, derived for the small strain limit, which approximates the average diameter of a cell d, as a function of strain ε, and the initial diameter d_o (Gent and Rusch, 1966):

$$d = d_o\left(1-\varepsilon\right)^{\frac{1}{2}}. \tag{2.10}$$

Furthermore, they assumed the gradient of the pressure in the fluid $\frac{dP}{dr}$, is proportional to the local stress in the fluid σ, and the characteristic length scale of the foam R, and is given as (after Gibson and Ashby, 1997)

$$\frac{dP}{dr} \approx -\frac{\sigma}{R}. \tag{2.11}$$

Coupling these previous relations with Darcy's law and continuity conditions, the average stress contribution of the fluid to the dynamic compressive response of the fluid-filled foam over the entire width of the foam is determined to be (after Gibson and Ashby, 1997)

$$\sigma_f = \frac{C\mu\dot{\varepsilon}}{1-\varepsilon}\left(\frac{R}{d_o}\right)^2 \tag{2.12}$$

where C is an empirical constant on the order of unity and $\dot{\varepsilon}$ is the strain rate of the foam or the time rate of change in the height of the foam $\dot{h}$, divided by the current height of the foam h. One of the main advantages of this model is the fact that it is tractable and useful for engineering design. Moreover, it readily allows for the contribution of each parameter to the response of the system to be identified. The key scaling observations are that the stress scales proportionally to the strain rate and the viscosity to the first power and the radius to the second power. The stress is also inversely proportional to the cell-size to the second power. Therefore, adjusting the characteristic dimensions of the foam has a much more significant impact than adjusting the properties of the fluid or the rate of deformation. This model is only applicable to Newtonian fluids since the scaling arguments do not allow for introduction of a strain-rate-dependent viscosity, which is required to describe a non-Newtonian fluid. Gibson and Ashby (1997) demonstrated this model qualitatively describes experimental data well for Newtonian flow over a limited range of strains and strain rates. However, they did not propose a range of parameters over which their model is valid nor is the model validated experimentally; therefore, the general

applicability of this model to a wide class of problems is not known. Overall, the flow of fluids through porous media, and in particular open-cell foam, has been investigated extensively for a variety of engineering applications, but characterizing the contribution of fluid to the response of fluid-filled foam under dynamic loading remains a critical area of research.

2.4 Applications of Fluid Impregnated Foam

Society could benefit greatly from the introduction of fluid-filled foam into a variety of engineering applications. In particular, fluid-filled foam is envisaged to have enormous potential in the area of protective equipment for energy absorption and blast wave protection. The versatile characteristics of fluid-filled foam, such as its flexibility, formability, and scalability, allow for it to be useful in everything from commercial helmets to vehicle armor. In addition, the inherent robustness due to its passive and reversible nature, makes fluid-filled foam suitable for long-term applications in adverse environments with little maintenance. Moreover, economically and practically, the low-cost and thin characteristic design make it appealing to both the manufacturer and the consumer. Finally, the highly controllable nature of fluid-filled foam (i.e. pore size, porosity, fluid properties) allows for it to be easily tailored to protect against a wide-range of design criteria, making it useful in mitigating the effects of dynamic impacts and blast waves.

2.4.1 Prior Art - Fluid Impregnated Materials

Recently, the effectiveness of fluid impregnated composites has been recognized in a variety of energy absorption research (Hayes and Robinovitch, 1997; Lee et al., 2003, Maranville and Ginder, 2005; Tan et al., 2005; Fischer et al., 2006; Deshmukh and McKinley, 2006; Decker et al., 2007;). All of these studies have

examined the use of either active or passive field-responsive fluids or fluids that change their properties in response to an externally applied field or load. The primary active fluids examined in these studies are magnetorheological fluids (Maranville and Ginder, 2005; Deshmukh and McKinley, 2006). These studies have shown magnetorheological fluids demonstrate enormous potential for controlled energy absorption applications; however, the disadvantage to active fluids is the need to control an externally applied field (i.e. magnetic or electric). This inherently builds in complications, such as reliability issues, increased cost, and increased weight. Therefore, passive fluids, such as shear thickening fluids, which respond automatically to an applied stress, have a substantial advantage over active fluids.

Shear thickening fluid impregnated composites have been proposed for hip protection pads (Hayes and Robinovitch, 1997), ballistic resistant armor (Lee et al., 2003 and Tan et al., 2005), blast resistant armor (Bettin, 2005a), and stab resistant fabrics (Decker et al., 2006). Each of these designs exhibited high flexibility, making them comfortable to wear as personal protective equipment. They also demonstrated the ability to harden during high rate impact, absorbing and shunting energy effectively. The results of each are summarized as follows: 1) the hip protection design reduced the load on the femur by approximately 50% over the impact load; 2) the ballistic resistant armor reduced the projectile penetration depth by 10-20% over neat Kevlar, 3) the stab resistant fabrics increased the peak load before penetration by 100-200%. **Fig. 2.10** shows a sample image of the enhanced stab resistance of Kevlar impregnated with a shear thickening fluid over that of neat Kevlar alone (Decker et al., 2007). The success of these studies indicates composites impregnated with shear thickening fluids are some of the most promising novel technologies in the area of protective equipment.

2.4.2 Energy Absorption

With the dramatic increase in fatalities each year from high energy impacts in transportation and sports, the need for improved energy absorption technologies is becoming increasingly apparent. As previously discussed, one of the primary areas of research in this field is to protect the head from impact loading. Recently, numerous studies have examined new energy absorbing technologies for bicycle helmets (Gilchrist and Mills, 1996; Mills and Gilchrist, 2006; Mills and Gilchrist, 2007), motorcycle helmets (Gilchrist and Mills, 1994; Shuaeib et al., 2002a; Shuaeib et al., 2002b; Shuaeib et al., 2007), and vehicle impacts (Fuganti et al., 2000; Deshmukh and McKinley, 2006). Using knowledge of the biomechanics of head injury, these studies have considered everything from new geometric configurations to revolutionary materials, such as magnetorheological fluid-filled foams (Deshmukh and McKinley, 2006), and novel metallic and polymeric foams (Fuganti et al., 2000; Shuaeib et al., 2007). They have also developed extensive finite element models (Gilchrist and Mills, 1994; Aare and Kleiven, 2005; Mills and Gilchrist, 2006; Shuaeib et al., 2007) to predict the effects of varying design parameters on the impact protection of commercial and military helmets. These techniques have great promise in helping to develop the optimal design configuration.

Ideally, protective equipment for the head would be lightweight, thin, comfortable, inexpensive, and reliable. In addition, it must efficiently absorb the energy of an impact without causing the head to exceed certain acceleration standards. Shuaeib et al., (2002a) provides an overview of the primary acceleration based standards for preventing brain injury, but the most commonly used standard is the Peak Linear Acceleration (PLA) standard. The PLA standard requires the head accelerates less than 300 g under direct impact of a 5 kg mass traveling at 6 m/s to 7.5 m/s (90 J to 40 J) (BS6658, 1985; Gilchrist and Mills, 1994; Shuaeib et al., 2007). Knowing the weight of the head (plus helmet if

applicable), the maximum allowable acceleration can be translated into a maximum peak load on the head or "threshold load" (Gilchrist and Mills, 1994). To make the design as thin and lightweight as possible, the deformation distance over which energy is absorbed would be minimized and the area over which the load is applied would be maximized. Therefore, since helmets are already designed to maximize the load distribution over the head, the optimal helmet design would absorb a given level of energy at the maximum achievable load. Since the maximum achievable load is limited by safety standards (threshold load), the optimally configured helmet would absorb the necessary amount of energy at the threshold load. Because the "plateau-like" stress response of foam under compression is ideal, foam has been accepted as the standard energy absorption material in helmets (Gilchrist and Mills, 1992; Shuaeib et al., 2002b). Currently, to absorb the necessary amount of energy, foam in helmets is usually relatively thick and made of an inelastic material (Shuaeib et al., 2007). This results in cumbersome helmets, which are only useful in single impact scenarios. Moreover, they are often brittle in nature, making them difficult to manufacture and uncomfortable to wear (Shuaeib et al., 2007). Shuaeib et al. (2007) has recently proposed a new, more resilient and flexible foam to address comfort issue and improve the multi-impact protection; however, this design still requires a relatively large thickness.

A liquid-filled foam composite helmet, on the other hand, can be engineered to have the desired dynamic response while being thin, lightweight, and cost effective. One of the greatest advantages of this type of design is its ability to enhance the multi-impact protection of helmets. This is an essential feature since real accidents often involve multiple, successive impacts. Shuaeib et al. (2007) discussed the crash kinematics of motorcycle accidents and noted successive, helmeted-head impacts may be equally as dangerous as the initial helmeted head impact. Therefore, the study of liquid-filled foam composite helmets is of

interest since they have enormous potential to reduce the overall thickness and weight of current brittle foam helmets while increasing the multi-impact protection.

2.4.3 Blast Wave Protection

Of possibly greater import is developing new technologies capable of defending against explosive devices. In the past much of the research in developing armor has focused on providing protection against ballistics. This research has culminated in highly advanced armor for defending against projectiles, but left armor highly inefficient at protecting against the enormous pressure gradients generated by explosive devices (Cheeseman, 2003). The recent surge in terrorist bombing has revealed the urgent need to focus on blast protection technologies. Fortunately, the scientific community has met this need with a recent deluge of research papers covering blast protection technologies; these studies have explored everything ranging from mechanized systems to infrastructure to the human body.

In today's tumultuous military climate some of the most critical lines of defense are armored transport vehicles and vessels. Although, there is a growing need for increased protection of armored vehicles from IED's, much of the current research on protecting military transport from blast waves is focused on marine vessels. Marine vessels can readily experience catastrophic failure from underwater explosions because of the wave propagation characteristics of water and higher pressures on submerged vessels. In particular, since the advent of the submarines, the effects of blast waves on marine vessels has become an even more important area of research. However, much of this research has been funded by national governments and remains restricted for the purposes of

national security. Nevertheless, a plethora of literature exists on the fundamental transient response of basic structures subjected to blast waves (Geers, 1971; Huang 1969; Huang, 1974). Recently, with the inception of commercially available finite element and finite volume codes has made numerical simulations of the devastating impact of blast waves on increasingly complex structures has become publicly available. Liang and Tai (2006), Greenhorn (1988), and Hung et al. (1999) all provide in depth numerical analyses of the transient response of marine vessels subjected to underwater explosions. These studies demonstrate that developing a blast-resistant armor for marine vessels remains a critical area of research. Many promising technologies have been proposed to protect military vessels from blast waves. Most of the current research focuses on integrated composite armor technologies. Abrate (2003), Tasdemirci et al. (2003), and Mines (2004) examine simple analytical stress wave analyses for lightweight multi-layer composite armor. Gama et al. (2001) explores the effects of incorporating an aluminum foam layer into composite armor to better defend against blast waves. Fleck and co-workers provide detailed analytical models for the response of sandwiched structures to shock loading (Fleck and Deshpande, 2004; Qiu et al., 2005). In addition, Hutchinson and Xue also studied the performance of various sandwich structures under impulse pressure loads (Xue and Huctchinson, 2005; Xue and Hutchinson, 2004; Hutchinson and Xue, 2005). Recently Mahfuz (2006) has also contributed to this field studying external effects such as temperature and rate sensitivity. All of these studies found composite armor with either foam or honeycomb layers has great potential to efficiently defend against blast loading. However, these technologies utilize irreversible, plastic deformation to defend against shock waves, making them ineffective against repeated loading. Furthermore, while these designs are relatively

lightweight, the thickness of the foam layers prohibits their use in some applications.

Due to the dramatic increase in terrorist bombings, developing armor for the protection of infrastructure from blast waves has recently been driven to the forefront of research. Elliot et al. (1992) and Ngo et al. (2007) provide excellent overviews of the effects of blast loading, caused by high explosives, on buildings. A number of researchers have explored experimental techniques for determining the most suitable materials for blast mitigation and containment (Fedorenko, et al., 2004; Louca, et al., 2004; Davidson, 2005). Clutter (2004) presents methods of using hydrocode simulations to asses the vulnerability of structures while Talaslidis et al. (2004) uses a standard finite element technique. Davidson et al. (2005) and Morison (2006) also use numerical simulations to analyze methods of mitigating the damage caused by blast waves using reinforced structures. Luccioni (2004) and Smith et al. (2001) experimentally analyze the effects of high explosives on infrastructure in urban settings and discuss schemes for protecting infrastructure against blast waves. With the increased use of improvised explosive devices (IED's) in urban warfare, improved methods for protecting infrastructure against blast loading is becoming more essential. One of the most well researched methods of defending buildings from the effects of blast loading is by way of a passive blast wall. Boh et al. (2005) provides a detailed overview of the state-of-the-art knowledge of the effectiveness of blast walls. However, utilizing blast walls in most structures is not practical due to space constraints and the high cost. A more promising, commercially available technology for the protection of infrastructure from blast waves is BlastWrap® manufactured by BlastGard Int. (Clearwater, FL). BlastWrap® uses a combination of multi-phase materials designed to absorb energy through permanent deformation. It has

shown great potential and is already being implemented in structures in Washington D.C. Unfortunately, this technology uses a non-reversible process to absorb energy, making it inefficient at resisting multiple impacts. It is also only suitable for structural applications where size and weight are not of critical importance.

Similar to structural protective measures, developing personal protective equipment, which has the ability to efficiently defend against blast loading, has historically been an active area of research. This area of research has dated back more than two centuries. In 1788, Jars first described the phenomenon of blast injury, which corresponds to today's definition of primary blast injury (Richmond, 1991). Primary blast injury describes an injury, typically to organs containing air, sustained directly from a blast wave impacting the body. Although records of fatalities caused by primary blast injuries can be found in nearly all major conflicts in the past century, blast injuries did not receive much attention until aerial bombings of civilian centers in World War II (Richmond, 1991). In the 1940's the U.S. government performed studies on air blasts and determined primary blast injury are of greatest concern for people in confined spaces or in submerged marine vessels (Richmond, 1991). However, over the past few decades, the strength of high explosives has increased, and the risk of blast injuries has risen dramatically in every part of society. This is most evident in recent terrorist attacks where improvised explosive devices are used in densely populated urban areas. These attacks have resulted in a significant number of military and civilian casualties due to blast injury.

Recent studies have concluded high-frequency, small amplitude waves play the dominant role in lung injury from blast loading, generating large pressure

gradients in the lung, as opposed to thoracic compression, caused by low-frequency, large-amplitude waves (Grimal, 2005, Cooper, and Richmond (1991)). Schardin (1950) proposed three primary mechanisms of injury. The first considers an engineering analysis of a shockwave propagating from a dense medium to a less dense medium. In this case much of the wave is reflected backwards as a tension wave, causing spalling at the interface of the media (Richmond, 1991). Another proposed mechanism of injury is based on the fact that the air in many organs is more readily compressed than other fluids. For large enough pressure gradients across membranes with fluid-air interfaces, the resulting stress can result in severe microstructural damage. For example, a pressure gradient across the alveolar-capillary interface on the order of $5x10^6$ N/m^3, can result in microscopic hemorrhaging and air embolisms caused by rupture of the alveolar septa and interstitial vessel walls (Argyros (1989), Candole (1967), Coppel (1976), and Leibovici et al. (1999)). A third mechanism of injury proposed relates to inertial effects. A shock wave is expected to cause matter of different masses to accelerate at different rates, which can also lead to microscopic hemorrhaging and air embolisms. All of these injury mechanisms can result in air entering adjacent pulmonary veins and causing cardiac arrest.

It is well known that a significant reduction in the magnitude of the pressure gradient of a blast wave would have enormous potential to prevent primary blast injuries. During World War II methods of protecting the body from blast waves were explored. Single layers of both soft and rigid materials were found to be ineffective at preventing injury (Richmond, 1991). In fact, many studies found a decrease in the threshold level of injury compared to controls without protection. Moreover, it was also discovered combinations of soft and rigid materials in the wrong order increased the potential for injury (Richmond, 1991).

However, when rigid materials, such as Kevlar, were placed over softer materials, such as foam, the resulting armor was found to be effective at significantly reducing the severity of injuries. This protection was provided by the impedance mismatch between the rigid and soft layers (Richmond, 1991). While this result was promising, a practical composite armor, capable of protecting against projectiles as well in a weight- and size- efficient manor, was not developed.

Composites with layers of open-cell, liquid-filled foam have extraordinary potential in all blast protection applications. The layer of liquid-filled foam is designed to impede shockwaves by increasing the time it takes stress waves to propagate through the foam medium and decreasing the resulting pressure gradient experienced by subsequent media. When a shockwave encounters a typical outer protective layer of armor, such as Kevlar, it is typically reflected, imparting a large momentum. In the case of standard body armor, this would impart a large impulse to the body under a very short time period. As the fluid-filled foam compresses, more of the stress wave is allowed to propagate through to the underlying structure. The effect is a delay in the transmission of the impulse into the underlying structure, and thus, a reduction in the pressure gradient of the shockwave, as it is forced to propagate through the composite armor over a longer duration of time. Liquid-filled foam armor not only has potential to increase the ability of armor to protect against blast waves, but it also has a number of other advantages. As previously discussed, the thickness and the weight of liquid-filled composite structures can be substantially less than many other designs. This is especially true considering there is no additional weight necessary as in the case of active components, such as the batteries and circuits necessary for electrorheological and magnetorheological systems. In fact,

the weight can be reduced even further by utilizing shear thickening fluids comprised of hollow spheres. In addition, the versatile characteristics of fluid-filled foam, such as their flexibility, functionality, reliability, and scalability, make them extremely attractive for a range of military applications where all of these factors are crucial. Moreover, economically, their low-cost is ideal for military blast protection technologies where mass production is a necessity. Finally, the highly controllable response of liquid-filled foams allows for them to be readily engineered to protect against a wide-range of blast loads, making them ideal for a plethora of blast mitigation technologies.

References

Aare, M. and Kleiven, S., (2005), "Evaluation of Head Response to Ballistic Helmet Impacts using the Finite Element Mehod", *Int J Impact Eng.*, **34**. 596-608.

Abrate, (2003), "Wave Propogation in Lightweight Composite Armor", *J. DE Phys. IV.* **110**, 657-62.

Abramowicz, W. and Wierzbicki, T., (1988), "Axial crushing of foam-filled columns", *Int J Mech Sci, 30*, 263-271.

Argyros, (1989), "Management of Primary Blast Injury", *Toxicology*, **121**, 105-115.

Barnes, H., (1989), "Shear-Thickening "Dilatancy" in Suspensions of Nonaggregrating Solid Particles Dispersed in Newtonian Liquids", *J. Rheo.* **33**, 329-366.

Bart-Smith, H., Bastawros, A., Mumm, D., Evans, A., Sypeck, D., Wadley, H., (1998), "Compressive Deformation and Yielding Mechanisms in Cellular Al Alloys Determined Using X-Ray Tomography and Surface Strain Mapping", *Acta Mat.* **46**, 3583-92.

Bear, J., (1972), "Dynamics of Fluids in Porous Media", Elsevier, New York, NY.

Bender, J. and Wagner, N., (1996), "Reverisible Shear Thickening in Monodisperse and Bidisperse Colloidal Dispersions," *J. Rheo.*, **40**, 899-916.

Bettin, G., (2005a), "Energy Absorption of Reticulated Foams Filled with Shear-Thickening Silica Suspensions", Doctoral Thesis. *Massachusetts Institute of Technology.*

Bettin, G. and McKinley, G.H., (2005b), "High Deformation Rate Behavior of Polymeric Foams Filled with Concentrated Silica Suspensions,".*Soc. Rheology 77th Annual Meeting.*

Bird, R.B. et al., (1987). Dynamics of Polymeric Liquids 2nd Edition. John Wiley & Sons. New York, NY.

Boh, J.W., Louca, L.A., and Choo, Y.S., (2004), "Energy Absorbing Passive Impact Barrier for Profiled Blastwalls", *Int. J. Impact Eng.*, **31**, 976-95.

Bossis, G. and Brady, J., (1989), "The Rheology of Brownian Suspensions", *J. Chem. Phys.*, **91**, 1866-74.

Brinkman, H., (1947), "A Calculation of the Viscous Forces Exerted by a Flowing Fluid in a Dense Swarm of Particles", *Appl. Sci. Res. A*, **1**, 27-34.

BS 6658, (1985), "Protective Helmets for Vehicle Users", *British Standards Institution*, London.

Candole (1967), Blast Injury, *Can. Med. Assoc. J.*, **96**, 207-14.

Catherall, A.A. et al., (2000), "Shear Thickening and Order-Disorder Effects in Concentrated

Colloids at High Shear Rates," *J. Rheo.*, **44**, 1-25.

Cheeseman, B. and Bogetti, T, (2003), "Ballistic Impact into Fabric and Compliant Composite Laminates", *Comp. Struct.*, **61**, pp. 161-173.

Chen, M., Rossen, W., Yortsos, Y., (2005), "The Flow and Displacement in Porous Media of Fluids with Yield Stress", *Chem. Eng. Sci.*, **60**, 4183-4202.

Chow, M. and Zukoski, C., (1995), "Non-Equilibrium Behavior of Dense Suspensions of Uniform Particles: Volume Fraction and Size Dependence of Rheology and Microstructure", *J. Rheo.*, **39**, 33.

Clarke, B., (1967), "Rheology of Coarse Settling Suspensions", *Trans. Inst. Chem. Eng.*, **45**, 251-56.

Clutter, J. and Stahl, M., (2004), "Hydrocode Simulations of Air and Water Shocks for Facility Vulnerability Assesments", *J. Haz. Mat.*, **106A**, 9-24.

Comiti, J. and Renaud, M., (1989), "A New Model for Determining Mean Structure Parameters of Fixed Beds From Pressure Drop Measurements: Application to Beds Packed with ParallelPipedal Particles", *Chem. Eng. Sci.*, **44**, (7), 1539-1545.

Comiti, J., Montillet, A., Seguin, D., and Hilal, M., (2002), "Modelling of Power Law Liquid-Slid Mass Transfer in Packed Beds at Darcy Regime", *Chem. Eng. J.*, **89**, 29-36.

Comiti, J., Sabiri, N., and Montillet, A., (2000), "Experimental Characterization of Flow Regimes in Various Porous Media-III: Limit of Darcy's or Creeping Flow Regime for Newtonian and Purely Viscous Non-Newtonian Fluids", *Chem Eng. Sci.*, **55**, 3057-3061.

Cooper, G., Townend, D., Cater, S., Pearce, B., (1991), "The Role of Stress Waves in Thoracic Visceral Injury from Blast Loading: Modification of Stress Transmissiono by Foams and High-Density Materials", *J. Biomech.* **24**, 273-295.

Coppel, (1976), "Blast Injuries of the Lungs". *Br. J. Surg.*, **63**, 735-737.

Darcy, H., (1856), Les Fontaines Publiques de la Ville de Dijon, Dalmont, Paris.

Davidson, J., Fisher, J., Hammons, M., Porter, J., and Dinan, R., (2005), "Failure Mechanism of Polymer-Reinforced Concrete Masonry Walls Subjected to Blast", *J. Struct. Eng.*, **131**, 8, 1194-1205.

Decker, M., Halbach, C., Nam, C., Wagner, N., Wetzel, E., (2007), "Stab Resistance of Shear Thickening Fluid (STF)-Treated Fabrics", *Comp. Sci. and Tech.* **67**, 565-78

Dementev, A. and Tarakanov, O., (1970a), "Effect of Cellular Structure on the Mechanical Properties of Plastic Foams", *Mekhanika Polimerov*, **4**, 519-525.

Dementev, A. and Tarakanov, O., (1970b), "Model Analysis of Cellular Structure of Plastic Foams of the Polyurethane Type", *Mekhanika Polimerov*, **5**, 744-749.

Deshmukh, S. and McKinley, G., (2007), "Adaptive Energy-Absorbing Materials Using Field-Responsive Fluid-Impregnated Cellular Solids", *Smart Mat. Struct*, **16**, 106-11334.

D'Haene, P. and Mewis, J., (1994), "Rheological characterization of bimodal colloidal dispersions", Rheologica Acta, **33**, 165-174.

Dullien, F., (1975), "Single Phase Flow Through Porous Media and Pore Structure", *Chem. Eng. J.* **10**, 1-34.

Dupuit, J., (1857), "Mouvement de l'eau a 'travers le terrains permeables", *Comptes Rendus de l'Acade´mie des Sciences*, **45**, 92–96.

Dybbs, A. and Edwards, R.V., (1984), "A new look at porous media fluid mechanics Darcy to turbulent", In: Bear, J. and Corapcioglu, Y. Editors, *Fundamentals of transport phenomena in porous media* Martinus Nishoff, Dordrecht, pp. 199–256.

Egres, R. and Wagner, N., (2005), "The Rheology and Microstructure of Acircular Precipitated Calcium Carbonate Colloidal Suspensions Through the Shear Thickening Transition" *J. Rheo.*, **49**, (3), 719-46.

Elliot, C.L., Mays, G.C., and Smith, P.D., (1992), "The Protection of Buildings against Terrorism and Disorder", *Proc. Inst. Civ. Eng. Struct. Build*, **94**, 287-97.

Everett, R., Matic, P., Harvey, D., and Kee, A., (1998), "The Microstructure and Mechanical Response of Porous Polymers", *Mat. Sci. and Eng.* **A249**, 7-13.

Farr, R.S. et al., (1997), "Kinetic Theory of Jamming in Hardsphere Startup Flows," *Phys. Rev. E*, **55**, 7203-11.

Fedorenko, A.G., Syrunin, M.A., and Ivanov, A.G., (2004), "Criterion for Selecting Composite Materials for Explosion Containment Structures (Review)," *Comb., Explosion, and Shock Waves*, **41**, 5, 487-95.

Fischer, C., Braun, S., Bourban, P., Michaud, V., Plummer, C., Manson, J., (2006), "Dynamic properties of sandwich structures with Integrated Shear-Thickening Fluids", *Smart Mat. & Struct.*, **15**, 1467-75.

Fitzgerald, C., Lyn, I., and Mills, N., (2004), "Airflow Through Polyurethane Foams with Near-Circular Cell-Face Holes", *J. Cell. Plastics.* **40**, 89-110.

Fleck, N.A. and Deshpande, V.S., (2004), "The Resistance of Clamped Sandwich Beams to Shock Loading", *J. Applied Mech.*, **71**, 386-401.

Foss, D.R. and Brady, J.F., (2000), "Structure Diffusion and Rheology of Brownian Suspensions by Stokesian Dynamics Simulation," *J. Fluid Mech.*, **407**, 167-200.

Fuganti, A., (2000), "Aluminum Foams for Automotive Applications", *Adv. Eng. Mat.*, **2**, (4), 200-

204.

Gama, B., Bogetti, T., Fink, B., Yu, C., Dennis Claar, T., Eifert, H., Gillespie, J., (2001), "Aluminum Foam Integral Armor: A New Dimension in Armor Design", *Comp. Struct.*, **52**, 381-395.

Geers, T., (1971), "Residual Potential and Approximate Methods for Three-Dimensional Fluid-Structure Interaction Problems", *J.Acoustical Soc. America*, **49**, 1505-10.

Gent, A. and Thomas, A., (1959), "Failure of Foamed Elastic Materials", *J. App. Poly. Sci.*, **2**, (6), 354-357.

Gent, A. and Thomas, A., (1963), "Mechanics of Foamed Elastic Materials", *Rubber Chem and Tech.* 597-610.

Gent, A. and Rusch, K. (1966), "Permeability of Open-Cell Foamed Materials", *J. Cell. Plas.*, 46-51.

Gibson, L.J. and Ashby, M.F., (1997), *Cellular Solids – Structures and Properties, 2nd Ed.*, Cambridge Univserisy Press, Cambridge.

Gilchrist, A. and Mills, N.J., (1994), "Modelling of the Impact Response of Motorcycle Helmets", *Int. J. Impact Eng.*, **15**, pp. 201-218.

Gilchrist, A. and Mills, N.J., (1996), "Protection of the side of the head", *Accident Anal. And Prev.*, **28**, pp. 525-535.

Gioia, G., Wang, Y., Cuitino, A., (2000), "The Energetics of Heterogeneous Deformation in Open-Cell Solid Foams", *Proc. R. Soc. Lond. A.*, **457**, 1079-96.

Gong, L., Kyriakides, S., and Jang, W., (2004), "Compressive Response of Open Cell Foams Part I: Morphology and Elastic Properties", *Int. J. Solids and Structures*, **42**, 1355-79.

Gopalakrishnan, V. and Zukoski, C., (2004), "Effect of Attractions on Shear Thickening in Dense Suspensions" *J. Rheo.*, **48**, (6), 1321-44.

Greenhorn, J., (1988), "The Assessment of Surface Ship Vulnerability to Underwater Attack", *Royal, Inst. Naval Architects*, 233-43.

Grimal, Naili, and Watzky, (2005), "A High-Frequency Lung Injury Mechanism in Blunt Throcic Impact", *J.Biomechanics.* **38**, 1247-54.

Hayes, W. and Robinovitch, S., (1997), "Bone Fracture Prevention Garment and Method", U.S. Patent 5599290. *Assignee: Beth Israel Hospital, Boston.*

Hilyard, N., (1971), "Observations on the Impact Behaviour of Polyurethane Foams; II. The Effect of Fluid Flow", *J. Cell. Plastics*, 84-90.

Hilyard, N., (1982), *Mechanics of Cellular Plastics*, Applied Science, Barking.

Hilyard, N. and Collier, P., (1987), "A Structural Model Air Flow in Flexible PUR Foams", *Cell. Poly.* **6**, 9-26.

Hilyard, N. and Cunningham, A., (1994), *Low Density Cellular Plastics*, Chapman and Hall, London.

Hilyard, N. and Kanakkanatt, S., (1970), "Mech Damping in Liquid-Filled Foams", *J. Cellular Plastics*, **6**, 87-90.

Hoffman, R., (1972), "Discontinuous and Dilatant Viscosity Behavior in Concentrated Suspensions. I. Observation of Flow Instability", *J. Rheo.*, **16**, (1), 155-73.

Hoffman, R.L., (1974), "Discontinous and Dilatant Viscosity Behavior in Concentrated Suspensions. II Theory and Experimental Tests," *J. Colloid Interface. Sci.*, **46**, 491-506.

Hoffman, R., (1982), "Discontinuous and Dilatant Viscosity Behavior in Concentrated Suspensions III. Necessary Conditions for Their Occurrence in Viscometric Flows", *Adv. Colloid and Interface Science*, **17**, 161-184.

Hoffman, R., (1998), "Explanations for the Cause of Shear Thickening in Concentrated Colloidal Suspensions," *J. Rheo.*, **42**, (1), 111-123.

Hoffman, R., (1998), "Explanations for the Cause of Shear Thickening in Concentrated Colloid Suspensions", *J. Rheo.*, **42**, (1), 111-123.

Hu, H. and Larson, R., (2002), "Measurement of Wall-Slip-Layer Rheology in Shear Thickening Wormy Micelle Solutions", *J. Rheo.*, **46** (4), 1001-21.

Huang, H., (1969), "Transient Interaction of Plane Acoustic Waves with a Spherical Elastic Shell", *J. Acou. Society America*, **45**, 3, 661-70.

Huang, H., (1974), "Transient Bending of a Large Elastic Plate by an Incident Spherical Pressure Wave", *J. Applied Mech.*, **41**, 772-76.

Hung, C., (1999), "Numerical Simulation of Structural Dynamics to Underwater Explosions", *Proc. 13th Asian Tech. Exchange and Advisory Meeting on Marine Structures*, Keelung, Taiwan, 155-164.

Hutchinson, J.W. and Xue, Z., (2005), "Metal Sandwich Plates Optimized for Pressure Impulses", *Int. J. Mech. Sci.*, **47**, 545-69.

Innocentini, M., Salvini, V., Pandolfelli, V., and Coury, J., (1998), "Assessment of Forchheimer's Equation to Predcit the Permeability of Ceramic Foams", *J. Am. Ceram. Soc.*, **82**, 1945-48.

Jones, R. and Fesman, G., (1965), "Air Flow Measurements and Its Relations to Cell Structure, Physical Properties, and Processibility for Flexible Urethane Foam", *J. Cell. Plas.*, **1**, 1, 200-216.

Kawase, Y. and Ulbrecht, J., (1983), "Non-Newtonian Fluid Particle Mass Transfer in Granular

Beds", *AICHE.* **29**, 689-91.

Laun, H. , Bung, R., Schmidt, F., (1991), "Rheology of Extremely Shear Thickening Polymer Dispersions", *J. Rheo.*, **35**, 999-1034.

Lee, S., Barthelat, F., Moldovan, N., Espinosa, H., and Wadley, H., (2006), "Deformation Rate Effects on Failure Modes of Open-Cell AL Foams and Textile Cellular Materials", *Int. J. Solids and Structuers*, **43**, 53-73.

Lee, Y. and Wanger, N., (2003), "Dynamic Properties of Shear Thickening Colloidal Suspensions", *Rheo. Acta*, **42**, 199-208.

Lee, Y., Wetzel, E., and Wagner, N., (2003), "The Ballistic Impact Characteristics of Kevlar Woven Fabrics Impregnated with a Colloidal Shear Thickening Fluid", *J. Mat. Sci.*, **38**, 2825-2833.

Lederman, J., (1971), "The Prediction of the Tensile Properties of Flexible Foams", *J. Appl. Poly. Sci.*, **15**, 696-703.

Leibovici, Gofrit, Shapira, (1999), "Eardrum perforation in explosion survivors: is it a marker of pulmonary blast injury?", *Ann. Emerg. Med.*, **34**, 168-72.

Liang, C.C. and Tai, Y.S., (2006), "Shock Responses of a Surface Ship Subjected to Noncontact Underwater Explosions", *Ocean Eng.*, **33**, 748-772.

Louca, L.A., Boh, J.W., Choo, Y.S., (2004), "Response of Profiled Barriers Subject to Hydrocarbon Explosions", *Proc. Inst. Civil Eng.*, **157**, 319-331.

Luccioni, Ambrosini, and Danesi, (2004), "Analysis of Building Collapse under Blast Loads", *Engineering Structures*, **26**, 63-71.

Mahfuz, H., Thomas, T., Rangaric, V., Jellanic, S., (2006), "On the Dynamic Response of Sandwich Composites and Their Core Materials", *Comp. Sci. Tech.*, **66**, 2465-72.

Maranville, C. and Ginder, J., (2005), "Small-Strain Dynamic Mechanical Behavior of Magnetorheological Fluids Entrained in Foams", *Int. J. Applied Electro. Mech.*, **22**, 25-38.

Maranzano, B.J., and Wagner, N.J., (2001a), "The Effects of Particle Size on Reversible Shear Thickening of Concentrated Colloidal Dispersions," *J. Chem. Phys.*, **114**, 10514-27.

Maranzano, B.J., and Wagner, N.J., (2001b), "The Effects of Interparticle Interactions and Particle Size on Reversible Shear Thickening: Hard-Sphere Colloidal Dispersions," *J. Rheo.*, **45** (5), 1205-1222.

Massimiliano, A., Belingardi, G., and Ibba, A., (2007), "Mechanical Models of Cellular Solids: Parameters Identification from Experimental Tests", *Int. J. Impact Eng.*,.**34**, 3-27.

Michalska, M. and Pecherski, R., (2003), "Macroscopic Properties of Open-Cell Foams based on Micromechanical Modelling", *Tech. Mechanik*, **23**, (2-4), 234-244.

Mills, N. and Lyn, G., (2002), "Modelling of Air Flow in Impacted Polyurethane Foam", *Cellular Polymers.* **21**, 343-65.

Mills, N., (2005), "The Wet Kelvin Model for Air Flow Through Open-Cell Polyurethane Foams", *J. Mat. Sci.*, **40**, 5845-51.

Mills N.J. and Gilchrist, A., (2006), "Bicycle Helmet Design", *Proc. IMechE.*, **220**, pp. 167-180.

Mines, (2004), "A One-Dimensional Stress Wave Analysis of a Lightweight Composite Armour", *Composite Structures,*. **64**, 55-62.

Morison, C., (2006), "Dynamic Response of Walls and Slabs by Single-Degree-of-Freedom Analysis a Critical Review and Revision", *Int. J. Impact Eng.*, **32**, 1214-47.

Ngo, T., Mendis, P., Gupta, A., and Ramsay, J., (2007), "Blast Loading and Effects on Structures-An Overview", *Loading and Struct.*, **EJSE Special Issue**, 76-91.

Qiu, X., Deshpande, V.S., and Fleck, N.A., (2005), "A One-Dimensional Response of Sandwich Plates to Underwater Shock Loading", *J. Mech. Phys. Solids*, **53**, 22347-2383.

Rehkopf, J., Brodland, G., and McNeice, G., (1994), "Experimentally Seperating Fluid and Matrix Contributions to Polymeric Foam Behavior", *Experimental Mechanics*, **36**, 1-6.

Rehkopf, J., McNeice, G., and Brodland, G., (1996), "Fluid and Matrix Components of Poly. Foam Behavior Under Cyclic Comp" *J. Eng. Mat. and Tech.*, **118**, 58-62.

Reid, S.R., Reddy, T.Y., and Peng, C., (1993), "Dynamic compression of cellular structures and materials", *Structural crashworthiness and failure*, Elsevier Applied Science, London, 295–339.

Richmond, D., (1991), "Blast Criteria for Open Spaces and Enclosures", *Scandinavian Audiology*, **34**, 49-76.

Rusch, K., (1969), "Load Compression Behavior of Flexible Foams", *J. App. Poly. Sci.*, **13**, 2297-2311.

Sabiri, N.E., Montillet, A., and Comiti J., (1996), "Pressure Drops of Non-Newt. Purely Viscous Fluid Flow Through Syn. Foams", *Chem. Eng. Comm.*, **156**, 59-74.

Sahimi, M., (1993), "Nonlinear Transport Processes in Disordered Media", *AIChE J.* **39**, (3), 369-386.

Schardin, H., (1950), "The Physical Principles of the Effects of a Detonation. *In German Aviation Med., WWII*, Air Force Surgeon General, Washington, DC.

Schraad, M. and Harlow, F., (2006), "A Multi-Field Approach to Modeling the Dynamic Response of Cellular Materials", *Int. J. Mech. Sci.*, **48**, 85-106.

Seguin, D., Montillet, A., Brunjail, D., and Comiti, J., (1996), "Liquid-Solid Masss Transfer in Packed Beds of Variously Shaped Particles at Low Reynold Numbers: Experiments and Model", *Chem Eng. J.*, **63**, 1-9.

Seguin, D., Montillet, A., and Comiti, J., (1998a), "Experimental Characterisation of Flow Regimes in Various Pourous Media-I: Limit of Laminar Flow Regime", *Chem Eng. Sci.*, **53**, 3751-3761.

Seguin, D., Montillet, A., Comiti, J., and Huet, F., (1998b), "Experimental Characterisation of Flow Regimes in Various Pourous Media-II: Transition to Turbulent Regime", *Chem Eng. Sci.*, **53**, 3897-3909.

Seguin, D., Montillet, A., and Comiti, J., (2000), "Experimental Characterisation of Flow Regimes in Various Pourous Media-III: Limit of Darcy's or Creeping Flow Regime for Newtonian and Purely Viscous non-Newtonian Fluids", *Chem Eng. Sci.* **55**, 3057-3061.

Shah, C. and Yortsos, Y., (1995), "Aspects of Flow of Power-Law Fluids in Porouse Media", *AIChE J.*, **41**, (5), 1099-1112.

Shim, V., Yap, K., and Stronge, W., (1992), "Effects of nonhomogeneity, cell damage and Strain-Rate on Impact Crushing of a Strain-Softening Cellular Chain", *Int. J. Imp. Eng.*, **12**, (4) 585-602.

Shuaeib, F., Hamouda, A., Radin Umara, R., Hamdan, R., Hashmi, M., (2002a), "Motorcycle Helmet Part I. Biomechanics and Computational Issues", *J. Mat. Process. Tech.*, **123**, pp. 405-421.

Shuaeib, F., Hamouda, A., Hamdan, R., Radin Umara, R., Hashmi, M., (2002b), "Motorcycle Helmet Part II. Materials and Design Issues," *J. Mat. Process. Tech.*, **123**, pp. 422-431.

Shuaeib, F., Hamouda, A., Wonga, S., Radin Umara, R., Ahmeda, M., (2007), "A new motorcycle helmet liner material: The finite element simulation and design of experiment optimization", Mat. and Design, **28**, pp. 182-195.

Smith, P., Whalen, L., Feng, L., Rose, T., (2001), "Blast Loading on Buildings From Explosions in City Streets", *Struct. Build.*, **1**, 47-55.

Stickel, J. and Powell, R., (2005), "Fluid Mechanics and Rheology of Dense Suspensions", *Annu. Rev. Fluid Mech.*, **37**, 129-49.

Suh, K. and Webb, D., (1985), "Cellular Materials", *Encyclopedia of Polymer Science*, **3**, 2nd Ed., Wiley, New York.

Talaslidis, D., Manolis, G., Paraskevopoulos, E., Panagiotopoulos, C., Pelekasis, N., Tsamopoulos, J., (2004), "Risk Analysis of Industrial Structures Under Extreme Transient Loads", *Soil Dynamics and Earthquake Eng.*, **24**, 435-48.

Tan, V., Tay, T., Teo, W., (2005), "Strengthening Fabric armour with Silica Colloidal Suspensions", *Int. J. Solid Struct.*, **42**, 1561-1576.

Tasdemirci, Hall, and Gama, (2003), "Stress Wave Propogation Effects in Two-and Three Layered Composite Materials", *J. Composite Mat.*, **38**, 995-1009.

Tek, M., (1957), "Development of a Generalized Darcy Equation", *J. Petro. Tech.*, **9**, 6, 45-47.

Wagstaff, I., and Chaffey, C., (1977), "Shear Thinning and Thickening Rheology", J. Colloid and Interface Sci., **59**, (1), 53-62.

Wang, Y. and Cuitino, M., (2002), "Full-Field Measurements of Heterogeneous Deformation Patterns on Polymeric Foams Using Digital Image Correlation", *Int. J. Solids Structures*, **39**, 3777-3796.

Warren, W. and Kraynik, A., (1988), "The Linear Elastic Properties of Open-Cell Foams", *Appl. Mech.*, **24**, 341-346.

Weaire, D. and Fortes, M., (1994), "Stress and Strain in Liquid and Solid Foams", *Adv. Phys.*, **43**, 685-738.

Wendle, B., (1976), "*Engineering Guide to Structural Foams*", Technomic Publishing Co., Westport, Connecticut.

White, F., (1999), *Fluid Mechanics, 4th Ed.*, McGraw-Hill Companies, New York.

Xue, Z. and Hutchinson, J.W., (2003), "Preliminary Assessment of Sandwich Plates Subject to Blast Loads", *Int. J. Mech. Sci.*, **45**, 687-705.

Xue, Z. and Hutchinson, J.W., (2004), "A Comparative Study of Impulse-Resistant Metallic Sandwich Plates," *Int. J. Impact Eng.*, **30**, 1283-1305.

Yoshimura, A. and Prud'Homme, R., (1988), "Wall Slip Corrections for Couette and Parallel Disk Viscometer", *J. Rheo.*, **32** (1), 53-67.

Yu, J., Li, J., and Hu, S., (2006), "Strain-Rate Effect and Micro-Structural Optimization of Cellular Metals", *Mech. Mat.*, **38**, 160-170.

Zhao, H. and Gary, G., (2002), "Behaviour Characterization of Polymeric Foams over a Large Range of Strain Rates", *J. Vehicle Design*, **30**, 135-143.

Zhu, H., Knott, J., and Mills N., (1997), "Analysis of the Elastic Properties of Open-Cell Foams with Tetrakaidecahedral Cells", *J. Mech Phys.Solids*, **45**, 319-343.

Figures

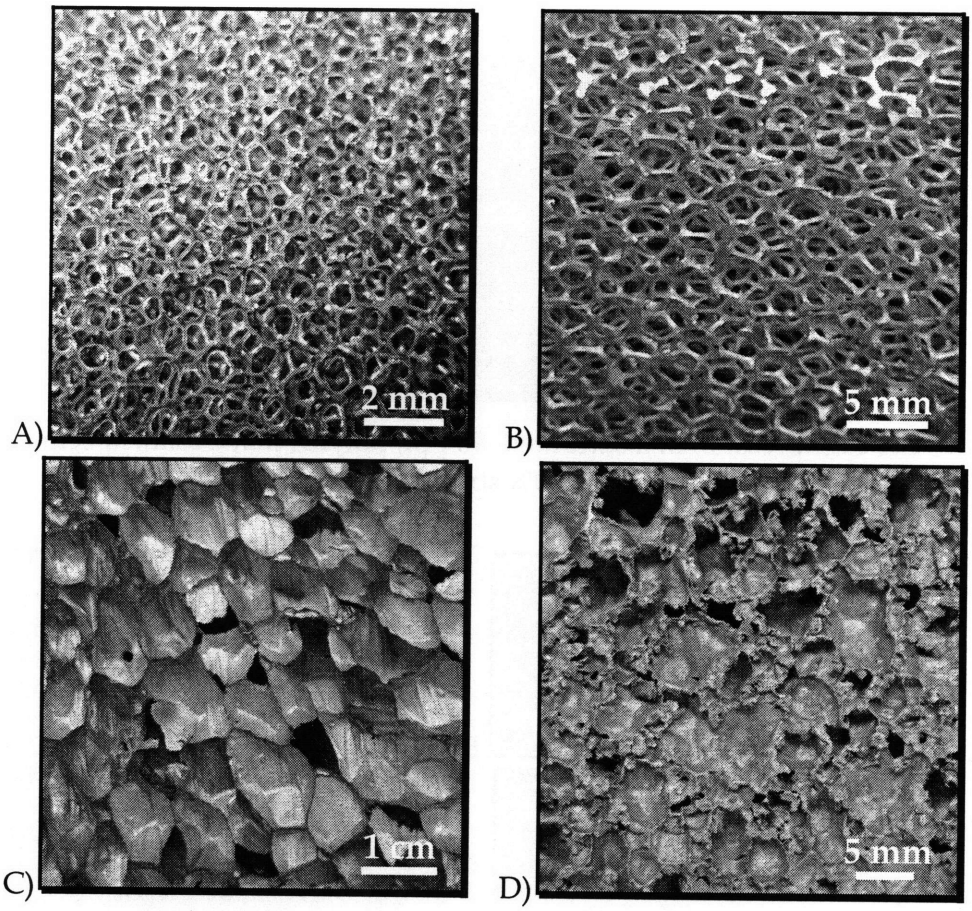

Figure 2.1: Optical micrographs of foams. A) Open-cell polyurethane foam; B) Open-cell aluminum foam; C) Closed-cell aluminum foam; D) Closed-cell aluminum foam.

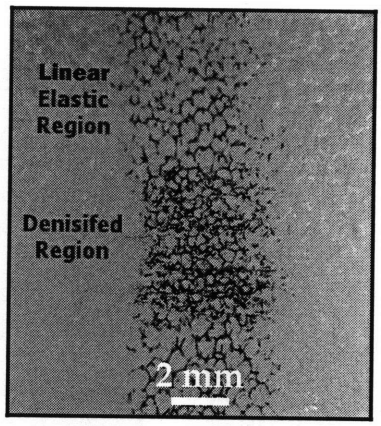

Figure 2.2: Compression of a saturated, 90 ppi, polyurethane foam specimen at 40% strain.

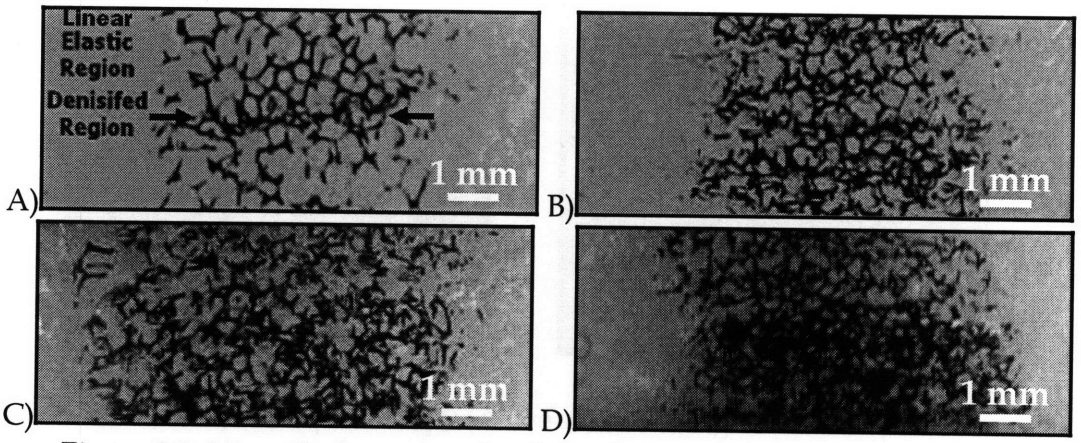

Figure 2.3: Magnified compression laps photos of densified region for a saturated, 90ppi, polyurethane foam specimen. (a) 20% strain (b) 40% strain (c) 60% strain (d) 80% strain.

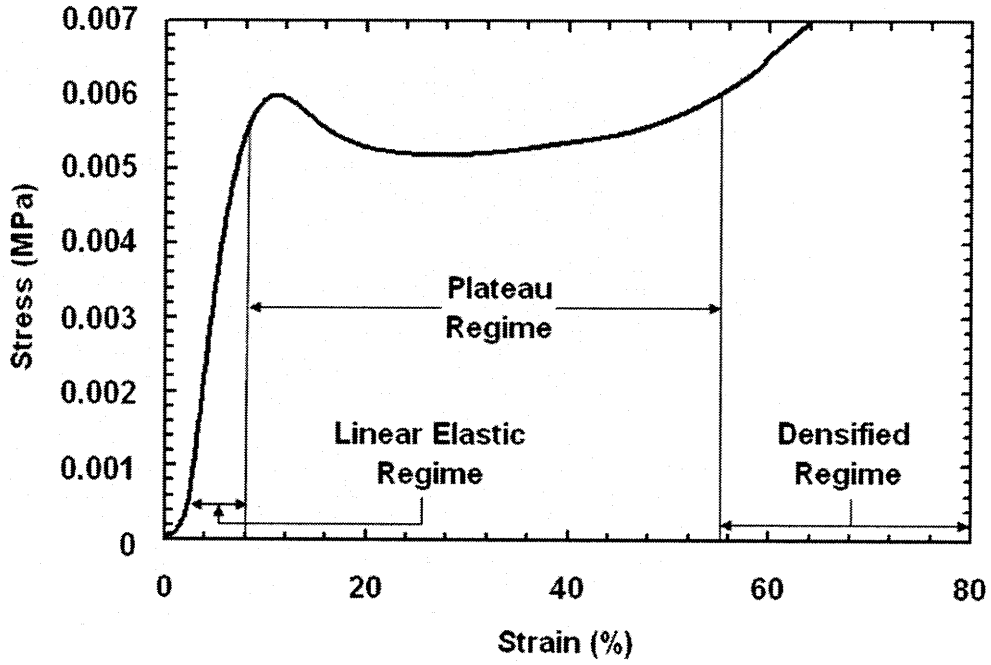

Figure 2.4. Typical quasi-static stress-strain response of 70 ppi foam under uniaxial compression.

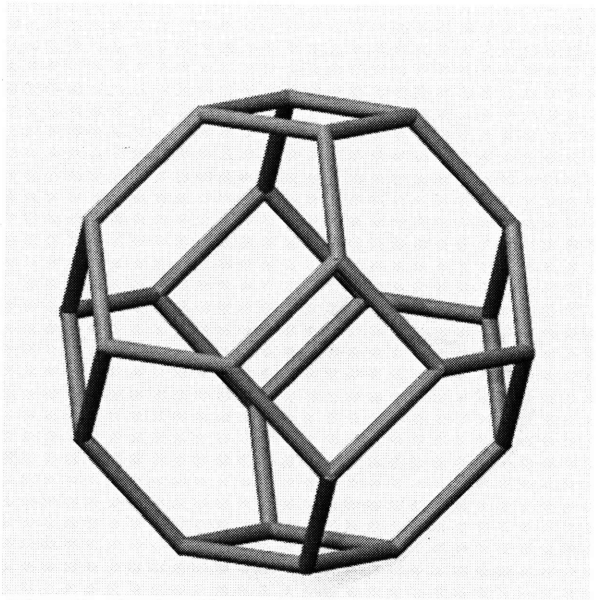

Figure 2.5: Tetrakaidecahedral cell model for a Kelvin foam made in Solidworks.

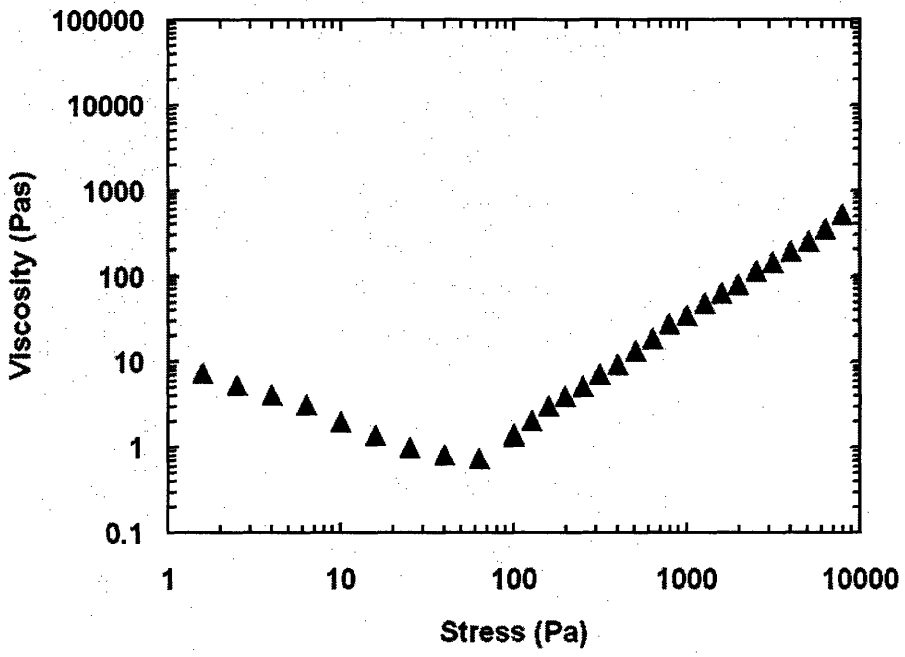

Figure 2.6: Viscosity plotted against shear stress for shear thickening precipitated calcium carbonate (PCC)/PEG suspension with a PCC volume fraction of 0.50.

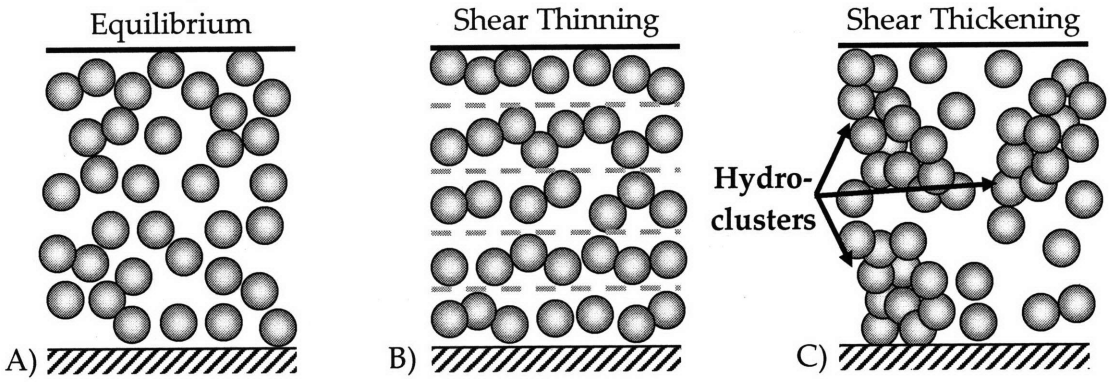

Figure 2.7: Model of distribution of spherical nano-particles in a suspension. A) in static equilibrium; B) undergoing shear, resulting in shear thinning; C) undergoing shear, resulting in the formation of hydroclusters, which is proposed to result in the shear thickening effect.

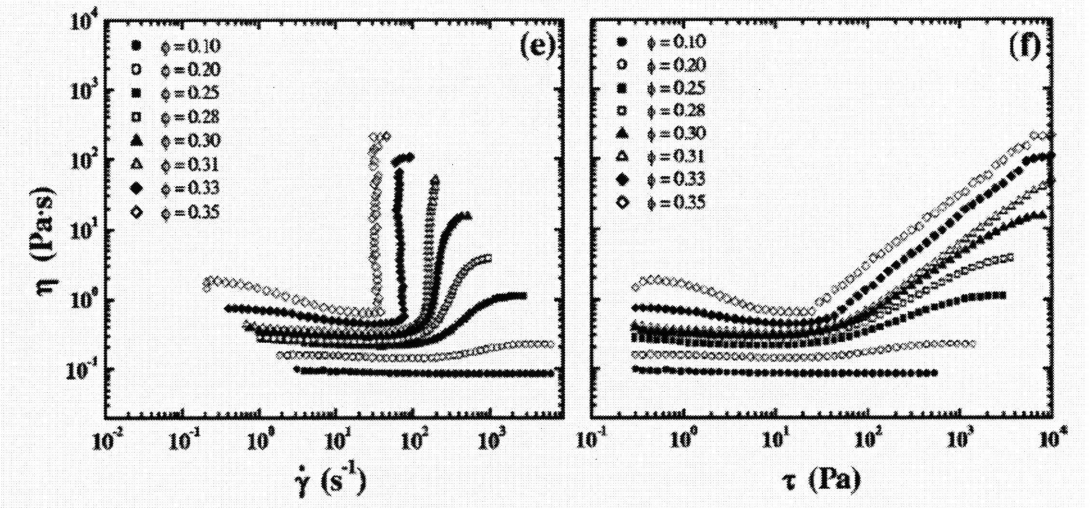

Figure 2.8: Steady shear viscosity plotted against shear rate (left) and shear stress (right) for shear thickening precipitated calcium carbonate (PCC)/PEG suspensions at several volume fractions. (Egres et al., 2005 with permission)

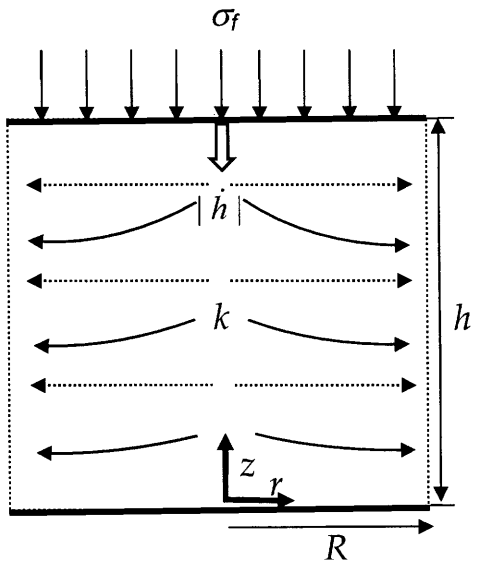

Figure 2.9: Axial compression of fluid-filled, open-cell foam. (after Gibson and Ashby, 1997).

A)

B)

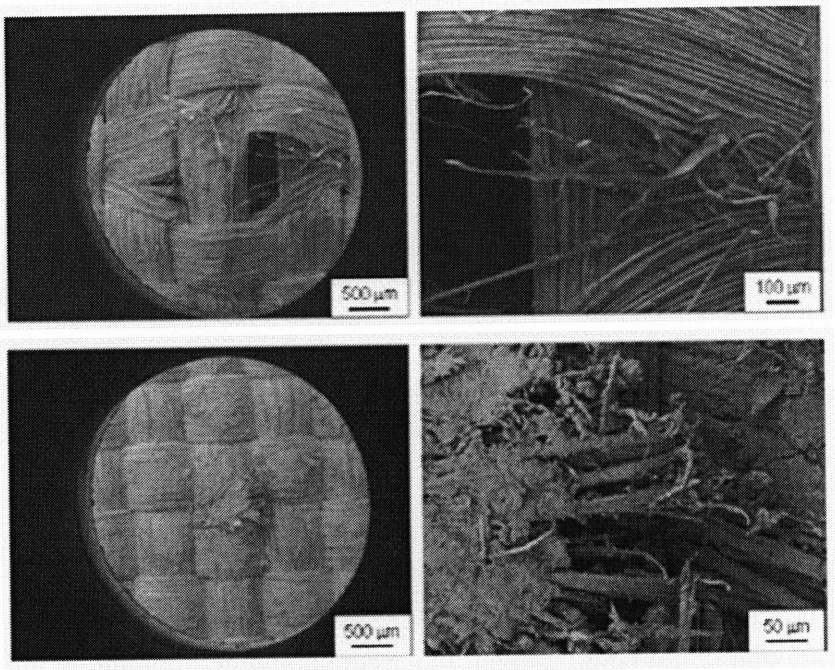

Figure 2.10: Images of back layers armor after drop tower spike testing at m = 2.33 kg and h = 0.75 m. A) Neat Kevlar; B) STF-impregnated Kevlar (Decker et al., 2007 with permission).

3 Permeability of Open-Cell Foam Under Compressive Strain

3.1 Introduction

Developing a comprehensive understanding of the dynamic response of fluid-filled foam requires knowledge of the fluid-structure-interaction under deformation. In this chapter, a model is explored, which relates the characteristic properties of the fluid and the foam to the characteristics properties of the flow through a factor called the intrinsic permeability. First, a model for the behavior of low-density, open-cell foam under compressive strain is proposed. Using this model, a tractable relationship between the normalized permeability and the applied compressive strain of open-cell foam filled with a Newtonian fluid is developed. An experimental study of the effect of strain on the permeability of open-cell, polyurethane foam is presented. The experimental results are used to determine a single empirical constant for the model. The experiments are performed using a Newtonian fluid in the fully laminar regime, where viscous forces are assumed to dominate. The model is found to describe the experimental data well and be independent of the foam cell size, the direction of flow with respect to the foam rise direction, and the properties of the saturating fluid.

3.2 Literature Review

The intrinsic permeability of open-cell foam has received limited attention in past research. However, Gent and Rusch (1966) studied the permeability of open-cell foam and demonstrated a significant finding, that the average cell diameter is a function of the applied compressive strain. They proposed a qualitative,

empirically based relation between the strain and the average cell diameter, developing a simple model based on flow through an array of smooth tubes. The theoretical transition from the fully laminar regime, where Darcy's law is applicable, to the inertial dominated regime should occur for $Re > 2000$ in a smooth walled tube. However, experimentally, they found the transition from viscous to inertial dominated flow in open-cell foam occurred for $Re \cong 1$. This result corresponded with the experimental findings of Tek (1957) for flow through porous rock and Dybbs and Edwards (1984) for fixed beds of spheres and cylinders. In all of these cases, the flow path is more tortuous than the case of flow through a smooth tube. Comiti et al. (2000) developed a theoretical model for this transition, proposing a theoretical transition value of $Re = 0.83 \cong 1$ for flow through porous media.

Hilyard and Collier (1987) extended Gent and Rusch's work, developing and testing a theoretical model for predicting the effect of strain on the permeability of a reticulated polyurethane foam. However, their experiments focused on air flow through foams with relatively large cell sizes. For all of their experiments $Re > 1$, so the effect of inertial forces could not be neglected. The flow of highly viscous fluids through open-cell foam under compressive loads, on the other hand, is laminar and dominated by viscous forces for nearly all achievable strain rates. Neither Gent and Rusch (1966) nor Hilyard and Collier (1987) studied this flow regime in depth.

3.3 Permeability Model

Assuming the foam can be described as isotropic, the relative density under uniaxial compression, is given as

$$\frac{\rho^*}{\rho_s} = \frac{\rho_o^*}{\rho_s} \frac{1}{(1-\varepsilon)(1+\nu\varepsilon)^2} \tag{3.1}$$

where ρ^* is the density of the foam at strain ε, and ν is Poisson's ratio of the foam. For compressive strains above about 0.075, the cells in open-cell flexible foams buckle and collapse without expanding laterally, so that their Poisson's ratio in this regime is approximately zero. Since the focus of this analysis is primarily in the behavior at high strains, $\nu\varepsilon$ is taken to be zero for low-density, open-cell, flexible foams. Substituting Eq. (3.1) into the porosity term of Brace's equation for porous media given by Eq. (3.2a), the intrinsic permeability k, of the foam is given by Eq. (3.2b) (after Brace, 1977)

$$k = Ad^2 \left(1 - \frac{\rho^*}{\rho_s}\right)^3 \tag{3.2a}$$

$$k = Ad^2 \left(1 - \frac{\rho_o^*}{\rho_s} \frac{1}{(1+\varepsilon)}\right)^3 \tag{3.2b}$$

where A is an empirical constant given by Brace as 0.025 for a porous microstructure consisting of tubes with circular cross-sections and d is the average diameter of the cells.

As the foam is compressed beyond the elastic buckling strain ε_{el}^* of 0.075,layers of cells buckle and collapse, generating local bands of large deformation in which the average diameter of the cells is reduced substantially. A detailed discussion of this banding phenomenon, which is widely seen in open-cell polymeric foams, is given by Gioia et al. (2000). As the initial collapse band forms, the rest of the specimen remains in the linear elastic regime, at a strain close to the elastic buckling strain, ε_{el}^*. As the overall strain increases, cells adjacent to the collapsed band also collapse, so that the length of the densified band increases while that of the remainder of the foam in the linear elastic regime decreases. The strain of the collapsed cells in these densified bands is assumed to be uniform and given by the densified strain ε_d **(Fig. 3.1)**. It is important to distinguish the densified strain ε_d, from the fully densified strain ε_D given in *Chapter 2*, where the former represents the onset of the densification regime, and the latter represents the end of the densification regime. In **Fig. 3.1** the average velocity of the fluid flowing through the foam is given by U, the permeability of the foam in the elastic buckling regime and the densified regime are given by k^*_{el} and k_d, respectively, and the volume fractions of the cells remaining in the linear elastic regime and the densified regime are given by χ^*_{el} and χ_d, respectively. **Fig. 3.2** demonstrates the existence of the two regimes in reticulated polyurethane foam with an approximate relative density of 0.03 under a compressive strain of 0.4. **Fig. 3.3** shows magnified images of the collapsed cells for compressive strains ranging from 0.2 to 0.8. The collapsed cells at strains of less than or equal to 0.6 are of comparable size while at higher strains, cells begin to densify further. Therefore, the densified strain is taken to be $\varepsilon_d = 0.6$ for all grades of reticulated polyurethane foams with an approximate relative density of 0.03. This corresponds well with Hilyard and Collier (1987) who proposed the compaction of cells invalidates any relations between the average cell size and the strain

beyond compressive strains of 0.60. Therefore, we focus our model at strains less than 0.60.

Gent and Rusch (1966) consider the foam to be modeled as an array of circular tubes. The average diameter of a cell, proportional to the ratio of the volume of a tube to the wetted surface area of a tube, is found to be proportional to the diameter of the cross-section of the tube. For a small uni-directional compressive deformation of low-density foam, they assume the cross-section of the flow channels deforms in the same proportion as the bulk material. Using a small strain approximation, they give the average diameter of a cell under 1-dimensional compressive strain in the elastic regime by

$$d_{el} \cong d_o(1-\varepsilon)^{1/2} \qquad \text{for} \quad 0 \le \varepsilon \le \varepsilon^*_{el} \qquad (3.3)$$

where d_o is the average cell size at 0% strain.

This model for the current average diameter of a cell as a function of the nominal strain was supported by experimental results. In this analysis we provide additional support to the applicability of this model using a finite element software ADINA (ADINA R&D inc., Watertown, MA) for strains up to the elastic buckling strain. As previously discussed a commonly used model for the repeating cell in foam is the tetrakaidecahedron. For the tetrakaidecahedron model shown in **Fig. 3.4**, we assume the material is taken to be a typical isotropic polyurethane, low-density foam with Poisson's ratio and Young's modulus of 0.3 and 150 Mpa, respectively. The length and diameter of the struts are taken, for simplicity, to be 100 μm and 10 μm, respectively. The loading is distributed as 4

equal point loads on the four corner nodes (P21, P22, P23, and P24) of the tetrakaidecahedron where the load is anticipated to be transmitted. Boundary conditions are applied at 3 of the base nodes (P1, P2, and P4), such that the nodes are allowed to translate and rotate in the x and y planes, but they are fixed in translation and rotation in the z plane. In order to have a fully stable structure node P3 is fixed in all degrees of freedom. It is important to note in a real cell all of the boundary conditions at all four base nodes should be identical, but since this model only consists of one cell, one node must be fixed to satisfy the structural stability. The discrepancy in boundary conditions should have negligible effect on determining the average diameter of a cell as a function of strain since this analysis only considers small deformations.

A characteristic diameter of the tetrakaidecahedral cells D_H, can be developed based on the hydraulic diameter found in fluid mechanics, given as six times the volume of the cell ($V_c = 8\sqrt{2}L_c^3$) divided by the surface area of the cell ($A_s = \left(6 + 24\sqrt{3}\right)L_c^2$), where L_c is the average length of a cell wall. In the linear elastic regime, the diameter of a cell as a function of strain was found to correspond well to the Gent and Rusch model given in Eq. (3.3). For example, the finite element analysis determined the ratio of the diameter at a strain of 0.03 to the initial diameter is 0.99, which corresponds well (to within rounding error) with the value predicted by the Gent and Rusch model (also found to be 0.99). **Fig. 3.5** shows the finite element simulation of the deformation of the tetrakaidecahedral cell at a strain of 0.03. This figure demonstrates as a cell is compressed in the z-direction expansion takes place in the x- and y-directions, further supporting the Gent and Rusch's model, which proposes the cell diameter does not decrease linearly proportionally to the compressive strain.

Overall, the finite element simulation provides strong support to the model proposed by Gent and Rusch, which gives the average cell diameter as a function of the strain in the linear-elastic regime. We further propose the average diameter of a cell in the densified regime d_d follows a similar form and is given as

$$d_d = d_o(1-\varepsilon)^a \qquad \text{for} \quad \varepsilon = \varepsilon_d \qquad (3.4)$$

where a is an empirical constant. The corresponding permeabilities in the linear elastic regime k_{el}, in the elastic buckling regime k^*_{el}, and in the densified regime k_d, are determined by coupling Eq. (3.2-3.4) and are given by

$$k_{el} = Ad_o^2(1-\varepsilon)\left(1-\frac{\rho_o^*}{\rho_s}\frac{1}{(1-\varepsilon)}\right)^3 \qquad \text{for} \quad 0 \le \varepsilon \le \varepsilon_{el}^* \qquad (3.5)$$

$$k_{el}^* = Ad_o^2(1-\varepsilon_{el}^*)\left(1-\frac{\rho_o^*}{\rho_s}\frac{1}{(1-\varepsilon_{el}^*)}\right)^3 \qquad \text{for} \quad \varepsilon = \varepsilon_{el}^* \qquad (3.6)$$

$$k_d = Ad_o^2\left(1-\varepsilon_d\right)^{2a}\left(1-\frac{\rho_o^*}{\rho_s}\frac{1}{(1-\varepsilon_d)}\right)^3. \qquad \text{for} \quad \varepsilon = \varepsilon_d \qquad (3.7)$$

Furthermore, the corresponding volume fractions of the cells remaining in the linear elastic regime χ^*_{el}, and the densified regime χ_d, after the onset of cell buckling, are given by

$$\chi_{el}^* = \frac{(\varepsilon_d-\varepsilon)(1+\varepsilon_{el}^*)}{(1+\varepsilon)(\varepsilon_d-\varepsilon_{el}^*)} \qquad \text{for} \quad \varepsilon_{el}^* \le \varepsilon \le \varepsilon_d \qquad (3.8)$$

$$\chi_d = \frac{\left(\varepsilon - \varepsilon_{el}^*\right)\left(1+\varepsilon_d\right)}{\left(1+\varepsilon\right)\left(\varepsilon_d - \varepsilon_{el}^*\right)}. \qquad \text{for} \quad \varepsilon_{el}^* \le \varepsilon \le \varepsilon_d \qquad (3.9)$$

Gent and Rusch (1966) developed a model relating the total pressure drop Δp across a specimen to the fluid properties, foam properties, and flow velocity U:

$$\frac{\Delta p}{h} = \frac{\mu}{k_T} U + \frac{\rho}{B_T} U^2 \qquad (3.10)$$

where h is the length of the specimen in the direction of flow, k_T is the effective permeability of the foam, and B_T is the inertial flow coefficient of the foam. The inertial flow coefficient has the dimensions of length and is characteristic of the geometry of the media, the cell size, and the nature of the flow. They attributed the first term on the right hand side of the equation to viscous forces, corresponding to Darcy's law governing laminar flow, and the second term to inertial forces dominant in the turbulent regime. The flow of highly viscous fluids in open-cell foam is dominated by viscous forces for nearly all achievable strain rates. Therefore, the focus of this analysis is the fully laminar regime, dominated by viscous flow, where the second term on the right-hand side of Eq. (3.10) can be neglected. Assuming the flow is laminar and dominated by viscous forces, the pressure drop Δp_i across each regime of the foam is given by

$$\frac{\Delta p_i}{h_i} = \frac{\mu}{k_i} U \qquad (3.11)$$

where h_i is the length of each regime in the direction of flow and k_i is the intrinsic permeability of each regime. The flow velocity U is assumed uniform and taken

to be constant through each regime because of continuity. Combining Eq. (3.10) and Eq. (3.11), noting the total pressure drop across the specimen is equal to the sum of the pressure drops across each regime, and noting that the length of each regime is proportional to the volume fraction of each regime, the effective permeability as a function of strain is given by

$$k_T = k_{el} \qquad \text{for } 0 \le \varepsilon \le \varepsilon_{el}^* \quad (3.12)$$

$$k_T = \frac{k_d k_{el}^*}{\chi_{el}^* k_d + \chi_d k_{el}^*}. \qquad \text{for } \varepsilon_{el}^* \le \varepsilon \le \varepsilon_d \quad (3.13)$$

Coupling the previous relations for low-density foam the normalized intrinsic permeability k_T/k_o can be approximated as

$$\frac{k_T}{k_o} \cong (1-\varepsilon) \qquad \text{for } 0 \le \varepsilon \le \varepsilon_{el}^* \quad (3.14)$$

$$\frac{k_T}{k_o} \cong \frac{(1-\varepsilon_d)^{2a}(1-\varepsilon_{el}^*)}{\chi_{el}^*(1-\varepsilon_d)^{2a} + \chi_d(1-\varepsilon_{el}^*)} \qquad \text{for } \varepsilon_{el}^* \le \varepsilon \le \varepsilon_d \quad (3.15)$$

where k_o is the permeability at 0.00 strain.

3.4 Materials and Methods

3.4.1 Materials

Specimens of open-cell, flexible, polyester-based polyurethane foams (Foamex, Linwood, PA), with nominal cell diameters of 175 μm, 210 μm, and 235 μm based

on manufacturers specifications (corresponding to grades of 90, 80, and 70 pores per inch (ppi), respectively) were used in the tests. The densities of the foams ranged from 0.0318 to 0.0322 g/cm^3. The relative density of the foams was taken to be $\rho^*/\rho_s \cong 0.03$, based on the manufacturer's value of the density of the solid polyurethane ($\rho_s = 1.078$ g/cm^3). The foam was cut using a round arch punch (McMaster-Carr Supply Co., Princeton, NJ) into uniform cylindrical specimens of 36.0 mm diameter with heights ranging from 32 to 34 mm. The dimensions of each sample were measured using a digital caliper (CD-6" CSX, Mitutoyo, Aurora, IL) accurate to within 0.01 mm. The mass of each sample was measured using an electronic balance accurate to 0.1 gram (PB3002, Mettler Toledo, Switzerland).

3.4.2 Experimental Procedure

The permeability of each specimen was measured for compressive strains ranging from 0.00 to 0.60, in increments of 0.05 and at the elastic buckling strain of 0.075. Prior to testing, each sample was fully saturated under a vacuum of 762 mm of mercury to ensure that every pore was completely filled with water, the working fluid. After saturation, the foam samples remained submerged in water for the duration of the experiment. Water was driven through the specimen using gravity-driven flow between two adjustable reservoirs, which stabilized the flow (**Fig. 3.6**).

The specimen was contained in a cylindrical glass tube with an inner diameter of 35.8mm (McMaster-Carr Supply Co., Princeton, NJ). The inlet and outlet of the tube were sealed with rubber stoppers equipped with pressure taps, allowing for measurement of the pressure drop across the foam specimen using a manometer

and a traveling microscope which read to the nearest 0.0254 mm (Titan Tool Supply Co, Buffalo, NY). The pressure drop was measured across the cylindrical glass tube and compression device alone (i.e. without the foam specimen) and found to be negligible for all flow rates used in this experiment. The flow rate was determined by measuring the mass of the water exiting the second reservoir over a specified period of time. The velocity of the fluid entering the specimen was found from the flow rate and the cross-sectional area of the glass tube, assuming the velocity distribution through the specimen was uniform. The sample time for each experiment was selected to be 90 seconds to ensure high accuracy. At each strain, six flow rates between 0.7 cm^3/sec to 2.0 cm^3/sec were selected and the corresponding pressure drop was measured. The temperature of the water in the system was maintained at 25.0 °C and continuously monitored at the inlet and exit reservoirs using digital thermometers. The viscosity of water at 25.0 °C is 8.9 x 10-4 Pa sec.

The foam within the cylindrical glass tube was compressed using mesh highly porous, copper grate mesh "platens" (McMaster-Carr Supply Co., Princeton, NJ) that were screwed together as shown in **Fig. 3.7** to impose increasing strain; the mesh has less than 1% cross-sectional interference with the specimens. The specimens were compressed axially, parallel to the direction of fluid flow. The glass tube had an inner diameter of 35.8 mm, giving negligible cross-sectional interference when the foam was uncompressed. However, the cross-sectional interference was sufficient to prevent flow around the foam specimen.

As previously discussed, the specimens do not significantly expand radially for the range of compressive strains used in these tests, so that the cross-sectional interference of the foam with the glass tube remains negligible. The large strains

used in these tests could result in some microstructural damage to the specimen. To ensure the specimens are as uniform and similar as possible, each specimen was precompressed to 0.75 strain once prior to testing.

To satisfy Darcy's law for laminar flow and neglect the inertial term in Eq. (3.2), all of the experiments were conducted with $Re < 1$. For instance, the maximum Reynolds number in the experiments was found to be 0.53, corresponding to a velocity of 2 mm/s in a 70 ppi foam with average cell diameter of 235 μm. For a maximum velocity of 2 mm/s, the viscous term in Eq. (3.2) is two orders of magnitude larger than the inertial term, so that the inertial term can be neglected. This allows the permeability to readily be determined from the slope of a plot of the pressure drop vs. the flow rate.

Nearly all prior experimental studies of permeability of an open-cell foam use air as the working fluid. In this experiment water is used, which is a highly polar fluid, known to have an effect on the properties of the solid polyurethane. In order to ensure these effects do not bias or invalidate the results, the effects of polar fluids on polyurethane foam were examined. Uniaxial compression tests of foam specimens were performed before saturation with the polar fluid, during saturation, and after removal of the fluid. The time degradation effects of saturating the foam with a polar fluid were also examined. The tests were performed using a Texture Analyzer (TA XT Plus, Stable Microsystems, Hamilton, MA), which is a commonly used mechanical testing machine for 'low strain rate' (10^{-6}–10^{0} s^{-1}) characterization of materials. The corresponding compression velocity of the machine ranges from 0.01 mm/s to 10 mm/s, with linear or exponential velocity profiles. This machine can utilize a number of interchangeable fixtures, but in these experiments a 1.5" diameter cylindrical flat

platen was selected. The load cell of the Texture Analyzer can measure up to a force of 50 kg with a resolution of 0.1 g, and the vertical displacement is determined with a resolution of 10^{-3} mm. The data acquisition system used was the Texture Exponent 32 code, which acquires both loading and positioning information for each test at a rate of 1 sample per second. The specimen was precompressed to 0.75 strain twice prior to testing. Based on Shen et al. (2000) the difference in the stress plateau between the 3rd, 4th, and 5th compressions should be negligible. The specimen was allowed to fully recover 24 hours between compression tests. The specimens were loaded to 0.60 strain at a strain rate of $1x10^{-3}$ s^{-1}, which is assumed to be the quasi-static response, so the contribution of the fluid flow to the strength and stiffness of the foam was taken to be negligible.

3.5 Results

3.5.1 Permeability vs. Strain Relation

A typical curve of the pressure drop vs. flow rate for an 80 ppi foam specimen with strains from 0.00-0.60 is given in **Fig. 3.8**. The coefficients of determination for these regressions were all above $R^2 = 0.99$. The permeability was determined from the slope of each of these regressions at the corresponding strain, ranging from 0.00-0.60. The small deviation of each regression from the origin is neglected and can be attributed to small air bubbles trapped in the pressure taps and the effect of surface tension in the manometer readings. These experiments were repeated with three different specimens for each of the three types of foams. The permeability measurements were highly repeatable with all data points falling within 15% of the average value. The permeability of the

specimens measured at 0.00 strain is given the symbol k_o. This value was determined before and after precompression of each specimen as shown in Table 1. Experimental data for the normalized permeability k_T/k_o is plotted against the strain ε in **Fig. 3.9a-3.9c**. The solid regression line represents the model presented by Eq. (3.12) and Eq. (3.13) where the coefficient a, is fitted to satisfy k_d. The best-fit coefficient a, for each grade of foam is given in Table 1. The broken regression lines are representative of the data found by Gent and Rusch (1966) and Hilyard and Collier (1987) for low density foams. Their data is found to be well approximated by the following regression equations:

Gent and Rusch Data $$\frac{k_T}{k_o} \cong (1-\varepsilon)^{1.8} \quad \text{for} \quad 0 \le \varepsilon \le \varepsilon_d \qquad (3.16)$$

Hilyard and Collier Data $$\frac{k_T}{k_o} \cong (1-\varepsilon)^{2.2} \quad \text{for} \quad 0 \le \varepsilon \le \varepsilon_d \qquad (3.17)$$

where k_o is the initial permeability after the precompression. **Fig. 3.10** is included to compare the model presented in this analysis for the normalized permeability to the models presented by Gent and Rusch (1966) and Hilyard and Collier (1987). The Gent and Rusch (1966) model is the same as the relation found in Eq. (3.14). The Hilyard and Collier (1987) model, which is based on empirical relations for low-porosity foam, is slightly more complex, containing non-linear functions of the porosity and strain. The data plotted in **Fig. 3.10** corresponds to the data in **Fig. 3.9b** for 70 ppi polyurethane foam. It is clear the model presented in this analysis improves upon the Gent and Rush model and provides a similar fit to the Hilyard and Collier model.

The low-density foams in this experiment are anisotropic with cell lengths in the rise direction approximately 1.8 times larger than those in the plane perpendicular to the rise direction. Experiments were performed with the fluid running either parallel or perpendicular to the rise direction with strain applied in the direction of fluid flow. For the 70 ppi specimens, the permeability at 0.00 strain was measured for flow parallel to the rise direction of the foam and for flow perpendicular to the rise direction of the foam. Table 1 shows the difference between these two measured permeabilities is negligible. A sample plot of the normalized permeability plotted vs. strain for 70 ppi foam with fluid flowing both perpendicular and parallel to the rise direction of the foam is given in **Fig. 3.11**. **Fig. 3.11** demonstrates that the relationships between the normalized permeability and the strain for the flow parallel or perpendicular to the rise direction of the foam are nearly identical.

3.5.2 Effect of Polar Fluid on Model

Fig. 3.12 plots stress vs. strain curve for an 80 ppi foam under uniaxial compression before saturation with the polar fluid, during saturation with the polar fluid, and after removal of the polar fluid. **Fig. 3.12** verifies the previously established results that saturating a polyurethane foam with a polar fluid reduces the stiffness and strength. Once the polar fluid is removed and the foam is completely dried, the stress-strain response of the foam is nearly restored. **Fig. 3.13** shows the stress-strain curves for a foam specimen saturated with water over a 72 hour period. The curves are for a specimen compressed to 0.60 at a strain rate of $1x10^{-3}$ s^{-1}. **Fig. 3.13** shows the plateau stress and modulus remain approximately constant over the time frame utilized for these experiments. Both **Fig. 3.11** and **Fig. 3.13** are plotted through 0.30 strain to provide higher resolution

of the linear elastic regime and plateau stress. The plateau stress and modulus remain approximately constant over the duration of the time frame considered.

3.6 Discussion

The permeability of each specimen measured before precompression is consistent with the range of expected values previously reported by the manufacturer (Foamex, Linwood, PA) and follows the expected trend with average cell size; permeability decreases with decreasing pore size. However, the permeability at 0.00 strain after precompression is not consistent with the expected trend. This phenomenon is also observed in Hilyard and Collier's (1987) study. Their data shows after mechanically conditioning (i.e. precompressing) the foam, the permeability was changed dramatically and the normal trend relating the permeability to the average cell size was no longer valid. In addition, the effect of saturating the foam with a polar fluid, may have affected the microstructure of each grade of foam differently, making one grade of foam disproportionately more compliant and more permeable than another.

The solid regression lines, representing the model for the normalized permeability as a function of strain, given by Eq. (3.12) and Eq. (3.13), describe the data in **Fig. 3.9a-3.9c** well. The normalized permeability at the elastic buckling strain k_{el^*}/k_O, is nearly constant for all three grades of foam (Table 1). The deviation on average from the elastic model given by Eq. (3.12) is approximately 2%. The normalized permeability at the densified strain k_d/k_O, differs slightly for all three grades of foams, giving distinctly different values for the best-fit coefficients a. However, averaging the coefficients for all three grades

of foams, giving $a = 0.80$, provides a reasonable model which fits the data well for all three foam grades.

In addition, this average model corresponds well with previously reported experimental results given by Gent and Rusch (1966) and Hilyard and Collier (1987). The range of cell sizes examined in these studies was up to an order of magnitude larger than those presented in this analysis, indicating the relation between the normalized permeability and the strain is independent of the cell size of the foam. Therefore, the model presented in Eq. (3.14) and Eq. (3.15) with coefficient $a = 0.80$ is taken to be applicable to all cell sizes of low relative density foam.

Fig. 3.10 compares the model presented in this analysis to the models given by Gent and Rusch (1966) and Hilyard and Collier (1987) for an 70 ppi polyurethane foam. The model presented in this analysis is found to improve significantly upon the model given by Gent and Rush and provide a similar fit to the Hilyard and Collier model. However, the model developed in this analysis provides a more physically based description of the behavior of the foam under compression. This allows for the model to be readily extended to more complex analyses such as analyzing the contribution of fluid flow to the stress-strain response of foam under dynamic compression as presented in *Chapter 4*.

Moreover, this model is also observed to be independent of whether the orientation of the rise direction of the foam is perpendicular or parallel to the direction of fluid flow. **Fig. 3.11** shows a negligible difference in the best fit relation between the permeability and the strain for the two flow directions. Therefore, the relations given in Eq. (3.14) and Eq. (3.15) are taken to be

independent of whether the rise direction of the foam is parallel or perpendicular to the fluid flow direction.

Furthermore, to ensure the model is independent of the saturating fluid, the effects of saturating the foam with a polar fluid were also examined. **Fig. 3.12** verifies the previously established results that saturating a polyurethane foam with a polar fluid immediately reduces its stiffness and strength. The polar fluid acts to weaken the microstructure of the foam by interfering with the hydrogen bonding, resulting in a decrease in the modulus of the solid polyurethane. Once the polar fluid is removed and the foam is completely dried, the stiffness of the foam is nearly restored. This is expected since the interference of the polar fluid with the hydrogen bonding of the polymer chains is removed. This corresponds well with the theory of Hogan et al. (1973); once water molecules are completely removed from the foam, hydrogen bonds in the polymer reform, and the original strength of the foam is restored. The slightly lower plateau stress in **Fig. 3.12** indicates the polar fluid allows for more rapid microstructural degradation during loading than a dry foam experiences. The buckling strain of the saturated foams also indicates microstructural changes to the foam are more readily caused by loading a foam where the hydrogen bonds are weakened by a polar fluid. Unlike the modulus and maximum buckling stress, which depend on the material properties, the buckling strain is completely dependent on the microstructure. The buckling strain of the foam saturated with water is slightly lower than that of the dry, unsaturated foam, indicating minute microstructural damage. Although saturation of a foam with a polar fluid weakens the bonding and allows for deformation to more readily damage the microstructure, the minor additional deformation due to a polar fluid should not alter the

permeability significantly from the permeability measured with a non-polar fluid.

In addition, in **Fig. 3.13** the plateau stress and modulus remain approximately constant, demonstrating saturating a polyurethane foam with a polar fluid does not degrade the microstructure over the time frame considered. Hogan et al. (1973) shows similar findings that the effect of relative humidity on the time degradation of polyurethane foam is negligible over the time frame considered in this study. Therefore, neglecting the effect of the polar fluid on the permeability of the foam specimens is valid, and the proposed relations given in Eq. (3.14) and Eq. (3.15) are found to be independent of the saturating fluid.

This chapter studies the effect of strain on the permeability of reticulated polyurethane foam saturated with a polar fluid in the laminar regime. Using the fact that the permeability is a function of the applied compressive strain, a physically based composite model, based on the permeability of the linear elastic regime and that of the densified regime, is developed. This relation is found to be applicable to a range of foam cell sizes, and independent of the direction of flow relative to the foam rise direction. Overall, this model is an important step toward the development of a comprehensive understanding of the complete fluid-structure-interaction of foam impregnated with a fluid under dynamic compression.

References

Brace, W., (1977), "Permeability from Resistivity and Pore Shape", *J. Geophys. Res.*, **82**, 3343-3349.

Comiti, J., Sabiri, N., and Montillet, A., (2000), "Experimental Characterization of Flow Regimes in Various Porous Media-III: Limit of Darcy's or Creeping Flow Regime for Newtonian and Purely Viscous Non-Newtonian Fluids", *Chem Eng. Sci.*, **55**, 3057-3061.

Dybbs, A., Edwards, R.V., (1984), "A New Look at Porous Media Fluid Mechanics-Darcy to Turbulent", In: Bear, J. and Cor., Y. *Fund. Trans. Phen. Porous Media* Martinus Nishoff, Dordrecht, pp. 199–256.

Gent, A., Rusch, K., (1966), "Permeability of Open-Cell Foamed Materials", *J. Cell. Plastics*, **2**, 46-51.

Gibson, L.J., Ashby, M.F., (1997), "Cellular Solids – Structures and Properties", 2nd Ed., Cambridge University Press, Cambridge.

Gioia, G., Wang, Y., Cuitino, A., (2000), "The Energetics of Heterogeneous Deformation in Open-Cell Solid Foams", *Proc. R. Soc. Lond. A.*, **457**, 1079-96.

Hilyard, N.C., (1971), "Observations on the Impact Behaviour of Polyurethane Foams; II. The Effect of Fluid Flow", *J. Cell. Plastics*. **7**, 84-90.

Hilyard, N., Collier, P., (1987), "A Structural Model Air Flow Flexible PUR Foams", *Cell. Poly.*, **6**, 9-26.

Hogan, J., Pearson, C., Rogers, T., and White, J., (1973), "Humidity Characteristics HR Hot Urethane Foams", *J. Cell. Plas.*, **9**, 219-225.

Mills, N., Lyn, G., (2002), "Modeling Air Flow in Impacted Polyurethane Foam", *Cell. Poly.*, **21**, 343-65.

Rehkopf, J., Brodland, G., McNeice, G., (1996), "Experimentally Separating Fluid and Matrix Contributions to Polymeric Foam Behavior", *Experimental Mechanics*, **36**, 1-6.

Schraad, M., Harlow, F., (2006), "A Multi-Field Approach to Modeling the Dynamic Response of Cellular Materials", *Int. J. Mech. Sci.*, **48**, 85-106.

Shen, Y., Golnaraghi, F., Plumtree, A., (2001), "Modeling Compressive Cyclic Stress-Strain Behaviour of Structural Foam", *Int. J. Fatigue*, **23**, 491-497.

Tek, M., (1957), "Development of a Generalized Darcy Equation", *J. Petro. Tech.*, **9**, (6), 45-47.

Tables

Table 3.1. Data for each grade of foam. The permeability at 0% strain for each grade of foam before and after precompression. The coefficient a is the best-fit exponent which satisfies Eq. (3.8). $\perp$ and $||$ correspond to the direction of flow being perpendicular and parallel to the rise direction, respectively.

		Before Pre-Compression	After Pre-Compression			
Foam Type (ppi)	**Avg. Cell Dia. (μm)**	k_o ($1x10^{-9}$ m^2)	k_o ($1x10^{-9}$ m^2)	k_{el}^*/k_o	k_d/k_o	a
70 $\|\|$	235	4.85	5.62	0.893	0.221	0.75
70 $\perp$	235	4.67	5.02	0.902	0.214	0.76
80 $\|\|$	210	3.70	3.68	0.897	0.198	0.80
90 $\|\|$	175	3.24	4.98	0.900	0.181	0.85

Figures

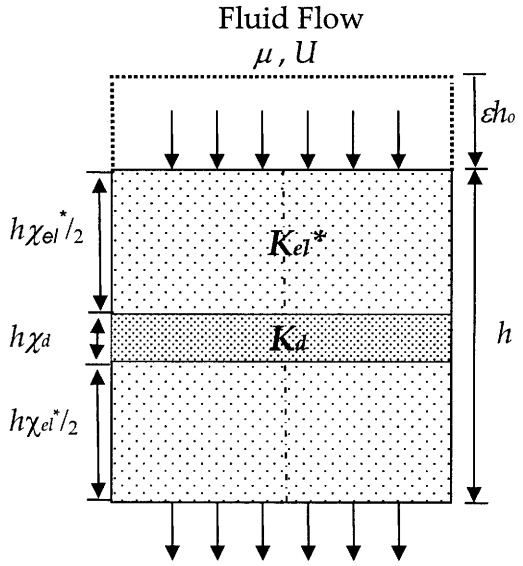

Figure 3.1. Model of fluid-filled cylindrical foam specimen compressed beyond elastic buckling strain, ε_{el}^*.

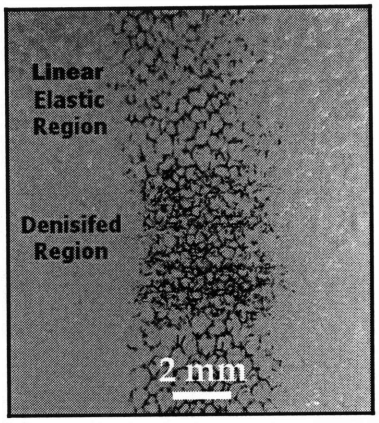

Figure 3.2. Compression of a saturated, 90 ppi, polyurethane foam specimen at 0.40 strain.

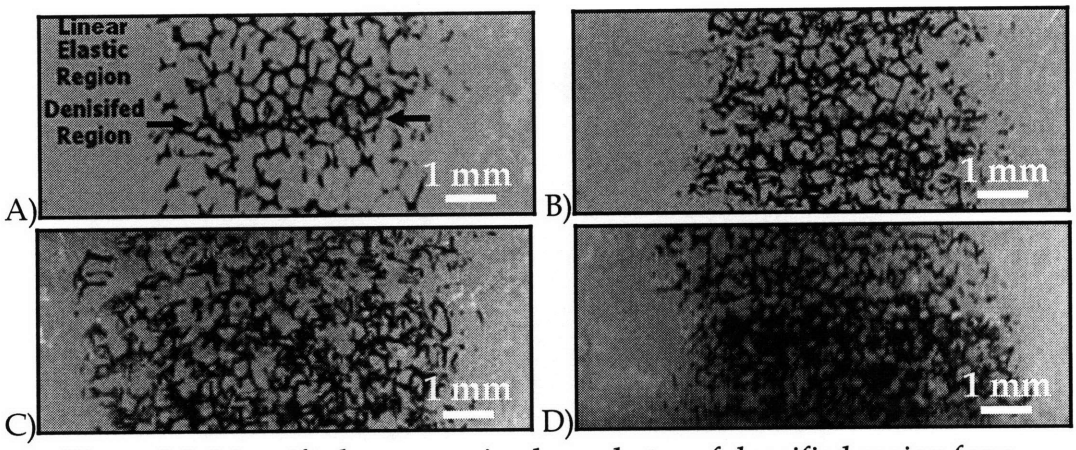

Figure 3.3. Magnified compression laps photos of densified region for a saturated, 90ppi, polyurethane foam specimen. A) 0.20 strain; B) 0.40 strain; C) 0.60 strain; D) 0.80 strain.

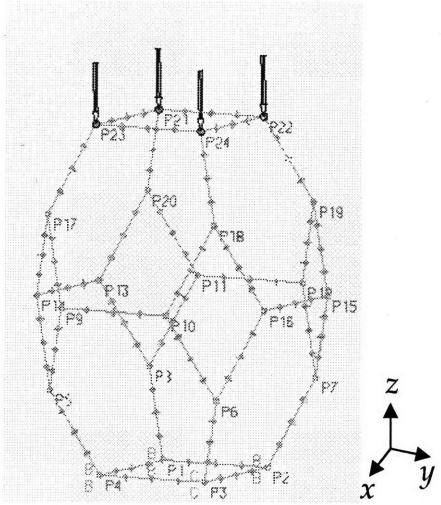

Figure 3.4: ADINA Tetrakaidecahedron Model

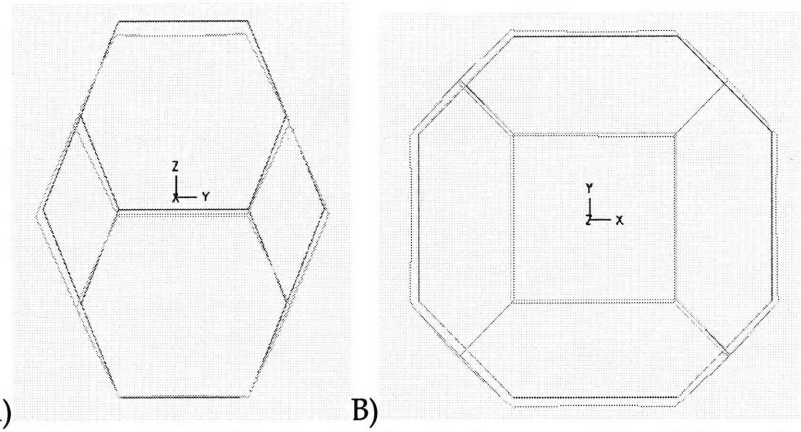

A) B)

Figure 3.5: Deformation of the tetrakaidecahedron model at 0.03 strain. A) Side view (loading parallel to plane); B) Top view (loading into plane).

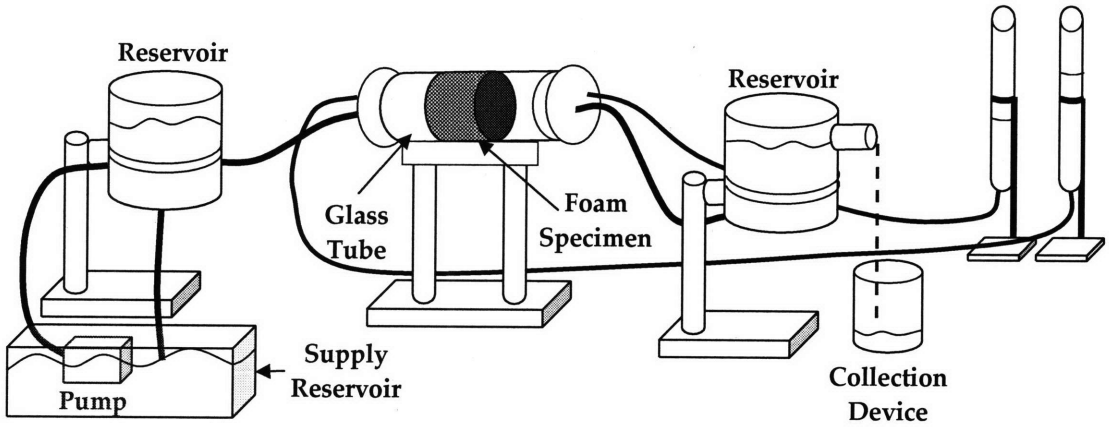

Figure 3.6. Schematic of the experimental setup.

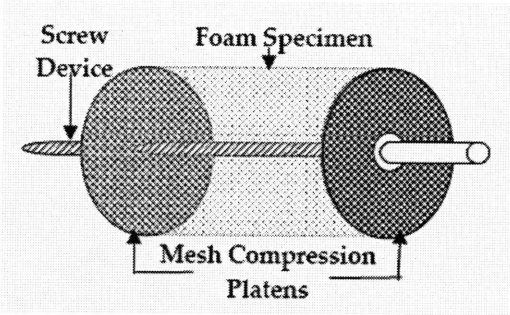

Figure 3.7. Foam compression device.

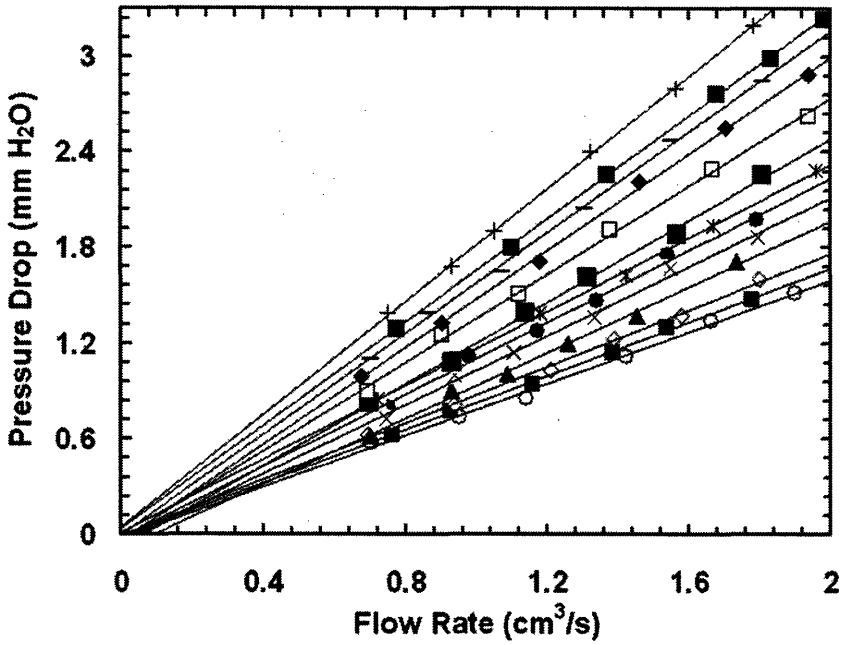

Figure 3.8. A typical plot of pressure drop vs. flow rate for an 80 ppi specimen. Each regression line corresponds to a different strain varying from 0.00 (O) to 0.60 (+) in increments of 0.05. The slope of each line increases correspondingly with increasing strain.

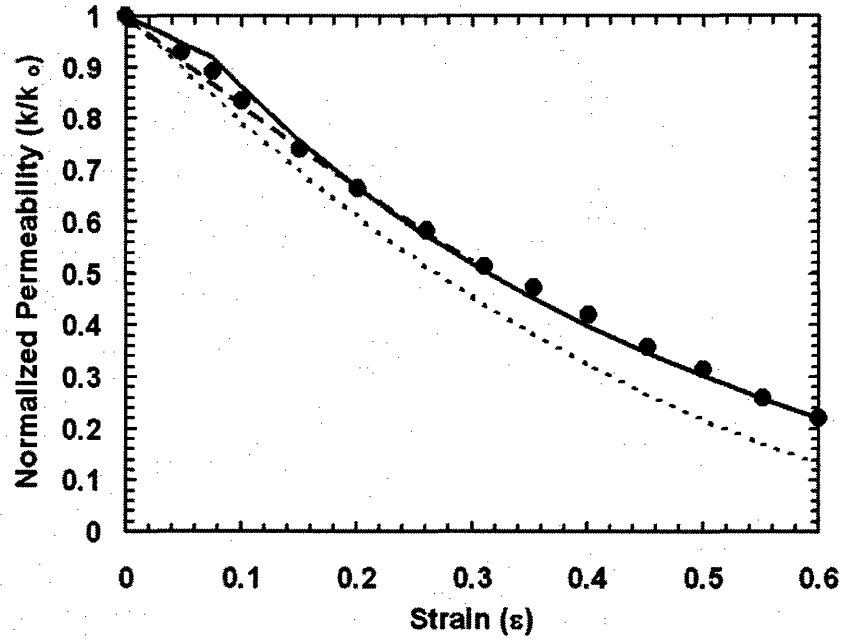

Figure 3.9a. The normalized permeability k/k_O plotted vs. strain ε for 70 ppi polyurethane foam. Gent and Rusch regression (- - -), Hilyard and Collier regression (·····), Dawson, Germaine, and Gibson Model (——). Experimental data from this study (●).

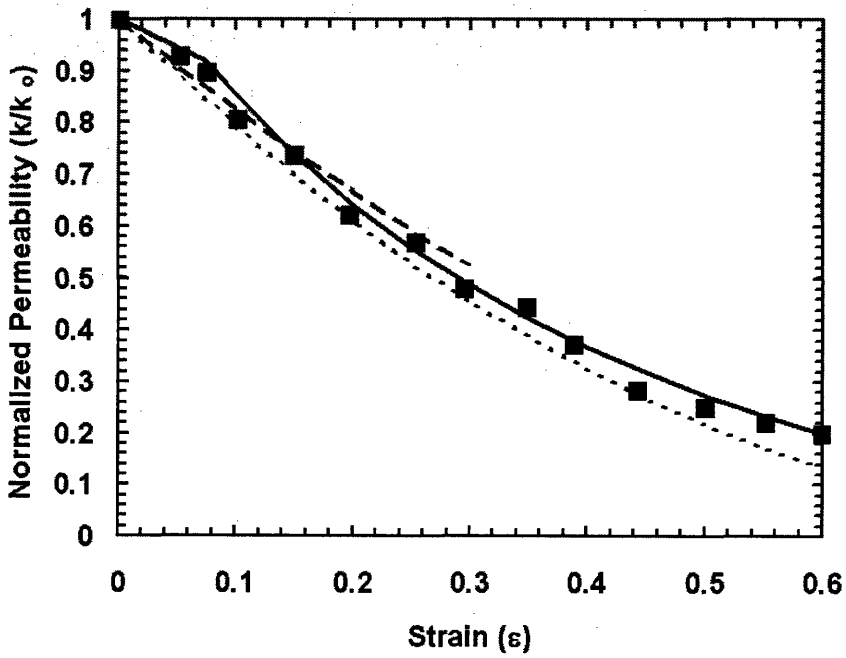

Figure 3.9b. The normalized permeability k/k_O plotted vs. strain ε for 80 ppi polyurethane foam. Gent and Rusch regression (- - -), Hilyard and Collier regression (·····), Dawson, Germaine, and Gibson Model (——). Experimental data from this study (■)

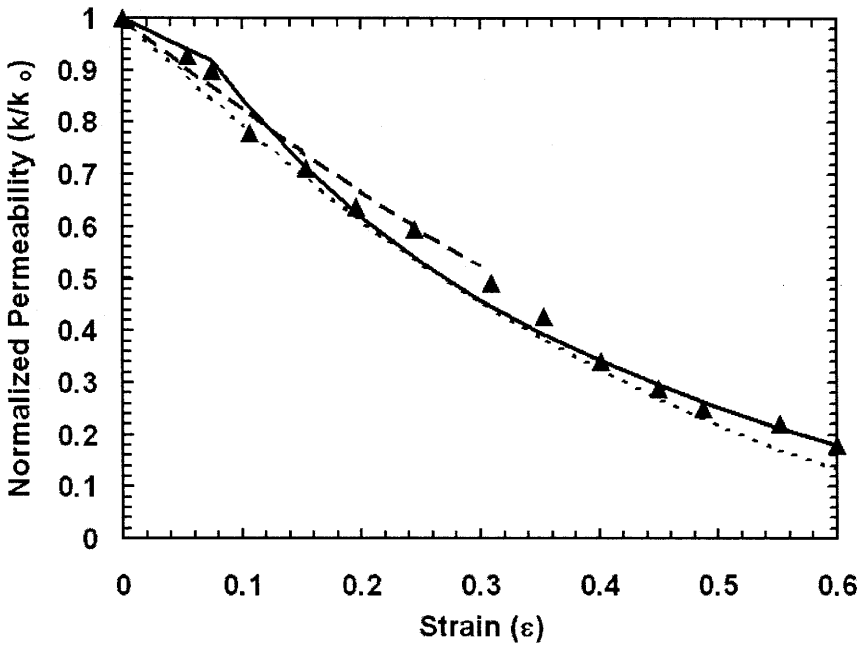

Figure 3.9c. The normalized permeability k/k_O plotted vs. strain ε for 90 ppi polyurethane foam. Gent and Rusch regression (- - -), Hilyard and Collier regression (·····), Dawson, Germaine, and Gibson Model (——). Experimental data from this study (▲).

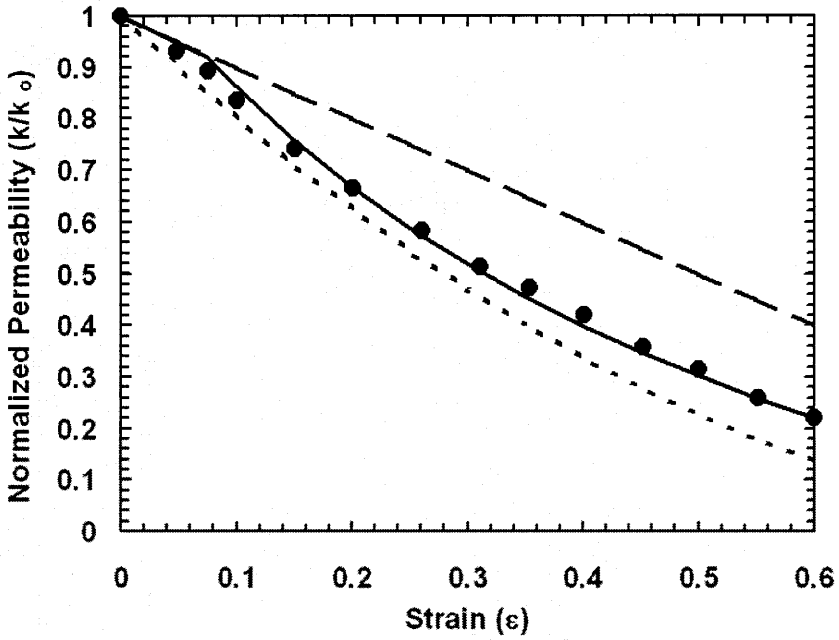

Figure 3.10. The normalized permeability k/k_O plotted vs. strain ε for the Gent and Rusch model (- - -), Hilyard and Collier model (·····), and Dawson, Germaine, and Gibson Model (——) against experimental data for 70 ppi polyurethane foam from this study (●).

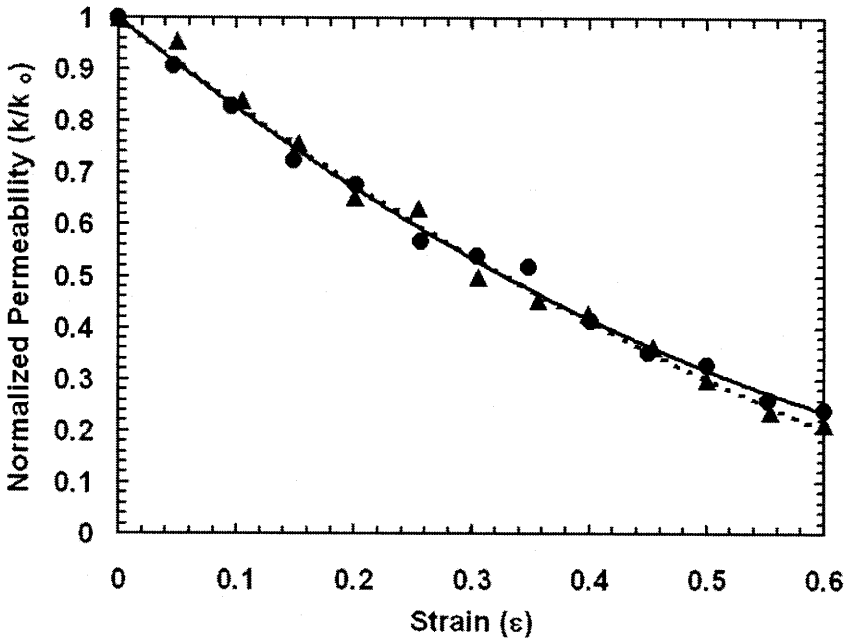

Figure 3.11. Flow orientation independence. The normalized permeability k/k_O plotted vs. strain ε for grade 70 ppi polyurethane foam. Direction of flow is perpendicular (- - -▲), parallel (——●) to the rise direction.

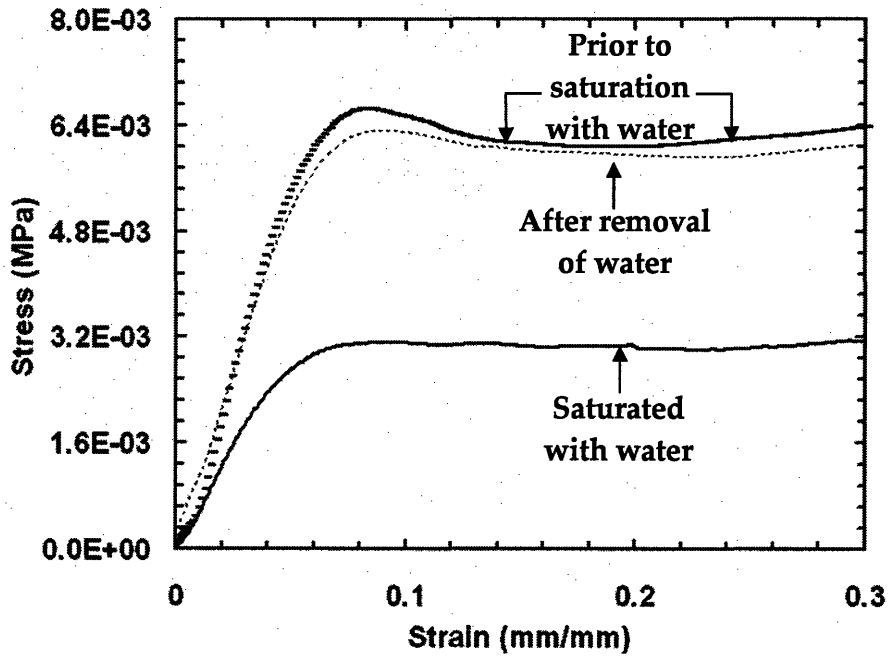

Figure 3.12. Fluid degradation effect. Stress plotted vs. strain for an 80 ppi foam. (- - -) Prior to saturation with water, (——) saturated with water, (·····) after removal of water.

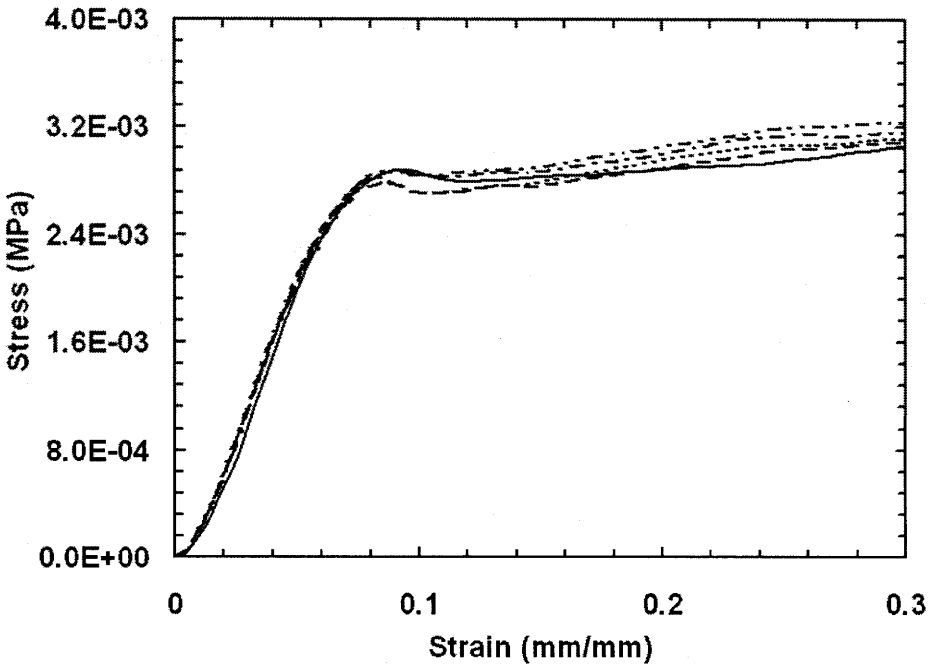

Figure 3.13. Fluid degradation effect with time. Stress plotted vs. strain for an 80 ppi foam saturated with water over time t. (———) t = 0 hours; (– – –) t = 12 hours; (— —) t = 24 hours; (– · – ·) t = 48 hours; (— · ·) t = 72 hours.

4 Dynamic Compressive Response of Open-Cell Foam Impregnated with a Newtonian Fluid

4.1 Introduction

This chapter explores the complete dynamic response of Newtonian fluid-filled foam. We consider the flow of a highly viscous Newtonian fluid in reticulated, elastomeric foam undergoing dynamic compression. As previously discussed, some complex, computational models have been developed to determine the dynamic response of open-cell foam impregnated with a Newtonian fluid, but there is currently no known closed-form analytical model. In this analysis, we develop a tractable, but comprehensive, analytical model for the additional contribution of viscous Newtonian flow to the stress-strain response of low-density, reticulated, fluid-filled, elastomeric foams under dynamic axial compression.

Elastomeric foams are known to deform uniformly in a linear-elastic manner, primarily by cell wall bending at strains below the elastic buckling strain. At strains between the elastic buckling strain and the densified strain, local bands of cells collapse, so that the foam has both a linear-elastic regime and a densified regime (bimodal behavior). As the overall strain increases, the densified regime expands at the expense of the linear elastic regime as discussed in *Chapter 3*. We consider a model which governs both the single regime behavior and the bimodal behavior of the fluid-filled foam. Therefore, the model is applicable for strains up to the densified strain for all grades of low-density, open-cell, elastomeric foam.

Based on the low values of the characteristic Reynolds number in the pores, the flow of highly viscous Newtonian fluids in reticulated foam is dominated by viscous forces for nearly all achievable strain rates; therefore, Darcy's law is assumed to govern the flow. Darcy's law is selected instead of the slightly more complicated Forchheimer-Darcy model, which incorporates both a viscous contribution and an additional term, attributed primarily to the inertial forces dominant in the high Reynold's number regime as discussed in *Chapter 3*. For the more complex bimodal regime problem, Darcy's law is used to formulate a boundary value problem with Laplace's equation as the governing differential equation. The solution to Laplace's equation in cylindrical coordinates for the pressure distribution in the fluid is formulated in terms of an infinite series of Bessel functions. The solution rapidly converges within the first few terms and is readily evaluated numerically. The pressure distribution is used to find the first known analytical model for the contribution of the fluid to the stress-strain response of the fluid-filled foam. The model is compared with experimental results of the stress-strain response of low-density polyurethane foam filled with glycerol under dynamic compression. The model is found to describe experimental data well for foam grades varying from 70 to 90 pores per inch (ppi) and for strain rates varying from 2.5×10^{-3} s^{-1} to 10^{1} s^{-1}. The full model can also be well approximated by a simpler model, based on the lubrication approximation; the lubrication approximation assumes the dimension of the foam in the direction of fluid flow (radial) is much greater than the dimension of the foam in the direction of loading (axial). The boundary value model is found to rapidly converge to the lubrication model in the limit of increasing aspect ratio given by the ratio of the radius R, to the height h, of the foam specimen. The error between these models is found to be negligible for aspect ratios greater than $R/h \sim 4$.

4.2 Literature Review

4.2.1 Microstructural and Global Response of Foam under Compression

To determine the accuracy of any model developed for the contribution of viscous fluid flow through open-cell foam under dynamic compression, we first must develop a comprehensive understanding of the dynamic response of open-cell foam alone. Gibson and Ashby (1997) previously developed a model for the compressive stress-strain response of reticulated foam, neglecting any contribution of a viscous fluid. This model and the governing equations were previously described in *Chapter 2*, Eq. (2.1) - Eq.(2.6). In *Chapter 3*, a detailed discussion of the microstructural behavior of low-density, reticulated foam under compressive strain is presented. Based on this model, we assume in the case of dynamic compression of fluid-impregnated, open-cell foam, the cells of the foam remain elastic up to the linear-elastic buckling strain **(Fig. 4.1)**. As the foam is compressed beyond the elastic buckling strain, cells buckle and collapse without expanding laterally, so that the Poisson's ratio in this regime is approximately zero. As in the case of dry foam, these collapsed regions generate local bands of large deformation in which the average diameter of the cells is reduced substantially. The strain of the collapsed cells in these densified bands is assumed to be uniform and given by the densified strain ε_d, while the cells outside the densified bands remain in the linear elastic regime, at strains given by the elastic buckling strain **(Fig. 4.2)**. Therefore, for strains less than the elastic buckling strain, the entire specimen is assumed to be uniform and completely within the linear elastic regime, resulting in a single regime problem. For strains greater than the elastic buckling strain but less than the densified strain, the foam

is assumed to be a two regime problem with both a linear-elastic region and a densified region **(Fig. 4.2)**. The corresponding values of the elastic buckling strain and the densified strain are based on the values presented in *Chapter 3*. Furthermore, using the models presented in *Chapter 3*, the volume fraction of the cells remaining in the linear elastic regime and the densified regime as well as the local permeability of the foam can be determined for any strain.

4.2.2 Flow in Porous Media

The flow of highly viscous Newtonian fluids in low density, open-cell foam with small cell sizes (typically less than 500 microns) is dominated by viscous forces for nearly all achievable strain rates. Therefore, the model presented in this analysis only considers flows in which the viscous effects dominate the inertial effects. The Reynolds number *Re*, a measure of the inertial forces to the viscous forces, can be used to determine where this model is applicable. A characteristic pore Reynolds number based on the average diameter of a pore d, and average relative velocity of the fluid with respect to the foam through that pore V, is given by

$$Re = \frac{\rho V d}{\mu} \tag{4.1}$$

Based on an analytical study, Comiti et al. (2000) proposed a transition from the viscous dominated regime to the inertial dominated regime at a critical pore Reynolds number of $Re^* = 0.83$ for flow through low-density, porous media. Therefore, the model presented in this analysis is taken to be applicable for $Re \ll 1$ when viscous forces dominate. Based on a transition number of $Re \approx 1$, the

maximum strain rate for which this analysis accurately models the flow of a highly viscous fluid in open-cell foam can be determined. The experimental results presented in this analysis consist of dynamic compression glycerol-filled, reticulated foam with an approximate radius and average cell diameter of 12.7 mm and 235 μm, respectively. At 23°C the density and viscosity of glycerol are taken to be $\rho = 1260$ kg/m^3 and $\mu = 1.1$ Pas, respectively. The maximum strain rate for which the flow will remain in the viscous regime is found to be approximately 600 s^{-1}. The maximum strain rate of the foam specimens in the experiments presented is 10 s^{-1}, which thus lies well within the viscous dominated regime.

4.3 Analysis

4.3.1 Fluid Contribution to the Stress-Strain Response

A comprehensive model for the contribution of the fluid to the stress-strain response of fluid-filled, elastomeric foam under dynamic compression can be developed by extending the model for the permeability of open-cell foam under compressive strain, presented in *Chapter 3*. We consider the case of axial compression of a cylindrical foam specimen where the lower plate is fixed and the upper plate is moving with the magnitude of the velocity given by $|\dot{h}|$, or the time rate of change of the height of the foam specimen as shown in **Fig. 4.1** and **Fig. 4.2a**. The initial height and radius of the specimen are taken to be h_0 and R. As the foam undergoes compression, the radius of the specimen remains unchanged while the current height is given as $h(t)$. This analysis considers both the response at strains less than the elastic buckling strain and the response at strains greater than the elastic buckling strain but less than the densified strain.

For strains less than the elastic buckling strain, the entire specimen is assumed to be uniform and completely within the linear elastic regime, resulting in a single regime problem **(Fig. 4.1)**. For strains greater than the elastic buckling strain but less than the densified strain, the foam is assumed to coexist in two states with both an linear-elastic regime and a densified regime **(Fig. 4.2a-4.2b)**.

4.3.2 Single Regime Model $\varepsilon < \varepsilon_{el}^*$

We first consider the single regime problem with strain less than the elastic buckling strain. As the upper plate compresses the foam, the foam is assumed to deform uniformly. The relative velocity of the fluid with respect to the foam in the compression direction (z-direction) is taken to be zero throughout the foam. Any non-zero relative velocity in the z-direction would require flow up a pressure gradient in the radial direction, which violates Darcy's law. Therefore, neglecting gravitational effects, the pressure gradient throughout the foam in the z-direction is taken to be zero. Thus, the radial velocity of the fluid in the linear-elastic regime V_e, is uniform in the z-direction and given as (after Gibson and Ashby, 1997)

$$V_e = \frac{-\dot{h}r}{2h\phi} \qquad \text{for} \quad 0 \le \varepsilon \le \varepsilon_{el}^* \qquad (4.2)$$

where ϕ is the porosity of the foam, r is the radial distance, h is given by $h(t) = h_o(1-\varepsilon)$. According to Darcy's law the gradient of the pressure across the specimen $\partial P/\partial r$ for viscous Newtonian flow in the r-direction is given as (Darcy, 1856)

$$\frac{\partial P}{\partial r} = \frac{-\mu V_e}{k_e} \qquad \text{for} \quad 0 \le \varepsilon \le \varepsilon_{el}^* \qquad (4.3)$$

where the linear-elastic permeability k_e, is taken to be isotropic. Combining Eq. (4.2) and Eq. (4.3) and integrating gives

$$P^* = \frac{\mu \dot{h}}{4\phi h k_e}\left(r^2 - R^2\right) \qquad \text{for} \quad 0 \le \varepsilon \le \varepsilon_{el}^* \qquad (4.4)$$

where P^* is the local pressure minus the atmospheric pressure at the free surface of the foam. Neglecting inertial effects, a force balance can be used to find an equivalent average uniform stress distribution σ_f, applied by the fluid to the top compression plate by integrating the pressure field over the radius giving

$$\sigma_f = \frac{-\mu \dot{h} R^2}{8\Phi h k_e}. \qquad \text{for} \quad 0 \le \varepsilon \le \varepsilon_{el}^* \qquad (4.5)$$

4.3.3 Bimodal Regime Model $\varepsilon_{el}^* < \varepsilon < \varepsilon_d$

For strains beyond the elastic buckling strain but less than the densified strain, the cells of the foam are assumed to be either at the elastic buckling strain or at the densified strain, corresponding to the bimodal regime model previously discussed. The resulting pressure distribution in both regimes is more complex than in the single regime problem and can be solved by means of coupling two boundary value problems. In formulating the boundary conditions for this problem, a model for the behavior of the foam must be developed. Under axial compression, densified bands are commonly observed to initiate in the center of the sample. Our model assumes the densified regime initiates in the center of the

foam and symmetrically propagates toward the plates through the elastic buckling of one layer of foam (of roughly one cell thickness) at a time as shown in **Fig. 4.2a**. The foam in the elastic regime below the densified regime (Region 1) is stationary while the foam in the elastic regime above the densified regime (Region 3) is moving downward with the upper plate at velocity $|\dot{h}|$ as shown in **Fig. 4.2a**. Therefore, the densified regime (Region 2) is moving downward at velocity ½ $|\dot{h}|$. In the reference frame of the densified regime of the foam, the problem can be viewed as a completely symmetric problem with the elastic regimes (Region 1 and Region 3) of the foam moving toward the densified regime, in opposite directions, at a speed of ½ $|\dot{h}|$. Since there is no flow across the center of the densified regime, by symmetry, we analyze only the top half of the foam in the reference frame of the densified regime as shown in **Fig. 4.2b**. The problem is analyzed as two one-regime models with local reference height ½ h_e and ½ h_d for the elastic and densified regimes, respectively, given as **(Fig. 4.2)**

$$h_e = \chi_{el}^{*} h \tag{4.6}$$

$$h_d = \chi_d h . \tag{4.7}$$

The boundary conditions at the foam-plate interfaces are no flux conditions since the relative velocity of the fluid with respect to the foam is zero. Therefore, according to Darcy's law, the corresponding pressure gradients in the z-direction are zero at both foam-plate interfaces. Boundary conditions applied at the interface between the two regimes are given. The pressure field is taken to be continuous between the two regimes with a discontinuity in the pressure gradient, corresponding to the change in the permeability. In addition, a mass

flux corresponding to the fluid exiting the layer undergoing elastic buckling enters both the linear-elastic and the densified regimes at the interface between the two regimes. We note the cross-sectional surface area of the layer undergoing elastic buckling, between the linear-elastic regime and the densified regime, is much greater than the perimeter surface area of the buckling layer at the free surface of the foam. Therefore, we neglect the radial flow in the buckling layer out of the foam and assume all of the fluid exiting the layer undergoing elastic buckling flows vertically into either the elastic or the densified regimes. The boundary conditions for the two regime problem are given as

$$P_d^* = P_e^* = 0 \qquad \text{on} \qquad r = R \qquad (4.8a)$$

$$\frac{\partial P_d^*}{\partial z} = 0 \qquad \text{on} \qquad z = 0 \qquad (4.8b)$$

$$\frac{\partial P_e^*}{\partial z} = 0 \qquad \text{on} \qquad z = \tfrac{1}{2}h \qquad (4.8c)$$

$$\frac{\partial P_d^*}{\partial z} = \frac{-(1-\alpha)\mu\dot{h}}{2k_d} \qquad \text{on} \qquad z = \tfrac{1}{2}h_d \qquad (4.8d)$$

$$\frac{\partial P_e^*}{\partial z} = \frac{\alpha\mu\dot{h}}{2k_{el}^*} \qquad \text{on} \qquad z = \tfrac{1}{2}h_d \qquad (4.8e)$$

$$P_d^* = P_e^* \qquad \text{on} \qquad z = \tfrac{1}{2}h_d \qquad (4.8f)$$

where α, determined below, is a constant representing the fraction of the flux into the linear-elastic regime, P_e^* is the pressure in the linear-elastic regime, and P_d^* is the pressure in the densified regime.

As before, Darcy's law is assumed to govern the flow of a viscous Newtonian fluid throughout each regime of the foam and is given as (Darcy, 1856)

$$\nabla P^* = \frac{-\mu V}{k} \tag{4.9}$$

where V is once again the relative velocity of the fluid with respect to the foam. Taking the divergence of both sides of Eq. (4.9), applying continuity for an incompressible Newtonian fluid, and considering there is no variation in the velocity of the foam within each region gives Laplace's equation

$$\nabla^2 P^* = \frac{\partial^2 P^*}{\partial r^2} + \frac{1}{r}\frac{\partial P^*}{\partial r} + \frac{1}{r^2}\frac{\partial^2 P^*}{\partial \theta^2} + \frac{\partial^2 P^*}{\partial z^2} = \frac{-\mu \nabla \cdot V}{k} = 0. \tag{4.10}$$

A well known method of solving Laplace's equation in cylindrical coordinates is separation of variables. We assume the pressure is not a function of the circumferential direction (θ-direction) and propose a solution in the form

$$P^* = R(r)Z(z). \tag{4.11}$$

Substituting Eq. (4.11) into Eq. (4.10) and dividing through by $R(r)Z(z)$ gives

$$\frac{1}{R(r)}\frac{\partial^2 R(r)}{\partial r^2} + \frac{1}{rR(r)}\frac{\partial R(r)}{\partial r} + \frac{1}{Z(z)}\frac{\partial^2 Z(z)}{\partial z^2} = 0. \tag{4.12}$$

Since the first two terms are functions of r only and the last term is a function of z only, Eq. (4.12) can be broken up into the following two equations:

$$\frac{1}{Z(z)}\frac{d^2Z(z)}{dz^2} = -\lambda \tag{4.13}$$

$$\frac{1}{R(r)}\frac{d^2R(r)}{dr^2} + \frac{1}{rR(r)}\frac{dR(r)}{dr} = \lambda \tag{4.14}$$

where λ is a constant. Equation (4.13) is a standard second order differential equation, which is readily solved. Equation (4.14) is one form of Bessel's equation and solutions can be expressed in terms of Bessel functions. Combining these solutions, the solution to Laplace's equation for the pressure distribution in either regime of the foam is given as

$$P_i^* = \sum_{n=1}^{\infty}\left(A_{ni}e^{k_n z} + B_{ni}e^{-k_n z}\right)J_o(k_n r) \tag{4.15}$$

where the index i represents either the elastic regime or the densified regime with indices e and d, respectively, A_{ni}, B_{ni}, and k_n are constants, and J_o is a zero order Bessel function of the first kind.

Applying both the Neumann and Dirichlet boundary conditions in Eq. (4.8) to the solution to Laplace's equation given in Eq. (4.15), the pressure distribution throughout the foam can be determined. It is recognized that each term in Eq. (4.15) will satisfy the free surface boundary condition given by Eq. (4.8a) if

$$J_o(k_n R) = 0\,. \tag{4.16}$$

Equation (4.16) therefore gives the values of k_n, corresponding to the zeros of the zero order Bessel function. The values can be determined from a table of Bessel functions. Typically these solutions converge very quickly, so we assume only the first 5 terms of the infinite series are necessary for most values of h/R. The corresponding values of k_n are given as

$$k_1 = \frac{2.405}{R}; \quad k_2 = \frac{5.520}{R}; \quad k_3 = \frac{8.645}{R}; \quad k_4 = \frac{11.792}{R}; \quad k_5 = \frac{14.931}{R}. \tag{4.17}$$

To solve for the unknowns A_{ni} and B_{ni}, the following orthogonality principle of zero order Bessel functions is utilized:

$$\int_0^R r J_o(k_n r) J_o(k_m r) dr = 0 \qquad \text{for} \quad n \neq m \tag{4.18}$$

where $J_o(k_n r)$ is orthogonal to $J_o(k_m r)$. Applying the boundary conditions given by Eq. (4.8b-4.8e) to Eq. (4.15), multiplying each side by r times a zero order Bessel function, and integrating, allows for each coefficients A_{ni} and B_{ni} to be determined by the following set of equations:

$$\left(A_{nd} k_n - B_{nd} k_n\right) \int_0^R r J_o^2(k_n r) dr = 0 \tag{4.19}$$

$$\left(A_{ne} k_n e^{\frac{1}{2}k_n h} - B_{ne} k_n e^{-\frac{1}{2}k_n h}\right) \int_0^R r J_o^2(k_n r) dr = 0 \tag{4.20}$$

$$\left(A_{nd} k_n e^{\frac{1}{2}k_n h_d} - B_{nd} k_n e^{-\frac{1}{2}k_n h_d}\right) \int_0^R r J_o^2(k_n r) dr = \frac{-(1-\alpha)\mu \dot{h}}{2k_d} \int_0^R r J_o(k_n r) dr \tag{4.21}$$

$$\left(A_{ne}k_n e^{\frac{1}{2}k_n h_d} - B_{ne}k_n e^{-\frac{1}{2}k_n h_d}\right)\int_0^R rJ_o^2(k_n r)dr = \frac{\alpha\mu\dot{h}}{2k_{el}^*}\int_0^R rJ_o(k_n r)dr. \tag{4.22}$$

Solving Eq. (4.19)-Eq. (4.22) gives the coefficients A_{ni} and B_{ni} as

$$A_{nd} = \frac{-(1-\alpha)\mu\dot{h}RJ_1(k_n R)}{2k_d(k_n R)^2\sinh(\frac{1}{2}k_n h_d)\left[J_o^2(k_n R)+J_1^2(k_n R)\right]} \tag{4.23}$$

$$A_{ne} = \frac{\alpha\mu\dot{h}RJ_1(k_n R)}{k_{el}^*(k_n R)^2(1-e^{k_n h_e})\left[J_o^2(k_n R)+J_1^2(k_n R)\right]} \tag{4.24}$$

$$B_{nd} = \frac{-(1-\alpha)\mu\dot{h}RJ_1(k_n R)}{2k_d(k_n R)^2\sinh(\frac{1}{2}k_n h_d)\left[J_o^2(k_n R)+J_1^2(k_n R)\right]} \tag{4.25}$$

$$B_{ne} = \frac{\alpha\mu\dot{h}RJ_1(k_n R)e^{k_n h_e}}{k_{el}^*(k_n R)^2(1-e^{k_n h_e})\left[J_o^2(k_n R)+J_1^2(k_n R)\right]} \tag{4.26}$$

where $J_1(k_nR)$ is a first order Bessel function. Substituting Eq. (4.23) - Eq. (4.26) into Eq. (4.15) and applying Eq. (4.16) gives the adjusted pressure distribution in both the densified regime and the elastic regime as

$$P_d^* = \sum_{n=1}^{\infty}\frac{-(1-\alpha)\mu\dot{h}R\cosh(k_n z)J_o(k_n r)}{k_d(k_n R)^2\sinh(\frac{1}{2}k_n h_d)J_1(k_n R)} \qquad \varepsilon_{el}^* \le \varepsilon \le \varepsilon_d \tag{4.27}$$

$$0 \le z \le \tfrac{1}{2}h_d$$

$$P_e^* = \sum_{n=1}^{\infty} \frac{\alpha\mu\dot{h}R\left(e^{k_n(z-\frac{1}{2}h_d)} + e^{k_n(h_e-z+\frac{1}{2}h_d)}\right)J_o(k_n r)}{k_{el}^*(k_n R)^2\left(1-e^{k_n h_e}\right)J_1(k_n R)}. \qquad \varepsilon_{el}^* \le \varepsilon \le \varepsilon_d \qquad (4.28)$$

$$\tfrac{1}{2}h_d \le z \le \tfrac{1}{2}h$$

Applying the remaining boundary condition in Eq. (4.8f), the constant α can be determined numerically. Since the terms of the pressure distribution given in Eq. (4.27) and Eq. (4.28) decay rapidly, a good approximation to α can be given using only the first term in the series

$$\alpha = \frac{k_{el}^* \tanh(\frac{1}{2}k_1 h_e)}{k_{el}^* \tanh(\frac{1}{2}k_1 h_e) + k_d \tanh(\frac{1}{2}k_1 h_d)}. \qquad (4.29)$$

The fraction of the flux into the linear-elastic regime α, as a function of strain is given in **Fig. 4.3**. A force balance can be used to find an equivalent uniform stress distribution σ_f, applied to the top compression plate by integrating the pressure field in the elastic regime at $z = {}^1/_2 h$ over the radius as follows:

$$\sigma_f \pi R^2 = \int_0^R P_e^*\,|_{\frac{h}{2}}\, 2\pi r dr \qquad \varepsilon_{el}^* \le \varepsilon \le \varepsilon_d \qquad (4.30a)$$

$$\sigma_f \pi R^2 = \left(\sum_{n=1}^{\infty} \frac{2\pi\alpha\mu\dot{h}R\left(2e^{k_n(\frac{1}{2}h_e)}\right)}{k_{el}^*(k_n R)^2\left(1-e^{k_n h_e}\right)J_1(k_n R)}\right)\left(\int_0^R rJ_o(k_n r)dr\right) \quad \varepsilon_{el}^* \le \varepsilon \le \varepsilon_d \qquad (4.30b)$$

$$\sigma_f R^2 = \sum_{n=1}^{\infty}\left(\frac{4\alpha\mu\dot{h}R}{k_{el}^*(k_n R)^2\left(e^{-k_n(\frac{1}{2}h_e)} - e^{k_n(\frac{1}{2}h_e)}\right)J_1(k_n R)}\right)\left(\frac{R^2 J_1(k_n R)}{(k_n R)}\right) \varepsilon_{el}^* \le \varepsilon \le \varepsilon_d \qquad (4.30c)$$

$$\sigma_f = \frac{-2\alpha\mu\dot{h}R}{k_{el}^*}\sum_{n=1}^{\infty}\frac{1}{(k_nR)^3\sinh(\frac{1}{2}k_nh_e)}. \qquad \varepsilon_{el}^* \le \varepsilon \le \varepsilon_d \qquad (4.30d)$$

Equation (4.30d) is taken to be the contribution of the fluid to the stress-strain response of foam filled with a Newtonian fluid under dynamic compression in the two regime model. The dependence of the response given by Eq. (4.30d) on strain is built in through the terms α and h_e, which are functions of the volume fraction of the cells remaining in the linear-elastic and densified regimes, and therefore, are functions of the strain.

4.3.4 The Effect of Tortuous and Anisotropic Foam Microstructure

A discrepancy is typically found between analytical models for flow through porous media and experimental measurements. Models are often adjusted by an empirical constant, which accounts for the tortuous shape of the foam microstructure (Comiti et al., 1988). Similarly, empirical constants have also been used to account for the tortuous microstructure of foam in studies of heat transfer through porous media. Glicksman (1994) determined an efficiency factor of 2/3 accounted for the effective loss in the thermal conductivity of porous media. Furthermore, it is known that the permeability of low-density, open-cell foam is slightly anisotropic, which may also lead to deviations of the model presented in this analysis from experimental data. The combination of these effects necessitates the addition of empirical constant C to the model. Therefore, we propose the stress contribution of a Newtonian fluid to the response of a fluid-filled foam under dynamic loading is given by

$$\sigma_f = \frac{-C\mu\dot{h}R^2}{8\phi h k_e} \qquad 0 \le \varepsilon \le \varepsilon_{el}^* \qquad (4.31)$$

$$\sigma_f = \frac{-2C\alpha\mu\dot{h}R}{k_{el}^*}\sum_{n=1}^{\infty}\frac{1}{(k_nR)^3\sinh(\frac{1}{2}k_nh_e)} \qquad \varepsilon_{el}^* \le \varepsilon \le \varepsilon_d \qquad (4.32)$$

where C is a single constant to be determined by regression from experiments.

4.3.5 Squeezing Flow between Parallel Plates

We now proceed to develop a more tractable model for the dynamic response of fluid-filled foam, which can be used to approximate the boundary value model in the lubrication limit, where the aspect ratio of the foam is much greater than unity. We first consider a model for squeezing flow between two parallel plates in the absence of an open-cell foam where the lower plate is fixed and the upper plate is moving similar to **Fig. 4.1.** The flow is assumed to be incompressible and locally fully-developed with no variation in the circumferential direction (θ-direction). The gravitational effects are assumed to be negligible. Since the flow is assumed to be dominated by viscous forces, inertial effects can also be neglected. The following velocity profiles are assumed:

$$V_r = V_r(r,z); \quad V_z = V_z(z); \quad V_\theta = 0 \qquad (4.33)$$

where V_r, V_z, and V_θ are the velocity components in the radial (r), axial (z) and circumferential (θ) directions, respectively. Coupling the equation of continuity with the full Navier-Stokes equations of motion, this problem is readily solved. The equation of continuity and the Navier-Stokes equations of motion in the radial and axial directions reduce to

$$\frac{1}{r}\frac{\partial(rV_r)}{\partial r}+\frac{\partial V_z}{\partial z}=0 \tag{4.34}$$

$$\mu\left(\frac{\partial}{\partial r}\frac{1}{r}\frac{\partial}{\partial r}(rV_r)+\frac{\partial^2 V_r}{\partial z^2}\right)-\frac{\partial P}{\partial r}=0 \qquad \text{(r-direction)} \tag{4.35}$$

$$\mu\left(\frac{1}{r}\frac{\partial}{\partial r}r\frac{\partial V_z}{\partial r}+\frac{\partial^2 V_z}{\partial z^2}\right)-\frac{\partial P}{\partial z}=0 \qquad \text{(z-direction)} \tag{4.36}$$

where P is the local pressure within the fluid. To solve Eq. (4.34-4.36) we initially impose a lubrication approximation in which the square of the ratio of the characteristic dimension in the radial flow direction to that in the axial compression direction is assumed to be much greater than unity, $(R/h)^2 >> 1$. The resulting equations of motion are given as

$$\mu\left(\frac{\partial^2 V_r}{\partial z^2}\right)-\frac{\partial P}{\partial r}=0 \qquad \text{(r-direction)} \tag{4.37}$$

$$\frac{\partial P}{\partial z}=0\,. \qquad \text{(z-direction)} \tag{4.38}$$

The corresponding boundary conditions are

$$V_r\big|_{z=h}=0\,;\quad \left.\frac{\partial V_r}{\partial z}\right|_{z=h/2}=0\,;\quad V_z\big|_{z=0}=0\,;\quad V_z\big|_{z=h}=\dot{h}\,;\quad P\big|_{r=R}=P_a\,; \tag{4.39}$$

where P_a is the atmospheric pressure on the free surface, and the magnitude of the velocity of the top plate is given by $|\dot{h}|$. Solving Eq. (4.37-4.38) gives the pressure profile as

$$P - P_a = \frac{3\mu\dot{h}}{h^3}\left(r^2 - R^2\right). \tag{4.40}$$

The pressure distribution is found to be independent of the z- and θ-directions. We propose that the pressure field given by Eq. (4.40) for squeezing, viscous flow is similar to the pressure field for squeezing flow in a low-density foam. Therefore, in the lubrication limit, the pressure field for an incompressible, viscous Newtonian flow through low-density foam is assumed to be independent of the z- and θ-directions.

4.3.6 Stress-Strain Response in the Lubrication Limit

The model of viscous squeezing flow between two parallel plates described above does not completely describe the flow field for axial compression of a fluid-filled foam because of the fluid-structure-interaction and the non-linear behavior of the foam under deformation; however, we assume that the pressure field of the parallel plate model is representative of that found in a lubrication model of a fluid-filled foam. Therefore, we take the pressure field in axially compressed fluid-filled foam to be independent of the z- and θ-directions.

Using this assumption, we extend the model given in *Chapter 3* for reticulated foam under compressive strain. We consider the case of axial compression of a cylindrical foam specimen where the characteristic radius is much greater than

the characteristic height. The initial radius and height of the specimen are taken to be R and h_0. As the foam undergoes compression the radius of the specimen remains unchanged while the instantaneous height is given as $h(t)$. Compression occurs between two plates where the lower plate is assumed to be fixed and the magnitude of the velocity of the upper plate is $|\dot{h}|$ as shown in **Fig. 4.1-4.2**. This analysis considers both the response at strains less than the elastic buckling strain and the response at strains greater than the elastic buckling strain but less than the densified strain. We first consider the single regime problem with strain less than the elastic buckling strain. The average radial velocity of the fluid in the elastic regime at any point in the specimen V_e, is given as (after Gibson and Ashby, 1997)

$$V_e = \frac{-\dot{h}r}{2h\phi} \qquad 0 \le \varepsilon \le \varepsilon_{el}^* \qquad (4.41)$$

According to Darcy's law the gradient of the pressure across the specimen $\partial P/\partial r$ for viscous Newtonian flow is given as (Darcy, 1856)

$$\frac{\partial P}{\partial r} = \frac{-\mu V_e}{k_e}. \qquad 0 \le \varepsilon \le \varepsilon_{el}^* \qquad (4.42)$$

Combining Eq. (4.41) and Eq. (4.42) and integrating gives

$$P - P_a = \frac{\mu\dot{h}}{4\phi h k_e}\left(r^2 - R^2\right) \qquad 0 \le \varepsilon \le \varepsilon_{el}^* \qquad (4.43)$$

Neglecting inertial effects, a force balance can be used to find an equivalent uniform stress distribution σ_f, applied to the top compression plate by integrating the pressure field over the radius giving

$$\sigma_f = \frac{-\mu \dot{h} R^2}{8\phi h k_e}. \qquad 0 \le \varepsilon \le \varepsilon_{el}^* \qquad (4.44)$$

For strains beyond the elastic buckling strain but less than the densified strain, the model is taken to be a two regime model as shown in **Fig. 4.2.** Based on the previous assumptions regarding no axial variations in the pressure field, the pressure drop from the any radius r to the outer radius R is assumed to be the same in both the elastic region and the densified region. Coupling this relation between the pressure drops in each region with Eq. (4.42) gives

$$\frac{V_e}{k_{el}^*} = \frac{V_d}{k_d} \qquad \varepsilon_{el}^* \le \varepsilon \le \varepsilon_d \qquad (4.45)$$

where V_d is the velocity of the fluid at any radius r in the densified region. Using Eq. (4.45), mass conservation about a cylindrical volume at any given r gives

$$V_e = \frac{-\dot{h} k_{el}^* r}{2h\phi\left(\chi_{el}^* k_{el}^* + \chi_d k_d\right)}. \qquad \varepsilon_{el}^* \le \varepsilon \le \varepsilon_d \qquad (4.46)$$

Coupling Darcy's law with Eq. (4.46), gives the pressure gradient across the specimen $\partial P/\partial r$ for viscous Newtonian flow (Darcy, 1856)

$$\frac{\partial P}{\partial r} = \frac{\mu \dot{h} r}{2h\phi\left(\chi_{el}^{*} k_{el}^{*} + \chi_d k_d\right)}. \qquad \varepsilon_{el}^{*} \le \varepsilon \le \varepsilon_d \qquad (4.47)$$

Integrating Eq. (4.47) and applying the atmospheric pressure boundary condition at the free surface gives

$$P - P_a = \frac{\mu \dot{h}}{4h\phi\left(\chi_{el}^{*} k_{el}^{*} + \chi_d k_d\right)}\left(r^2 - R^2\right). \qquad \varepsilon_{el}^{*} \le \varepsilon \le \varepsilon_d \qquad (4.48)$$

As before, neglecting inertial effects, a force balance can be used to find an equivalent uniform stress distribution σ_f, applied to the top compression plate by integrating the pressure field over the radius giving

$$\sigma_f = \frac{-\mu \dot{h} R^2}{8h\phi\left(\chi_{el}^{*} k_{el}^{*} + \chi_d k_d\right)}. \qquad \varepsilon_{el}^{*} \le \varepsilon \le \varepsilon_d \qquad (4.49)$$

4.3.7 Convergence of the Boundary Value Model to the Lubrication Model

In this analysis, we consider the convergence of the boundary value model to the lubrication model in the limit of large *R/h*. A parametric study is used to compare the model given by Eq. (4.31) and Eq. (4.32) for varying ratios of *R/h* to the lubrication model given by Eq. (4.44) and Eq. (4.49). The models can be readily compared if each model is rewritten in the following form

$$\sigma_f = -C_1\left(\frac{\mu \dot{h} R^2}{h k_e}\right) \qquad 0 \le \varepsilon \le \varepsilon_{el}^{*} \qquad (4.50)$$

$$\sigma_f = -C_1\left(\frac{\mu \dot{h} R^2}{h k_{el}^*}\right) \qquad \varepsilon_{el}^* \le \varepsilon \le \varepsilon_d \qquad (4.51)$$

where C_1 is the dimensionless coefficient corresponding to the numerically evaluated portion of each model, including the empirically derived coefficient C, which will be determined in the experimental section of this chapter. For strains less than the elastic buckling strain, the coefficient C_1 for the model presented in this analysis is independent of the aspect ratio of the specimen. Therefore, for strains less than the elastic buckling strain, the model presented in this analysis is identical to that presented in the lubrication analysis for all aspect ratios of the foam. Thus, there is no difference in the coefficients C_1, for the lubrication and boundary value models in this regime. However, for strains greater than the elastic buckling strain but less than the densified strain, the coefficient C_1 for the boundary value model is a function of the aspect ratio of the foam and the strain while that for the lubrication model is only a function of strain. Therefore, the convergence of this bimodal model toward the lubrication model, with increasing aspect ratio, is presented for three different strains in Table 4.1. To determine the coefficient C_1 for both the bimodal model presented in this analysis and the lubrication model, the necessary parameters are evaluated numerically based on the data. As given in *Chapter* 3, the permeability of the foam at the densified strain is taken to be 20% of that of the foam at the elastic buckling strain, $k_d = 0.20\, k_{el}^*$, the elastic buckling strain is taken to be $\varepsilon_{el}^* = 0.05$; the densified strain is taken to be $\varepsilon_d = 0.60$; the porosity is taken to be $\phi = 0.97$.

4.3.8 Solid Matrix Contribution to the Stress-Strain Response

To accurately assess the contribution of the fluid to the dynamic response of the fluid-filled foam, we must also determine the contribution of the solid foam matrix to the stress-strain response. The models given in Eq. (2.1) – Eq. (2.6) are useful in determining the contribution of the foam matrix to the overall dynamic response of fluid-filled foam. All of the parameters required for evaluating those equations are readily acquired, except for the modulus of the foam. Gibson and Ashby (1997) present a model for the quasi-static, effective modulus of the foam, which depends on the modulus of the solid from which the foam is made E_S, and the relative density of the foam:

$$E^* = E_S \left(\frac{\rho_o^*}{\rho_s} \right)^2 . \tag{4.53}$$

Based on a material modulus E_S, of 150 MPa and a relative density of 0.03, the Gibson and Ashby model predicts a quasi-static, effective foam modulus E^*, of 0.135 MPa for open-cell, flexible, polyurethane foam. However, the effective modulus of the foam is known to depend strongly on the strain rate due to viscoelastic effects in the quasi-static loading regime and due to micro-inertial effects and localization phenomenon in the high-rate loading regime. Since no known analytical model exists to assess the magnitude of these effects on the effective modulus, a finite element analysis using ADINA is performed based on the tetrakaidecahedral cell presented in *Chapter 3*. This analysis is useful in determining an order of magnitude estimation of the contribution of micro-inertial effects to the effective modulus of foam. We first examine the accuracy of the finite element model by performing a quasi-static analysis and comparing the resulting quasi-static modulus to that given by the Gibson and Ashby model (Eq.

4.53). Then a fully dynamic analysis is performed, to assess the effect of the loading rate on the effective modulus.

The model of a tetrakaidecahedral cell presented in *Chapter 3* is used to determine the quasi-static modulus in the linear-elastic regime with an 8 subdivision x 2 node meshing scheme. To determine the stress the sum of the four point loads is divided by the cross-sectional area of the foam over which the load is applied on a macroscopic basis. This equivalent cross-sectional area of a tetrakaidecahedral cell is 5.828 L^2, where L is the length of one strut. The finite element model results in the stress-strain plot given in **Fig. 4.4** for a tetrakaidecahedron under quasi-static loading. The calculated effective modulus is determined to be 0.130 MPa, which is supported by the Gibson and Ashby prediction of 0.135 MPa. Furthermore, a meshing efficiency study was performed to assess the quality of meshing in the finite element simulation. The 8x2 meshing scheme was found to be more than sufficient for the purposes of this analysis, generating the largest displacement of the meshes considered. The largest displacement ensures this structure has the most degrees of freedom, allowing the model to behave more like a continuum and more accurately represent the actual behavior of the structure.

Considering the finite element simulation accurately models the quasi-static scenario, we extend this analysis to the dynamic loading scenario. The first step in a dynamic analysis is to determine the natural frequencies of the structure (without consideration of loading). The lowest natural frequency of the tetrakaidecahedral structure is found to be 4.5×10^4 rad/sec. Using a highly stable, implicit Newmark method, a dynamic analysis was carried out over 20 time steps up to a strain of 0.03 to determine the modulus as a function of the load

rate. The time step is taken to be the period of the lowest natural frequency over 20, giving approximately $7x10^{-6}$ s. To ensure the period of the applied loading is greater than the natural period of the structure, the applied loading was analyzed over three periods of $1x10^{-5}$ s, $1x10^{-4}$ s, and $1x10^{-3}$ s. The results for the effective modulus of the tetrakaidecahedral cell as a function of the loading period are shown in Table 4.2. As the strain rate is decreased, the effective modulus converges toward a value, which is very close to the static modulus, as expected. This convergence is expected since it is known that the deviation from the static response decreases substantially as the frequency of loading converges toward the first natural frequency of the structure. As the frequency of the load rate is increased (strain rate of the foam is increased), the effective modulus is found to increase due to micro-inertial effects. The change in the effective modulus with increasing strain rate is evident, but not dramatic, increasing approximately 50% over two orders of magnitude in the strain rate. Therefore, the dynamic effects do not result in dramatic changes in the effective modulus of the foam, especially over the loading rates considered in this analysis; however, they are significant enough that they should not be neglected. From this finite element analysis it is apparent that the effective modulus of low-density, open-cell, polyurethane foam should be on the same order of magnitude over several orders of magnitude in strain rate. This finding is useful in supporting the results presented in the experimental section of this chapter where a simple method to account for the affect of dynamic loading on the effective modulus is developed (*Section 4.4.4*).

4.4 Experiments

4.4.1 Materials

Specimens of open-cell, flexible, polyester-based polyurethane foams (New Dimension Industries, Moonachie, NJ), with nominal cell diameters of 175 μm, 210 μm, and 235 μm based on manufacturers specifications (corresponding to grades of 90, 80, and 70 pores per inch (ppi), respectively) were used in the tests. The densities of the foams ranged from 0.0318 to 0.0322 g/cm^3. Based on the manufacturer's value of the density of the solid polyurethane (ρ_s = 1.078 g/cm^3) the relative density of the foams was taken to be $\rho^*_o/\rho_s \cong 0.03$. Using Eq. (1.4) the corresponding fully densified strain, is determined to be $\varepsilon_D = 0.958$. The foam was cut into uniform cylindrical specimens with diameter and height, D = 25.4 mm and h = 12.8 mm, respectively. The dimensions of each sample were measured using a digital caliper accurate to within 0.01 mm. The Newtonian fluid used in these experiments is glycerol (VWR, West Chester, PA) where the density and viscosity are measured to be ρ = 1260 kg/m^3 and μ = 1.1 Pa-s at 23 °C.

4.4.2 Experimental Testing Apparatuses

To examine a large range of strain rates (several orders of magnitude), both a Texture Analyzer (TA XT Plus, Stable Microsystems, Hamilton, MA) and a servohydraulic Instron testing machine (Instron Model 1321, Instron Corp., Canton, MA) were used in these experiments. As previously discussed in *Chapter 3.4.2* the Texture Analyzer is commonly used for 'low strain rate' experiments (10^{-6}–10^0 s^{-1}) with corresponding compression velocity ranges from 10^{-2} mm/s to 10^1 mm/s. The load cell of the Texture Analyzer can measure up to a force of 50 kg with a resolution of 0.1 g, and the vertical displacement is

determined with a resolution of 10^{-3} mm. The data acquisition system used was the Texture Exponent 32 code, which acquires both loading and positioning information for each test at a rate of 1 sample per second. The Instron testing machine is typically used for 'mid-range strain rates' (10^{-3}–10^{1} s^{-1}) with corresponding velocities of approximately 10^{-2} to 10^{2} mm/s. Two Instron load cells were used, depending on the expected output load, for higher resolution of the data. The load cells were a 10,000 lb load cell and a 1 kN load cell with a load resolution of 0.1 N and a distance resolution 0.01 mm. The maximum cross-head speed of the Instron is 250 mm/s. The data acquisition system utilized Labview software and was able to take data at a rate in excess of 1000 samples per second.

4.4.3 Experimental Procedure

Prior to testing, each sample was saturated with glycerol. Since the viscosity of glycerol is a strong function of temperature, it was heated to 40°C before saturation to aid in the saturation process (Incufridge, RS-IF-202, Revolutionary Science, Lindstrom, MN). Samples were axially compressed by machine, while submerged in glycerol, and uncompressed at 1 mm/s. This process was repeated a minimum of three times while flipping the samples in between each compression cycle to remove as much air from the fluid-filled foam as possible. Hager and Craig (1992) demonstrated the indentation force deflection loss (a measure of the load bearing capability of flexible polyurethane foam) of polyurethane foam compressed to 0.75 strain for a short duration of time is almost completely recoverable. Therefore, a compressive strain of 0.75 was selected for saturating the sample to minimize the microstructural damage caused by the filling process. After saturation, the fluid-filled foam was brought to a steady temperature of 23°C and allowed to recover (Incufridge, RS-IF-202,

Revolutionary Science, Lindstrom, MN). Based on data for the recovery of low-density polyurethane foam after 0.75 compression presented by Hager and Craig (1992), a recovery time of 2 hours was selected.

The compressive stress-strain response of each glycerol-filled specimen was measured with the rise direction of the foam parallel to the direction of loading, from 0 to 0.60 strain over a range of strain rates from $\dot{\varepsilon} = 2.5\text{x}10^{-3}$ s^{-1} to 10^{1} s^{-1}. For strain rates of $\dot{\varepsilon} = 1$ s^{-1} or less a Texture Analyzer was used at constant strain rate; for strain rates greater than $\dot{\varepsilon} = 1$ s^{-1} an Instron testing machine was used at constant velocity. The samples were removed from the incufridge (Incufridge, RS-IF-202, Revolutionary Science, Lindstrom, MN), which maintained the temperature of the samples at 23.0°C ± 0.1°C, and tested immediately in an environment also maintained at 23.0°C to ensure the glycerol retains nearly a constant viscosity. Since the flow is assumed to be instantaneously fully developed, the model presented in this analysis is applicable to both constant velocity and constant strain rate loading. Experimental results are presented for 144 specimens in this chapter, spanning 3 foam grades, and several orders of magnitude in strain rate.

4.4.4 Experimental Results

A typical plots of the stress-strain response of 90 ppi foam filled with glycerol loaded at a constant strain rate of $\dot{\varepsilon} = 0.01$ s^{-1} is shown in **Fig. 4.5.** This strain rate is assumed to most accurately represent quasi-static loading where the loading is slow enough that the fluid is not expected to contribute significantly to the response of the specimen, yet fast enough that viscoelastic effects in the foam are negligible. Using **Fig. 4.5**, the parameters and constants governing the response

of the foam structure, given in *Chapter 2* (Eq. (2.1) - Eq. (2.6)), can be determined. A detailed discussion of the microstructural behavior of open-cell foam under compressive loading in the direction of the rise direction of the foam is given by Gong and Kyriakides (2005). They discuss the complex local and global buckling behavior of low-density, open-cell foam. We consider a simplified model for the elastic buckling strain ε_{el}^*, taken to be the average value of the strain at which the behavior of the foam begins to deviate from the linear-elastic regime and the strain corresponding to the peak stress prior to the plateau region as shown in **Fig. 4.5**. The elastic buckling stress σ_{el}^*, is taken to be the stress at the elastic buckling strain ε_{el}^*. As previously discussed, ε_p^* corresponds to the strain at which the stress at the end of the plateau region is equal to the elastic buckling stress as shown in **Fig. 4.5**. The values for the elastic buckling strain ε_{el}^*, the strain at which the stress at the end of the plateau stress is equal to the elastic buckling stress ε_p^*, and the corresponding constant are provided for grades of 70, 80, and 90 ppi foam in Table 4.3. The elastic buckling strains correspond well with previous literature on low-density foams (Gibson and Ashby, 1997).

The final unknown parameter in the model for the response of the saturated foam structure given in *Chapter 2* (Eq. (2.1a)) is the effective modulus, E^*. As previously discussed, the effective modulus of the saturated foam is known to depend strongly on the strain rate. In the quasi-static loading regime, the effective modulus depends on the viscoelastic effects, while in the high-rate loading regime, it depends on micro-inertial effects and localization phenomenon. Based on the finite element simulation in *Section 4.3.8*, it is determined that the dynamic effects do not have a dramatic effect on the effective modulus used in Eq. (2.1) – Eq. (2.2), but they should not be neglected. A simple way to account for the dynamic effects on the effective modulus of the

fluid-filled foam is to develop an empirical model by measuring the modulus over a range of strain rates where the fluid contribution is considered to be negligible. Using this technique, an empirical model for the effective modulus of the foam saturated with a polar fluid E*, can be found. This effective modulus can then be evaluated in Eq. (2.2) to determine the dynamic contribution to the stress response from the foam matrix. The modulus E^*, is found to be well approximated by $E^* = X \ln(\dot{\varepsilon} / \dot{\varepsilon}_o) + Y$ over the strain rates presented in this analysis where $\dot{\varepsilon}_o$ is taken to be $\dot{\varepsilon}_o = 1\ s^{-1}$ and the constants X and Y are provided in Table 4.3. Based on Eq. (2.2) – Eq. (2.4) and the parameters given in Table 4.3, the contribution of the foam matrix to the total dynamic response of fluid-filled foam can be determined.

To plot the fluid model, the permeabilities at the elastic buckling strain and at the densified strain are required. These values are obtained using the equations for the local permeability supplied in *Chapter 3* and the corresponding intrinsic permeability at zero strain k_o. It has been observed that large strain compression causes microstructural damage to low-density foam, altering the permeability at zero strain (Hilyard and Collier, 1987). Therefore, the permeability at zero strain for each specimen was measured after the specimens were subjected to the compressive filling technique used for saturating the foam with glycerol. The permeability was measured using the technique given in *Chapter 3*. Table 4.4 provides the measured permeability at zero strain and the corresponding permeabilities utilized in modeling the stress-strain response.

A typical plot of the stress-strain response for 70 ppi foam filled with glycerol loaded at a constant strain rate of $\dot{\varepsilon} = 1.0\ s^{-1}$ is given in **Fig. 4.6**. The actual

response of the fluid-filled foam is plotted along with the model for the total contribution to the stress-strain response, resulting from the combination of the solid contribution given in *Chapter 2* and the fluid contribution given by Eq. (4.31-4.32). The solid and fluid contributions are also given separately to demonstrate their relative contributions.

To fit the constant C, given in Eq. (4.31) and Eq. (4.32), a measure of the goodness of fit is established. The measure for the goodness of fit R^2, is taken to be the sum of the squares of the difference between the experimental values and the average experimental value divided by the sum of the squares of the difference between the experimental values and the predicted values. This measure of the goodness of fit was maximized, over the sample of experimental data discussed in the following sections, to establish the empirical constant.

In **Fig. 4.7** we show the stress response of 70 ppi foam filled with glycerol at $\varepsilon =$ 0.60 strain, corresponding to an aspect ratio of 2.5, plotted against the strain rate. Each data point is the average of three experiments with error bars corresponding to 1 standard deviation. The error bars for most data points are not apparent since they are smaller than the size of the data points. The fluid and solid contributions of the stress, given in *Chapter 2* and Eq. (4.32), respectively, are plotted separately showing their relative contributions. In **Fig. 4.8** we show the stress at $\varepsilon = 0.30$ strain and $\varepsilon = 0.60$ strain, corresponding to aspect ratios of 1.4 and 2.5, respectively, for all three grades of reticulated foam filled with glycerol plotted against the strain rate. Each data point is again the average of three experiments with error bars corresponding to 1 standard deviation. The total contribution to the stress-strain response, resulting from the combination of

the solid contribution and the fluid contribution given by Eq. (4.32), is also shown in **Fig. 4.8.**

All of the data used to generate the plots in **Fig. 4.8** is used to determine the empirical constant C. Using each data point along the 0.3 and 0.6 strain curves, consisting of the average of three experimental points, for all three foam grades, the empirical constant is determined to be $C = 0.59$. Based on the data in **Fig. 4.8**, the R^2 values for each grade of foam at both $\varepsilon = 0.30$ and $\varepsilon = 0.60$ are given in Table 4.5; it is clear that the model describes the data well up to the densified strain for a range of foam grades and strain rates as shown in **Fig. 4.8**. The empirical constant C, which primarily accounts for the tortuous and anisotropic microstructure of the foam, is independent of all of the parameters considered in this analysis. **Fig. 4.8** supports this initial assumption, demonstrating that C is independent of the cell-size of low-density foam, the aspect ratio of the foam, the strain imposed on the foam, and the strain rate applied to the foam. Additional experimental studies, not presented here, varying the aspect ratio of the foam specimen also support this proposal. Using $C = 0.59$, the model given by Eq. (4.32) accurately describes data for fluid-filled foam samples over several orders of magnitude of strain rate with an aspect ratio of approximately 10 at $\varepsilon = 0.60$.

4.5 Discussion

A boundary value model for the contribution of viscous Newtonian fluid flow to the stress-strain response of a fluid-filled foam under dynamic compression is given by Eq. (4.31) and Eq. (4.32). The model governing viscous flow in the bimodal regime of the foam is given in the form of an infinite series of Bessel

functions. As expected, this solution converges rapidly with an increasing number of terms, such that the boundary value model is readily evaluated numerically with only the first few terms. Based on the permeability studies in *Chapter 3*, the models presented in this analysis are taken to be applicable for all grades of low-density foam and independent of whether the orientation of the rise direction of the foam is perpendicular or parallel to the direction of fluid flow. As previously discussed, the models in this analysis assume that the flow is dominated by viscous forces, which is shown to be the case for nearly all achievable strain rates. The boundary value model further assumes an instantaneous change in the velocity field of the foam at the elastic buckling strain ε_{el}^*, which is the strain at which the model transitions from the single regime to the bimodal regime. The transition behavior between these two regimes is neglected, resulting in a small discontinuity in the stress response of the boundary value model. However, as the aspect ratio of the foam R/h, is increased, the effect of the assumed velocity field of the foam becomes negligible, and the boundary value model rapidly approaches a continuous solution. In addition, with increasing R/h, the bimodal model becomes independent of the location of the densified bands of the foam.

The boundary value model presented in this analysis is found to describe the experimental results presented in this chapter well for foam grades varying from 70 to 90 ppi and strain rates varying from $\dot{\varepsilon} = 2.5\text{x}10^{-3}$ s^{-1} to 10^{1} s^{-1}. All of the strain rates in these experiments satisfy the viscous flow requirements of the models with $Re < 1$. The maximum Reynolds number in the experiments was found to be $Re = 0.017$, corresponding to strain rate of $\dot{\varepsilon} = 10$ s^{-1} in a 70 ppi foam with average cell diameter of 235 μm.

Fig. 4.6 shows the individual contributions of both the solid model and the boundary value fluid model to the model of the total stress-strain response of 70 ppi fluid-filled foam. The total model fits the data well over the entire range of interest, slightly overestimating the response at low strains. The previously discussed discontinuity in the models near the buckling strain is evident but shown to be negligible. Furthermore, **Fig. 4.7-4.8** demonstrate that the boundary value model is representative of the actual response of the fluid-filled foam at both $\varepsilon = 0.30$ and $\varepsilon = 0.60$ for a range of foam grades and strain rates. The standard deviations of nearly all of the data are observed to be very small; on the order of the size of the data point. Overall, the goodness of fit measure given in Table 4.5 demonstrates that the boundary value model fits the data well for all grades of foam at both $\varepsilon = 0.30$ and $\varepsilon = 0.60$ for the range of strain rates considered. The boundary value model also fits the data well over all strains less than the densified strain, but the strains of $\varepsilon = 0.30$ and $\varepsilon = 0.60$ were selected as representative strains. The empirical constant $C = 0.59$, primarily accounts for the tortuous and anisotropic microstructure of the foam and is found to be similar to the efficiency factor of 2/3 found by Glicksman (1994) in his study of the thermal conductivity of porous media. Furthermore, the empirical constant is proposed to be independent of all of the parameters considered in this analysis. **Fig. 4.8** supports this proposal demonstrating that C is independent of the cell-size of low-density foam, the aspect ratio of the foam, the strain of the foam, and the strain rate of the foam.

While the boundary value model is readily evaluated and compared with experimental results, extending it to a more advanced study of dynamic loading of non-Newtonian fluid-filled foam is challenging. However, this model is useful in validating the applicability of the more tractable lubrication model,

which assumes the radius of the foam is much greater than the height of the foam. The boundary value model is found to converge rapidly to within 5 % of the lubrication model for aspect ratios greater than four (R/h >4). The small discrepancy between the coefficient for the lubrication model and that for the boundary value model may be attributed to the fact that the lubrication model assumes a uniform radial flow, neglects pressure gradients in the z-direction, and neglects the flow in the z-direction; whereas the boundary value model does not make these assumptions.

Table 4.1 demonstrates that as R/h is increased, the numerical coefficients at $\varepsilon =$ 0.05 and $\varepsilon = 0.30$ strain increase asymptotically while the coefficient at $\varepsilon = 0.60$ strain decreases asymptotically. At any given strain, the coefficient C_1 is governed primarily by the following two factors: the aspect ratio of the foam sample and the distance between the collapsing band and the compression plate. For all strains as R/h is decreased, the dependence of the stress, given by Eq. (4.51), on R/h also decreases. In the limit of very small R/h, the stress contribution of the fluid becomes completely independent of R/h.

At $\varepsilon = 0.60$ strain the stress is independent of the distance between the collapsing band and the compression plate ($\frac{1}{2} h_e$) since the collapsing band is effectively always at the interface between the compression plate and the foam. Therefore, it is expected that as R/h decreases, the coefficient C_1 would increase proportionally, such that the stress is independent of R/h in the limit of very small R/h. However, at 0.05 and 0.30 strain, the distance between the collapsing band and the compression plate ($\frac{1}{2} h_e$) is also an important factor, which strongly influences the coefficient C_1. As R/h is decreased, the relative distance between the fluid in the collapsing band and the compression plate ($\frac{1}{2} h_e$) to that of the

fluid in the collapsing band and the free surface (~R) increases; therefore, it is expected that the overall stress on the compression plate would decrease. For lower strains this effect is more pronounced since the band is effectively farther from the compression plate, explaining the phenomenon observed in Table 4.1.

In the limit that $R/h \gg 1$, the effect of the distance between the collapsing bands and the compression plate is found to be inconsequential for all strains, and the stress becomes independent of the vertical location of the collapsing bands. Table 4.1 demonstrates the model presented in this analysis becomes approximately independent of the aspect ratio of the foam for $R/h > 4$. As expected, this indicates the lubrication model provides a good approximation to the flow for a large range of R/h values. Overall, the convergence of the more comprehensive boundary value model toward the lubrication model strongly supports the validity of the lubrication approximation. This is an important finding since the lubrication model is readily extended to more complex analyses, such as the study of the stress-strain response and energy absorption capabilities of a foam filled with a rate-dependent non-Newtonian fluid under dynamic loading.

4.6 Conclusion

In this analysis, a comprehensive boundary value model for the contribution of viscous Newtonian fluid flow to the stress-strain response of a fluid-filled, elastomeric foam under dynamic compression is presented. Experimental results strongly support this model for a variety of foam grades over several orders of magnitude of strain rate. A simple explicit analytic solution based on a

lubrication approximation is also presented. The robust boundary value model is found to converge rapidly toward the lubrication model as the aspect ratio of the foam is increased. This validation of the lubrication model is important since it is more readily extended to more complex analyses, such as the dynamic response of foam filled with a non-Newtonian fluid. Furthermore, using a lubrication model, both the Newtonian and non-Newtonian models can be extended to determine the energy absorption and impact resistance capabilities of a fluid-filled foam under dynamic loading, which is critical to the development of energy absorption equipment or armor capable of impeding shockwaves.

References

Comiti, J. and Renaud, M., (1988), "A New Model for Determining Mean Structure Parameters of Fixed Beds From Pressure Drop Measurements: Applications to Beds Packed with Parallelpipedal Particles", *Chem Eng. Sci.*, **44**, pp. 1539-45.

Comiti, J., Sabiri, N., and Montillet, A., (2000), "Experimental Characterization of Flow Regimes in Various Porous Media-III: Limit of Darcy's or Creeping Flow Regime for Newtonian and Purely Viscous Non-Newtonian Fluids", *Chem Eng. Sci.*, **55**, 3057-3061.

Hager, S.L. and Craig, T.A., (1992), "Fatigue Testing of High Performance Flexible Polyurethane Foam", *J. Cell. Plastics* **28**, pp. 285-303.

Hilyard, N. and Collier, P., (1987), "A Structural Model Air Flow in Flexible PUR Foams", *Cell. Poly.*, **6**, pp. 9-26.

Gibson, L.J. and Ashby, M.F., (1997), "Cellular Solids – Structures and Properties, 2nd Ed.", Cambridge Univserisy Press, Cambridge.

Glicksman, L., (1994), "Heat Transfer in Foams-Low Density Cellular Plastics Ed.", Hilyard, N. C. and Cunningham, A., Chapman and Hall, London.

Gong, L. and Kyriakides, S., (2005), "Compressive Response of Open Cell Foams Part II: Initiation and Evolution of Crushing", *Int. J. Solids and Struct.*, **42**, pp. 1381-99.

Tables

Table 4.1. Table of coefficients for the bimodal model as a function of the aspect ratio of the foam and for the lubrication model, corresponding to Eq. (4.50) and Eq. (4.51).

R/h	C_1 ($\varepsilon = 0.05$)	C_1 ($\varepsilon = 0.30$)	C_1 ($\varepsilon = 0.60$)
½	0.031	0.111	0.827
1	0.057	0.127	0.501
2	0.069	0.132	0.404
4	0.072	0.133	0.378
8	0.073	0.133	0.371
16	0.074	0.133	0.369
32	0.074	0.133	0.368
Lubrication	0.076	0.137	0.380

Table 4.2. Effective modulus of tetrakaidecahedral structure under various loading rates using ADINA finite element software.

Period of Loading (sec)	Effective Modulus (Pa)
1.00E-05	1.80E+05
1.00E-04	1.28E+05
1.00E-03	1.18E+05

Table 4.3. Static parameters and constants. The elastic buckling strain ε_{el}^*, the strain at which the stress begins to exceed the plateau stress ε_p^*, and the constants X, Y, and D for use in Eq. (2.2) – Eq. (2.6).

Foam Grade (ppi)	ε_{el}^*	ε_p^*	X (Pa)	Y (Pa)	D
70	0.058	0.55	1.07E+04	1.35E+05	2.3
80	0.049	0.54	1.28E+04	1.70E+05	2.3
90	0.057	0.55	1.09E+04	1.42E+05	2.3

Table 4.4. Permeability data for pre-compressed foam. The permeability at zero strain k_o, for each grade of foam is given after being subjected to the saturation process. The permeabilities at the elastic buckling strain and densified strain are determined using the equations supplied in *Chapter 3*.

Foam Grade (ppi)	k_o(1x10^{-9} m^2)	k_{el}*(1x10^{-9} m^2)	k_d(1x10^{-9} m^2)
70	5.82	5.45	1.28
80	5.21	4.93	1.04
90	4.68	4.39	0.85

Table 4.5. The measure for the goodness of fit of the boundary value model at 0.30 and 0.60 strain for each grade of foam.

	R^2	
Foam Grade (ppi)	0.30 Strain	0.60 Strain
70	0.97	0.99
80	0.99	0.99
90	0.95	0.99

Figures

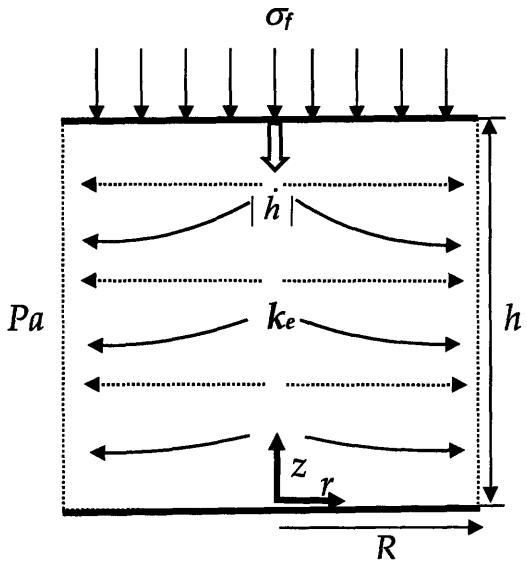

Figure 4.1. One-regime model of fluid-filled cylindrical foam with strain less than the elastic buckling strain, $\varepsilon < \varepsilon_{el}^*$. Absolute velocity of fluid ⟶. Relative velocity of fluid with respect to velocity of foam ⇢.

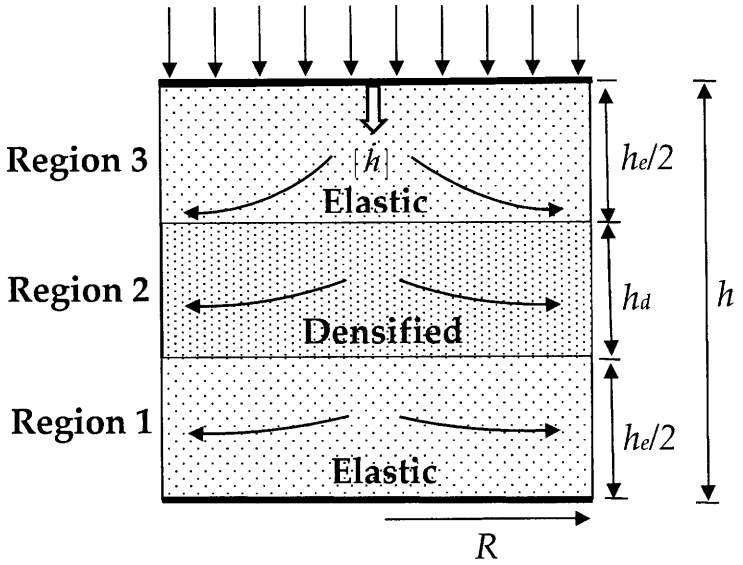

Figure 4.2a. Bimodal-regime model of fluid-filled cylindrical foam compressed beyond elastic buckling strain, $\varepsilon_{el}^* < \varepsilon < \varepsilon_d$. Velocity of fluid ⟶.

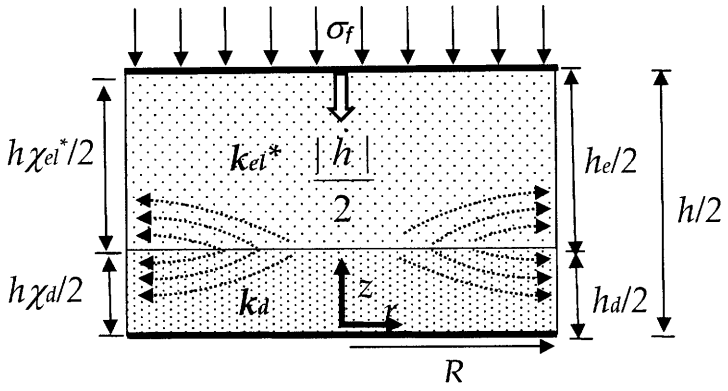

Figure 4.2b. Top symmetric half of bimodal-regime model of fluid-filled cylindrical foam compressed beyond elastic buckling strain, $\varepsilon_{el}^* < \varepsilon < \varepsilon_d$, in the reference frame of the densified regime. Relative velocity of fluid with respect to velocity of foam ⋯⋯▸.

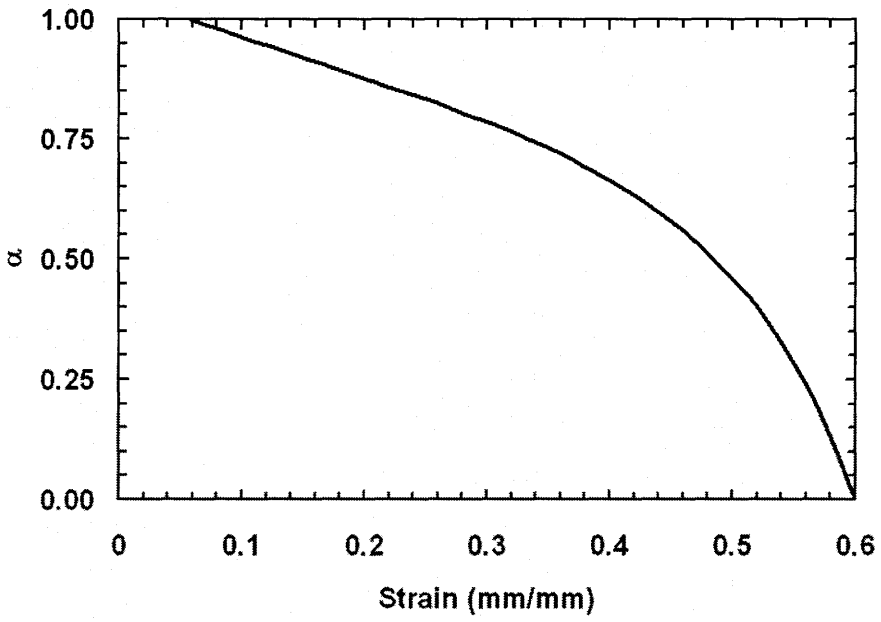

Figure 4.3. The fraction of the flux into the linear-elastic regime (α) as a function of strain in the bimodal model.

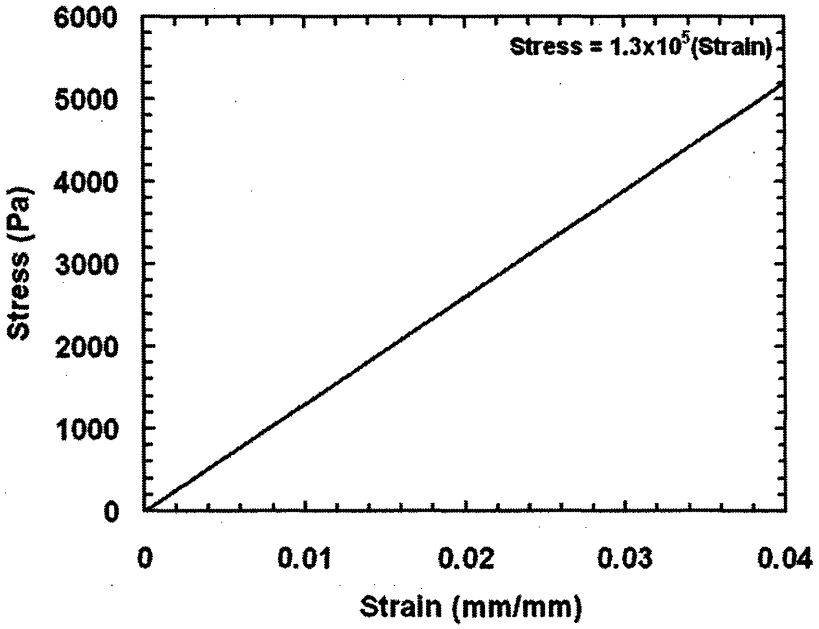

Figure 4.4. Stress-strain response of tetrakaidecahedral. The effective modulus of the foam is given by the slope of the regression equation.

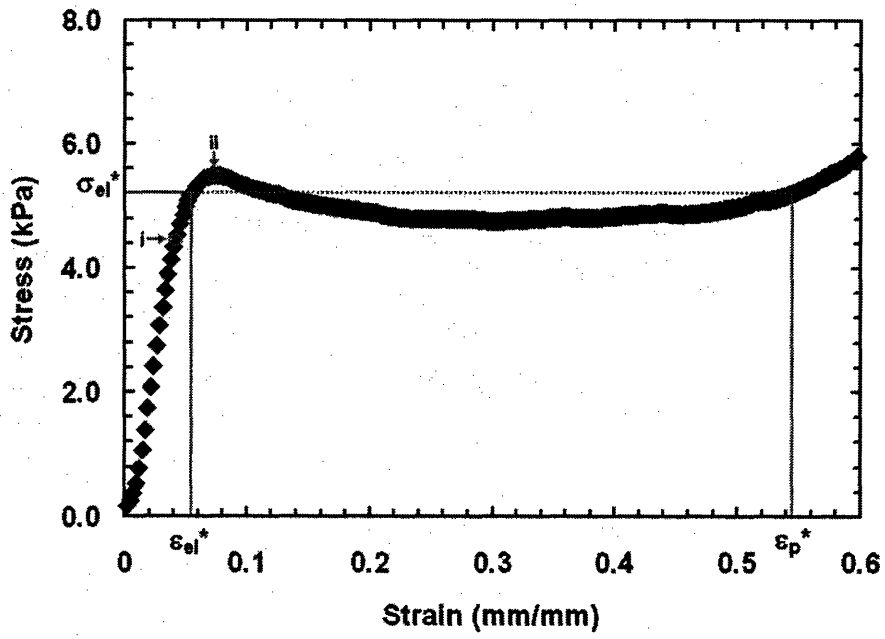

Figure 4.5. Stress-strain response of 90 ppi foam filled with glycerol under a quasi-static load rate of $\dot{\varepsilon} = 1\text{x}10^{-2}\ s^{-1}$. The deviation from linear-elastic regime is denoted by (i). The peak stress before the plateau region is denoted by (ii).

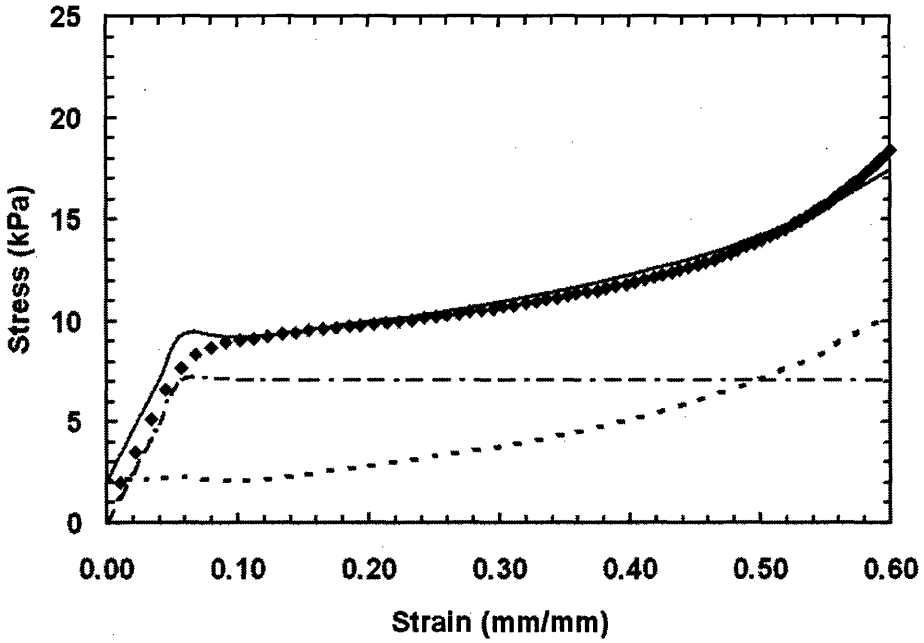

Figure 4.6. Stress plotted against strain for 70 ppi foam filled with glycerol loaded at 1.0 s^{-1}. Experimental data (◆). Contribution to the stress response of fluid model given by Eq. (4.31-4.32) (- - - ·), solid model given in *Chapter* 2 (— · —), and the total model (——).

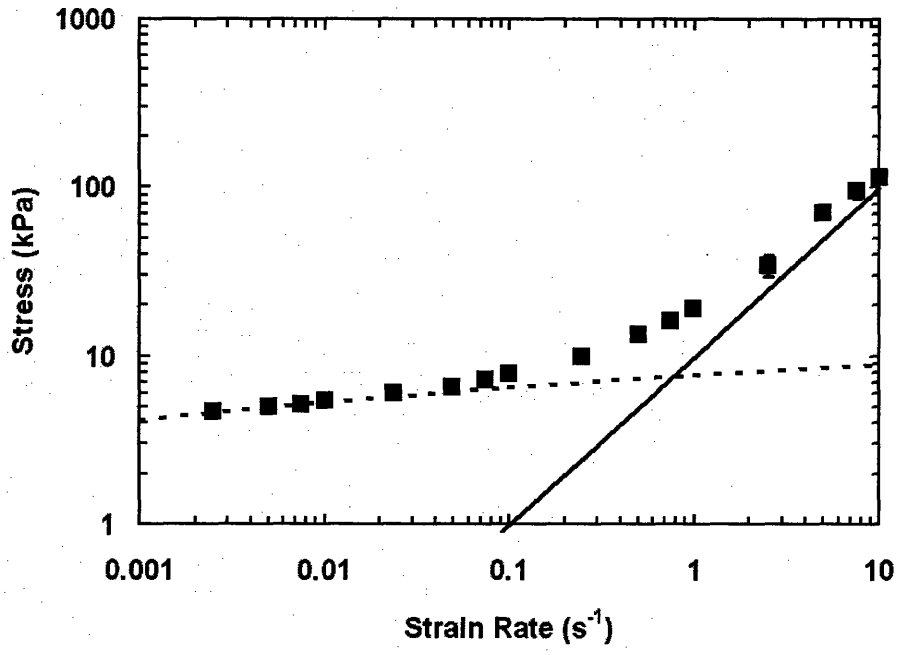

Figure 4.7. Stress plotted against strain rate for 70 ppi foam filled with glycerol at $\varepsilon = 0.60$. The experimental data (■), the contribution to the stress response of fluid model given by Eq. (4.31-4.32) (———) and solid model given in *Chapter 2* (– – – ·).

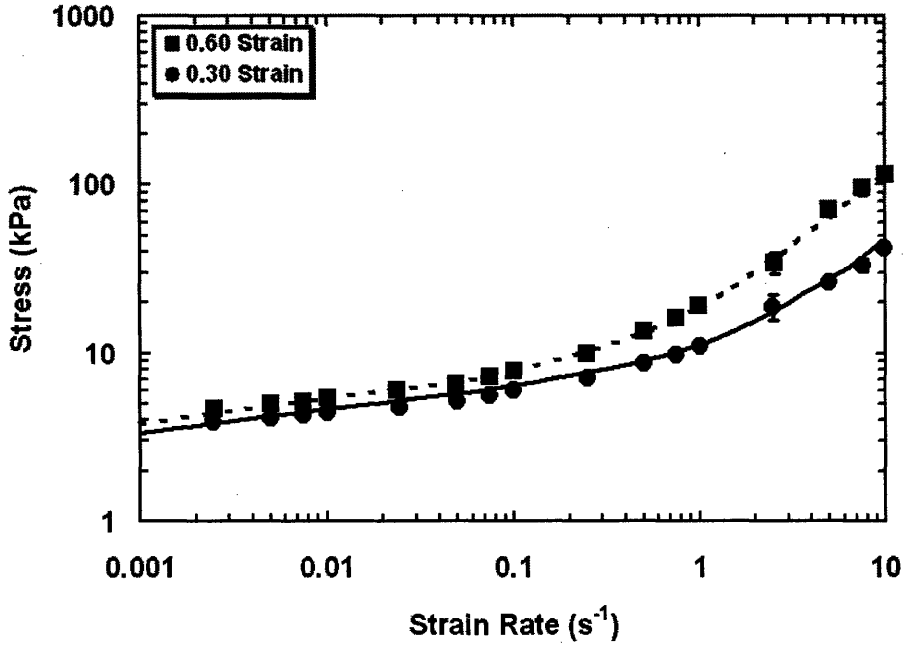

Figure 4.8a. Stress plotted against strain rate for 70 ppi foam filled with glycerol. The experimental data at 0.60 strain (■), and 0.30 strain (●), respectively. Model given by combining the solid model with Eq. (4.32) at $\varepsilon = 0.30$ (——) and $\varepsilon = 0.60$ (– – –).

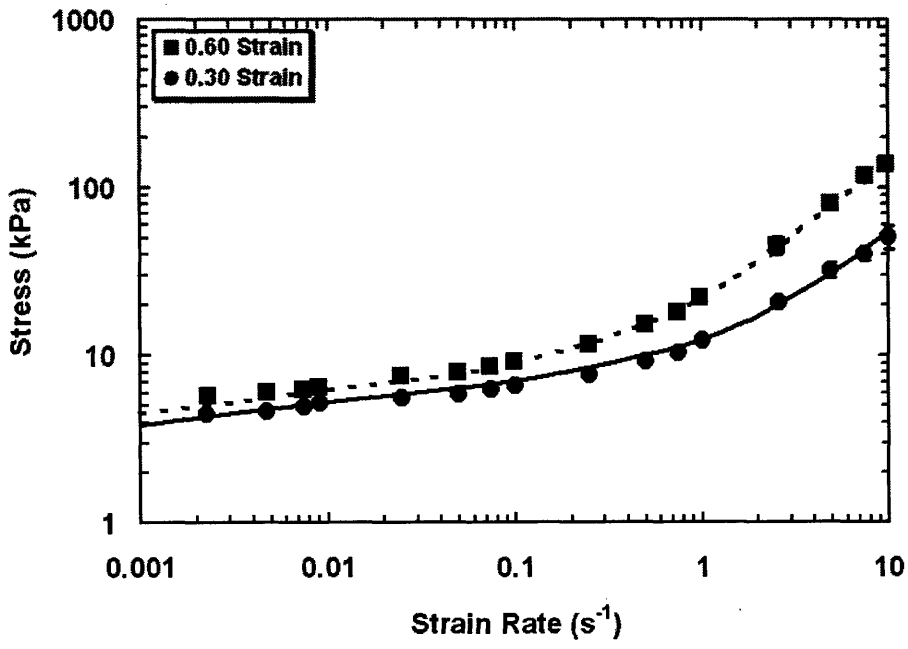

Figure 4.8b. Stress plotted against strain rate for 80 ppi foam filled with glycerol. The experimental data at 0.60 strain (■), and 0.30 strain (●), respectively. Model given by combining the solid model with Eq. (4.32) at $\varepsilon = 0.30$ (——) and $\varepsilon = 0.60$ (– – –).

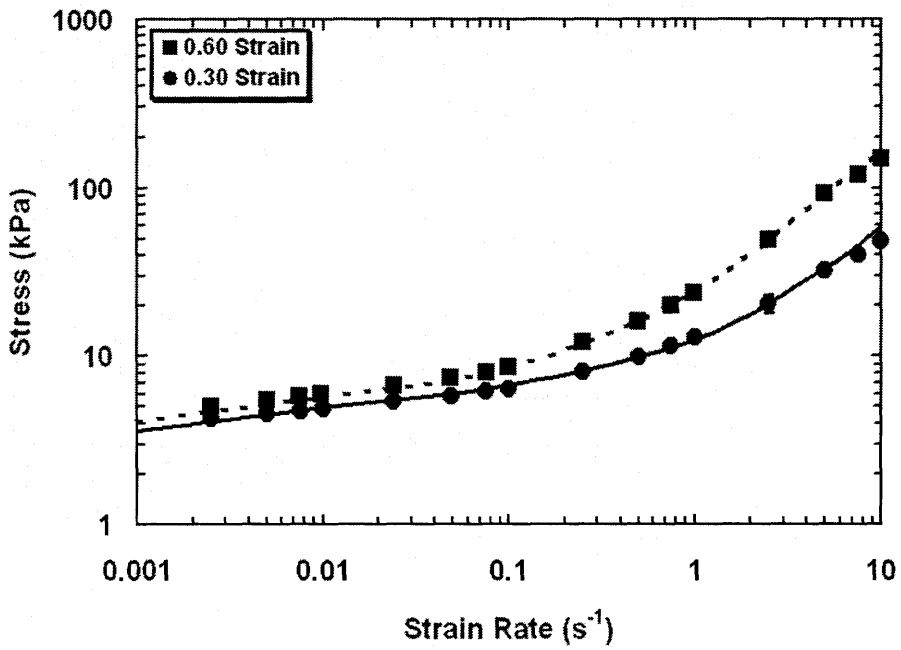

Figure 4.8c. Stress plotted against strain rate for 90 ppi foam filled with glycerol. The experimental data at 0.60 strain (■), and 0.30 strain (●), respectively. Model given by combining the solid model with Eq. (4.32) at $\varepsilon = 0.30$ (——) and $\varepsilon = 0.60$ (– – –).

Supplement

The velocity profiles in the absence of foam for the analysis in section 4.3.5 *Squeezing Flow between Parallel Plates* are given as

$$V_r(r,z) = \frac{3\dot{h}r}{h}\left(\left(\frac{z}{h}\right)^2 - \frac{z}{h}\right) \tag{4.53}$$

$$V_z(r,z) = 6\dot{h}\left(\frac{1}{2}\left(\frac{z}{h}\right)^2 - \frac{1}{3}\left(\frac{z}{h}\right)^3\right) \tag{4.54}$$

5 Dynamic Compressive Response of Open-Cell Foam Impregnated with a Non-Newtonian Fluid

5.1 Introduction

In this chapter, the response of a non-Newtonian fluid-filled (NNF-filled), low-density, reticulated, elastomeric foam under dynamic axial compression is studied. Under compression beyond local strain rates on the order of 1 s^{-1}, the non-Newtonian fluids examined in this chapter undergo dramatic shear thickening and then proceed to shear thin. The response after these fluids have undergone shear thickening is particularly important since the fluid will nearly always be in this regime for most engineering designs under dynamic loading.

Scaling arguments demonstrate that after the shear thickening transition, the contribution of the foam itself and the contribution of the fluid-structure interaction to the overall response can be neglected. Based on these arguments, an analytically tractable lubrication model for the stress-strain response of a non-Newtonian fluid-filled, reticulated, elastomeric foam under dynamic compression between two parallel plates, at varying instantaneous strain rates, is developed. The resulting lubrication model is applicable when the characteristic dimension of the foam in the direction of fluid flow (radial) is much greater than that in the direction of loading (axial). Based on the response of reticulated foam filled with a Newtonian fluid under dynamic compression given in *Chapter 4*, we assume this model is valid if the ratio of the radius to the height of the foam is greater than unity. The corresponding range of instantaneous strain rates of the NNF-filled foam over which this model is applicable is also given. It is anticipated this model is applicable for nearly all expected instantaneous strain

rates caused by either impact loading or blast wave loading. The lubrication model is analytically tractable, depending only on the characteristic fluid properties, the characteristic radius to height ratio of the NNF-filled foam and the instantaneous strain rate of the foam. Furthermore, it is independent of all of the parameters of low-density, elastomeric foam, such as foam grade. While a number of authors have studied the pressure drop of general power-law, non-Newtonian fluids through porous media (Seguin et al., 1996; Comiti et al., 1989; Sabiri et al., 1995), this is the first known comprehensive model for the response of non-Newtonian fluid-filled foam under dynamic compression.

Experimental characterization of two types of non-Newtonian, shear thickening fluids are presented. A discussion of the complex behavior of these fluids under various strain rates is given and related to the observed dynamic response of NNF-filled foam. Furthermore, experimental measurements of the dynamic compressive response of low-density, polyurethane foam filled with one of the non-Newtonian fluids is presented. The previously derived model is found to be strongly supported by experimental results for a range of aspect ratios and instantaneous strain rates of the foam. Finally, the significance of this model is discussed with respect to the design of energy absorption and blast wave protection equipment.

5.2 Analysis

5.2.1 Model Assumptions

This analysis considers dynamic axial compression of a low-density, elastomeric foam fully saturated with a non-Newtonian, power-law fluid between two

parallel plates. The fluid is assumed to remain in a cylindrical shape with uniform radius while undergoing deformation, where the radius of the cylinder can be determined by conservation of mass of an incompressible fluid **(Fig. 5.1)**. In addition, the fluid is assumed to be a power-law fluid with a highly shear thickening regime, such that the maximum viscosity is several orders of magnitude greater than the minimum viscosity. For known nano-particle based non-Newtonian fluids, this will result in a maximum viscosity greater than 10^3 Pas. In this viscosity range, the stress within the fluid is three orders of magnitude greater than that in the foam alone. Furthermore, the characteristic dimension of the colloidal particles in the fluid is several orders of magnitude smaller than the characteristic dimension of the foam pore size. These two observations ensure that the response of the elastomeric foam, as well as the fluid-structure interaction between the foam and the non-Newtonian fluid, can be neglected, so that the system behaves as if the foam were non-existent. This assumption is supported by **Fig. 5.2** where magnified images of the cells of the foam are shown before loading and during loading. In **Fig. 5.2** it is evident that the foam struts are readily torn apart by the highly viscous fluid flow at relatively low strain, supporting the hypothesis that the structural support from the foam and the fluid-structure interaction is negligible. This result is in contrast to the result presented in *Chapter 4* for lower viscosity, Newtonian fluid-filled foam where the structural response of the foam and the fluid-structure interaction are significant. The analysis presented in this chapter is also based on a lubrication approximation, which assumes the ratio of the characteristic radius of the specimen to the characteristic height of the specimen, the aspect ratio, is much greater than one. *Chapter 4* gives a detailed analytical description of the applicability of the lubrication approximation to a comparable problem with a Newtonian fluid and demonstrates the rapid convergence of the lubrication

model to the exact solution as the aspect ratio increases. They conclude that beyond aspect ratios of four, the lubrication model can be used to approximate the exact solution; however, even beyond aspect ratios of unity the lubrication solution is shown to approximate the exact solution to within 10% for most strains. Finally, after the shear thickening transition, the flow is assumed to be dominated by viscous forces for all instantaneous strain rates of the foam considered in this analysis.

5.2.2 Fluid Flow in a Rectangular Channel

We first consider a model for pressure driven flow of a power-law fluid through a rectangular channel **(Fig. 5.3)** where the length of the channel is L, the width is W, and the height is $2B$ with $2B \ll W \ll L$. The flow is assumed to be incompressible and locally fully-developed. The gravitational effects are assumed to be negligible. Since the flow is assumed to be dominated by viscous forces, inertial effects can also be neglected. The following velocity and pressure profiles are assumed:

$$\begin{aligned} V_z &= V_z(x,y); \\ V_x &= V_y = 0; \\ P &= P(z); \end{aligned} \tag{5.1}$$

where V_x, V_y, and V_z are the velocity components in the horizontal (x), vertical (y), and axial (z) directions, respectively. Coupling the equation of continuity with the full Navier-Stokes equations of motion, this problem is readily solved. Applying the lubrication approximation, the Navier-Stokes equations of motion in the axial direction reduces to

$$\frac{\partial \tau_{yz}}{\partial y} = -\frac{\partial P}{\partial z} \qquad \text{(z-direction)} \quad (5.2)$$

where τ_{yz} is the shear stress in the fluid. In this flow the shear stress in the fluid is related to the corresponding component of the rate of strain tensor and the viscosity η, and given by

$$\tau_{yz} = -\eta \frac{\partial V_z}{\partial y}. \qquad (5.3)$$

As given before, the viscosity for a power-law fluid is given by the relation

$$\eta = m\left(\dot{\gamma}\right)^{n-1}. \qquad (5.4)$$

$\dot{\gamma}$ is calculated by taking the square root of one-half of the dot product of the rate of strain tensor with itself. Using Eq. (5.2) the shear stress in the fluid can be written in terms of the pressure drop and given by

$$\tau_{yz} = -\frac{\partial P}{\partial z} y + C_1 \qquad (5.5)$$

where C_1 is a constant determined using the boundary conditions. Using Eq. (5.3) and Eq. (5.4) the shear stress in the fluid can also be related to the shear rate of the fluid and the power-law parameters as

$$\tau_{yz} = -m\dot{\gamma}^{n-1}\frac{\partial V_z}{\partial y} = -m\left(\frac{\partial V_z}{\partial y}\right)^n. \tag{5.6}$$

The necessary boundary conditions are based on symmetry and no wall-slip at the wall and can be given by

$$\begin{aligned} \tau_{yz}\,|_{y=B} &= 0; \\ V_z\,|_{y=0} &= 0; \end{aligned} \tag{5.7}$$

Combining the expressions for the shear stress in the fluid in Eq. (5.5) and Eq. (5.6) and applying the boundary conditions given by Eq. (5.7), the velocity profile is found to be

$$V_z = \left(-\frac{1}{m}\frac{\partial P}{\partial z}\right)^{\frac{1}{n}} \frac{1}{\left(\frac{1}{n}+1\right)}\left(B^{\frac{1}{n}+1} - (B-y)^{\frac{1}{n}+1}\right). \tag{5.8}$$

Integrating the velocity profile over the area gives the flow rate, Q

$$Q = 2WB^2\left(-\frac{B}{m}\frac{\partial P}{\partial z}\right)^{\frac{1}{n}} \frac{1}{\left(\frac{1}{n}+2\right)} \tag{5.9}$$

which corresponds with the results presented by Bird et al. (1987).

5.2.3 Radial Fluid Flow in a Cylindrical Specimen Squeezed Between Parallel Plates

In the lubrication limit, flow in a rectangular channel can be transformed to radial squeezing flow between two parallel plates where the lower plate is fixed

and the upper plate is moving as shown in **Fig. 5.4**. As previously discussed, the fluid is assumed to remain in a cylindrical shape with uniform radius while undergoing deformation. By conservation of mass the aspect ratio at any given axial strain ε, is given by

$$\frac{R}{h} = \frac{R_o}{h_o}\left[\frac{1}{1-\varepsilon}\right]^{3/2} \tag{5.10}$$

where R_o is the initial radius of the NNF-filled foam at zero strain, h_o is the initial height at zero strain, and ε is given by $(1-h/h_o)$ **(Fig. 5.4)**. In **Fig. 5.4** the magnitude of the velocity of the top plate is given by $|\dot{h}|$. The transformations from the 2-dimensional, rectangular channel, planar flow problem in *Section 5.2.2* to the squeezing flow problem between parallel plates in cylindrical coordinates are given as (after Bird et al., 1987)

$$\begin{aligned} Q &\rightarrow Q(r); \\ W &\rightarrow 2\pi r; \\ B &\rightarrow \frac{h}{2}; \\ \frac{\partial P}{\partial z} &\rightarrow \frac{\partial P}{\partial r}; \end{aligned} \tag{5.11}$$

Eq. (5.9) can be rewritten for the lubrication squeezing flow between parallel plates as

$$Q(r) = \pi r h^2 \left(\frac{-h}{2m}\frac{\partial P}{\partial r}\right)^{\frac{1}{n}} \frac{1}{\left(\frac{1}{n}+2\right)} \tag{5.12}$$

which accordingly corresponds with Bird et al. (1987). Furthermore, the equation of continuity can be used to find a relation between the volumetric flow rate and the change in height of the fluid giving

$$Q(r) = \pi r^2 \left(-\dot{h}\right). \tag{5.13}$$

Combining Eq. (5.12) and Eq. (5.13) and solving for the pressure profile gives

$$P(r) - P_a = \frac{2m(-\dot{h})^n}{h^{2n+1}} \left(\frac{2n+1}{n}\right)^n \frac{R^{n+1}}{n+1} \left[1 - \left(\frac{r}{R}\right)^{n+1}\right]. \tag{5.14}$$

For a power-law fluid σ_{zz} is zero on the surface of the plate. Neglecting inertial effects, a force balance can be used to find an equivalent uniform stress distribution or true stress σ_f, applied to the top compression plate by integrating the pressure field over the radius and dividing by the area of the plate giving

$$\sigma_f = 2\left(\frac{2n+1}{n}\right)^n \frac{m}{n+3} \left(\frac{R_o}{h_o}\right)^{n+1} \left(\frac{-\dot{h}}{h}\right)^n \left(\frac{1}{1-\varepsilon}\right)^{\frac{3(n+1)}{2}} \tag{5.15}$$

where $-\dot{h}/h$ is the instantaneous strain rate of the NNF-filled foam. It is important to distinguish the instantaneous strain rate of the foam from the magnitude of the strain rate of the fluid $\dot{\gamma}$, which is also referred to as the local strain rate. In our experiments described below, the fluid flows through an open-cell foam, which introduces a tortuosity to the fluid path. We account for the tortuosity by introducing a constant into Eq. (5.15).

5.3 Experimental Methods

5.3.1 Materials

Specimens of open-cell, flexible, polyester-based polyurethane foams (New Dimension Industries, Moonachie, NJ), with nominal cell diameters of 175 μm, 210 μm, and 235 μm (corresponding to manufacturer specified grades of 90, 80, and 70 pores per inch (ppi), respectively) were used in the experiments. The densities of the foams ranged from 0.0318 to 0.0322 g/cm^3. Based on the manufacturer's value of the density of the solid polyurethane (ρ_s = 1.078 g/cm^3), the relative density of the foams was $\rho^*_o/\rho_s \cong 0.030$. The foam was cut into cylindrical specimens with nominal diameter D = 25.4 mm and height h_o = 12.6 mm. In this chapter experimental results are presented for 55 samples of 70 ppi foam, 2 samples of 80 ppi foam, and 2 samples of 90 ppi foam. The dimensions of each sample were measured using a digital caliper accurate to within 0.01 mm.

Selecting the appropriate non-Newtonian fluid is imperative in this study. Ideally, during characterization of the non-Newtonian fluid it would exhibit reversible behavior with no slip. As previously discussed in the *Chapter 2*, the two most commonly used non-Newtonian fluids are precipitated calcium carbonate (PCC) suspensions and silica suspensions in ethylene or polyethylene glycol (Egres et al., 2005 and Bender and Wagner, 1996). To select the best fluid for this analysis we examine these two fluids consisting of precipitated calcium carbonate nanoparticles (Opcarb, Minerals Technologies, Inc., New York, NY) and silica nanoparticles (Fuso Chemical Co., Osaka, Japan) suspended in ethylene glycol (VWR, West Chester, PA). Images of the particles were taken using the scanning electron microscope (XL30 FEG ESEM, FEI/Philips, Hillsboro,

Oregon) as shown in **Fig. 5.5**. The characteristic diameters of the silica particles were determined using SEM images. The characteristic dimensions of the PCC particles were not determined from the SEM images because the variation in particle shapes and sizes was too large to have sufficient confidence in the results. The diameters of 100 silica particles were measured and analyzed using Scion Image analysis software (Scion Corporation, Frederick, Maryland). The average particle diameter of the silica particles was found to be nearly monodisperse (**Fig. 5.5c**) with an average diameter of 293 nm +- 31 nm. The density of the PCC and silica nanoparticles was taken to be that given by the supplier of 2.83 g/cm^3 and 1.95 g/cm^3, respectively. The density and viscosity of the ethylene glycol suspending fluid were taken to be $\rho = 1.11$ g/cm^3 and $\mu =$ 2.1x10^{-2} Pa-s at 20 °C.

5.3.2 Preparation of the Shear Thickening Fluid

The non-Newtonian suspensions were first washed with ethylene glycol three times. The washing process began by centrifuging the solution at 2,700 g for 4 hours using a Sorvall Legend Mach 1.6 Centrifuge (Fisher Scientific, Suwanee, Ga). After this centrifuging process, the suspension consisted of a sedimented layer and a layer of supernatant, which was subsequently poured off. Ethylene glycol was then added to the remaining sedimented layer and the mixture was resuspended using a VWR digital vortex mixer (VWR, West Chester, PA). In order to determine the volume fraction of the sedimented particles after centrifuging and removal of the supernatant, the sediment, for instance, was dried until no significant change in mass over a 24 hour period was detected. Based on this drying experiment, the volume fraction of the silica sediment was determined to be ~69% particles by volume. The volume fraction of the sediment

after centrifuging and removal of the supernatant was found to be constant to within measures of uncertainty. The sediment was immediately redispersed in ethylene glycol after centrifuging to achieve the final suspension volume fraction. To redisperse the sediment and create the desired volume fraction, a vortex mixer was used until the sediment appeared to be completed suspended in the fluid. Then the NNF was sonicated for 1 hour using an ultrasonic bath.

5.3.3 Selection of a Shear Thickening Fluid

To determine which fluid is preferred for experimental testing of the model presented in this analysis, the steady state rheological properties of the PCC and colloidal silica suspensions (non-Newtonian fluids) under shear flow were measured using a controlled stress rheometer (ARG 2000, TA Instruments, New Castle, DE). The initial geometry was selected to be a 40 mm aluminum parallel plate geometry with a gap ranging from 250 μm to 1000 μm. Although a cone and plate geometry is preferred for steady state shear properties, the parallel plate geometry is more suitable for use with sandpaper, which is required to reduce slip of a high viscosity fluid. A detailed discussion on the effects of wall slip in rheological measurements can be found in Yoshimura et al. (1988). In summary, the presence of slip in viscosity measurements is detected by substantial shifts in the viscosity plots with varying gap thickness between the parallel plates (in some cases shifts in the viscosity can be in excess of an order of magnitude). To eliminate slip in the rheological measurements, the parallel plate geometry was covered with 1000 grit sandpaper, for which the characteristic size of the grit or roughness is of the same order of magnitude as the diameter of the particles. The rheological measurements of the silica based NNF were found to be very similar with gap ranges varying from 250 μm to 1000 μm, indicating this

sandpaper nearly eliminated the effect of wall slip; however, the effect of wall slip was not successfully eliminated with the PCC based NNF. **Fig. 5.6** gives a plot of the viscosity against the shear stress in the fluid for both a PCC based suspension with a volume fraction of approximately ~50% and a silica based suspension with ~48% volume fraction of particles. The PCC based suspension clearly demonstrates a variable viscosity plot with varying gap height, indicating slip is present **(Fig. 5.6a)**; however, in the case of the silica based suspension, the negligible change in the viscosity plots between a gap of 250 μm and 500 μm demonstrates that for silica based non-Newtonian fluids slip can be successfully eliminated **(Fig. 5.6b)**. The reason for the differences between the reduction of slip between these two fluids may be attributed to the anisotropy of the particles, particularly in that the PCC has a highly non-uniform distribution. In addition to slip studies, both fluids were examined to determine their reversibility. Ascending and descending stress sweeps were performed for both suspensions. The PCC suspension repeatedly demonstrated a strong tendency to have irreversible behavior **(Fig. 5.7a)** while the silica based suspension demonstrated minimal hysteresis **(Fig. 5.7b)**, exhibiting the reversibility of the silica based fluid found by Bender and Wagner (1996). These hysteresis or reversibility studies are evident in **Fig. 5.7**, where plots are given for the viscosity of each fluid against the shear stress. Based on these studies, it was determined the silica based non-Newtonian fluid is more ideal for this analysis; therefore, all experiments discussed throughout the rest of this chapter utilize this silica based suspension.

5.3.4 Viscosity of the Silica Suspension

To fully characterize the silica based non-Newtonian fluid the following procedures were followed. The steady state rheological properties of the

colloidal silica suspension under shear flow was measured using a controlled stress rheometer (ARG 2000, TA Instruments, New Castle, DE). As before, the parallel plate geometry was covered with 1000 grit sandpaper to eliminate the possibility of slip during the experiments. The final geometry was selected to be a 40 mm aluminum parallel plate geometry with 500 μm gap. All experiments were performed at 22.5 °C and controlled with a Peltier temperature control. A volume fraction of 61% silica particles was selected as the highest achievable and standard for these experiments. Based on the assumption of ideal mixing, the density of the resulting NNF was estimated to be 1.6 g/cm^3.

After loading the sample into the viscometer, the sample was loaded under a preshear stress ramp from 10 to 100 Pa and then allowed to rest for 15 minutes to eliminate any effects of sample loading. A stress sweep was performed from 10 Pa to a maximum shear stress in the fluid of approximately 15,400 Pa with 10 points per decade, each of which was measured for 60 seconds. However, for samples with a lower volume fraction of particles than the standard 61% sample, the maximum shear stress value in the fluid could not be achieved due to rate limitations of the rheometer, so the maximum shear stress achievable was recorded. The steady state shear viscosity was measured along with the shear stress in the fluid and local shear rate under controlled stress loading. Because of the complexity of the manufacturing process, determining the exact volume fraction of silica particles is difficult, so variations in the volume fraction are expected. To assess the sensitivity to variations in the volume fraction of silica and determine the overall characteristic behavior of high volume fraction silica based fluids, this procedure was used for volume fractions of approximately ~48%, ~50%, ~52%, and ~61%. Note, these volume fractions themselves may also have errors and should not be used for extracting detailed information.

5.3.5 Dynamic Compression Tests on Non-Newtonian Fluid-Filled Foam

Samples of reticulated, polyurethane foam saturated with the 61% volume fraction silica-based NNF were then prepared. Since even the minimum viscosity of the NNF is large, samples of reticulated foam were filled by the capillary effect through axial compression cycles while submerged in a bath of NNF shaken by a vortex mixer. Hager and Craig (1992) demonstrated that the deflection of a polyurethane foam compressed to 0.75 strain for a short duration of time is almost completely recoverable. Therefore, an attempt was made not to exceed a strain of 0.75 during the filling process to minimize the microstructural damage caused by the filling process. After saturation, the NNF-filled foam was allowed to recover for 2 hours prior to testing, based on data for the recovery of low-density polyurethane foam presented by Hager and Craig (1992).

The compressive true stress-strain response of the NNF-filled foam was measured with the rise direction of the foam parallel to the direction of loading, up to a strain of 0.6 and over a range of instantaneous strain rates of the foam from $-\dot{h}/h = 1.0\ s^{-1}$ to $4x10^2\ s^{-1}$. For instantaneous strain rates less than $-\dot{h}/h = 50\ s^{-1}$ an Instron testing machine (Instron Model 1321, Instron Corp., Canton, MA) was used at constant velocities ($-\dot{h}$ = 12.5, 31.25, 62.5, 93.75, 125, and 250 mm/sec); for instantaneous strain rates greater than $-\dot{h}/h = 50\ s^{-1}$ a Dynatup drop-tower (Dynatup 9200 Series, Instron Corp., Canton, MA) was used. The Dynatup drop-tower has the capability to impact specimens with energies in excess of 1600 J at speeds in excess of 20 m/s using a spring assisted velocity accelerator. The load cell is able to record forces up to 45 kN at a speed of 5 MHz. The tup and bottom fixture were modified to produce an impact between two flat, circular plates. The drop-tower impact experiments were arranged to be

nearly constant velocity. Data was only collected up to strains of approximately 50%, at which point built in stoppers in the drop tower absorbed the remaining energy. The drop-tower weight was approximately 21.7 kg, resulting in an impact energy that was substantially greater than the energy absorbed by the NNF-filled foam or the energy gained due to potential energy effects. Since the energy of the drop-tower weight was nearly constant, the resulting experiments were nearly constant velocity ($-\dot{h} \approx$ 0.75, 1.00, 1.25, 1.50, 1.75, 2.00, 2.25, 2.50, 2.75, and 3.00 m/sec). During testing the temperature was maintained at 22.5°C to ensure the fluid properties are consistent. Since the flow is assumed to be instantaneously fully developed, the model presented in this chapter is applicable to constant velocity loading.

5.4 Fluid Viscosity Results and Discussion

In **Fig. 5.8** the viscosity is plotted against the shear stress in the fluid and the local strain rate for a series of NNF fluids with volume fractions of ~48%, ~50%, and ~52%. The rheological behavior of the fluid under steady state shear viscosity testing in the controlled stress rheometer was consistent for all volume fractions tested. The viscosity data also correspond well with similar experiments performed by Maranzano and Wagner (2001a). We assume that the viscosity plots in **Fig. 5.8** are typical of the behavior for all silica-based, non-Newtonian fluids with the shear thinning and thickening regimes discussed in this chapter.

Fig. 5.9 provides more detail of the characteristic behavior of these curves for the ~50% volume fraction sample by denoting regimes of distinct behavior. At extremely low local strain rates the fluid acts as a shear thinning fluid (regime

R_1). The shear thinning or "yield stress" behavior observed at low local strain rates occurs when the particles in an ordered phase begin to orient themselves so that the direction of closest packing of the spheres aligns with the flow velocity, such that the planes containing the closest packing spheres are parallel to the shearing surfaces (Lee et al., 1999). Therefore, the three-dimensional ordered phase transforms into a two-dimensional layered phase that permits flow, resulting in a dramatic drop in viscosity. At a critical local strain rate dramatic shear thickening occurs, evident in regime R_2. The onset of this dramatic shear thickening occurs when the hydrodynamic forces driving particles together exceed the repulsive forces due to interparticle (i.e. electrostatic or steric) potentials and Brownian motion (Maranzano and Wagner, 2001a). At this point the particles fail to remain in their ordered state and begin to form three-dimensional clusters of particles. This dramatic shear thickening is also evident in **Fig. 5.9b** at nearly constant local strain rate. This dramatic shear thickening is often termed "critical shear thickening" when a discontinuity is observed as shown in **Fig. 5.9b**. As previously discussed the jamming phenomenon is attributed to shear thickening, but critical shear thickening is only observed for very high volume fractions of solid particles. Following shear thickening, a plateau viscosity is reached (regime R_3). A number of theories have been proposed for this phenomenon, but it is generally accepted that the clusters begin to break down and form a random three-dimensional packing (Barnes, 1989). These first three regimes are characteristic of most non-Newtonian fluids with shear thickening regimes (Barnes, 1989). However, after the maximum plateau, the fluid is often found to enter one of three stages: fracture, an extended plateau viscosity independent of shear rate, or a shear thinning regime (Barnes, 1989). This regime of behavior is controlled by particle size distribution, particle content, the volume fraction of particles, particle-particle interactions, and the

viscosity of the continuous phase. For the particular fluid discussed in this chapter, another shear thinning regime, R_4, occurs and finally, for suspensions with particle volume fractions of ~48%, ~50%, and ~52% a lower plateau viscosity is reached (regime R_5), which is approximately equal to the minimum viscosity previously obtained (**Fig. 5.8**). A large body of literature attempts to explain the behavior in all the regimes described (Hoffman, 1998; Bender and Wagner, 1996; Laun et al., 1992; Boissis and Brady, 1989) but the explanations for some phenomenon are still under dispute, so a detailed description is excluded from this discussion. However, the general regimes described here are found to be consistent with this body of literature as seen in Hadjistamov (1984) and Barnes (1989). The primary debate around this shear thinning regime is whether or not slip is causing it. In addition to the evidence presented by Hadjistamov (1984) and Barnes (1989), Hoffman (1974) also demonstrated distinct shear thinning regimes after shear thickening for monodisperse polymeric resin colloids. We believe much of the recent literature has avoided the debate around this topic by not publishing data in the high stress regime examined in this study. For instance, the maximum shear stresses examined for comparable silica-based non-Newtonian shear thickening fluids given by Bender and Wagner (1996), Fagan and Zukoski (1997), Lee et al. (1999), and Maranzano et al. (2001a) range from the order of 100 Pa to the order of 1000 Pa. None of these studies attempts to examine the stress regime approaching and exceeding 1 $x10^4$ Pa, presented in this study. However, more recent studies by Egres and Wagner (2005) have demonstrated measurements in this regime are possible. They have also shown with a precipitated calcium carbonate based STF distinct plateau regimes, corresponding to R_3, followed by what appears to be the beginning of shear thinning regimes, corresponding to R_4. In addition to this support, we believe a number of factors indicate slip is not contributing to the behavior in this regime.

The first is the extensive slip study that was previously discussed **(Fig. 5.6)**. The results of that study were that varying the gap thickness had a negligible effect on the viscosity plots. Furthermore, it is evident in **Fig. 5.8** that the shear thinning transition occurs over a range of magnitude in shear stress. We believe if slip were causing this behavior the shear stress at which it would appear would be more consistent. Moreover, the consistency in the slopes of the shear thinning regime, indicate this behavior is not being induced by slip, which in all likelihood would result in a more erratic result. Finally, the results of the stress-strain response of the NNF-filled foam, discussed later in this chapter, provide further evidence that this shear thinning regime really does exist.

Fig. 5.10 plots the viscosity against the shear stress in the fluid and the local strain rate for 61% volume fraction silica/ethylene glycol solution. Limitations in the maximum torque capacity of the viscometer did not allow us to obtain data for the full range of regimes R_4 and R_5. Assuming that the trends in the viscosity of the fluid with 61% volume fraction silica particles are similar to those at lower volume fraction of particles, we can extrapolate the existing R_4 data using a linear regression of the log data (equations shown on the figures). We note that, for particle volume fractions of ~48%, ~50%, and ~52%, the value of the viscosity for the lower plateau (R_5) is similar to that at the minimum of R_1; we expect the transition from R_4 to R_5 to be similar for the fluid with 61% volume fraction of particles. For the 61% volume fraction NNF, the parameters m and n for the power-law model in regime R_3 and R_4 are found to be m = 7,700 Pas; n = 1.0 and m = 10,800 Pas; n = 0.19, respectively, as shown by the plateau data points and the shear thinning trend line in **Fig. 5.10.**

5.5 Fluid-Filled Foam Results and Discussion

A plot of the true stress-strain responses of the 70 ppi foam saturated with the 61% volume fraction non-Newtonian fluid loaded at constant velocities ranging from 31.25 mm/sec to 250 mm/sec is given in **Fig. 5.11a**. The dramatic increase in the true stress of the NNF-filled foam with strain is evident. The true stress of the NNF-filled foam is taken to be the load divided by current area, which is calculated based on conservation of mass, as previously discussed. At any given strain, the true stress of the NNF-filled foam and corresponding instantaneous strain rate of the foam can be determined. The recorded data and **Fig. 5.11a** are used to generate the sample curve of the true stress response of the NNF-filled foam plotted against the instantaneous strain rate of the foam given in **Fig. 5.11b**. For instantaneous strain rates less than 50 s^{-1}, strains varying from 0.1 to 0.6 are plotted in increments of 0.1, corresponding to aspect ratios ranging from approximately 1 to 4. For instantaneous strain rates greater than 50 s^{-1} strains varying from 0.1 to 0.4 are plotted, corresponding to aspect ratios ranging from 1 to 2.

The dynamic compressive response of the saturated NNF-filled foam exhibits multiple regimes of behavior similar to the simple shear behavior of the fluid itself given by the previous rheological experiments (**Fig. 5.8-5.10**). As shown in **Fig. 5.11b**, this behavior corresponds to the first four regimes (R_1-R_4) of the fluid, previously discussed. At low instantaneous strain rates of the foam, the rate of increase of true stress of the NNF-filled foam with instantaneous strain rate is actually less than that of a comparable Newtonian fluid, indicating the viscosity is dropping with increasing instantaneous strain rate, corresponding to the shear thinning regime, R_1. The onset of the shear thickening regime, corresponding to

R_2, is also evident and, as expected, is found to occur with increasing strain (or aspect ratio) or increasing instantaneous strain rate. Similarly, behavior corresponding to regimes R_3 and R_4 are also evident. While distinguishing the transition between the upper plateau regime, R_3 and the shear thinning regime, R_4 in **Fig. 5.11b** may be difficult at the given scale, the distinction is more apparent in expanded scales provided later in **Fig. 5.12.**

In this study, we are primarily interested in modeling the behavior after shear thickening has occurred (R_3 and R_4) since most engineering applications will utilize the NNF in this regime. For example, the expected impact velocities for a helmeted head in a motorcycle accident and a chest covered by standard body armor subjected to a 1 kg TNT blast wave at a distance of 1 meter are on the order of 5 m/sec and 10 m/sec, respectively. This results in instantaneous strain rates for a 0.01 m thick foam sample of 500 s^{-1} and 1000 s^{-1}, which are clearly beyond the instantaneous strain rate of the foam required for the fluid to transition from regime R_2 to regime R_3 (**Fig. 5.11b**). In addition, our focus was on modeling the behavior in regime R_3 and beyond because analytically modeling the behavior at strain rates less than those of regime R_3 is a complex task, which requires accounting for the fluid structure interaction and the dramatic variation of the viscosity across the specimen. As previously discussed this problem is avoided for strain rates beyond the transition strain rate between regimes R_2 and R_3, where the effects of the fluid-structure interaction and the foam itself can effectively be neglected.

To compare our model (Eq. 5.15) with our data, in the upper plateau regime, R_3 and in the shear thinning regime, R_4, we examine data beyond the transition

strain rate between regimes R_2 and R_3. **Fig. 5.12** shows the true stress response of 70 ppi foam filled with the non-Newtonian fluid under dynamic compression plotted against the instantaneous strain rate of the foam for a range of strains varying from $\varepsilon = 0.10$ to $\varepsilon = 0.40$ and a range of instantaneous strain rates ranging from ~50 s^{-1} to ~400 s^{-1}. Each point is the average of 4 data points with error bars corresponding to one standard deviation. The error bars in the true stress direction are quite large, as expected, since small variations in the volume fraction of the silica particles in the fluid can result in large changes in viscosity but nearly no change in the exponent variable n. Correspondingly, the error bars in the instantaneous strain rate direction arise because changes in the energy absorption of the NNF-filled foam result in changes in the energy of impacting drop tower, and thus, its velocity. The true stress contribution predicted by the model given by Eq. (5.15) is plotted in **Fig. 5.12** for both the plateau regime, R_3 and the shear thinning regime, R_4 with their corresponding parameters m and n. To fit the true stress model constants C_{Ri} were introduced for each regime (where $_i$ corresponds to the regime) into Eq. 5.15 giving

$$\sigma_{avg} = 2C_{Ri}\left(\frac{2n+1}{n}\right)^n \frac{m}{n+3}\left(\frac{R_o}{h_o}\right)^{n+1}\left(\frac{-\dot{h}}{h}\right)^n\left(\frac{1}{1-\varepsilon}\right)^{\frac{3(n+1)}{2}}. \tag{5.16}$$

The constants C_{R3} *and* C_{R4} given in Eq. (5.16) were found by establishing a measure of the goodness of fit and finding the value of C_{R3} *and* C_{R4} which maximizes this measure. The measure for the goodness of fit R^2, is taken to be the sum of the squares of the difference between the experimental values and the average experimental value divided by the sum of the squares of the difference between the experimental values and the predicted values. Based on this

measure of the goodness of fit, the empirical constants for regimes R_3 and R_4 are determined to be $C_{R3} = 0.94$ and $C_{R4} = 80$, respectively. These constants can be attributed primarily to two factors. First, as previously discussed, even small variations in the volume fraction of particles can result in large changes in the viscosity curves, and thus, the observed average true stress. Second, the increased tortuosity of the fluid path in the foam may also play a substantial role since the flow through the foam is not identically in shear flow.

Using the constants C_{R3} and C_{R4}, the transition between the plateau regime R_3 and the shear thinning regime R_4 is found by setting Eq. (5.16), evaluated with constants (m and n) corresponding to the plateau regime, equal to Eq. (5.16), evaluated with constants (m and n) corresponding to the shear thinning regime. The resulting equation governs the transition between R_3 and R_4 and is found to be

$$\left(\frac{-\dot{h}}{h}\right)=\left(\frac{C_{R4}}{3C_{R3}}\right)^{1.23}\left(\frac{h_o}{R_o}\right)(1-\varepsilon)^{3/2}. \tag{5.17}$$

Using Eq. (5.17), for any given initial aspect ratio and strain, the instantaneous strain rate, corresponding to the transition between regimes R_3 and R_4, can be determined. While Eq. (5.17) is not generalized for all fluids discussed in this chapter, it is applicable to the 61% silica-based non-Newtonian fluid, which is the focus of this analysis. Since there is no model for the transition between the shear thickening regime R_2 and the plateau regime R_3, the onset of the behavior corresponding to R_3 is not predicted in this study; the model was plotted down to an arbitrary instantaneous transition strain rate of the foam selected to be 50 s^{-1}.

The constants C_{R3} *and* C_{R4}, are found to be independent of the initial aspect ratio, the strain, and the instantaneous strain rate of the foam as demonstrated by **Fig. 5.12**. Furthermore, the constants C_{R3} *and* C_{R4}, are also found to be independent of the grade of the foam beyond the shear thickening transition. An additional study was performed to analyze the effects of varying the pore size of the foam. The true stress response of the NNF-filled foam was compared for 70, 80, and 90 ppi foam both prior to and after shear thickening (regimes R_2 and R_4). Prior to shear thickening, the true stress response is found to be highly dependent upon the grade of the foam as demonstrated with Newtonian fluids (Dawson, McKinley, and Gibson, 2008). Prior to shear thickening, the standard deviation in the true stress response of the three foam grades as a percentage of the average value was found to be 17.7%, which corresponds well with the results presented in Dawson, McKinley, and Gibson (2008). However, after shear thickening has occurred the true stress response of the NNF-filled foam is found to be independent upon the grade of the foam, with a standard deviation in the true stress as a percentage of the average value of only 2.7%. This finding further supports the evidence shown in **Fig. 5.2** that the fluid-structure interaction is negligible at high loading rates (high stresses) after shear thickening has occurred. Thus, the constants C_{R3} *and* C_{R4}, are independent of the grade of the foam beyond the shear thickening transition.

The need for the introduction of the empirical constants C_{R3} *and* C_{R4}, is expected. These constants can primarily be attributed to the fact that small variations in the volume fraction of the silica particles in the fluid can result in large changes in viscosity, corresponding to m in Eq. (5.16), but nearly no change in the exponent variable n. This effect could readily account for such an apparently large constant while explaining the fact that the true stress scales accurately with all of

the parameters in Eq. (5.16). The need for different empirical constants for each regime (C_{R3} vs. C_{R4}) can also be seen through this argument. If the actual plateau viscosity is higher than that measured in the rheological experiments, the need for a constant greater than unity is evident for regime R_4. Correspondingly, this effect would necessitate a constant greater than unity in regime R_3 as well; however, since regime R_3 only spans a very short range of local strain rates and local strain rates are expected to vary strongly over the radius of the foam, it is expected that not all of the fluid is accurately modeled by the maximum plateau viscosity (regime R_3). This would result in the model overestimating the average viscosity in the fluid and necessitate a constant less than unity to account for this overestimation. This effect would be less pronounced in the shear thinning regime R_4, since the range of local strain rates spanned by this regime is much larger than that of R_3. Therefore, the need for different constants for each regime (C_{R3} vs. C_{R4}) is evident. The effects, overall, result in a constant for regime R_3, which is on the order of unity and a constant for regime R_4, which is much greater than unity.

The empirical constants C_{R3} *and* C_{R4}, may also indicate that a number of effects, which have been neglected based on the assumptions of the analysis, may be important. For instance, this analysis does not consider the tortuosity in the fluid path in the open-cell foam, which may also contribute to the need for the constants C_{R3} *and* C_{R4}, to be introduced. In addition, this model assumes that the radial velocity is uniform in the z-direction or that the fluid remains in a cylindrical shape as it undergoes deformation. This is a strong assumption as demonstrated by **Fig. 5.1**, where little variation in the radius up to 0.30 strain is detectable. However, even small variations in the radius of the NNF-filled foam can result in changes in the local shear rate profile. This would give rise to large

discrepancies between the predicted viscosity and the actual viscosity in the experiment, and thus, a discrepancy in the true stress response of the NNF-filled foam. Furthermore, this model uses the lubrication approximation, which assumes that the velocity in the z-direction is much less than the velocity in the r-direction, and that the corresponding pressure drop in the z-direction is negligible compared to that in the r-direction. The lubrication approximation technique is known to be a powerful method for solving complex viscous flows. When applied to actual systems, the fluid response is often found to converge very rapidly to the lubrication approximation as the aspect ratio is increased. In *Chapter 4*, it was discovered that the lubrication approximation for a Newtonian fluid-filled foam under dynamic compression is highly applicable beyond an aspect ratio of four; however, examining the data shows even for aspect ratios as small as one, the lubrication model provides a good approximation. In the experiments presented in this chapter the aspect ratios ranged from 1.17 to 3.95. Again, this could result in a small discrepancy between the model and the experimental results. Moreover, the fluid flow may not be considered entirely in shear flow, which would result in a much lower predicted true stress response than actually observed experimentally. In addition, the local shear rate of the fluid may actually differ from that predicted by the model, in part, due to dependence on the fluid-foam interaction. Although, this contribution is expected to be negligible since the load response of the NNF-filled foam is three orders of magnitude beyond that of the foam alone, and the characteristic diameter of the particles in the silica suspension is three orders of magnitude smaller than the characteristic pore size of the foam. Lastly, as previously discussed, this model assumes that the flow is dominated by viscous forces. This is an extremely robust assumption for the experiments presented in this analysis, considering the fluid viscosity increases approximately 3 orders of magnitude

and approaches that of "solid-like" behavior after the shear thickening transition. As previously discussed, the shear thinning regime R_4 occurs over roughly four orders of magnitude of the local strain rate of the fluid, based on the behavior of fluid with lower volume fractions of particles, which have plateau regimes R_5 at a viscosity corresponding to the minimum viscosity of the fluid. Therefore, it is expected that the shear thinning regime R_4, would also last several orders of magnitude of the instantaneous strain rate of the NNF-filled foam. Based on this, the fluid maintains an extremely high viscosity, with increasing instantaneous strain rate, for several orders of magnitude beyond the transition between the shear thickening regime R_2 and the plateau regime R_3. In the experiments presented in this chapter, the maximum Reynolds was $Re = 0.027$, which is much less than unity, demonstrating that the assumption that the flow is dominated by viscous forces is highly applicable. However, for extremely high-rate loading scenarios inertial forces may become more important and this viscous fluid assumption may no longer be valid. Therefore, this model may only provide an order of magnitude estimate beyond loading velocities of ~50 m/s (instantaneous strain rates of ~5×10^3 s^{-1}) for samples with similar aspect ratios as those discussed in this chapter. As previously discussed, nearly all comparable engineering designs used in dynamic compression, ranging from motorcycle helmets to blast loading protective equipment, would have loading rates applicable to this model.

Overall, the model for the true stress response of a non-Newtonian fluid-filled foam under dynamic compression given by Eq. (5.16) is strongly supported by experimental results, despite the need for a constant in each regime to account for some of the assumptions of the model. The model is found to describe the experimental results well for a variety of aspect ratios, strains, and instantaneous

strain rates of the foam on the order of $-\dot{h}/h = 1.0\text{x}10^2\ s^{-1}$. It is also found to be independent of foam grade for low-density elastomeric foam. The model is found to fall within one standard deviation of all of the experimental data presented in **Fig. 5.12.** A method is also presented to identify the transition instantaneous strain rate between regimes R_3 and R_4, given an initial aspect ratio and strain.

5.6 Conclusion

A model for the true stress-strain response of a shear-thickening-fluid-filled, reticulated, elastomeric foam under dynamic compression beyond the shear thickening transition is presented. This model is analytically tractable and useful in developing an understanding of the effects of material design parameters on the response of an NNF-filled foam under dynamic loading. To the authors' knowledge this is the first such analytical model, which explains this complex phenomenon for this select group of non-Newtonian fluids and may be useful in the development of innovative new products in the field of protective equipment. In particular, this analytical model will be an essential step toward the successful development of a composite armor capable of impeding shockwaves caused by blast loading by providing insight into the energy absorption capabilities and wave propagation characteristics of an NNF-filled foam under dynamic loading.

References

Barnes, H.A., (1989), "Shear-Thickening ('Dilatancy') in Suspensions of Nonaggregating Solid Particles Dispersed in Newtonian Liquids", *J. Rheo.*, **33**, 329-66.

Bender, J. and Wagner, N., (1996), "Reverisible Shear Thickening in Monodisperse and Bidisperse Colloidal Dispersions", *J. Rheo.*, **40**, 899-916.

Bird, R, Hassager, O., Armstrong, R., (1987), Dynamics of Polymeric Liquids 2nd Edition. John Wiley & Sons. New York, NY.

Comiti, J.M., (1989), "A New Model For Determining Mean Structure Parameters of Fixed Beds From Pressure Drop Experiments: Application to Packed Beds with Prallelpipedal Particles", *Chem. Eng. Sci.*, **44**,1539-45.

Comiti, J., Sabiri, N., and Montillet, A., (2000), "Experimental Characterization of Flow Regimes in Various Porous Media-III: Limit of Darcy's or Creeping Flow Regime for Newtonian and Purely Viscous Non-Newtonian Fluids", *Chem Eng. Sci.*, **55**, 3057-3061.

Egres, R. and Wagner, N., (2005), "The Rheology and Microstructure of Acircular Precipitated Calcium Carbonate Colloidal Suspensions Through the Shear Thickening Transition" *J. Rheo.*, **49**, (3), 719-46.

Fagan, M., and Zukoski, C., (1997), "The Rheology of Charged Stabilized Silica Suspensions", *J. Rheo.*, **41**, 373-397.

Farr, R., Melrose, J., and Ball, R., (1997), "Kinetic Theory of Jamming in Hardsphere Startup Flows", *Phys. Rev. E*, **55**, 7203-11.

Foss, D.R. and Brady, J.F., (2000), "Structure Diffusion and Rheology of Brownian Suspensions by Stokesian Dynamics Simulation", *J. Fluid Mech.*, **407**, 167-200.

Hager, S.L. and Craig, T.A., (1992), "Fatigue Testing of High Performance Flexible Polyurethane Foam", *J. Cell. Plastics* **28**, pp. 285-303.

Hoffman, R.L., (1998), "Explanations for the Cause of Shear Thickening in Concentrated Colloidal Suspensions", *J. Rheo.*, **42**, (1), 111-123.

Lee, J.D., So, J.H., Yang, S.M., (1999), "Rheological Behavior and Stability of Concentrated Silica Suspensions", *J.Rheo.* **43**, pp. 1117-24.

Laun, H. , Bung, R., Schmidt, F., (1991), "Rheology of Extremely Shear Thickening Polymer Dispersions", *J. Rheo.*, **35**, 999-1034.

Maranzano, B.J., and Wagner, N.J., (2001a), "The Effects of Particle Size on Reversible Shear Thickening of Concentrated Colloidal Dispersions", *J. Chem. Phys.*, **114**, 10514-27.

Maranzano, B.J., and Wagner, N.J., (2001b), "The Effects of Interparticle Interactions and Particle Size on Reversible Shear Thickening: Hard-Sphere Colloidal Dispersions", *J. Rheo.*, **45** (5), 1205-1222.

Sabiri, N.E. and Comiti, J.M., (1995), "Pressure Drop in Non-Newtonian Purely Viscous Fluid Flow Through Porous Media", *Chem. Eng. Sci.*, **50**,1193-1201.

Seguin, D., Montillet, A., Brunjail, D., and Comiti, J., (1996), "Liquid-Solid Masss Transfer in Packed Beds of Variously Shaped Particles at Low Reynold Numbers: Experiments and Model", *Chem Eng. J.*, **63**, 1-9.

Yoshimura, A. and Prud'homme, R., (1988), "Wall Slip Corrections for Couette and Parallel Disk Viscometer", *J. Rheo.*, **32** (1), 53-67.

Figures

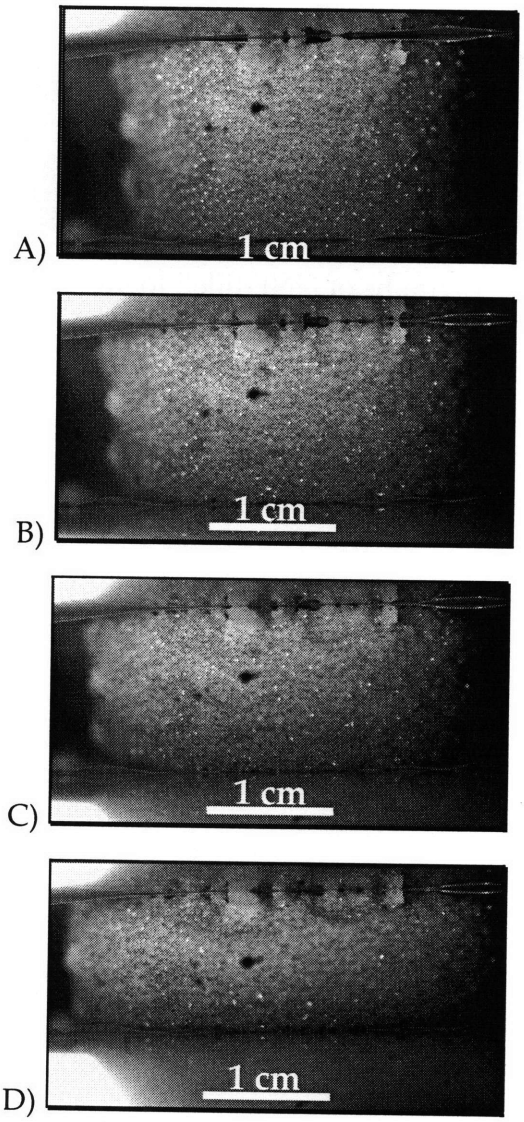

Figure 5.1: High resolution images of 70 ppi foam filled with ~61% volume fraction silica based non-Newtonian fluid loaded in axial compression at 250mm/sec. A) 0.00 strain; B) 0.10 strain; C) 0.20 strain; D) 0.30 strain.

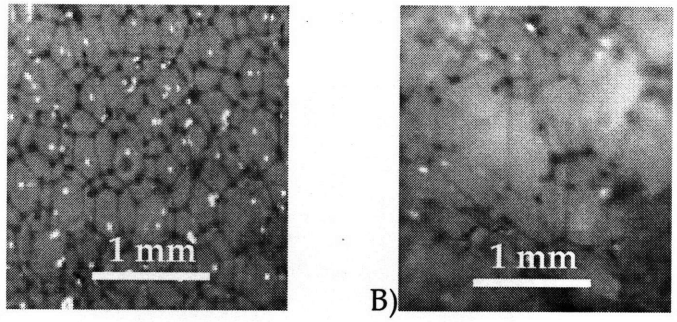

Figure 5.2. Optical micrographs of NNF-filled foam. A) $\varepsilon = 0$ strain; B) $\varepsilon = 0.3$ strain.

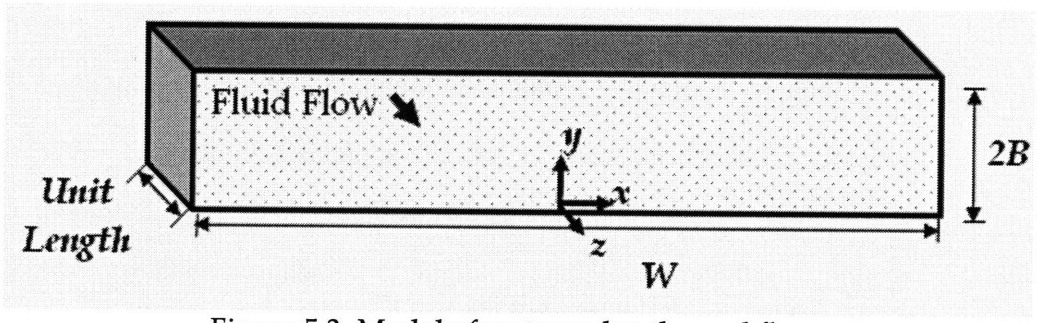

Figure 5.3. Model of rectangular channel flow.

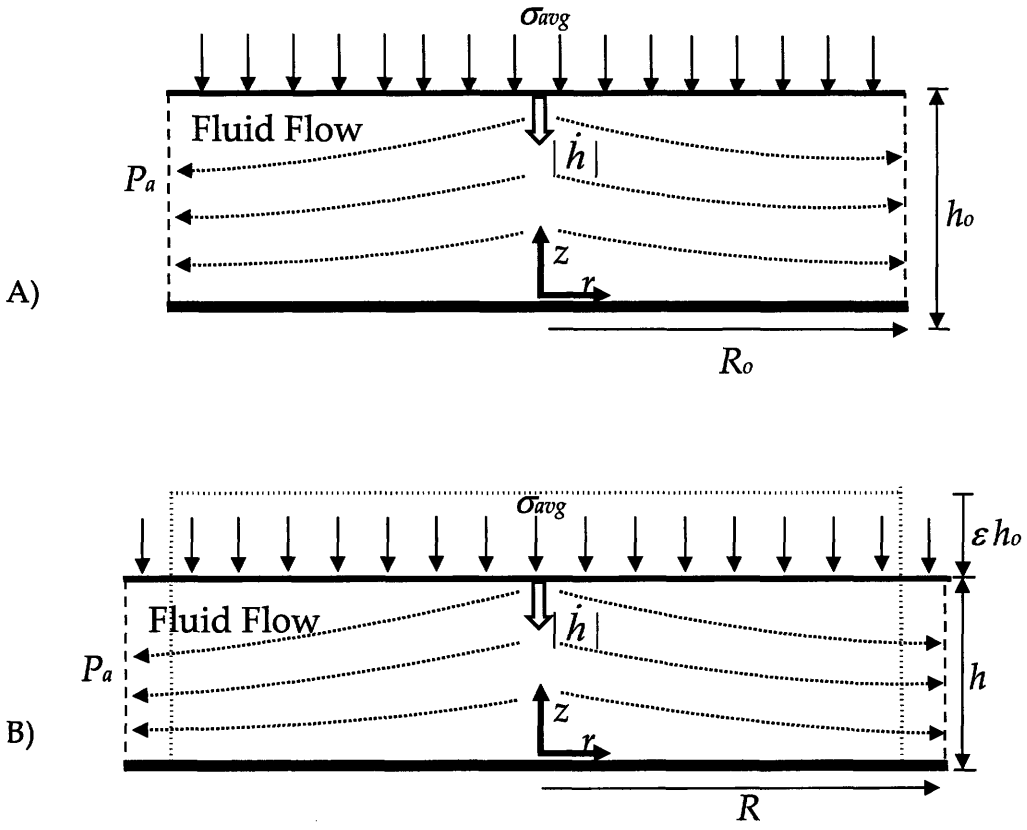

Figure 5.4. Lubrication fluid flow model assuming the absence of foam. A) At 0% strain; B) At any given strain ε.

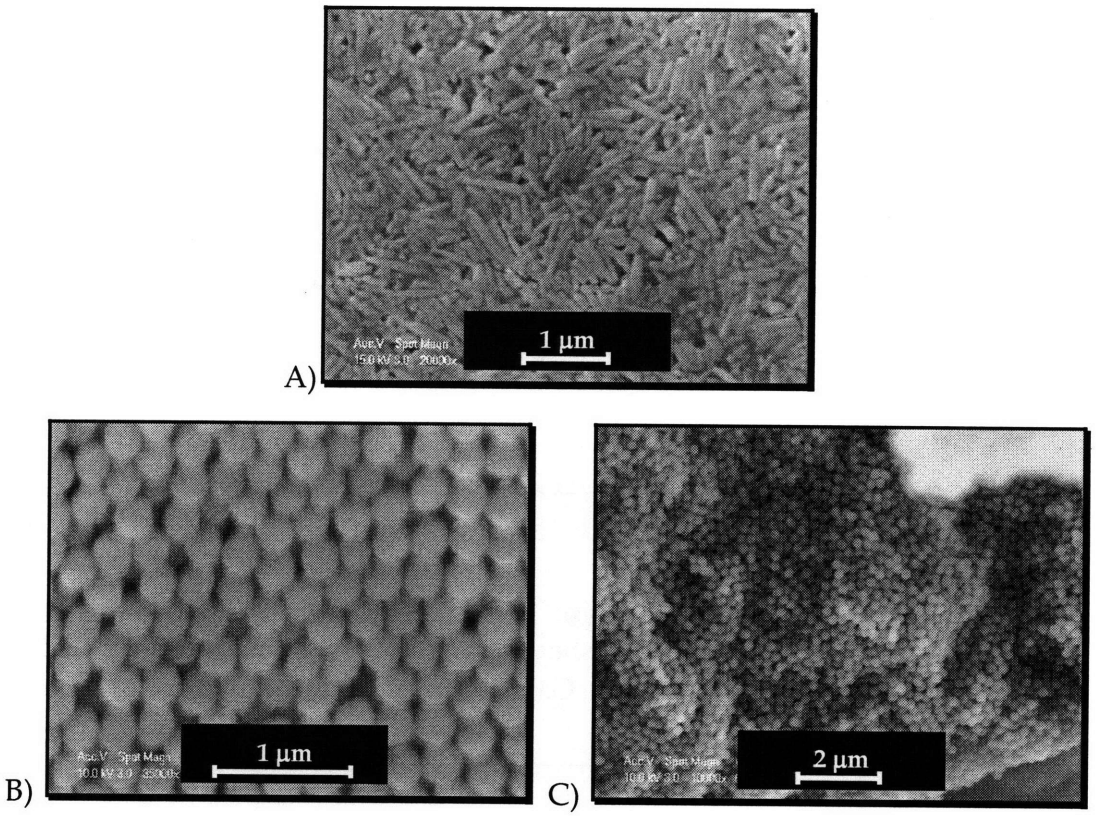

Figure 5.5. SEM Images of: A) Precipitated calcium carbonate particles; B) Silica particles; C) Silica Particles.

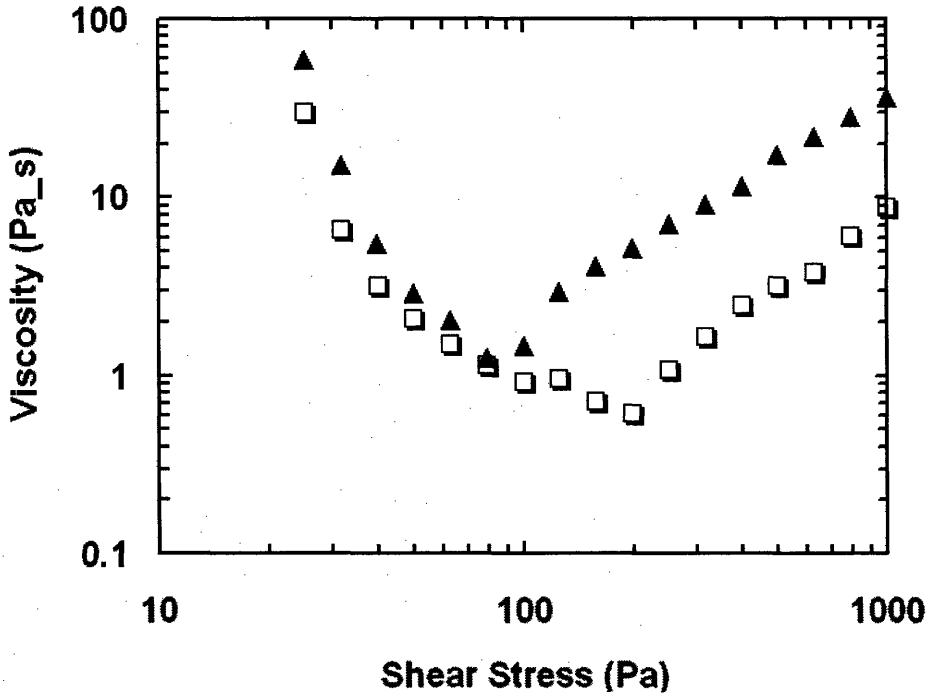

Figure 5.6a. Viscosity plotted against shear stress. ~50% volume fraction of PCC based non-Newtonian fluid. Gap: 500 μm (▲); 1000 μm (□).

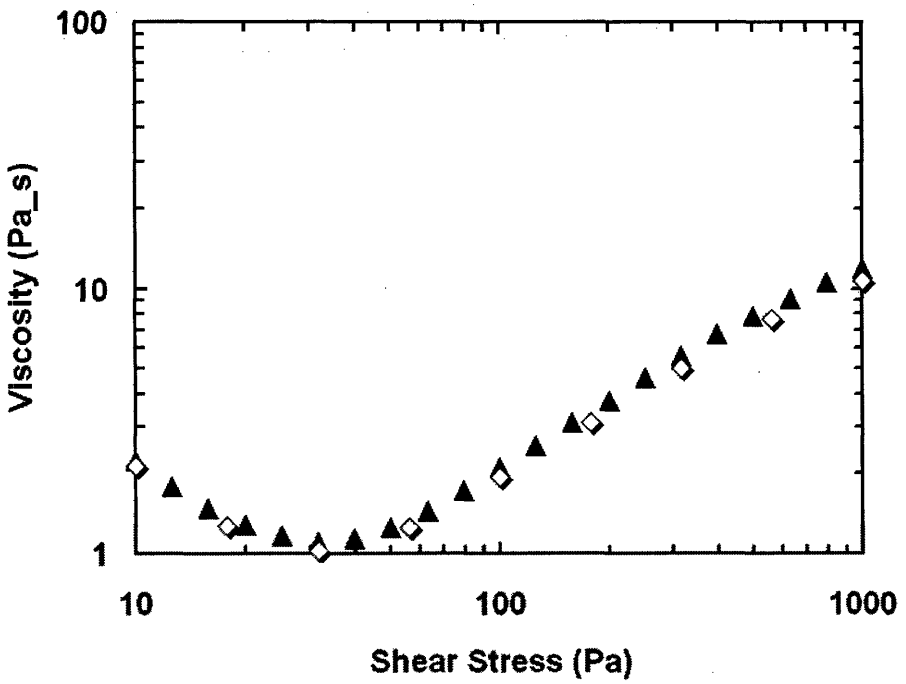

Figure 5.6b. Viscosity plotted against shear stress. ~48% volume fraction of silica based non-Newtonian fluid. Gap: 500 μm (▲); 250 μm (◇).

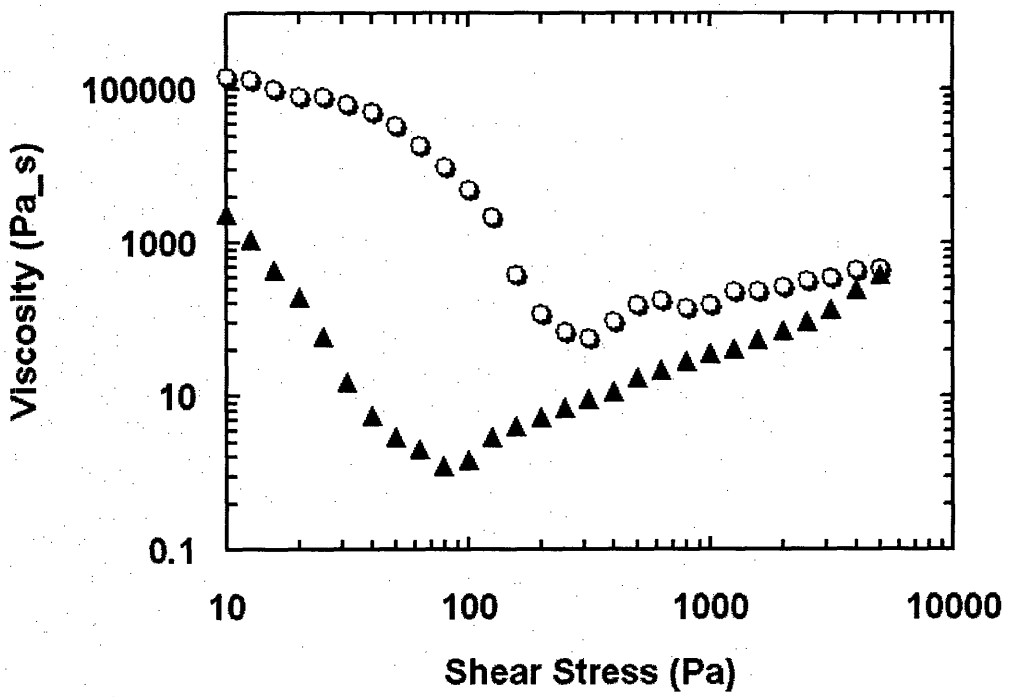

Figure 5.7a. Viscosity plotted against shear stress. ~50% volume fraction of PCC based non-Newtonian fluid. Ascending stress sweep (▲); Descending stress sweep (o).

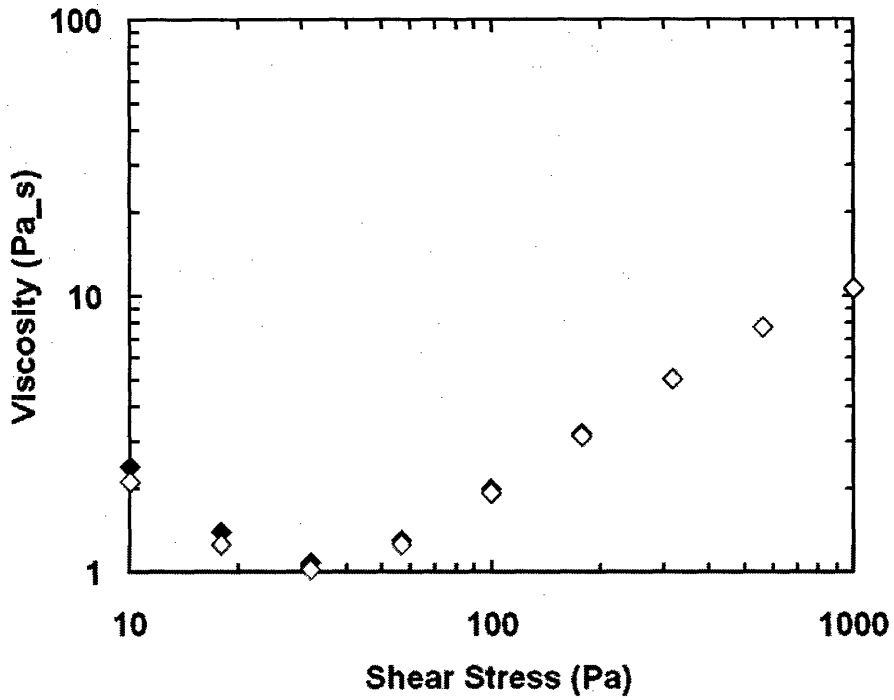

Figure 5.7b. Viscosity plotted against shear stress. ~48% volume fraction of silica based non-Newtonian fluid. Ascending stress sweep (◆); Descending stress sweep (◇).

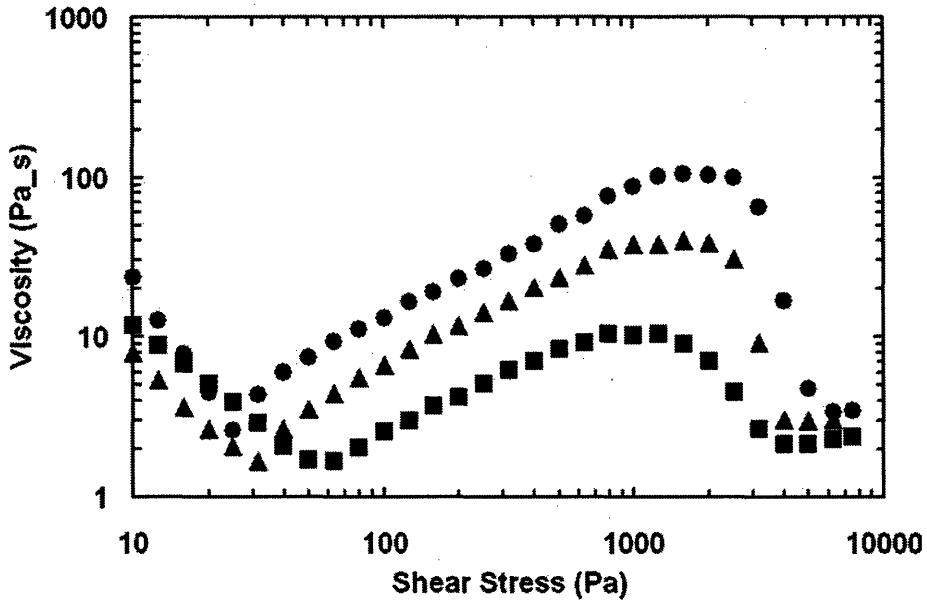

Figure 5.8a. Viscosity plotted against shear stress. Volume fraction of silica based non-Newtonian fluid ~48% (■); ~50% (▲); and ~52% (●).

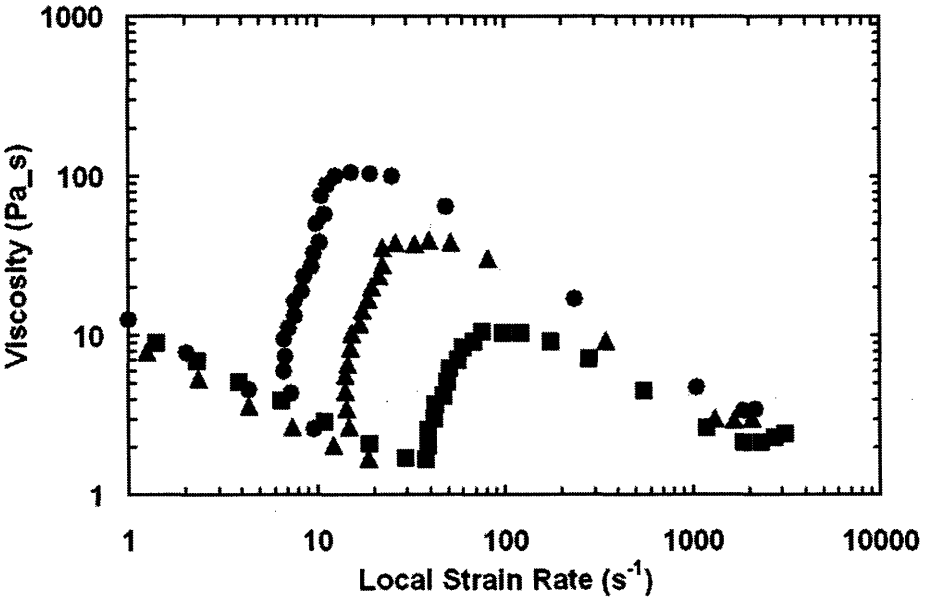

Figure 5.8b. Viscosity plotted against local strain rate. Volume fraction of silica based non-Newtonian fluid ~48% (■); ~50% (▲); and ~52% (●).

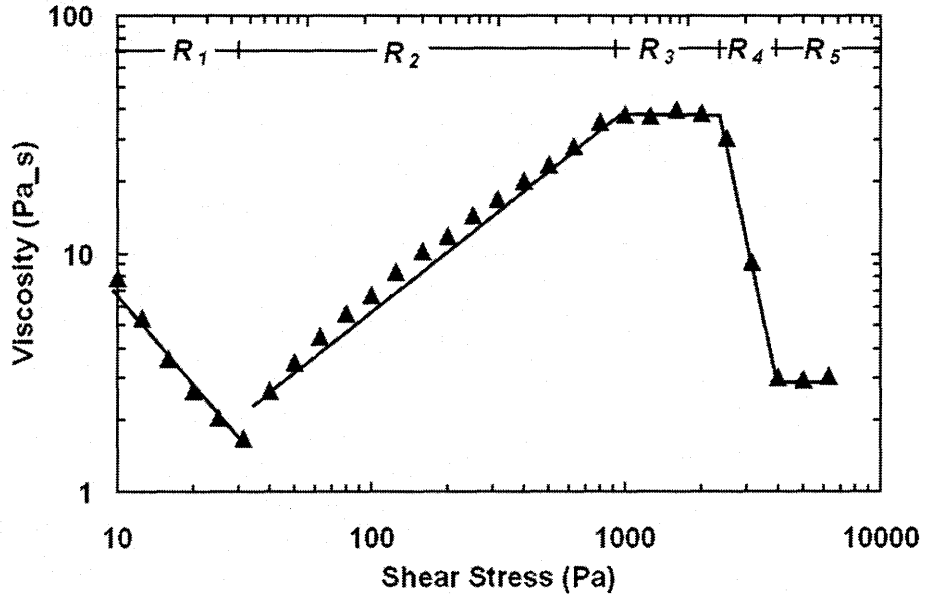

Figure 5.9a. Viscosity plotted against shear stress for ~50% volume fraction silica based non-Newtonian fluid.

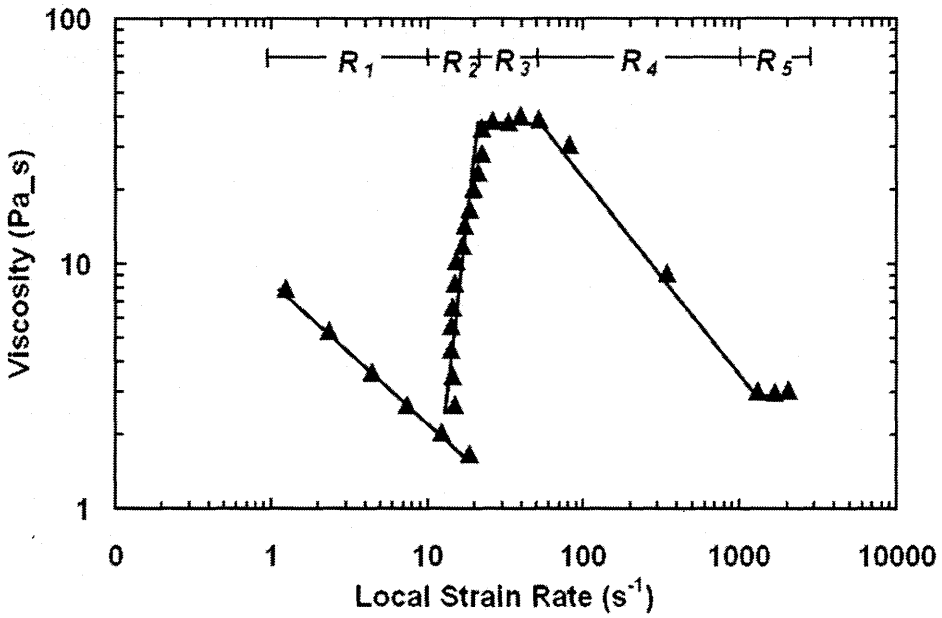

Figure 5.9b. Viscosity plotted against local strain rate for ~50% volume fraction silica based non-Newtonian fluid.

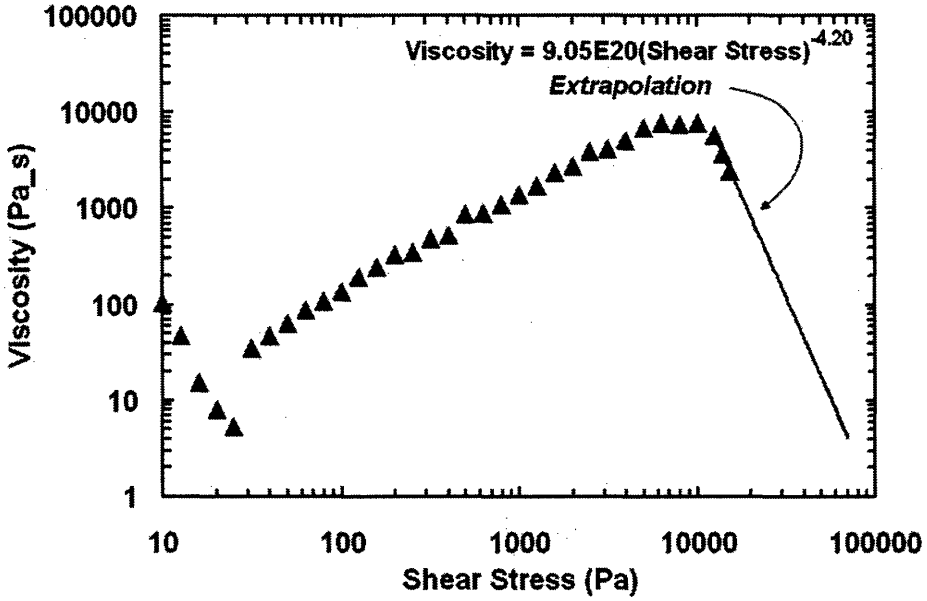

Figure 5.10a. Viscosity plotted against shear stress for ~61% volume fraction silica based non-Newtonian fluid.

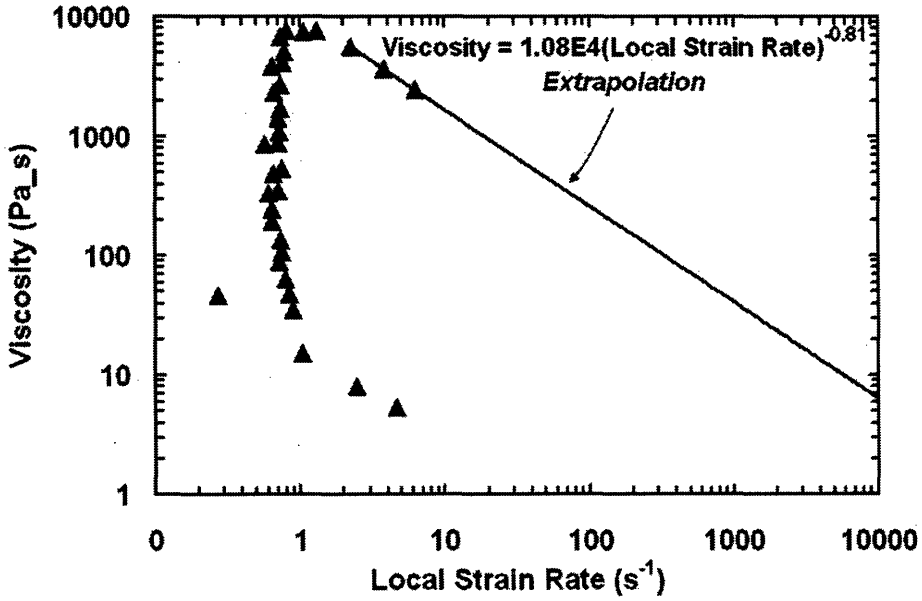

Figure 5.10b. Viscosity plotted against local strain rate for ~61% volume fraction silica based non-Newtonian fluid.

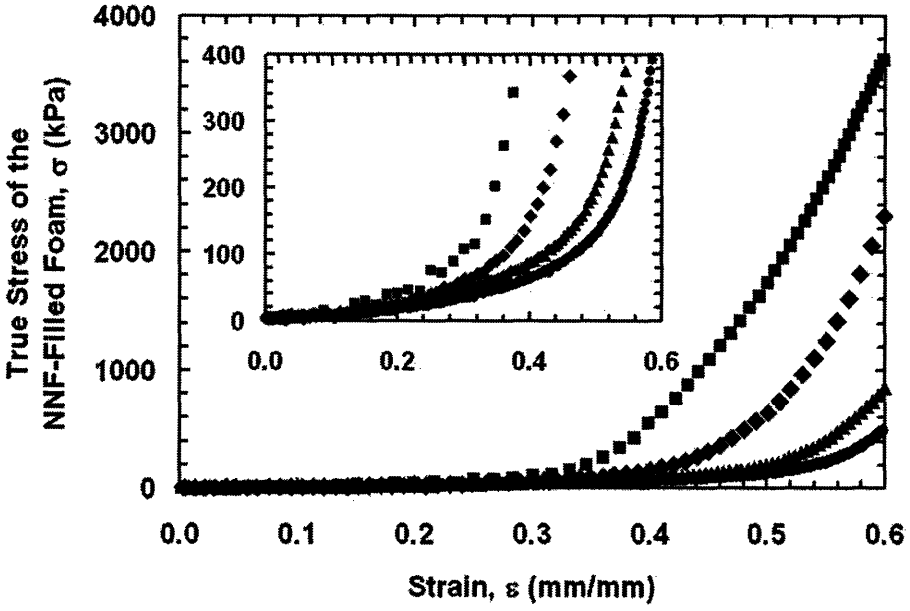

Figure 5.11a: True stress plotted against strain for 70 ppi foam filled with ~61% volume fraction silica based non-Newtonian fluid. $-\dot{h}$ = 31.25 mm/sec (●); 62.5 mm/sec (▲); 125 mm/sec (◆); 250 mm/s (■), corresponding to instantaneous strain rates of 2.5 s^{-1}, 5 s^{-1}, 10 s^{-1}, and 20 s^{-1} at 0.0 strain, respectively.

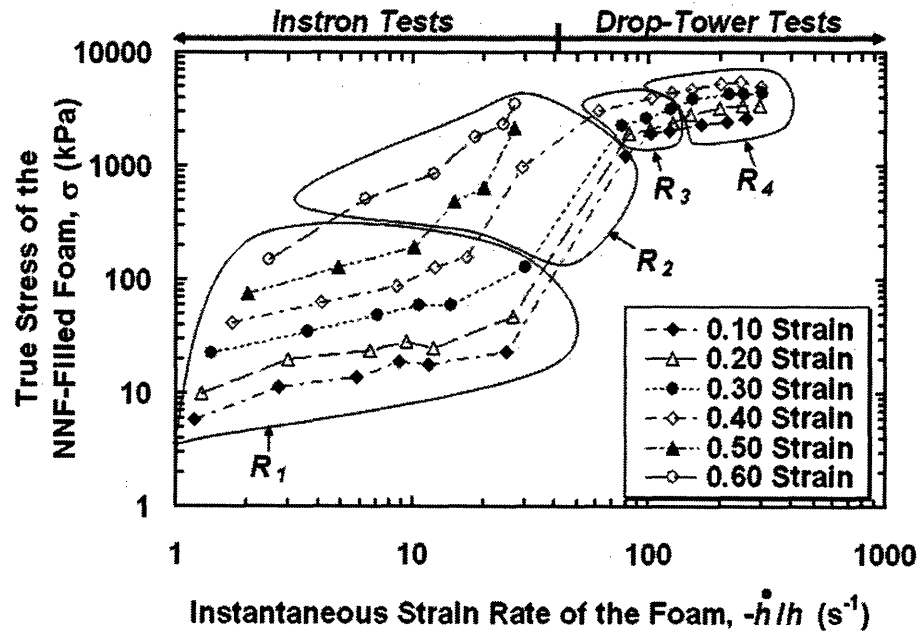

Figure 5.11b: True stress plotted against instantaneous strain rate for 70 ppi foam filled with ~61% volume fraction silica based non-Newtonian fluid. Regimes R_1-R_4 correspond to fluid behavior regimes.

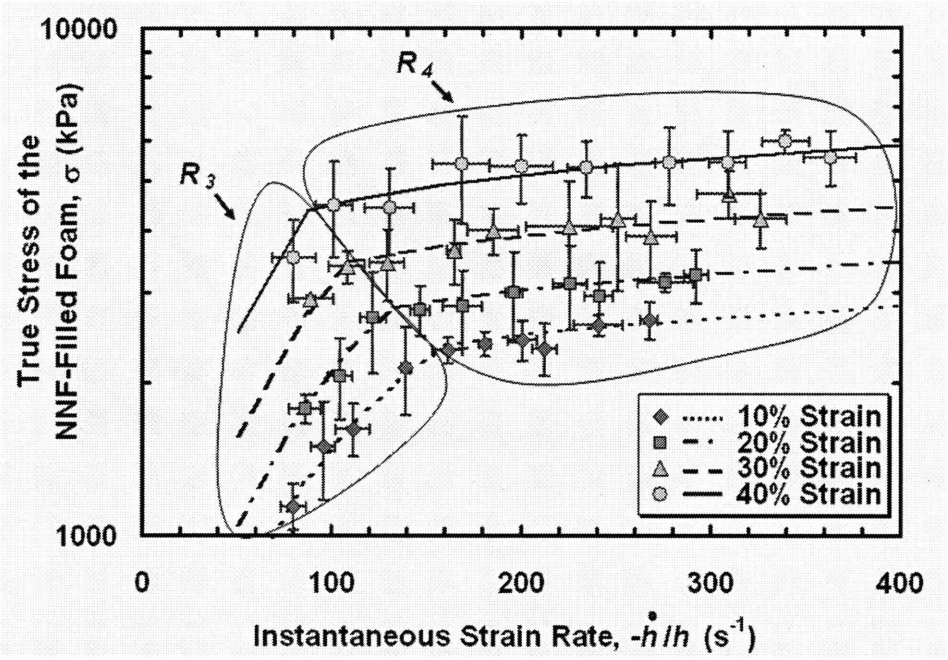

Figure 5.12. True stress plotted against instantaneous strain rate for 70 ppi foam filled with ~61% volume fraction silica based non-Newtonian fluid, ranging from 0.10 to 0.40 strain. Model corresponds to regimes R_3 and R_4 of the fluid given by Eq. (5.16).

6 Applications of Liquid-Impregnated Open-Cell Foam in Motorcycle Helmet Design

6.1 Introduction

The novel liquid-impregnated, open-cell foam discussed throughout this thesis can be used in a variety of energy absorption applications. As previously discussed, improving protective equipment is one of the most critical areas of research in the field of energy absorption. In particular, the need to enhance the protective capabilities of motorcycle helmets has been made manifest over the years with the disproportionately large number of fatalities associated with motorcycle accidents. This chapter uses experimental methods to examine the advantages of incorporating a layer of liquid-impregnated, open-cell foam in motorcycle helmets.

Improving upon existing helmet designs requires a comprehensive understanding of head injury mechanisms and preventative measures currently in use. A brief discussion of the various types of injury mechanisms is presented along with the state-of-the-art or standard helmet technology used to prevent head injury. Based on the biomechanics of head injuries and the state-of-the-art technology, we propose modified helmet designs that demonstrate a substantial weight reduction over existing designs and satisfy current standards for preventing head injuries. These designs tend toward a more optimal use of the dense outer shell material, typically ABS (Acrylonitrile Butadiene Styrene copolymer). In particular, one of these designs incorporates a unique, weight efficient composite layer of highly dense, reticulated, polyurethane combined with low-density polyurethane saturated with a highly viscous liquid. This

design has potential to improve multi-impact performance, which is of great importance since a single crash may involve multiple impacts. The other design examines a similar reduction in the thickness of the outer-shell layer and a corresponding increase in the thickness of the standard energy absorbing material already utilized in helmets. The primary advantage of these designs is the dramatic reduction in the weight of the helmets, which should encourage increased utilization of helmets; and therefore, reduce the number of motorcycle accident fatalities.

The focus of this chapter is on experimental methods for the design of a helmet with a layer of liquid-filled foam. Experimental results are presented comparing the performance of each design presented in this chapter to a comparable composite plate representing the state-of-the-art existing helmet design. Flat composite plates are loaded in a drop tower according to the existing standards for motorcycle helmets. The energy absorption characteristics of each design are found to be comparable, but the proposed designs presented in this analysis demonstrate substantial reductions in the overall weight. A discussion of the potential of these designs in motorcycle helmets, and in particular the liquid-filled foam design, is presented based on the experimental findings.

6.2 Literature Review

6.2.1 Head Injury Mechanisms and Standards

To develop an improved motorcycle helmet requires a comprehensive understanding of the head injury mechanisms and current safety standards. Severe head injuries can typically be classified into three categories: 1) skull

fracture; 2) focal brain injuries; 3) diffuse brain injuries (Voo et al., 1994). Skull fracture is typically not considered a primary concern for a helmeted head since brain damage caused by excessive acceleration is often found to occur at much lower loads than those required to cause skull fracture (Shuaeib et al., 2002a). Moreover, skull fracture which does not result in brain injury can be argued to be a natural energy absorption method. For a non-helmeted head, a conservative measure for depressed skull fracture in the temporal area is given by a localized pressure exceeding 4 MPa over an area of 5 cm^2 (2 kN localized force) (Hume, 1995). In order to achieve such a loading for a helmeted head, the impacting object would have to be sharp and rigid enough to penetrate entirely through the helmet. One of the strictest criterion for helmet standards requires the helmet prevents a conical steel indenter with a 90 J impact energy from penetrating to touch the head form (BS 6658, 1985). Since the frequency of such highly localized loads in real life accidents is extremely small, Hume et al. (1995) argued helmet testing standards should reflect more realistic loading scenarios. Instead of the use of conical anvils, Hume et al. (1995) proposed hemispherical or flat strikers as more representative of actual penetration loading scenarios.

However, the primary purpose of a helmet is not to prevent penetration of rigid objects but to prevent large accelerations of the brain, which can result in traumatic brain injury (TBI). The two main types of non-penetrating TBI are diffuse and focal brain injury. Diffuse brain injuries refer to bulk mechanical effects associated with axonal, neural, microvascular, and brain swelling injuries, typically affecting large volumes (Bandak, 1996). Focal brain injuries are typically localized regions of the brain subjected to large tensile or compressive stresses, often resulting in injuries such as subdural hematomas. Shuaeib et al. (2002a) provide an extensive review of the mechanisms for brain injury,

concluding that diffuse brain injuries are of primary concern in helmeted head impacts and reducing the acceleration of the brain during an impact is an extremely important parameter in helmet design. In particular, reducing the linear (translational) acceleration is important since Mills and Gilchrist (2006) concluded the rotational acceleration is typically insufficient to cause serious diffuse brain injuries.

Standards for brain injuries are much better established than those for skull fracture. Shuaeib et al. (2002a) provides an overview of the primary acceleration based standards for preventing brain injuries. For the purposes of this analysis, we only consider the most commonly used standard which is based on the Peak Linear Acceleration (PLA) criterion that only requires a single design parameter. Most international standards require the maximum acceleration of the head does not exceed 300g under a direct impact of a 5 kg mass traveling at 6 m/s to 7.5 m/s, resulting in impact energies ranging from 90 J to 140 J, respectively (Shuaeib, et al. 2007). Further consideration should be given to the applicability of this standard to motorcycle helmet design. While most helmets designed for other applications weigh less than 1 kg, motorcycle helmets often weight more than 1 kg, as shown by Gilchrist, A., et al (1996) who experimented with a motorcycle helmet weighing 1.33 kg. Considering the 50th percentile human head has a mass of 4.4 kg (Muzzy et al. 1986), a more accurate standard for motorcycle helmets would incorporate an impact mass between 5.5 kg and 6 kg.

6.3 Standard Design vs. Proposed Design

The current design of the state-of-the-art commercial helmets used today is relatively standard. The helmet design consists of three primary layers as shown in **Fig. 6.1**: 1) the shell, 2) the foam liner, and 3) the comfort foam. The shell of the helmet is primarily for penetration resistance of sharp, rigid objects as previously discussed. Often the shell is either injection molded ABS or rubber-toughened polycarbonate thermoplastic. While the shell also absorbs energy, the primary energy absorbing component of a helmet is the foam liner, which is usually made from polystyrene beads. To allow a helmet to comfortably fit a range of head sizes, a third layer of comfort foam, typically made of low-density, reticulated polyurethane, is included as the innermost layer in the helmet design.

Much of the focus on improving helmet design is on enhancing the energy absorbing, foam liner. Polystyrene is often selected as the foam liner because of its low density, economic molding process, and high impact energy absorption capability. However, recent research has examined other suitable materials to replace polystyrene (Shuaeib et al., 2007) since it has exhibits poor multi-impact performance, presents challenges in manufacturing associated with ventilation holes, and has limitations in fitting a range of head sizes. While improving the foam liner is important, an even more substantial improvement can be made by optimizing the use of the outer ABS shell. Recent research has suggested the outer ABS shell thickness could be reduced. Shuaeib et al. (2007) proposed if the ABS shell thickness was reduced to 3mm from the typical 5 mm, it would still provide sufficient penetration resistance for existing standards. Shuaeib et al. (2002b) also indicates in existing helmet designs the shell absorbs very little of the total impacting energy. In the standard helmet design if the thickness of the

outer shell was reduced, the thickness of the inner polystyrene layer would have to be increased slightly or another layer of energy absorbing material would have to be added in order to maintain similar energy absorption characteristics. Maintaining similar energy absorption characteristics, which are characterized by the maximum load sustained under the standard testing procedure previously defined, is essential in minimizing the acceleration of the brain under impact loading, and therefore, minimizing potential brain damage. Further reductions in the outer ABS shell thickness could also be considered with the development of more accurate testing standards. As previously mentioned, many experts in the field suggest changing existing standards to more accurately represent expected loading scenarios by replacing the conical anvil indenter with a hemispherical anvil or a flat anvil (Hume et al., 1995; Shuaeib et al., 2002b). This change in existing testing standards could result in a dramatic reduction of the outer shell thickness required to prevent penetration of the helmet. Provided a thin, light-weight layer could be added to compensate for the energy absorbing capacity of the displaced ABS, this change in testing standards would allow for an even more dramatic reduction in the thickness of the ABS shell, and thus, in the overall weight of the helmet.

In this chapter, we discuss two proposed, more weight efficient, modifications to the standard design. The first design (D_1) reduces the thickness of the ABS shell and replaces it with the same thickness of polystyrene. The primary advantage of this design is a substantial weight reduction. However, the polystyrene layer absorbs more energy through plastic deformation than the ABS shell, so it is less efficient in multi-impact scenarios compared to the standard design (S_1). The second design (D_2) is slightly less cumbersome than the standard design and demonstrates improved multi-impact performance. This design replaces a

portion of the outer ABS shell with a lighter-weight composite layer that is more resilient under repeated loading. The additional composite layer consists of a combination of low-density, reticulated polyurethane foam impregnated with a high viscosity fluid and high-density, reticulated polyurethane foam as shown in **Fig. 6.2.** The fluid is contained in the foam by the capillary effect. The design given in **Fig. 6.2** was determined empirically by a trial and error approach, using combinations of parameters, including the diameter and thickness of the fluid-filled foam as well as the volume fraction of the fluid in the foam and the material constituents of the polyurethane based materials. The ideal ratio of the cross-sectional area of the high-density foam to that of the low-density foam (area ratio) found in this analysis is approximately 4:1. It is important to note that this ratio was found empirically and could be further refined to improve the overall performance. In addition, the ratio was selected to reduce the weight while maintaining similar energy absorption characteristics to that of the equivalent standard design S_1. Other parameters on which this design could be optimized will be discussed later. The inherent advantage of a composite layer of polyurethane foam is the increased resilience and therefore enhanced multi-impact performance, especially for successive low-energy impacts, which are characteristic of actual loading scenarios experienced in an accident. Furthermore, the highly efficient energy absorption capabilities of high viscosity fluid flow through porous media described in *Chapters 3* and *4* allow for this design to maintain similar energy absorption characteristics as the standard design at equivalent thickness and at a reduced weight.

6.4 Experiments

6.4.1 Materials

The outer shell material was comprised of ABS (Farnell, Leeds, U.K.) with a density of 1.08 g/cm^3, which acts as the primary penetration-resistant layer on the outside of the helmet (**Fig. 6.1**). The primary energy absorption layer was high-density polystyrene (Cordek, West Sussex, U.K.) with density 0.055 g/cm^3. Two types of open-cell, flexible, polyester-based polyurethane (PU) foams were used for the energy absorption layer in design D_2 presented in this chapter. The first was a high-density, reticulated polyurethane (McMaster Carr Supply Co., Atlanta, GA) with density 0.32 g/cm^3. The second was a low-density, 90 pore per inch (ppi), reticulated polyurethane foam (New Dimension Industries, Moonachie, NJ) with density 0.032 g/cm^3. The high viscosity Newtonian fluid used to impregnate the low-density polyurethane was glycerol of density and viscosity measured to be 1260 kg/m^3 and 1.1 Pa-s, respectively at 23 °C. The third layer of comfort foam was omitted from experiments since its energy absorption capacity is negligible compared to the other layers.

6.4.2 Experimental Procedure

Experiments were performed to simulate the weight efficiency improvement of the designs presented in this analysis over the standard motorcycle helmet design utilized commercially. Every sample was made of square cross sections of 100 mm x 100 mm, which is assumed to accurately approximate the cross-sectional area of the helmet used to absorb most of the impact energy under standard testing conditions (after Gilchrist and Mills, 1994). While the curvature in actual helmets increases the loading resistance and energy absorption

capabilities, for the purpose of demonstrating the weight efficiency improvement, flat plates are used in these experiments. As previously discussed, the standard design (S_1) consists primarily of two energy absorbing layers: a layer of ABS and a layer of polystyrene (**Fig. 6.1**). The first proposed design (D_1) presented in this chapter, consists of the same materials as the standard design but modifies the thickness of both the ABS shell and the polystyrene foam. The second proposed design (D_2), incorporating an additional composite PU/PU-glycerol layer into the standard design, is shown in **Fig. 6.2**. A cross-sectional view of the PU/PU-glycerol composite layer is shown in **Fig. 6.2b**. All of these designs are compared in Table 6.1, which gives the thickness and weights of each design. All of the designs are of equivalent overall thickness, determined from the standard design (S_1) which is consistent throughout most studies (Gilchrist and Mills, 1996; Shuaeib et al., 2002b). The outer ABS layer for the proposed designs is 2mm thinner than the standard design, based on the previous discussion and, the thickness of the inner energy absorbing layers are adjusted correspondingly. The specimens were prepared by bonding the corresponding layers together using a lightweight, high-strength adhesive (Gorilla Glue, McMaster Carr Supply Co., Atlanta, GA), which added negligible mass to the design. Design D_2 required saturation of the low-density polyurethane foam with glycerol. The low-density foam was filled by repeated compression while submerged in a bath of glycerol, utilizing the capillary effect. These fluid-filled polyurethane foams were then press-fit into the high-density polyurethane foam. Each layer was again bonded by a lightweight, high-strength adhesive, which added negligible mass.

After allowing the samples to completely cure for 8 hours, the samples were loaded in a Dynatup drop-tower (Dynatup 9200 Series, Instron Corp., Canton, MA). The drop tower mass was 7.15 kg, and the impact velocity was set to 6 m/s. The overall impact energy was approximately 129 J, in accordance with most international standards for head protection. A flat, cylindrical striker with a 4 cm diameter was used to impact the center of the 10 cm x 10 cm samples following the research of Gilchrist and Mills (1996). The compressive load-displacement response of each sample under impact was measured. The impacted sample was then retested under the same loading conditions to determine its resistance to repeated loading. The strain under the second impact test was based on the height of the specimen after the first loading.

The optimal performing design D_2, which is given in Table 6.1 was selected based on a parametric study. In the parametric study a number of parameters of the PU/PU-glycerol layer were adjusted including the vertical placement of the composite layer, the thickness of the layer, and the ratio of the cross-sectional area of the high-density PU (HDPU) layer to the low-density PU (LDPU) layer, which from here on is referred to as the area ratio. The performance of the overall design was found to be substantially reduced when the composite PU/PU-glycerol layer was not directly in contact with the ABS layer, so the results of these experiments are not included in this study. In addition, the studies including variations in thickness are also neglected in this chapter since increasing the thickness of the PU/PU-glycerol layer only resulted in a decreased performance. Therefore, the thinnest layer composite commercially obtainable was utilized (3 mm). The primary parameter adjusted in this parametric study was the area ratio. The parametric study sought to minimize the weight of the design while providing superior impact performance for both single and

successive loading scenarios. Experiments were performed using samples with area ratios ranging from approximately 1:1 to 9:1 (i.e. 50 cm^2 : 50 cm^2; 66 cm^2 : 33 cm^2; 75 cm^2 : 25 cm^2; 80 cm^2 : 20 cm^2; 83 cm^2 : 17 cm^2; 86 cm^2 : 14 cm^2; 88 cm^2 : 12 cm^2; 89 cm^2 : 11 cm^2; 90 cm^2 : 10 cm^2). All of the configurations were developed to have a uniform, repeatable pattern, such that the loading response would be as consistent as possible, independent of the impact site with respect to the two layers comprising the composite PU/PU-glycerol foam.

6.4.3 Experimental Results

As previously discussed, to determine the optimal configuration for design D_2 a parametric study was performed varying the area ratio of the design from 1:1 to 9:1. **Fig. 6.4** plots the maximum load sustained for each configuration under the given testing conditions previously specified for the first impact of each sample against the weight of that specimen normalized by the standard weight of sample S_1. The optimal area ratio was selected to be that which minimized the weight while maintaining similar energy absorption characteristics to that of the standard design S_1. The energy absorption characteristic of the standard design is represented by the maximum load under the specified testing conditions given by the horizontal line (~10 kN) in **Fig. 6.4**. Based on this criterion, the optimal area ratio is approximately 4:1, which is given as the circled point. In **Fig. 6.4** as the area ratio is reduced toward 1:1, the maximum load is reduced but the weight of the sample increases dramatically because the heavier fluid-filled layer comprises more of the composite layer. Similarly, as the area ratio is increased, the overall weight of the composite is decreased, but the load bearing capability of the layer, and thus, that of the overall design, also decreases dramatically. Therefore the configuration for the optimized design D_2 was based on an ideal

area ratio of 4:1. We selected this optimization method since the current design satisfies existing standards and our primary objective is to minimize the weight and improve the multi-impact performance; however, other methods for optimizing this design could also be selected. One such method is to find the point on a unit normalized scale at which the tangent line to the area ratio curve is at 45° to the axes, which would represent an optimization based on minimizing the weight and the energy absorption, simultaneously.

A typical plot of the load-strain response for all three designs given in Table 6.1 is given in **Fig. 6.5.** All designs satisfy the international standards for maximum acceleration of 300g, which can be translated into a maximum force of 15 kN for a 5 kg helmeted head. The energy absorption characteristics of all three designs on the first impact are approximately the same, giving maximum loads within 20% of one another under the standard helmet testing conditions. However, at an equivalent thickness, designs D_1 and the optimized design D_2 demonstrate significant weight savings over the standard design S_1 of approximately 30% and 11%, respectively. **Fig. 6.6** plots the maximum load sustained normalized by the maximum allowable load (15kN) under the given testing conditions previously specified for the first impact of each sample against the weight of that specimen normalized by the standard weight of sample S_1. Each data point represents the average of 3 repeated experiments and the corresponding error bars signify one standard deviation. Ideally, a superior performance would minimize both the weight and the maximum load under a given loading scenario as indicated by the arrows in **Fig. 6.6.** To determine the optimal design a theoretical optimal design point must be established. The optimal design point shown on **Fig. 6.6** is determined by assuming an idealized minimal weight material (0.10 g/cm^3) could absorb the specified amount of energy under a constant load over a

deformation of 0.90 strain. Using the required energy absorbed under impact and assumed deformation, the ideal maximum load is determined to be 4.81 kg. Based on this plot it is clear the best overall performance is achieved by design D_1; however, the optimized design D_2 also shows substantial improvement over the standard design.

To determine the performance under repeated loads, which are expected to occur in real accidents, all of the samples were retested again under the same loading conditions. **Fig. 6.7** plots the normalized maximum load sustained under the standard testing conditions for the second impact of each sample against the weight of that specimen normalized by the standard weight of sample S_1. This plot clearly shows the optimized design D_2 has superior multi-impact performance characteristics when compared to either of the other two designs.

6.5 Discussion

It is clear there is a need to reduce the weight of existing helmets, particularly motorcycle helmets, without sacrificing performance. The primary performance metric which must be considered in the design of an improved helmet is the ability of a helmet to prevent diffuse brain damage due to excessive acceleration. In this chapter, we follow the proposal by Shuaeib (2002b) that the thickness of the outer ABS shell of a helmet can be reduced while maintaining acceptable performance levels and penetration resistance. Moreover, there is strong evidence to support changing existing testing standards to more accurately represent actual loading scenarios, which would allow for an even greater reduction in the thickness of the ABS shell. In this analysis we found replacing

this displaced layer with a light-weight energy absorbing layer of equal thickness results in a significant reduction in the overall weight of the helmet and a reduction in the maximum load sustained during impact loading.

Design D_1 clearly demonstrates the best overall performance of the three designs in this analysis under initial loading, tending toward the theoretical optimal design achievable in **Fig. 6.6**. The primary advantage of this design is its substantial decrease in weight over the standard design of approximately 30%. While the experimental composite plates in this analysis do not exactly represent the actual performance of a comparable helmet under the same loading conditions, similar improvements in the weight efficiencies of helmets using the designs presented in this analysis are expected. The implications of this design are that significant weight savings may be achievable in a variety of helmet designs if the thickness of the outer shell of helmets is optimally designed for the required penetration resistance. One of the most prominent applications can be clearly be seen in motorcycle helmets where the reduction of the overall bulk (of up to 30%) could lead to a dramatic increase in the utilization of helmets. Furthermore, implementing this design change could be readily done because little change is needed to the existing manufacturing process. Therefore, a substantial increase in the overall cost of this design is not expected and market penetration could occur quickly.

While design D_1 demonstrates the greatest overall performance under initial impact, the optimized design D_2 has the capacity to substantially enhance the multi-impact performance of the helmet. This is an important feature since real accidents typically involve multiple, successive impacts. To the author's knowledge it would be very difficult to determine if brain damage resulted from

the initial impact or successive impacts in a real accident scenario. Therefore, we believe increased multi-impact performance coupled with a lighter-weight helmet has great potential to reduce the overall number of brain injuries from motorcycle accidents. Furthermore, a computational study, which parametrically established the optimal design parameters for the optimized design D_2 could result in even better performance and greater weight savings. However, the increased manufacturing difficulty of this design may prohibit its practical application. While the cost of materials is extremely low, the manufacturing process becomes slightly more complex, which could increase the cost of manufacturing this design significantly.

6.6 Conclusion

A review of the current state-of-the-art motorcycle helmet design along with existing safety standards is given. A discussion is presented on improving the weight efficiency and material utilization in existing motorcycle helmets. Based on the efficiency improvements, two new motorcycle helmet designs are proposed. The first design, which utilizes existing technology, exhibits the most substantial weight improvement over the standard design, but sacrifices multi-impact performance. The second design, utilizing a liquid-filled foam composite, demonstrated a slight weight improvement over the standard design while maintaining comparable first impact energy absorption characteristics; however, the liquid-filled foam composite exhibited exceptional performance upon repeated loading, which the other designs did not. This improvement is due to the recoverable nature of the composite comprised of elastic, open-cell polyurethane foams. The composite layer, which couples a fluid-filled, low-

density polyurethane foam with a high-density polyurethane foam, is found to reduce the overall weight of a helmet by ~10%. While both of the proposed designs in this analysis are more weight efficient than the standard design, the optimized liquid-filled composite design exhibits enhanced multi-impact protection, which may be useful in preventing injuries in motorcycle accidents. This enhanced multi-impact protection alone is a major advancement in motorcycle helmet design. Furthermore, the potential for weight reduction may lead to a substantial increase in the utilization of helmets by motorcyclists, preventing countless injuries and fatalities.

References

Bandak, F.A., (1996), "Biomechanics of Impact Traumatic Brain Injury", Crashworthiness of Transportation Systems Struc. Impact and Occ. Proc., Ambrosio, J., Periera, F., Pina de Silva, F., (Eds.), Kluwer Academic Publishers ,pp. 53-93.

BS 6658, (1985), "Protective Helmets for Vehicle Users", *British Standards Institution*, London.

Gilchrist, A. and Mills, N.J., (1994), "Modelling of the Impact Response of Motorcycle Helmets", *Int. J. Impact Eng.*, **15**, pp. 201-218.

Gilchrist, A. and Mills, N.J., (1996), "Protection of the side of the head", *Accident Anal. And Prev.*, **28**, pp. 525-535.

Hume, A., Mills, N.J., and Gilchrist, A., (1995), "Industrial head injuries and the performance of the helmets", *Proc. Int. IRCOBI Conf. Biomech. Impact, Switzerland.*

Mills N.J. and Gilchrist, A., (2006), "Bicycle Helmet Design", *Proc. IMechE.*, **220**, pp. 167-180.

Muzzy, W., Seemann, M., Willems, G., Lustic, L., Bittner, A., (1986), "The effect of mass distribution parameters on head/neck dynamic response", *SAE Trans.*, **86**, pp. 716-727.

Shuaeib, F., Hamouda, A., Radin Umara, R., Hamdan, R., Hashmi, M., (2002a), "Motorcycle Helmet Part I. Biomechanics and Computational Issues", *J. Mat. Process. Tech.*, **123**, pp. 405-421.

Shuaeib, F., Hamouda, A., Hamdan, R., Radin Umara, R., Hashmi, M., (2002b), "Motorcycle Helmet Part II. Materials and Design Issues," *J. Mat. Process. Tech.*, **123**, pp. 422-431.

Shuaeib, F., Hamouda, A., Wonga, S., Radin Umara, R., Ahmeda, M., (2007), "A new motorcycle helmet liner material: The finite element simulation and design of experiment optimization", Mat. and Design, 28, pp. 182-195.

Voo, L. et al., (1994), "Biomechanical Analysis of Tractor-Induced Head Injury", *SAE* Transaction Paper No 941725, pp. 178-183.

Tables

Table 6.1: Design specifications for a standard helmet design (S_1) and proposed helmet design (D_1 and D_2). (100 mm x 100 mm)

	Material	Thickness (mm)	Weight (g)
S_1	ABS	5	54.0
	Polystyrene	25	13.8
	Total	**30**	**67.8**
D_1	ABS	3	32.4
	Polystyrene	27	14.9
	Total	**30**	**47.3**
D_2	ABS	3	32.4
	Polystyrene	24	13.2
	PU/PU-Glycerol	3	14.8
	Total	**30**	**60.4**

Figures

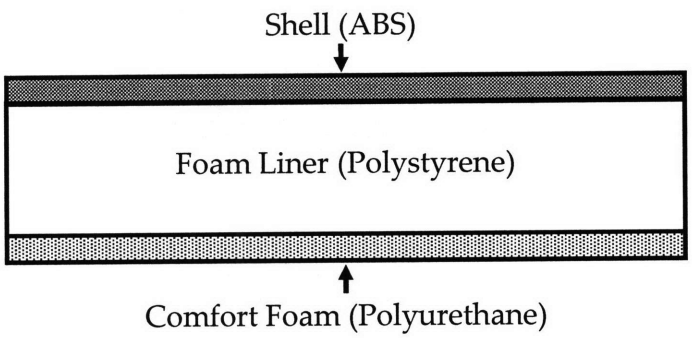

Figure 6.1. Model of standard helmet design (S_1).

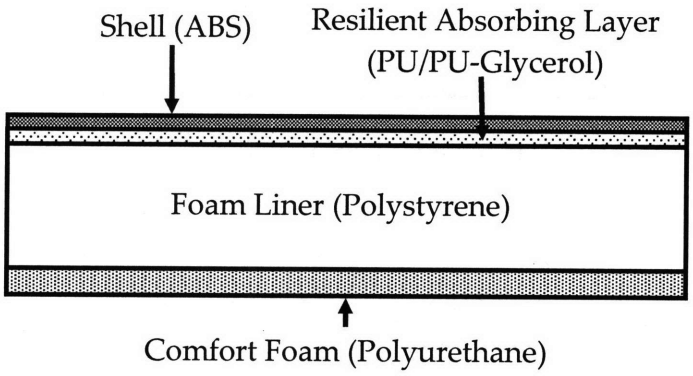

Figure 6.2a. Model of proposed helmet design (D_2).

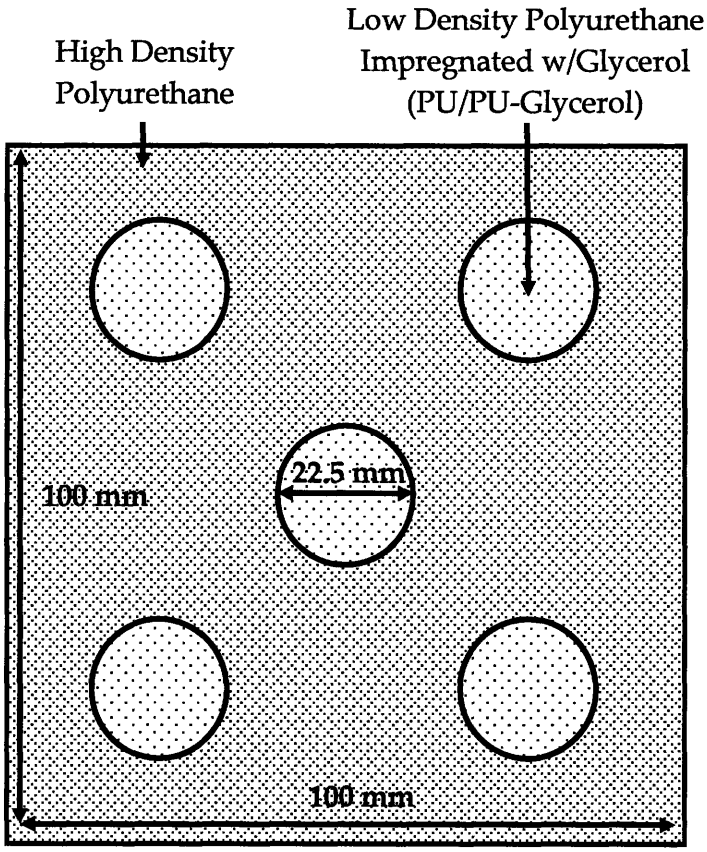

Figure 6.2b. Model of cross-section of proposed helmet design (D_2). Optimal configuration based on parametric study (area ratio ~4:1).

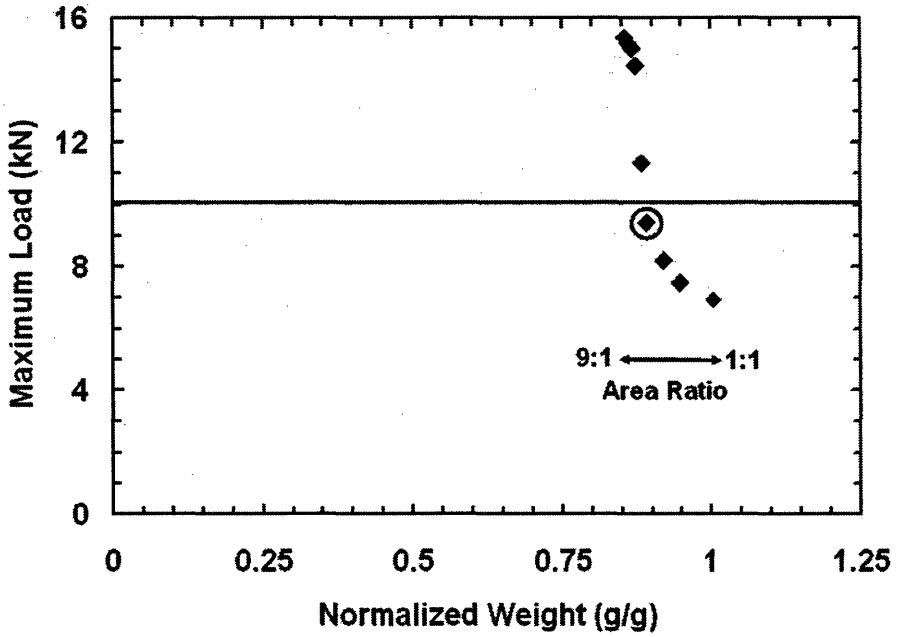

Figure 6.3 Maximum load plotted against the sample weight normalized by the weight of the standards sample S_1. All experiments are for Design D_2 with varying area ratios ranging from 1:1 to 9:1 in increments of approximately 1. The maximum load for the standard design is given by the horizontal line.

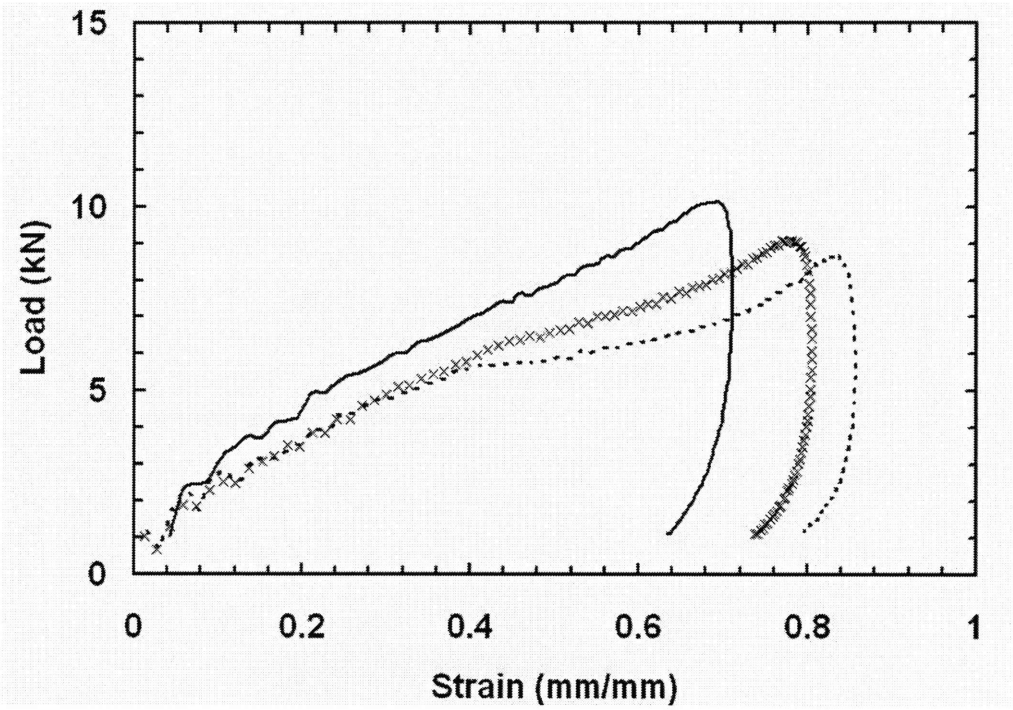

Figure 6.4. Load plotted against strain for the three helmet designs. Standard (S_1) (——); Design 1 (D_1) (·····) and Design 2 (D_2) (xxxx).

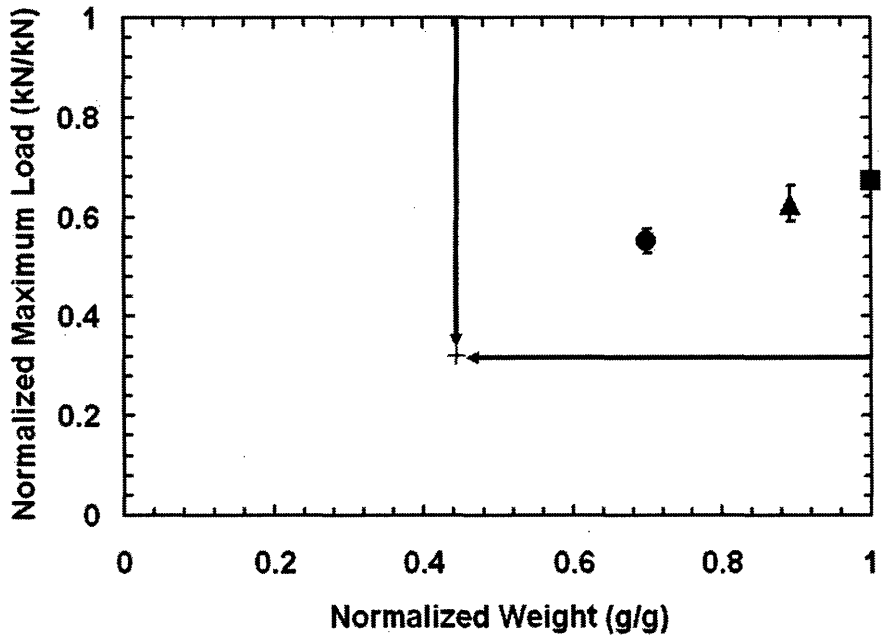

Figure 6.5. Maximum load normalized by the maximum design load plotted against the sample weight normalized by the weight of the standards sample S_1. Standard (S_1) (■); Design 1 (D_1) (●) ; Design 2 (D_2) (▲); Optimal Design (+).

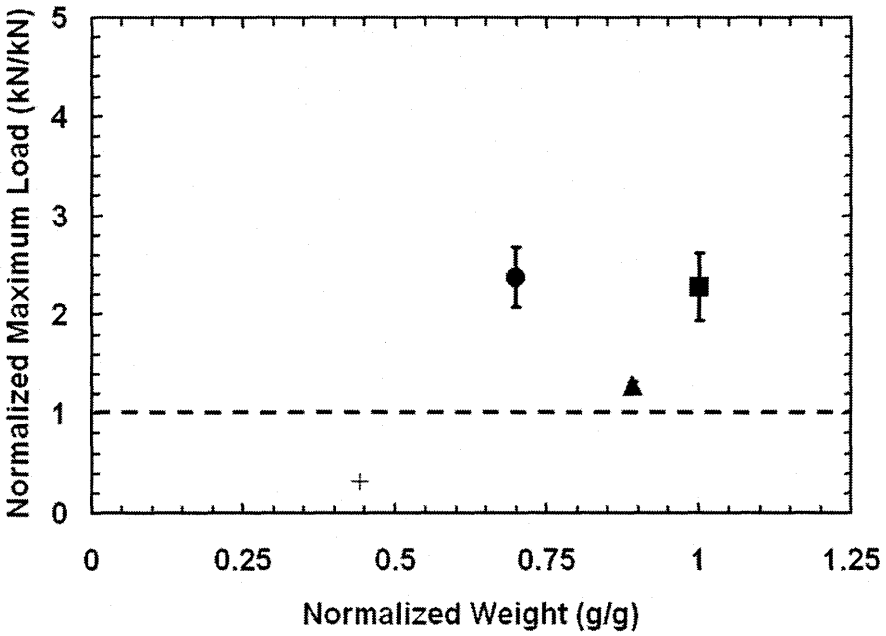

Figure 6.6. Maximum load normalized by the maximum design load plotted against the sample weight normalized by the weight of the standards sample S_1. Standard (S_1) (■); Design 1 (D_1) (●) ; Design 2 (D_2) (▲); Optimal Design (+); Maximum design load (– – – ·).

7 Applications Liquid-Impregnated Open-Cell Foam in Blast Protection of Infrastructure

7.1 Introduction

For the past four centuries terrorist plots to bomb critical infrastructure have plagued society. Today, it has become one of the most prominent forms of terrorism worldwide. The novel liquid-impregnated, open-cell foam discussed throughout this thesis may have potential to protect against such terrorist attacks. Specifically, in this chapter, we examine a new composite blast-resistant technology for the protection of critical infrastructure from a potential explosive attack. This new technology has the potential to substantially reduce the maximum load imparted to a building by an explosive device compared to that imparted to a building without any modifications while being simple, inexpensive, lightweight, and robust.

To assess the performance of a blast plate, which incorporates a layer of liquid-impregnated foam, requires a comprehensive understanding of blast wave loading of structures. A brief review of blast waves and their interaction with structures is presented along with a review of the current explosives threat to critical infrastructure and the current state-of-the-art technology to protect against such a threat. Based on the expected dynamic loading of a structure from an explosive device and the previously developed models given in *Chapter 4* and *Chapter 5*, a highly efficient infrastructure protection technology can be developed, consisting of a steel face plate backed by a layer of low-density, reticulated, flexible, fluid-filled foam. Coupling relations for momentum conservation and the dynamic response of fluid-filled foam, a numerical scheme

is developed to analyze the performance of the design. This numerical code is utilized in a parametric study to identify designs that minimize the peak stress on the underlying structure as well as the weight of the design. The parameters included in this study are the thicknesses of each composite layer, the ratio of the thickness of each layer to one another, the properties of the fluid in the fluid-filled core, the aspect ratio (ratio of the radius of the foam core to the thickness of the foam core), and the number of composite layers. Through this parametric study, the effects of various design parameters on the effectiveness of a fluid-filled, blast-resistant plate can be readily determined. Moreover, this study identifies a range of parameters for which the proposed blast-resistant plate demonstrates substantial reductions in the peak load transmitted to a structure under a prescribed blast loading. Based on this study, it is evident that a fluid-filled blast-resistant plate, configured according to the optimization trends, could readily defend infrastructure against a standard terrorist attack. Using the parametric study, an optimal configuration is presented, which demonstrates the potential to reduce the peak stress on an underlying structure by as much as 90% over a monolithic plate. Furthermore, this optimal configuration also shows promise to outperform existing state-of-the-art blast protection devices with a greater reduction in the peak stress at a given thickness.

7.2 Literature Review

7.2.1 State-of-the-Art Blast Protection Technologies

While blast protection technologies have existed for decades, recently, research on advanced materials and structures for blast protection has drawn tremendous interest. One of the most promising structural improvements for blast protection

has proven to be the development of composite plates with a low-density, porous, metal core also termed 'sandwich panels'. The three primary authors spearheading this area of research have been J.W. Hutchison, V.S. Desphande and N.A. Fleck. They have conducted numerous analytical and computational studies on the expected performance of various types of sandwich panels under a range of shock loads (Xue and Hutchinson (2003); Fleck and Deshpande (2004); Xue and Hutchinson (2004); Qiu, Deshpande, and Fleck (2005); Hutchinson and Xue (2005); Radford, Fleck, and Deshpande (2006)). The advantage of this type of composite structure under blast loading was first recognized by Taylor (1963) and explained in detail by Kambouchev, Noels, and Radovitzky (2006). The fundamental concept is that the motion of the structure due to the deformation of core relieves the pressure acting on it, reducing the transmitted impulse. Due to this phenomenon, optimized sandwich plates have demonstrated the ability to outperform monolithic plates of comparable weight under impulsive loads by incompressible fluids (Fleck and Deshpande (2004) and Xue and Hutchinson (2004)). A more detailed discussion of the findings of Fleck, Deshpande, and their coworkers is presented in this analysis. While Taylor's analysis primarily held for the case of a fluid of negligible compressibility impinging on a plate, Kambouchev, Noels, and Radovitzky (2005) found that the effect of nonlinear compressibility further enhanced the mitigation of transmitted impulse provided by the fluid-structure-interaction. This finding suggests that blast mitigation strategies utilizing sandwich panel construction may be even more beneficial in the case of blasts where the impinging fluid is a highly compressible fluid, such as air.

While the models developed by Hutchinson and coworkers as well as Fleck, Deshpande, and their coworkers demonstrated that sandwich panels have enormous potential to protect against impulsive-pressure loading, all of these models utilized the assumption that the time scales of the fluid-structure-interaction stage and the core-compression stage were substantially different. This assumption allowed these authors to separate the analysis of the two stages to limit the computational complexity. In this analysis, we do not make that assumption so that the duration of the fluid-structure-interaction stage and the core-compression stage are not considered disparate enough to separate as in the case of an air blast. Furthermore, previous research has resulted in the development of analytical and computational models applicable to composite structures with porous metallic cores where the pores are filled with a fluid with negligible viscosity, such as air. None of these models has attempted to describe the dynamic response of a composite plate loaded by a blast loading where at least one of the composite layers is flexible, reticulated foam filled with a high viscosity, incompressible fluid. In this analysis, the performance of such a fluid-filled blast protection device is examined. It is also compared to that of an equivalent, state-of-the-art design, which is based on current technology and the models presented by Fleck, Deshpande, and their coworkers.

7.2.2 Blast Loading Assumptions

The greatest explosive threat to critical infrastructure is typically delivered in the form of a vehicle bomb. Excellent reviews of terrorist attacks on infrastructure are given by Elliot et al. (1992) and Ngo et al. (2007). Elliot et al. (1992) provides a detailed discussion of possible attack mechanisms. Moreover, they propose critical infrastructure should be designed for a maximum size vehicle bomb of

230 kg (500 lb) of TNT equivalent explosive. While size or weight W, of an explosive is an important consideration, it is not the only consideration. Possibly of greater importance is the distance between the explosive and the target, D. A generally accepted practice is to measure the effectiveness of an explosive by the scaled blast distance parameter, Z, which is given as

$$Z = \frac{D}{W^{1/3}} \tag{7.1}$$

where W is the equivalent weight of the explosive in kg of TNT and D is the distance between the explosive and the target in meters.

Improvised explosive devices (IED's) can come in many forms and be comprised of many materials, but the primary threat today is in the form of solid-state, secondary, high explosives, which when detonated generate a blast (shock) wave (Ngo et al., 2007). Common examples of this form of explosive are trinitrotoluene (TNT) and ammonium nitrate-fuel oil (ANFO). These explosives are known to generate widespread damage to the surroundings and have been studied extensively. The resulting blast waves from these explosives have been classified into three categories: free-air blasts, air blasts, and surface blasts (Remennikov, 2003). The latter two types of blasts consider coupling of reflected pressure waves off the surroundings with the incident pressure wave, resulting in an amplified reflected pressure wave impacting the structure. However, most studies neglect these secondary effects and only consider free-air blasts since the surroundings are often difficult to incorporate into an analysis. Furthermore, analyses often focus on the case of free-air blasts since standard charts have been well established for this case (U.S. Army, 1986). In the free-air blast loading

scenario, reflection is also very important. Taylor (1963) found that the perfect reflection of an incoming wave by an infinitely rigid structure would result in an imparted momentum to that object that is nearly twice that of the incoming wave. However, Taylor's work is not applicable to strong air shocks where the compressibility of the air adds to the momentum imparted to the structure. In this case, reflection factors may enhance the incident pressure waves by as much as an order of magnitude. In fact, Elliot et al. (1992) gives the reflected pressure wave ranging from two to thirteen times the incident pressure wave in the worst case scenario where the wave interacts with the structure at a zero angle of incidence.

In this analysis, the design of a blast plate subjected to the worst case reflected pressure generated by a vehicle bomb filled with 233 kg of high explosive at a distance of 2 m from the blast plate is examined. The effective power of this explosive corresponds to a scaled blast parameter of $Z = 0.325$ m/kg$^{1/3}$. Based on the TM5-855-1 chart given in the **Fig. 7.1**,which was developed by the U.S. Army (1986) and converted to S.I. units by Elliot et al. (1992), the initial maximum reflected over pressure on the plate is taken to be approximately $P_{ro} = 100$ MPa. Since this analysis only considers air blasts, the contribution of the dynamic pressure component is negligible (~0.07 MPa, based on 1.2 kg/m^3 air traveling at the speed of sound) in comparison to the reflected static pressure component. In addition, the effects of diffusion of the pressure wave around the structure and drag on the structure are neglected (Elliot, 1992). The pressure exerted on the structure by the blast wave P, is known to decay over time t, and is given by (Fleck and Deshpande, 2004)

$$P(t) = P_{ro} e^{-t/\tau} \tag{7.2}$$

where τ is the time constant of the pressure decay, which both Fleck and Deshpande (2004) and Xue and Hutchinson (2004) assumed to be on the order of 0.1 ms. This assumption is consistent with the results presented by Hetherington and Smith (1994), who developed charts for the time constant as a function of the characteristic blast distance parameter. For characteristic blast parameters less than unity ($m/kg^{1/3}$), corresponding to relatively large blasts, Hetherington and Smith (1994) demonstrated the duration of the positive pressure phase of a blast is on the order of 1 ms. This indicates the duration of the time constant for the blast pressure decay is on the order of 0.1 ms. Therefore, in this analysis the time constant for the pressure decay is assumed to be 0.1 ms. The response of the blast wall also has a characteristic time constant associated with it, which is dependent upon the properties of the structure. In the analysis of Fleck and Deshpande (2004), the characteristic time for the core compression stage is on the order of 0.4 ms. While Fleck and Deshpande (2004) consider the time constants to be distinct enough to separate the analyses for the blast loading phase and the core compression phase, reducing the computational complexity, in this analysis we do not make that assumption. Instead, the time scale for the blast-wave-structure-interaction and the response of the structure are taken to be of the same order of magnitude and the response is analyzed accordingly.

7.3 Analysis

7.3.1 Proposed Blast Protection Designs

This analysis considers a blast protection technology designed to be attached to the exterior of a building. This technology is necessary in the case where critical infrastructure does not have the adequate stand-off distance from a potential explosive device. Two types of new cylindrical blast shield designs are proposed as shown in **Figs. 7.2** and **Fig. 7.3**. The first design, referred to as the single-core design, consists of an outer steel face plate and an inner, fluid-filled foam core, which is attached flush against the structure **(Fig. 7.2)**. In **Figs. 7.2** and **Fig. 7.3** the numerical subscript $_1$, corresponds to the layer and the index subscript $_i$, corresponds to the single-core design. The outer face plate has thickness h_{1i} and density ρ_{1i}. The inner fluid-filled foam core has thickness $h_{2i}(t)$, which is a function of time as the core undergoes compression. The second design, referred to as the dual-core design, consists of two alternating layers of face plates and fluid-filled foam cores with the outermost layer being a face plate layer and the innermost layer, adjoined to the structure, being a fluid-filled foam core as shown in **Fig. 7.3**. Again each layer has a specified thickness, with the solid face plates having thicknesses h_{1ii} and h_{3ii} and the fluid-filled cores having thicknesses $h_{2ii}(t)$ and $h_{4ii}(t)$.

Each design is assumed to be loaded by a uniform pressure load (given by Eq. (7.2)) on the outermost face plate. The steel face plates and the underlying structure are considered infinitely rigid compared to the fluid-filled foam. Therefore, there is no deformation in either the face plates or the structure itself during the dynamic compression of the core. The dynamic compression of the

core is assumed to be similar to that given in *Chapter 4*. Under extremely high strain rates, such as those experienced in a large blast load, the expected stress response of the Newtonian fluid-filled foam given in *Chapter 4*, based on the permeability of the foam, exceeds that presented by the experiments for a non-Newtonian fluid-filled foam given in *Chapter 5*. Therefore, based on the discussion given in *Chapter 5*, the fluid-structure interaction can be neglected for high stresses, such as expected under blast loading, since the structure of the foam is readily destroyed by the stress in the fluid. Thus, for blast loading, the fluid-structure-interaction is neglected for both the Newtonian and non-Newtonian fluid-filled foam under blast loading. The model developed in *Chapter 5* for the non-Newtonian fluid-filled foam is given for a power-law fluid where the viscosity of the fluid η, can be described in various regimes by

$$\eta = m\left(\dot{\gamma}\right)^{n-1}. \tag{7.3}$$

As given in *Chapter 5*, the average stress applied over the core filled with a non-Newtonian fluid (NNF) can be modeled as

$$\sigma_f = 2\left(\frac{2n+1}{n}\right)^n \frac{m}{n+3}\left(\frac{R}{h}\right)^{n+1}\left(\frac{-\dot{h}}{h}\right)^n. \tag{7.4a}$$

The equivalent Newtonian-fluid-filled foam model can be derived from the fact that the power law exponent n, is equal to unity for a Newtonian fluid and the power law coefficient m, is equal to the dynamic viscosity μ. Therefore the average stress applied over the core for a Newtonian fluid-filled foam is given as

$$\sigma_f = \frac{3}{2}\mu\left(\frac{R}{h}\right)^2\left(\frac{-\dot{h}}{h}\right). \tag{7.4b}$$

7.3.2 Global Conservation Equations

Utilizing both the external pressure loading as a function of time (Eq. 7.2) and the internal dynamic response of the fluid-filled foam (Eq. 7.4), a global conservation of momentum can be taken around each solid plate in the system. The dynamic response of each blast wall and the resulting loading on the underlying structure can then be determined. Conservation of momentum M_i in the differential form can be written around each plate for both designs as follows:

Single-Core Design

$$\frac{dM_i}{dt} = \rho_{1i} h_{1i} \frac{dV_{1i}}{dt} = P - \sigma_{f\_2i} \qquad \text{(Plate 1i)} \tag{7.5}$$

where V_{1i} is the velocity of the outer plate and σ_{f_2i} corresponds to the average stress distribution in the foam layer. Again, the numerical subscripts correspond to the layer and the index subscripts correspond to the single-core design (i) vs. the dual-core design (ii). The corresponding rate of change of the height of the foam layer $\dot{h}_{2i}$ is given by

$$\dot{h}_{2i} = -V_{1i} \tag{7.6}$$

Dual-Core Design

$$\frac{dM_{ii}}{dt} = \rho_{1ii} h_{1ii} \frac{dV_{1ii}}{dt} = P - \sigma_{f\_2ii} \qquad \text{(Plate 1ii)} \quad (7.7)$$

$$\frac{dM_{ii}}{dt} = \rho_{3ii} h_{3ii} \frac{dV_{3ii}}{dt} = \sigma_{f\_2ii} - \sigma_{f\_4ii}. \qquad \text{(Plate 3ii)} \quad (7.8)$$

The corresponding rate of change of the heights of the foam layers $\dot{h}_{2ii}$ and $\dot{h}_{4ii}$ are given by

$$\dot{h}_{2ii} = V_{3ii} - V_{1ii} \qquad (7.9)$$

$$\dot{h}_{4ii} = -V_{3ii}. \qquad (7.10)$$

For each design a system of first order, ordinary differential equations is given. The initial conditions are given as all layers are in static equilibrium with zero velocity prior to the blast wave impinging on the outermost plate. As previously discussed, the duration for the response of the blast wall is on the same order of magnitude as the time constant for the decay of the applied pressure from the blast loading; therefore, the final state of the system is assumed to be approximated by the solution at ten time constants (1.0 ms). Both designs are also subject to a constraint that the maximum allowable compressive strain of a core layer is 0.90. If this strain is exceeded prior to the desired final state, the design is rejected.

7.3.3 Material Properties

Solving the system of equations for conservation of momentum also requires knowledge of the material properties in each design. Each design consists of at

least one layer of steel with density of 7.80 g/cm^3 and at least one layer of fluid-filled foam. The fluid-filled foam is assumed to be 80 ppi, open-cell, flexible, low-density, polyurethane foam with density of 0.032 g/cm^3, corresponding to a relative density of approximately $\rho^*_o/\rho_s \cong 0.03$. The dynamic response of each design is compared using three types of fluid. The first fluid is a relatively high viscosity, Newtonian fluid (after honey with 15.5% H_2O), corresponding to a density and viscosity @ 25°C of 1.45 g/cm^3 and $\mu = 13.8$ Pa-s, respectively. The second fluid (glycerol) is a slightly lower viscosity Newtonian fluid, and was used in previous chapters. The density and viscosity are given again to be 1.26 g/cm^3 and $\mu = 1.49$ Pa-s, respectively. The third fluid is a non-Newtonian, shear thickening fluid, comprised of 50% silica particles suspended in ethylene glycol with a density of 1.5 g/cm^3. The parameters n and m are given for each regime in Table 7.1 based on the data in **Fig. 7.4**, given in *Chapter 5*. The transition between each power-law regime in the fluid-filled foam is derived from Eq. (7.4a) by equating the average stress for each regime and solving for the transition value ψ, of the strain rate $\dot{h}/h$, multiplied by the current aspect ratio R/h, as given in Table 7.1. The transition between each power-law regime is more clearly seen in the plot of the viscosity against the strain rate of the fluid given in **Fig. 7.4**.

7.4 Results and Discussion

7.4.1 Parametric Studies

Equations (7.5-7.10) can be used in a parametric study to analyze the proposed design for protection against explosive devices. An optimal design would reduce the maximum load imparted to a structure while minimizing the overall

cost. Since peak stress σ_p, is a measure of the maximum load imparted to a structure and weight (or areal density) is a measure of the total cost of implementing the design, these two variables are calculated. The measure of performance is determined by normalizing the peak stress imparted to the structure by the maximum pressure exerted on the outer face plate, P_{ro}, which is the equivalent of the peak pressure exerted on the structure if there was no protective blast wall. The areal density of the design is given by w_f. A number of free variables are used for the parametric study including the radius to thickness ratio of the fluid-filled foam layers, the thickness of each layer of material, the properties of the fluid impregnating the open-cell foam, and, for the dual-core design, the ratio of the thickness of each similar layer of material.

7.4.2 Single-Core Design

First, consider the single-core design **(Fig. 7.2)**, which provides insight into the effects of the aspect ratio, the thickness of each layer, and the properties of the impregnating fluid on the performance of the blast wall. Throughout the parametric study, the performance of each design is compared by plotting the normalized peak stress on the structure against the areal density of the design.

In Eq. (7.4) the average stress in the fluid-filled foam is proportional to the aspect ratio raised to a power greater than unity, making the aspect ratio, or the ratio of the radius of the foam to the height of the foam a critical parameter to study. This indicates changes to this parameter have a more significant impact on the response of the system than comparable changes to either the velocity at which the foam is compressed or the properties of the impregnating fluid. **Fig. 7.5** plots the normalized peak stress on the structure σ_p / P_{ro}, against the areal density w_f,

for a single-core design with glycerol as the impregnating fluid, where the outer face thickness is selected to be 10 mm. Three different values of the radius of the foam were selected of R = 0.5 m, 0.75 m, and 1 m, and the initial thickness of the core h_{2o}, was varied from 5 mm to 100 mm in increments of 5 mm, allowing the effect of the aspect ratio R/h to be studied.

Some of the most important findings in this analysis are directly related to the effect of the initial aspect ratio on the performance of each design. In particular, two limit phenomena are observed throughout all of the parametric studies as the initial aspect ratio tends toward infinity and zero. This can be observed in **Fig. 7.5** on any of the constant radius lines as the initial core thickness h_{2o}, tends toward zero or infinity. As aspect ratio R/h_2, approaches infinity and the initial core thickness approaches zero, the stress response becomes extremely large, as shown by Eq. (7.4). This dramatic increase in the stress response results in the fluid-filled foam acting much like the infinitely rigid plate. Therefore, in the case of a simple infinitely rigid plate, the peak stress on the building is expected to be that of the peak pressure on the plate. Hence, as the initial core thickness tends toward zero (or the initial aspect ratio tends toward infinity) the normalized stress is expected to tend toward unity, which is clearly observed in **Fig. 7.5**. In the other limit, as the aspect ratio R/h_2, approaches zero, as the initial core thickness becomes very large, Eq. (7.4) indicates a negligible amount of stress will be absorbed for a majority of the initial compression distance, since the aspect ratio over most of the deformation is comparably small. Therefore, in this limit, the outer face plate is effectively freely loaded by the blast wave without influence from the response of the core. During the free loading phase, the plate achieves a certain velocity characteristic of its inertia. Then as the core thickness decreases during the compression, the stress contribution from the fluid-filled

foam becomes significant. Thus, in the limit of very large initial core thickness (small initial aspect ratio), the dynamic response of the system is approximately independent of the initial core thickness, explaining the plateau response on the right hand side of **Fig. 7.5**. In some cases the response between these two limits is not monotonic; this is observed for $R = 0.5$ m in **Fig. 7.5**. This phenomenon can be explained by first reconsidering the fact that the inherent difference between the limit of very small initial aspect ratios and very large initial aspect ratios is that the outer plate is either "freely loaded" during the blast loading or there is resistance from the core during the blast loading period. In the limit of very small initial aspect ratios, the freely loaded plate is accelerated with little resistance from the core. Based on the aspect ratio arguments previously seen, a small radius design (i.e. $R = 0.5$ m) would require a small core thickness to result in a response of the core that is not negligible. Therefore, in the limit of large initial aspect ratios (small R/h_{2o}) a large core deformation is required to achieve this smaller core thickness during compression. Since the stress response in Eq. (7.4) is proportional to the core thickness raised to the third power, a substantial and dramatic increase in the stress response of the foam is observed to impede the incoming plate. This explains the relatively high normalized peak stress plateau response for the small radius $R = 0.5$ m. However, in the case of $R = 0.5$ m , as one decreases the initial core thickness h_{2o}, the initial aspect ratio is increased. At some point the initial aspect ratio results in a stress response that is no longer negligible during the blast loading period. This results in a more uniform response of the core and a lower normalized peak stress, which can be observed in **Fig. 7.5** as the non-monotonic response.

In between these two limits, it is apparent in **Fig. 7.5** that increasing the initial aspect ratio, or the radius at a constant initial core thickness (as shown by the

contour lines), results in a substantial reduction in the normalized peak stress on the underlying structure at a constant areal density. This effect is intuitive since increasing the radius corresponds to a higher stress response over a longer core compression distance. This more closely approaches the ideal plateau stress response where the normalized peak stress is minimized. As previously discussed, there are limits to the applicability of this result. In practical considerations, blast plates for infrastructure with radii larger than ~1 m become impractical to install and may be less aesthetically pleasing. Furthermore, too avoid the rigid plate response previously discussed in the limit of large initial aspect ratio, as the radius is increased, the thickness of the core must also be increased. Therefore, there is a practical limit based on initial core thickness and areal density, at which increasing the radius no longer gives the desired optimal response. Considering all of these factors, the optimal radius is selected to be 1 m.

In addition to the initial aspect ratio, other important parameters include the thicknesses of the face plate and the thickness of the core. In **Fig. 7.6**, the effect of changing these two parameters is examined. The single-core design impregnated with glycerol is selected to have a radius of 1 m. Four different face plate thicknesses are examined, ranging from 5 mm to 20 mm in increments of 5 mm, for a range of initial core thicknesses from 5 mm to 100 mm. It is observed that increasing the face plate thickness h_1, increases the areal density and reduces the peak stress. This observation can be understood by considering the inertia of the plate. In the limit of small initial aspect ratios, a thin plate with lower inertia is accelerated freely by the blast loading to a higher velocity than a thicker plate with higher inertia. Accordingly, more work is done on the plate with less inertia since the same pressure has been applied over a greater distance.

Therefore, it is logical that a larger normalized peak stress would be required to dissipate the larger amount of energy carried by the plate with lower inertia. However, it is important to consider the initial loading assumption. In this analysis, the worst case maximum reflected pressure is assumed, which is only applicable for an infinitely rigid system. In the case of a lighter plate, which is allowed to move during loading, the actual maximum reflected pressure would be less than that applied to a heavier plate. Therefore, a strong assumption in this analysis is that the plates are all loaded by a consistent uniform pressure. Overall, this analysis shows the advantage in reducing the normalized peak stress gained by increasing the plate thickness must be balanced with the corresponding increase in the areal density of the design. Based on this parametric analysis, the optimal plate thickness for the specified loading is selected to be h_1 = 20 mm and the best initial core thickness h_{2o}, is between 25 and 50 mm.

Fig. 7.6 also demonstrates important findings with regard to the initial core thickness h_{2o}. As expected, increasing the initial core thickness results in a decrease in the peak stress transmitted to the underlying structure. But there is a relatively dramatic transition where the rate of reduction in the peak stress with respect to increasing initial core thickness dramatically decreases. This transition is dependent upon the fluid and plate properties, but for the parameters in this analysis it typically occurs when the initial core thickness is such that the areal density of the core is between 20% and 40% the areal of the plate.

The final parametric study for the single-core design involves analyzing the effect of the fluid properties. In particular, the effect of the viscosity on the performance of the blast wall is studied with consideration of both Newtonian

and non-Newtonian fluids. In **Fig. 7.7**, the performances of the single-core design impregnated with glycerol, honey, and a silica based NNF is given where the silica based NNF is modeled by the power-law model. Each design considers an outer face plate thickness of 20 mm and radius of 1 m, which tend toward the optimal design. Again, the initial core thickness is varied from 5 mm to 100 mm. The viscosities of the three fluids in **Fig. 7.7** range from a minimum of 1 Pas to a maximum of 40 Pas. In this range, the optimal fluid viscosity is actually shown to be the middle viscosity for most designs considered, corresponding to the honey-filled foam. Using this methodology, the optimal fluid viscosity could be selected based upon the desired performance metrics. Under the loading conditions with the materials and dimensions selected for this analysis, a fluid with a viscosity on the order of honey appears to be approaching the optimal fluid. It is also important to consider the tradeoff between areal density and viscosity. Since honey is a high density fluid, the rate of reduction in the peak stress with increasing initial core thickness is less steep than in a comparable lower density fluid, such as glycerol. One advantage of a non-Newtonian fluid-filled foam is that, despite its higher density, it is still capable of demonstrating a dramatic rate of reduction in the peak stress with increasing initial core thickness for small core thicknesses as seen in **Fig. 7.7**. Although the non-Newtonian fluid is approximately the same areal density as honey, for small initial core thicknesses the variable viscosity is more conducive to a dramatic reduction in the peak stress with increasing initial core thickness.

7.4.3 Dual-Core Design

The dual-core design is useful in examining if enhancements in performance can be achieved through increasing the number of layers. To determine the effect of

increasing the number of layers, all comparisons between the dual-core design and the single-core design are done on a comparable areal density and thickness basis. Therefore, it is assumed the combined thickness of the two face plates in the dual-core design is equal to the thickness of the one face plate in the single-core design, and the combined thickness of the two cores in the dual-core design is equal to that of the core in the single-core design. In **Fig. 7.8**, the normalized peak stress imparted to the structure is plotted against the areal density for the dual-core design. Again, the radius is selected to be 1 m, and the impregnating fluid is glycerol. The inner and outer plate thicknesses were selected to be equal as were the initial inner and outer core thicknesses. The combined thickness of the inner and outer plates is varied from 5 mm to 20 mm, as in the case of the single-core design. Similarly, the combined thickness of the cores is varied from 5 mm to 100 mm. In comparing the performance of the dual-core design **(Fig. 7.8)** to that of an equivalent single-core design **(Fig. 7.6),** it is clear the single-core design has superior performance at comparable areal density.

Although the uniform equivalent dual-core design is not as efficient as the single-core design, the dual-core design provides the ability to vary more parameters. In particular, the effects of varying the thickness ratio of the outer face plate to that of the inner face plate is examined in **Fig. 7.9**. Again, the radius is taken to be 1 m, with glycerol as the impregnated fluid, and the core layers are of equal thickness, but the combined thickness can be varied as in previous single-core analyses. Three curves are plotted corresponding to inner plate thicknesses of 2.5 mm, 5.0 mm, and 7.5 mm where the combined face plate thickness is 10 mm. It is apparent as the ratio of the thickness of the outer plate to that of the inner plate is decreased, the peak stress on the underlying structure is reduced. Although the peak stress is substantially less than that analyzed in

Fig. 7.8 for equal face plate thicknesses, the overall performance is still not as good as the single-core design (**Fig. 7.6**). In addition, if the ratio of the face plate is improperly designed, the system can actually perform worse than if there was no protective blast plate (which results in a peak stress on the structure equal to the peak pressure of the blast wave). Improper coupling between the layers can actually amplify the peak stress on the underlying structure above that of the maximum reflected pressure as shown by the top curve in **Fig. 7.9**.

The dual-core design not only allows for the study of the effect thickness ratio between the outer and inner face plates, but it also allows for the study of the thickness ratio between the outer and inner cores as shown in **Fig. 7.10**. For a dual-core design with radius 1 m, impregnated with glycerol and outer face plate thickness of 2.5 mm with inner face plate thickness of 7.5 mm, the normalized peak stress is plotted against the areal density of the design. The ratio of the initial outer core thickness to that of the inner core is varied from 1/15 to 15. In **Fig. 7.10** it is shown that reducing the initial outer core thickness is also optimal. For ratios of the initial thickness of the outer core to that of the inner core less than unity, the performance is approximately constant. This can be observed by the overlapping results for this region. Overall, **Fig. 7.9** and **Fig. 7.10** indicate that in the limit of decreasing outer plate thickness and decreasing initial outer core thickness the optimal solution is achieved. Therefore, the results from **Fig. 7.9** and **Fig. 7.10**, also support the conclusion from **Fig. 7.8** that the single-core design is ideal.

7.4.4 Optimal Design

Overall, **Fig. 7.7** and **Fig. 7.9-7.11** indicate the optimal configuration is found to tend toward a single-core layer design. For the characteristic loading scenario presented in this analysis, the ideal configuration also tends toward maximizing the radius, within practical constraints. Furthermore, the ideal configuration for minimizing the peak stress also tends toward maximizing the plate thickness h_1; however, increasing the plate thickness also results in an increased areal density. Similarly, increasing the initial core thickness h_{2_0} also tends to decrease the peak stress on the underlying structure while increasing the areal density of the blast plate. However, with increasing initial core thickness there is an apparent transition where the rate of reduction in the peak stress with respect to increasing initial core thickness dramatically decreases. This transition depends on the loading scenario and characteristics of the blast plate, but is found to be approximated by a initial core thickness such that the areal density of the core is on the order of 30% that of the plate. The ideal fluid impregnating the foam would intuitively have a minimum density, but the optimal viscosity is dependent upon the blast loading and the characteristic properties of the composite blast plate. However, it can be concluded a relatively high viscosity fluid, on the order of 10 Pas, is preferred. It is also noted that the characteristic behavior found in some shear thickening fluids has a desired effect on the response of the composite blast plate. Considering all of these optimal parameters, the composite blast plate with a layer of fluid-filled foam has the potential to reduce the normalized peak stress up to 85% at an areal density of approximately 220 kg/m^2 and by more than by more than 90% with an areal density in excess of 300 kg/m^2.

7.4.5 Comparable Standard Blast Shield Design

To assess the viability of a new blast protection technology, it is important to compare its performance to existing technology. As previously discussed, a number of commercially available blast protection walls are available. Since there are many types of blast protection technologies, such as those that require active control (i.e. magnetorheological or electrorheological fluids) and those that require a stand-off distance from the structure, the comparison in this analysis is limited to similar technologies. Comparable designs are assumed to be adjacent to the structure and to be comprised of inexpensive materials that do not require active control. Most designs of this nature are in the form of a standard sandwich panel, where a semi-compressible core is placed in series with one or more layers of comparably rigid face plates. It is envisaged that as the outer face plate is accelerated by the blast load, the core material is allowed to deform, absorbing energy and reducing the maximum force applied to the underlying structure.

One such standard, wall-mounted, blast shield designed to protect against a 600lb ANFO blast, is available from Creative Building Products. This standard attachable blast wall contains three steel face plates with a combined thickness of 10 mm and density of $\rho = 7800$ kg/m^3. The face plates are separated by two layers of sand-filled, open-cell, polyethylene plastic core material. The areal density of this protective blast wall is 330 kg/m^2. This gives an idea as to the typical standard areal density, which can be used to assess the efficiency of both the optimally designed fluid-filled sandwich blast plate and the optimally designed standard sandwich blast plate. However, since the behavior of the internal core is not readily modeled, to develop an accurate model for the performance of this design, a modified design based on the results of Fleck and Deshpande (2004) is

considered. They considered a blast plate comprised of a three layer composite with inner and outer steel face plates sandwiching a porous, steel core. They analyzed a variety of microstructure core configurations, but one of the most commonly used cores they analyzed was the foam configuration, which is known to demonstrate superior performance in sandwich plate designs.

In this analysis, the standard blast plate foam core is assumed to be made of steel ($\rho_s = 7800$ kg/m^3; $\sigma_y = 300$ MPa) with an initial density ρ_o, current relative density $\bar{\rho}$, and yield strength, σ_{ny}. The core is treated as a rigid, ideally plastic, crushable solid with a normal compressive strength $\sigma_{ny} = 0.3(\bar{\rho})^{1.5}\sigma_y$ (after Gibson and Ashby, 1997). After densification has been achieved, it is assumed that the core is rigid. Both commercially available blast walls and theoretically proposed blast walls have a variety of layering configurations. To compare the ideal fluid-filled design to the standard design, in this analysis, we consider one outer face plate layer and one foam core layer (identical to the proposed designs shown in **Fig. 7.2** with the fluid-filled foam core replaced by the steel foam core). This design differs slightly from the Fleck and Deshpande sandwich structure in that there is no inner face plate layer. Since this design is attached directly to the underlying structure, which is assumed infinitely rigid, there is no need for an infinitely rigid inner face plate layer. To maintain the comparison between the optimal fluid-filled design and the standard design, the face plate thickness is selected to be 20 mm. Selecting a face plate with smaller thickness may have a greater reduction in the weight of the standard design, but would not provide the same rigidity or resistance to shrapnel from the blast. A practical constraint is also placed on the core thickness of the standard design. Since one of the main disadvantages of a standard foam core design is typically the large thickness

required, we require the core thickness to be less than 100 mm for all of the designs considered. This constraint is also applied to the core thickness of the optimal fluid-filled core design.

Fig. 7.11 plots the normalized peak stress imparted to the structure against the areal density for the honey-filled composite blast plate and the standard blast plate with foamed steel core. Three standard designs are shown with initial relative core densities of $\rho_0/\rho_s = 0.25$, 0.2, and 0.15, corresponding to densities of 1950, 1560, and 1170 kg/m^3, respectively. For each design the initial thickness of the core h_{2o}, is varied up to the maximum allowed core thickness of 100 mm in increments of 5 mm. The results of the standard design are independent of the radius of the design, so a radius of 1 m is selected. From **Fig. 7.11** it is clear the standard foamed steel core design also substantially reduces the peak stress on the underlying structure at areal densities comparable to that of the honey-filled blast-resistant plate. It is also apparent, minimizing the initial relative density of the standard steel, foam core design tends toward an optimal configuration for reducing the peak stress at a given areal density; however, the applicable range of core thicknesses of this design is also dramatically reduced. The optimal relative density of the steel foam core is taken to be 0.15 since densities lower than this require core thicknesses greater than 100 mm to mitigate the incoming blast wave. Table 7.2 gives the optimal configuration for both the fluid-filled composite blast-resistant plate and the standard foam composite blast-resistant plate. While there is very little difference in the level of blast mitigation at a given areal density between the optimal fluid-filled design and the optimal standard design, the optimal fluid-filled design results in a significant reduction in the overall thickness compared to the standard design at a given areal density. This can be more clearly seen in **Fig. 7.12** which is a magnified plot of **Fig. 7.11**.

In **Fig. 7.12**, the points corresponding to initial core thicknesses of 75 mm and 100 mm are overlaid on the plots for the optimal honey-filled configuration and the optimal standard configuration. For a comparable thickness the optimal honey-filled design demonstrates reductions in the normalized peak stress of approximately 15% over the optimal standard design.

7.5 Conclusion

This chapter examines the potential of a novel blast protection composite, which incorporates a layer of low-density, flexible, reticulated foam filled with either a Newtonian or a non-Newtonian fluid. A review of blast loading of structures and the current state of the art technology for protecting against such loads is given. The potential of the proposed design to protect against blast loading and reduce the maximum stress transmitted to the underlying structure is assessed. Tractable relations are developed which readily allow for a parametric study of this design. An optimal design is found to be a single-core layer with a relatively large initial aspect ratio saturated with a relatively high viscosity, Newtonian fluid. In addition, a critical transition for the thickness of the core is also observed, at which point the rate of reduction in the peak stress with respect to increasing initial core thickness dramatically decreases. Furthermore, it is observed that increasing the thickness of the face plate increases the areal density of the design but results in similar percent reductions in the peak stress transmitted to the underlying structure. Overall, the optimal design is found to reduce the normalized peak stress on an underlying structure by more than 90% compared to that on an unmodified structure. Moreover, the optimal design is shown to outperform comparable blast plate designs with greater reductions in

the peak stress at a given thickness. Finally, this analysis of composite, fluid-filled blast protection technologies, shows this design has enormous potential to be readily extended to the development of new protection equipment for a range of energy absorption applications. In particular, this technology may be useful in the design of blast protection equipment for military personnel and vehicles as well as impact protection equipment for commercial helmets and vehicles.

References

Elliot, C.L., Mays, G.C., and Smith, P.D., (1992), "The Protection of Buildings against Terrorism and Disorder", *Proc. Inst. Civ. Eng. Struct. Build,* **94**, 287-97.

Fleck, N.A. and Deshpande, V.S., (2004), "The Resistance of Clamped Sandwich Beams to Shock Loading", *J. Applied Mech.*, **71**, 386-401.

Gibson, L.J. and Ashby, M.F., (1997), *Cellular Solids – Structures and Properties, 2nd Ed.*, Cambridge Univserisy Press, Cambridge.

Hetherington, J.G. and Smith, P.D., (1994), "Blast and Ballistics Loading of Structures", *Butterworth-Heinemann Ltd.*, Oxford, Great Britain.

Hutchinson, J.W. and Xue, Z., (2005), "Metal Sandwich Plates Optimized for Pressure Impulses", *Int. J. Mech. Sci.*, **47**, 545-569.

Kambouchev, N., Noels, L., and Radovitzky, R., (2006), "Nonlinear Compressibility Effects in Fluid-Structure Interaction and Their Implications on the Air-Blast Loading of Structures", *J. App. Physics,* **100**, 063519:1-11.

Ngo, T., Mendis, P., Gupta, A., and Ramsay, J., (2007), "Blast Loading and Effects on Structures-An Overview", *Loading and Struct.*, Special Issue, 76-91.

Qiu, X., Deshpande, V.S., and Fleck, N.A., (2005), "A One-Dimensional Response of Sandwich Plates to Underwater Shock Loading", *J. Mech. Phys. Solids,* **53**, 22347-2383.

Radford, D.D, , Fleck, N.A., and Deshpande, V.S., (2006), "The Response of Clamped Sandwich Beams Subjected to Shock Loading", *Int. J. Impact Eng.*, **32**, 968-987.

Remennikov, A.M., (2003), "A Review of Methods for Predicting Bomb Blast Effects on Buildings", *J. Battlefield Tech.*, **6**, 3, 5-10.

Taylor, G.I., (1963), "In Aerodynamics and the Mechanics of Projectiles and Explosions", *The Scientific Papers of Sir Geoffrey Ingram Taylor,* **3**, pp. 287-303.

U.S. Army, (1986), "Fundamentals of Protective Design for Conventional Weapons," *TM5-855- 1.*

U.S. Department of State, (2007), "Country Reports on Terrorism", *National Counterterrorism Center: Annex of Statistical Information.*

Xue, Z. and Hutchinson, J.W., (2003), "Preliminary Assessment of Sandwich Plates Subject to Blast Loads", *Int. J. Mech. Sci.*, **45**, 687-705.

Xue, Z. and Hutchinson, J.W., (2004), "A Comparative Study of Impulse-Resistant Metallic Sandwich Plates", *Int. J. Impact Eng.*, **30**, 1283-1305.

Tables

Table 7.1: Viscosity exponents n, and coefficients m, for power-law models of 50% silica based non-Newtonian fluid in various regimes.

n	m	(Aspect Ratio)(Strain Rate), ψ
1.00	40	$\psi < 32$
0.17	1200	$\psi > 32$

Table 7.2: Optimal configurations and performance for both the fluid-filled and standard blast-resistant plates.

Fluid-Filled Core Design		Standard Core Design	
Core Material	Honey-Filled PU Foam	Core Material	Steel Foam $\rho_o/\rho_s = 0.15$
h_1 (mm)	20	h_1 (mm)	20
h_{2o} (mm)	100	h_{2o} (mm)	100
ρ_1 (kg/m^3)	7800	ρ_1 (kg/m^3)	7800
ρ_{2o} (kg/m^3)	1290	ρ_{2o} (kg/m^3)	1170
w (kg/m^3)	300	w (kg/m^3)	273
σ_p/P_{ro}	0.09	σ_p/P_{ro}	0.11

Figures

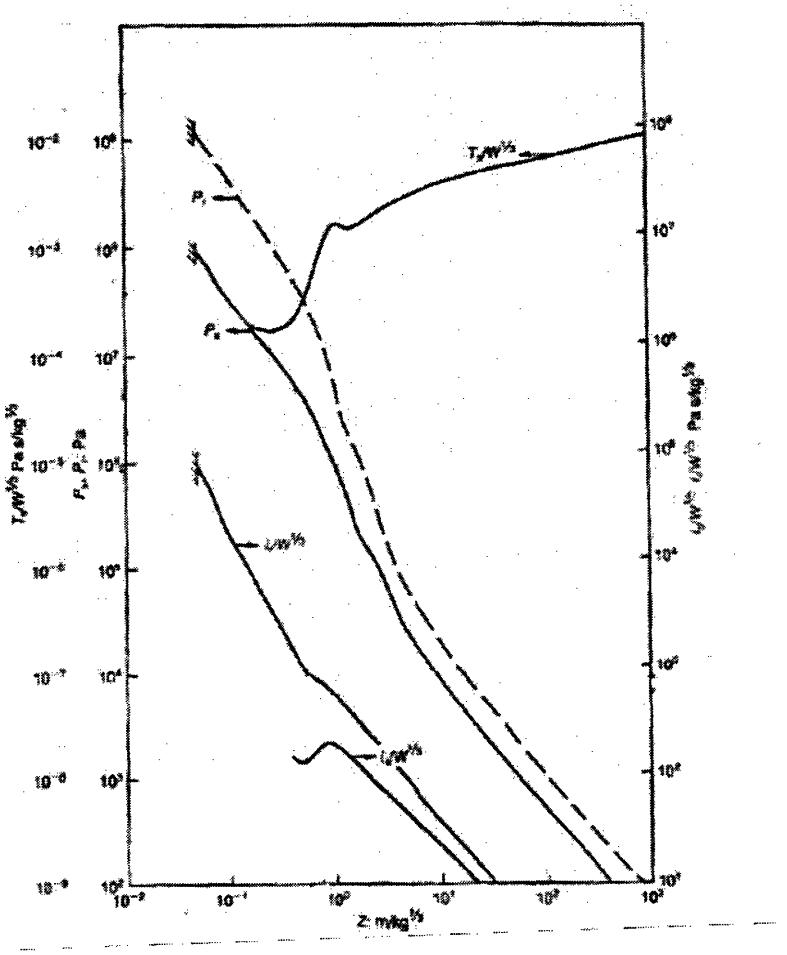

Figure 7.1 Blast parameters for spherical TNT charge in free air (Elliot, 1992)

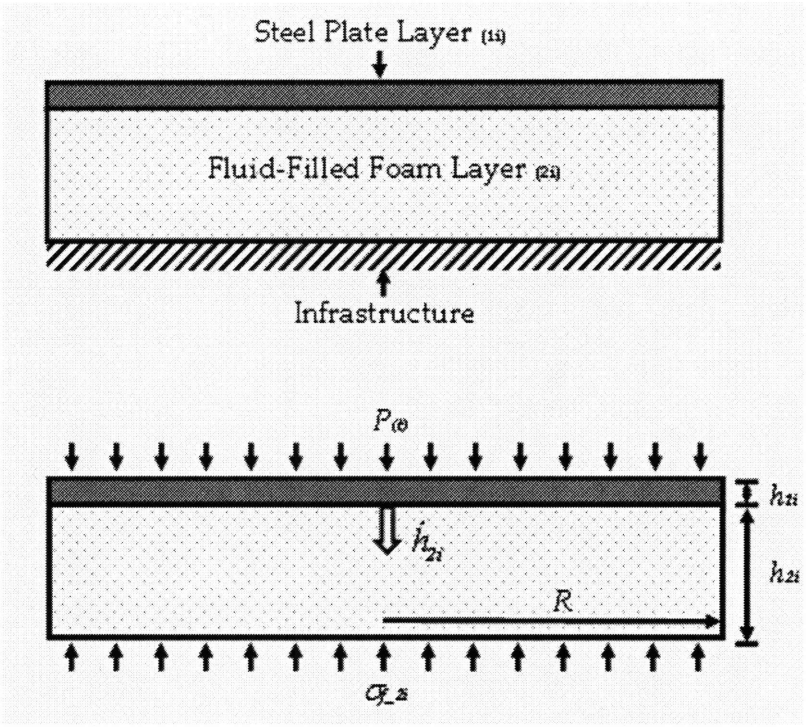

Figure 7.2. Model of Single Core Blast Protection Design.

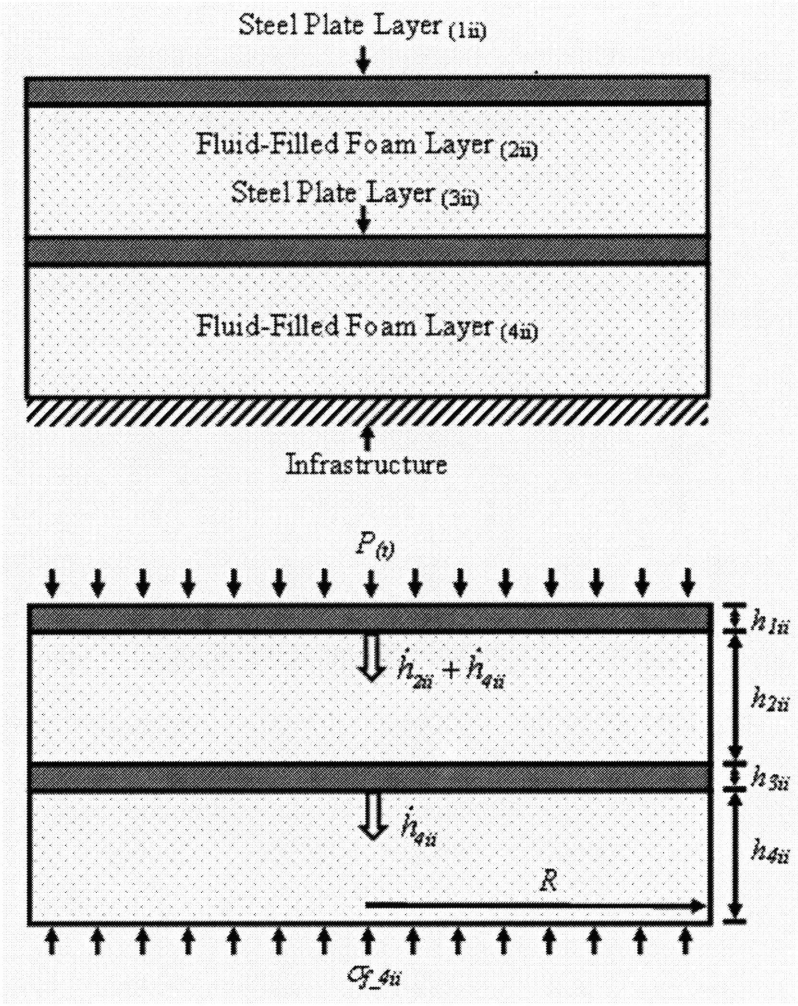

Figure 7.3. Model of Dual-Core Blast Protection Design.

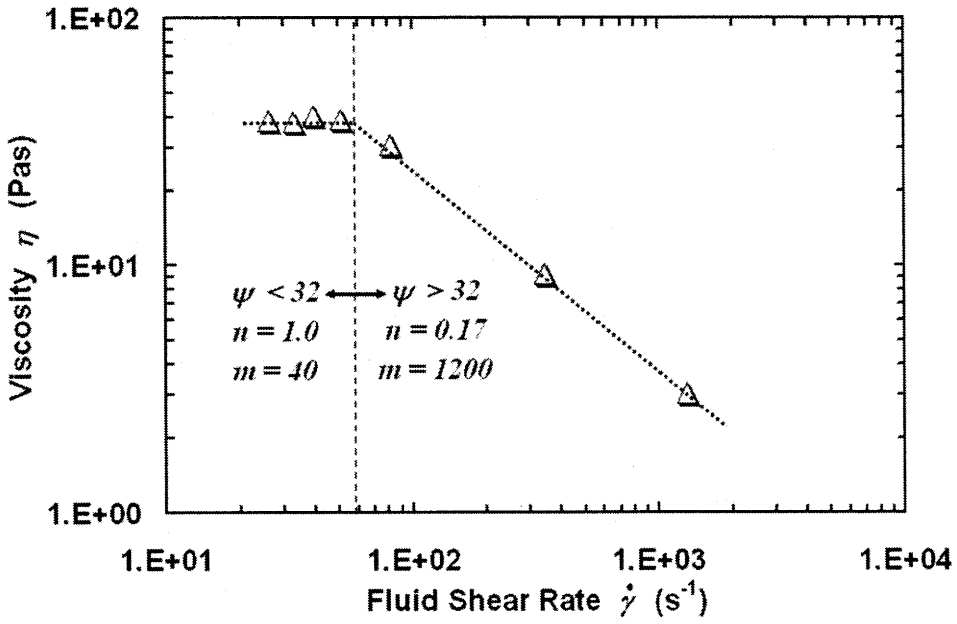

Figure 7.4. The viscosity of the silica based non-Newtonian fluid plotted against the shear rate of the fluid.

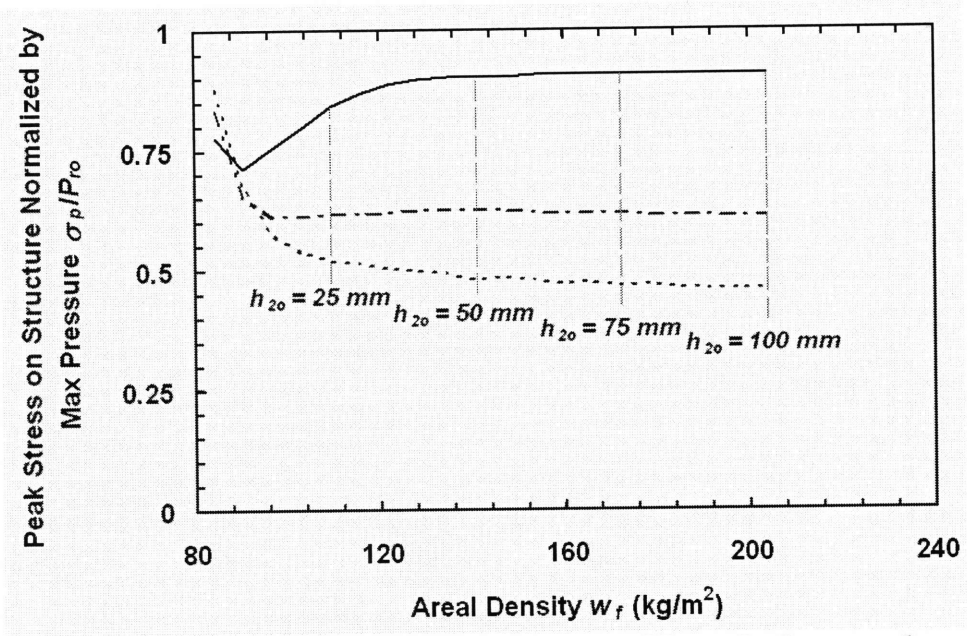

Figure 7.5. The peak stress on a structure protected by a single-core, glycerol-filled composite plate normalized by the maximum blast pressure plotted against the areal density of the composite plate. Radius of blast plate: 0.5 m (——); 0.75 m (— ·); 1 m (·····). Outer face plate thickness h_1 = 10 mm.

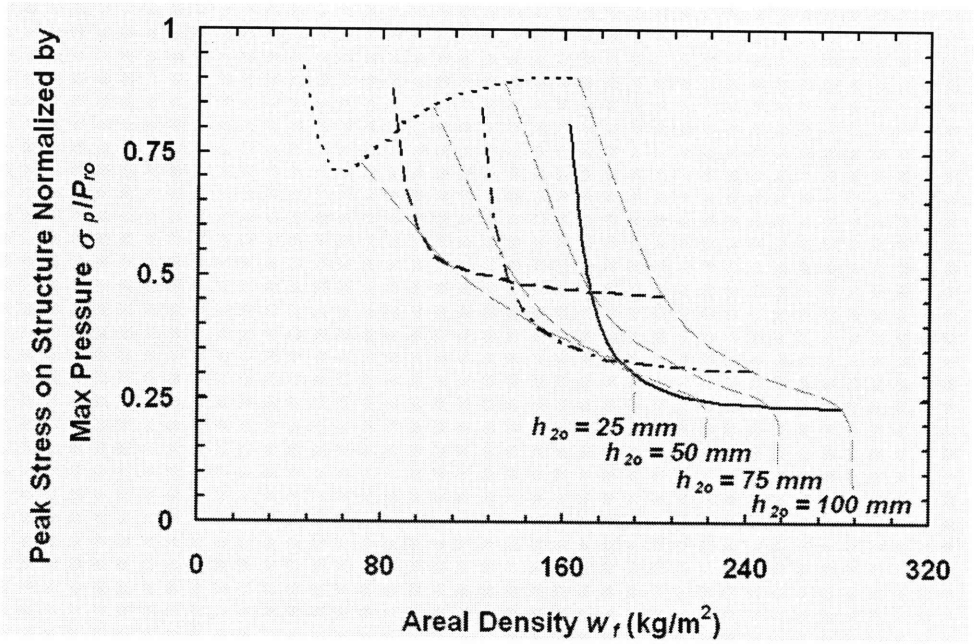

Figure 7.6. The peak stress on a structure protected by a single-core, glycerol-filled composite plate normalized by the maximum blast pressure plotted against the areal density of the composite plate. Outer plate thickness h_1: 5 mm (·····); 10 mm (– –); 15 mm (— ·); 20 mm (——); R = 1 m.

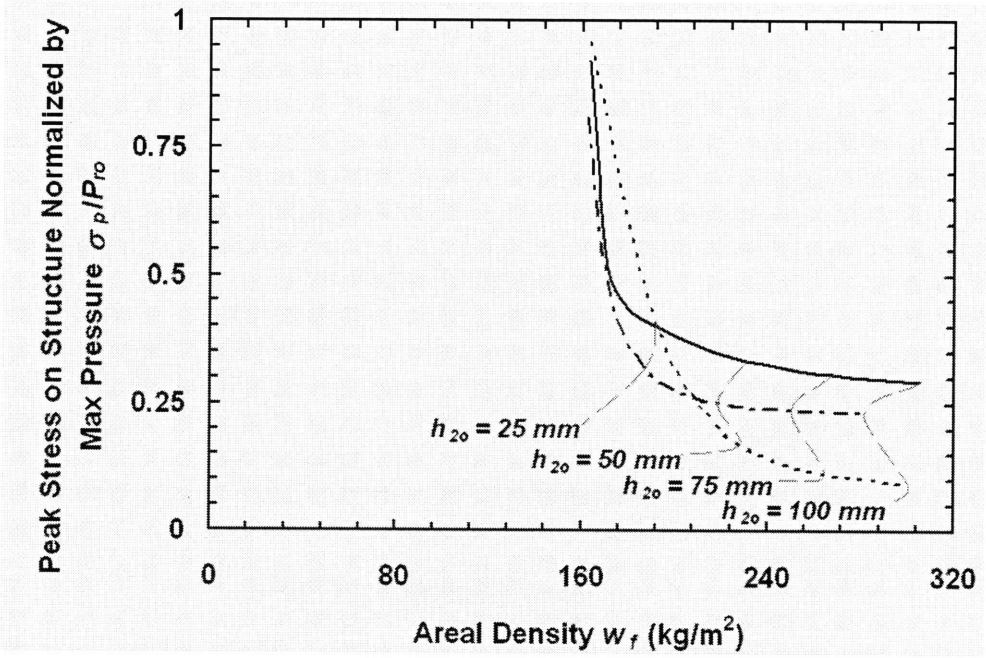

Figure 7.7. The peak stress on a structure protected by a single-core, fluid-filled composite plate normalized by the maximum blast pressure plotted against the areal density of the composite plate. Fluid: Honey (·····); Glycerol (— ·); Silica Based NNF (——). h_1 = 20 mm; R = 1 m.

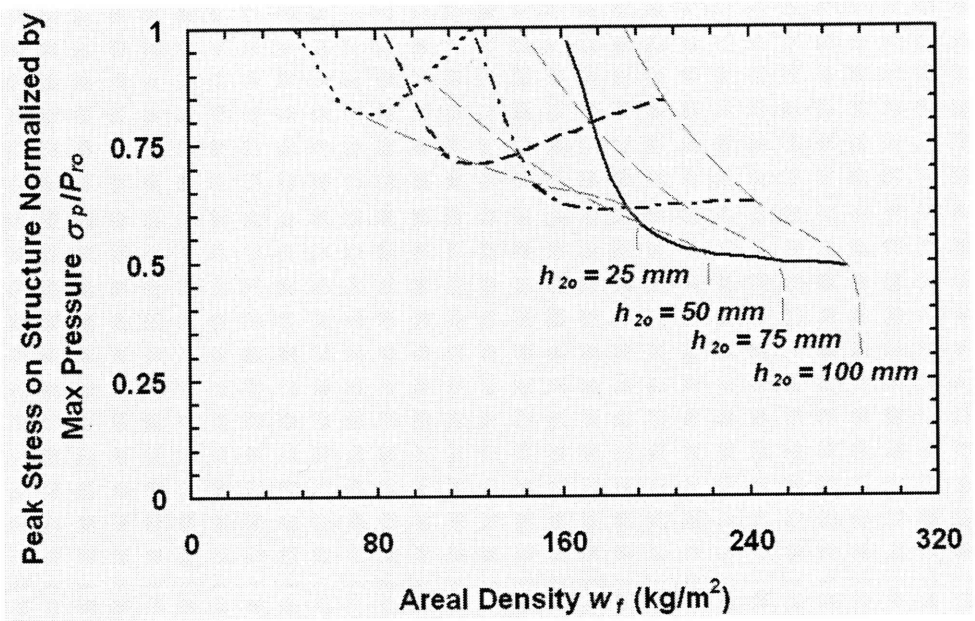

Figure 7.8. The peak stress on a structure protected by a dual-core, glycerol-filled composite plate normalized by the maximum blast pressure plotted against the areal density of the composite plate. Total combined plate thickness $h_{1ii} + h_{3ii}$: 5 mm (·····); 10 mm (– –); 15 mm (— ·); 20 mm (——). R = 1 m.

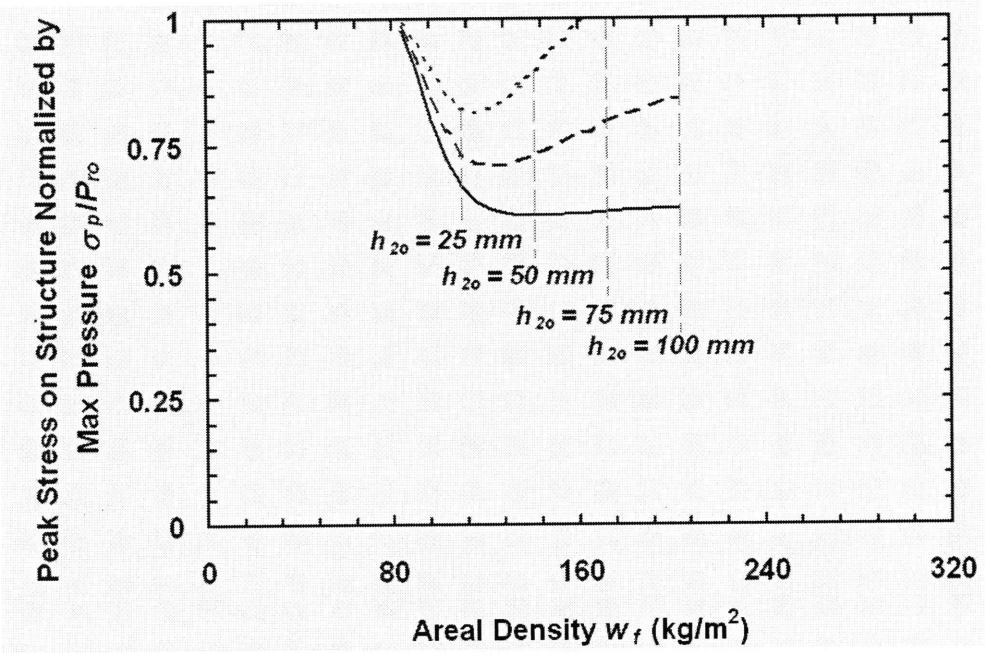

Figure 7.9. The peak stress on a structure protected by a dual-core, glycerol-filled composite plate normalized by the maximum blast pressure plotted against the areal density of the composite plate. Ratio of plate thicknesses h_1/h_3: 3/1 (·····); 1/1 (– –); 1/3 (——). R = 1 m; $h_{1ii} + h_{3ii}$ = 10 mm.

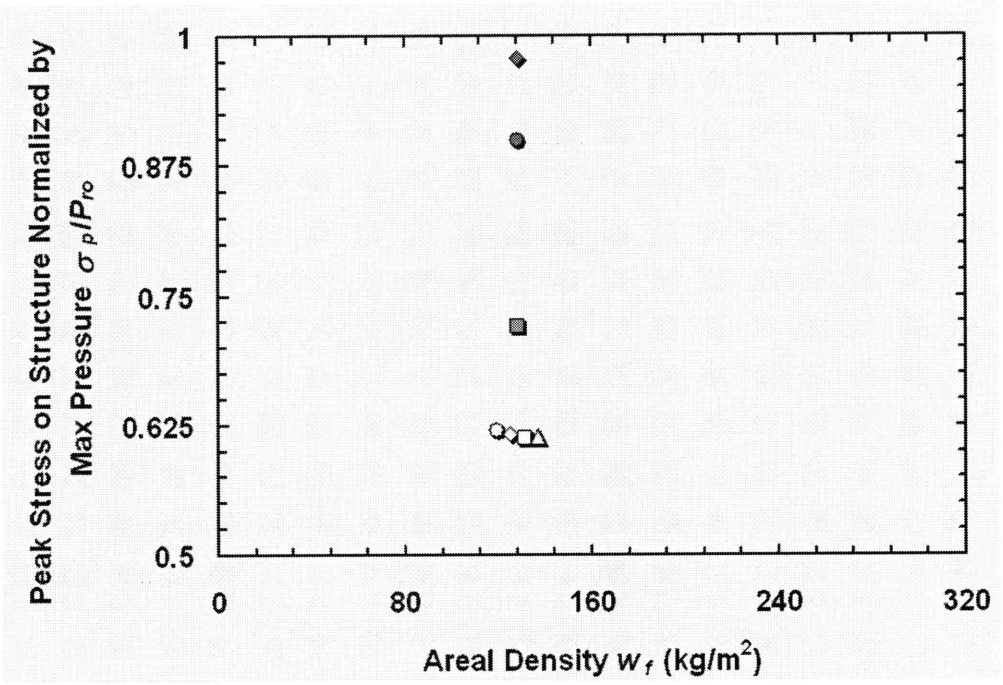

Figure 7.10. The peak stress on a structure protected by a dual-core, glycerol-filled composite plate normalized by the maximum blast pressure plotted against the areal density of the composite plate. Ratio of initial core thicknesses h_{2o}/h_{4o}: 15 (◆); 7 (●); 3 (■); 1 (Δ); 1/3 (□); 1/7 (○); 1/15 (◇); Where all areal densities w_f, are exactly 128 kg/m^2, but the lower cluster of points are offset to make them more visible. R = 1 m; $h_{1ii} + h_{3ii}$ = 10 mm.

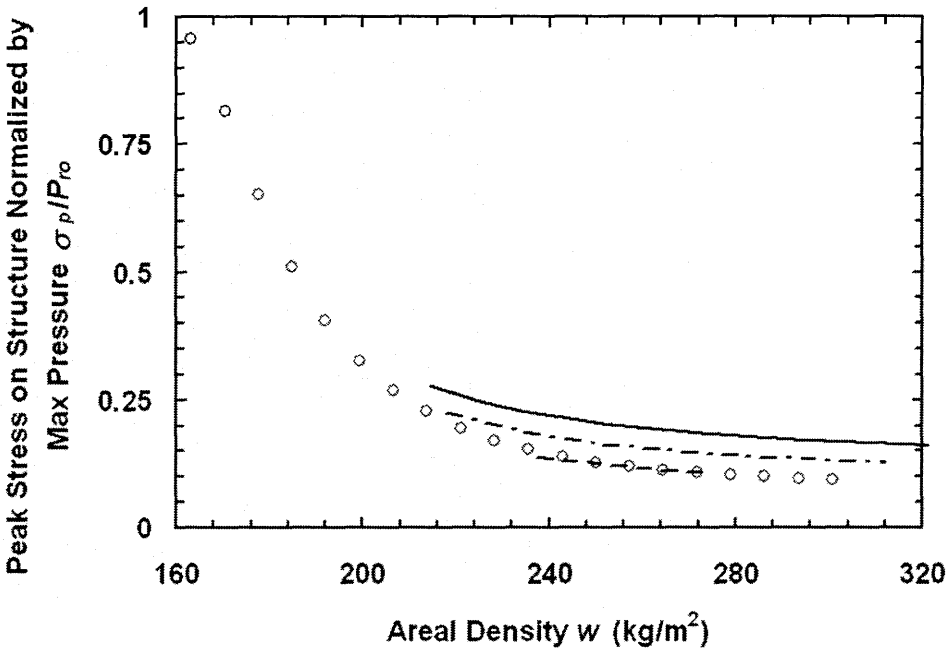

Figure 7.11. The peak stress on a structure protected by a single-core composite plate normalized by the maximum blast pressure plotted against the areal density of the composite plate. Core: Honey-filled (o); Standard steel foam ρ_0/ρ_s = 0.15 (– –); Standard steel foam ρ_0/ρ_s = 0.20 (— ·); Standard steel foam ρ_0/ρ_s = 0.25 (——). h_1 = 20 mm; R = 1 m; h_{2o} varied from 5 mm to 100 mm.

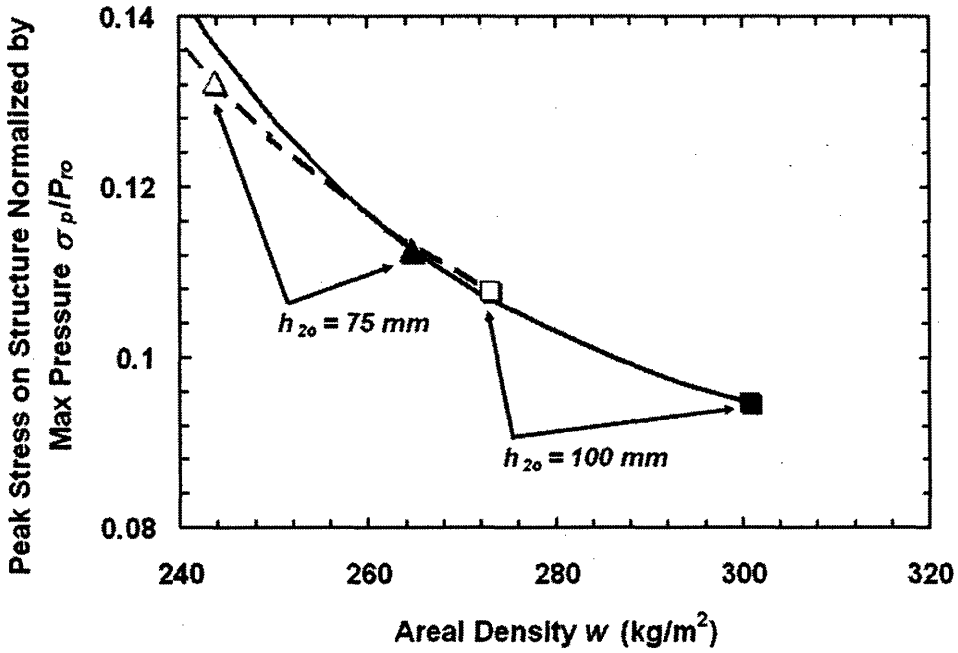

Figure 7.12. The peak stress on a structure protected by a single-core composite plate normalized by the maximum blast pressure plotted against the areal density of the composite plate. Core: Honey-filled (——,▲, ■); Standard steel foam $\rho_o/\rho_s = 0.15$ (– – , Δ, □); $h_1 = 20$ mm; $R = 1$ m; h_{2o} varied from 5 mm to 100 mm.

8 Conclusion and Recommendations

8.1 Conclusions

It is apparent that there is a tremendous and rapidly growing need to develop improved protective equipment for both resisting high energy impacts and impeding blast waves. The overarching goal of this dissertation is to address this need by exploring the potential of a novel, fluid-impregnated foam suitable for both energy absorption and blast wave protection. In this thesis, we have established a robust theoretical and experimental foundation upon which future research in this field can be grounded.

While it has been well known for sometime that the permeability of open-cell foam is a function of the applied compressive strain, in this analysis we develop a highly tractable, physically based analytical model describing the relation between the compressive strain and the permeability. This model was based on the observation that after cells in the foam begin to buckle and collapse, the cells remain at either one of two strains, the elastic buckling strain or the densified strain. Experimental results provided strong support for this model over a wide range of strains and cell sizes, and also demonstrated the model to be independent of the anisotropy of the foam and the fluid properties.

Understanding the microstructural behavior of foam under deformation was a critical step toward the development of a comprehensive description of the dynamic compressive response of fluid-impregnated foam. In this dissertation, the first known comprehensive, analytical model describing the complex phenomenon of the dynamic compressive response of Newtonian fluid-

impregnated, reticulated, elastomeric foam is presented. Extensive experimental studies were carried out, which strongly support this model for a range of strains, a variety of foam grades, and several orders of magnitude of strain rate. A more simple explicit analytic solution based on a lubrication approximation is also presented. The generalized, comprehensive model is found to converge rapidly to within 5% of the lubrication model as the aspect ratio of the foam is increased beyond four. One of the primary advantages of this tractable lubrication model is that it reveals important scaling relations for the dynamic response. Specifically, the average stress response is found to scale proportional to the characteristic dimension in the direction of flow (radial) to the second power and to the viscosity and the strain rate of the foam to the first power. It is also found to be inversely proportional to the permeability to the first power. These scaling relations are extremely useful in the design of dynamic engineering systems incorporating a layer of fluid-impregnated foam. Furthermore, the lubrication model can be readily extended to more complex analyses, such as the dynamic response of foam impregnated with a non-Newtonian fluid.

In addition to a Newtonian model, the first known, comprehensive model for the dynamic compressive response of a non-Newtonian, shear thickening fluid-impregnated foam was also discussed in this dissertation. Like the Newtonian model, scaling relations were also observed for the dynamic response of the non-Newtonian fluid-filled foam model, which are useful in engineering design. This non-Newtonian model only considered the response beyond the shear thickening transition, corresponding to strain rates where most high rate, dynamic engineering applications will operate. Primarily, this model is developed for the latter shear thinning regime (regime R_4), which is expected to occur for several orders of magnitude in strain rate. While the exact mechanism

of this shear thinning regime is under debate, we have provided several pieces of evidence supporting the existence of this regime. Specifically, extensive slip studies were conducted with the shear thickening fluid and no slip was found to occur. In addition, the consistency of the slope in the shear thinning regime, indicates it is not caused by an erratic slip phenomenon. Furthermore, it is evident that the shear thinning transition occurs over one order of magnitude in shear stress, depending on the volume fraction of the fluid. Finally, the dynamic response model based on this shear thinning regime, provides the strongest evidence. The overall dynamic response model was found to be supported by experimental results with all data points lying within one standard deviation of the predicted values. Again, the model is independent of the foam grade and applicable over a large range of strains, strain rates, aspect ratios, and shear thickening fluids.

The fundamental research developed in the beginning of this thesis has been applied in two case studies. The first examines the unique ability of fluid-filled foam to efficiently absorb significant amounts of energy under a controllable stress level at low cost. The need for improved protective, energy absorption equipment has become increasingly apparent, particularly for motorcycle helmets, where there is a great need for an energy absorption technology which is both lightweight and suitable. In this dissertation, we examine the benefits of a fluid-filled foam composite helmet over existing technologies. The main advantage of the fluid-filled foam composite helmet is found to be its resistance to multiple impacts, which is of utmost importance in a real accident scenario. Suggestions are also made to reduce the overall weight of motorcycle helmets without sacrificing performance. The proposed helmet technology with reduced weight and enhanced multi-impact protection has potential to increase the

utilization of helmets and reduce the overall number of brain injuries from motorcycle accidents.

In addition, a case study on the development of blast-resistant plates, with a layer of fluid-filled foam, for infrastructure protection is also presented. A parametric study is used in conjunction with the models from this thesis to determine the effects of various parameters on the ability of a blast protection plate to minimize the peak stress transmitted to an underlying structure. A number of important discoveries were made including the fact that a single-core, single face plate design is more efficient and more versatile than a comparable dual-core design. In general, the ideal liquid would have a minimum density and a relatively high viscosity, but not so high that the response is similar to a solid, reducing the benefit of a compressible foam core as seen in the case of a non-Newtonian shear thickening fluid. It was also determined the optimal design tends toward maximizing the radius and the face plate thickness to within practical constraints. Furthermore, increasing the initial core thickness h_{2_0} tends to reduce the peak stress on the underlying structure while increasing the areal density of the blast plate; however a critical transition phenomenon is also observed, at which point the rate of reduction in the peak stress with respect to increasing initial core thickness dramatically decreases. Overall, the optimal design is found to reduce the normalized peak stress on an underlying structure by more than 90% compared to that on an unmodified structure. The optimal design is also found to have an areal density comparable to standard commercially available blast-resistant designs. Finally, this parametric case study demonstrates that the models developed in this thesis have potential in the practical design of technologies incorporating a layer of fluid-filled foam and

that these novel structures have potential to protect against impact loading and blast loading.

All in all, this dissertation has revealed there is potential for fluid-impregnated foam in a variety of engineering applications, such as energy absorption devices and blast protection equipment. The intrinsic versatility of fluid-impregnated foam makes it a promising technology for effective energy absorption and blast protection devices, which are efficient, cost-effective, reliable, and scalable. Moreover, the comprehensive analytical models presented in this dissertation provide a clear, tractable, and robust method for successfully developing and implementing this novel technology into engineering structures.

8.2 Recommendations for Future Research

While the models presented in this dissertation have demonstrated potential in describing the dynamic compressive response of fluid-impregnated foam in a tractable way, the derivation of these models required a number of assumptions. Extending the models developed in this thesis by reexamining the key assumptions, has the potential to result in even more robust models that are more descriptive and more applicable to a wider class of problems encountered in real applications. In particular, reexamining the assumption that the fluid-structure-interaction can be neglected beyond a certain loading rate is important if the foam matrix has a higher relative density or higher yield strength than the foam considered in this thesis. This assumption arose because this thesis considered low-density polyurethane foam where the local stress in the fluid far exceeded the yield stress of the polyurethane under high rate loading. If a

different foam matrix material was used, this would be of importance in high rate loading applications such as blast protection equipment. Moreover, under high energy impact or blast loading, the strain in the foam could exceed the densified strain, so extending the models to this regime would be highly advantageous. In addition, under extremely high rate loading, the inertial effects may also become important. Extending the analytical studies to account for this contribution would be a substantial contribution to modeling the overall dynamic response of fluid-impregnated foam. Finally, real loading scenarios may also involve out of plane loads (i.e. shear, torsion, etc.) and different geometric configurations (i.e. not cylindrical). Developing analytical scaling arguments to assess the importance of out of plane loads compared to the uniaxial compressive load would be useful in a comprehensive design. Furthermore, developing an understanding of more realistic geometric configurations would also help in more precise analytical descriptions of actual designs.

While analytically treating all of the previously described phenomena would be ideal, the inherent complexity of these phenomena limits this approach. Therefore, we suggest a rigorous experimental approach to fully characterize the effects of each. Of most importance is studying the response under realistic blast loading scenarios. This study will elucidate the importance of inertial effects and out-of-plane loads. Another major experimental study, which should be undertaken involves the practical implementation of a fluid-impregnated foam in any design. Additional methods for impregnating the foam on a large scale should be explored, particularly with regard to high viscosity liquids, such as the non-Newtonian fluids discussed in this dissertation. One such possibility is to utilize evaporative techniques to impregnate the foam with a highly

concentrated suspension. Developing an energy and cost efficient way impregnate the foam on a commercial scale is crucial to the successful deployment of fluid-impregnated foam in any commercial application.

Although analytical and experimental methods for characterizing the foam are essential, dramatic improvements could also be made through computational methods. Specifically, more comprehensive parametric studies on new technologies utilizing fluid-impregnated foam could be performed. Even more advanced optimization techniques could also be explored. With the large number of tunable parameters in these systems, Monte Carlo methods or quasi-random techniques (such as the Sobel sequence) could be particularly advantageous. The techniques could result in generalized code that could be applicable to optimizing the weight and stress transmission of a wide range of designs, which incorporate fluid-filled foam.

These additional computational studies would be useful in developing a better understanding of the applications in which the fluid-impregnated design is most advantageous. In addition to an extensive search of energy absorption technologies as well as blast protection technologies, a search for other technologies where improvements could be made using fluid-impregnated foams could also be carried out. This search could be constrained to technologies which require high rate or cyclic loading in a device that is required to be inexpensive, efficient, reliable, and geometrically confined.

Also, consideration of more complex structures could increase the number of applications in which fluid-impregnated foam could be used. As previously discussed, allowing for variable geometric configurations would substantially

increase the applicability of this technology. But possibly other advances have even more potential, such as developing new foam matrix materials or new types of fluids. The fluids for instance, could have higher viscosities or lightweight, hollow particles giving them a lower density or consist of a solvent that has a larger temperature range for which it remains a liquid. In addition, considering innovative methods for using these structures can also be highly beneficial. One such proposal is to add confining, elastic membranes around the fluid-impregnated foams, which rupture at specified strains or stresses, allowing the fluid to expand to a new geometry. This type of design would give greater control over the energy absorption profile, allowing for a larger compression distance and increased compression time at a tailored stress level. Another proposal is to utilize networks of interconnected fluid-filled foams in both parallel and series to readily control the stress response of an engineering system. Overall, increasing the number of parameters and their ranges of properties increases the usefulness of fluid-impregnated foam by providing more ways to tailor an engineering design. All in all, there is great potential to improve the understanding of the dynamic response of fluid-impregnated foam and discover new methods of implementing this unique technology in fields such as energy absorption and blast mitigation.

Acknowledgements- This thesis benefited greatly from the insight provided Professor Lorna J. Gibson of the Department of Material Science and Engineering, Massachusetts Institute of Technology. In addition, I am thankful for the assistance of Professor Gareth H. McKinley and Professor Anette E. Hosoi of the Department of Mechanical Engineering as well as that of Dr. John T. Germaine and Professor Chiang Mei of the Department of Civil and Environmental Engineering. This research was performed while on appointment as a National Defense Science and Engineering Graduate Fellow administered by the American Society for Engineering Education (ASEE). This material is based upon work supported by the National Science Foundation under Grant No. 0408259. Any opinions, findings, and conclusions or recommendations expressed in this material are those of the author(s) and do not necessarily reflect the views of the National Science Foundation or ASEE.

Author's Publications

Dawson, M.A. and Gibson, L.J., (2006), "Biomimetics: extending nature's design of thin-wall shells with cellular cores", *Design and Nature III.* WIT Press Southhampton, UK.

Dawson, M.A. and Gibson, L.J., (2007), "Optimization of cylindrical shells with compliant cores", *Int. J. Solids and Struct.*, **44**, (3-4), 1145-1160.

Dawson, M.A, Germaine, J., and Gibson, L., (2007), "Permeability of Open-Cell Foams Under Compressive Strain", *Int. J. Solids Struct.*, **44**, (16), 5133-5145.

Dawson, M.A., McKinley, G.H., and Gibson, L.J., (2008a), "The Stress-Strain Response of Open-Cell Foam Impregnated with a Newtonian Fluid Under Compression," *J. Applied Mech.*, (In Press).

Dawson, M.A., McKinley, G.H, and Gibson, L.J., (2008b), "The Dynamic Response of Open-Cell Foam Impregnated with a Non-Newtonian Fluid Under Compression" *J. Exp. Mech.(to be submitted.)*

Appendix I: Matlab Code

The following scripts (.m files) were used in Matlab to assess the performance of various blast-resistant plate designs:

A.1 Code for single-core, fluid-filled design (Newtonian and non-Newtonian fluids)

```
function [] = BlastLoadingSingleCore(varargin)
%=========================================================================
% Sample of How To Run Code:
%BlastLoadingSingleCore()
% BlastLoadingSingleCore('write','on','radius', R, 'core_thickness', h2, 'plate_thickness', h1,
%'method', 'glycerol')
%=========================================================================
%Description: Code is designed to perform a parametric study for a single-layer core with single
%layer face plate composite protective blast plate for building armor. This code can be used to
%study the effects of various parameters.
%=========================================================================
%Assumptions: Based on assumption of time constant for overpressure order 0.1 ms and the
%fluid stress governed by fluid only behavior %since the stress is very high.
%=========================================================================
% Inputs:
%   varargin: variable inputs
%
% Outputs:
%    Max Stress on Building
%    Weight of Design
%=========================================================================
%Copyright Matthew A. Dawson 2007. All Rights Reserved.
%=========================================================================
close all

% displays error if odd number of inputs
if mod(nargin,2)==1
  error('Incorrect number of inputs');
end

% Examine pairs of inputs
m=length(varargin);
for i=1:2:m
  switch lower(varargin{i})
    case 'method'
      method=lower(varargin{i+1});
      if strcmp(method,'glycerol')==1
        method=1;
```

```
            fname = 'Glycerol (Newtonian Fluid)';
        elseif strcmp(method,'nnf')==1
            method=2;
            fname = 'Silica/EG 50 (Non-Newtonian Fluid)';
        elseif strcmp(method,'honey')==1
            method=3;
            fname = 'Honey (Newtonian Fluid)';
        else
            error('Method Not Recognized')
        end
    case 'max_time'
        max_time=varargin{i+1};
    case 'core_thickness'
        h2=varargin{i+1};
    case 'plate_thickness'
        h1=varargin{i+1};
    case 'radius'
        R=varargin{i+1};
    case 'mass_tnt'
        W=varargin{i+1};
    case 'distance'
        D=varargin{i+1};
    case 'plot'
        graph=lower(varargin{i+1});
        if strcmp(graph,'on')==1
            graph=1;
        elseif strcmp(graph,'off')==1
            graph=0;
        else
            error('Graph command not recognized')
        end
    case 'write'
        writedata=lower(varargin{i+1});
        if strcmp(writedata,'on')==1
            data=1;
        elseif strcmp(writedata,'off')==1
            data=0;
        else
            error('Write command not recognized')
        end
  end
end

% Set Defaults
%Choose Design NFF,NNFF, or Standard
if exist('method','var')==0
  method=1;
  fname = 'Glycerol (Newtonian Fluid)';
```

```
end
%Max Time
if exist('max_time','var')==0
  tspan=[0,.002]; %Integration Time
else
  tspan=[0,max_time]; %Integration Time
end
%Thickness of Core Layer
if exist('h2','var')==0
  h2=0.02;
end
%Thickness of Outer Plate Layer
if exist('h1','var')==0
  h1=0.01;
end
%Radius
if exist('R','var')==0
  R=1;
end
%Plotting Command
if exist('graph','var')==0
  graph=0;
end
%Writing Command
if exist('data','var')==0
  data=0;
end
%{
%Specify Blast Mass TNT (kg)
if exist('W','var')==0
  W=230;
end
%Specify Distance (m)
if exist('D','var')==0
  D=2;
end
%}
%
%=========================================================================
%
%Material Parameters (All units SI standard: m, Pa, m/s, etc.)
%Outer Plate Layer (Steel)
row1=7800; % Density
%Middle Fluid-Filled Foam Layer
h2o = h2;
if method ==1 %(@20C Glycerol = 1260kg/m3;1.49 Pas
  row2 = 1260; % Density
  mu = 1.49; % Viscosity
```

```
elseif method ==2 %(Silica/EG 50% NNF = 1500 kg/m3)
    row2 = 1500; % Density
    n = 0.166; % Power-Law Exponent
    m = 1200;  % Power-Law Coefficient
    CR4 = 1; % Power-Law Empirical Constant
elseif method ==3 %(Honey @25C and 15.5% H2O content = 1450kg/m3 ; 13.8 %Pas)
    row2 = 1450; %Density
    mu = 13.8; %Viscosity
end
%Weight Core Normalized by Weight Face sheets (kg/kg)
Wc_Wf = row2*h2o/(row1*h1);
%Weight of Standard Design Assume 67.5 lbs/ft^2 = 330.25kg/m^2 as seen %with sand steel
%design
WT_Norm = (row1*h1+row2*h2o)/(330.25);

%Blast Properties
tconst = 1E-4;
if exist('W','var')==0
  Pr = 1E8;
else
  if exist('D','var')==0
    D=2;
  end
  Z = D/(W^(1/3)); %Scaled blast parameter distance
  Pa = 101.3E3;
  Ps = 1E3*(1772/(Z^3)-114/(Z^2)+108/Z);
  Pr = 2*Ps*(7*Pa+4*Ps)/(7*Pa+Ps);
  Disp('Peak Reflected Pressure Calculated from Input Blast Weight and Distance')
end
%
%=========================================================
% Initialize and Solve ODE's
if (method == 1 || method == 3)
y0=[0 h2o]; %inital y values [V1o h2o]
options = []; %Dummy Vector for ODE45
[T,Y] = ode45(@odenewtonian,tspan,y0,options,h1,row1,R,mu,Pr);
elseif method == 2
y0=[0 h2o]; %inital y values [V1o h2o]
options = []; %Dummy Vector for ODE45
[T,Y] = ode45(@odeNNF,tspan,y0,options,h1,row1,R,n,m,CR4,Pr);
end
%
%=========================================================
% Calculate Results
if (method == 1 || method ==3)
sigN = 1.5*mu*(R^2)*(1./Y(:,2)).^3.*(Y(:,1))/(Pr);
elseif method == 2
  for ii = 1:length(Y(:,1))
```

```
    if Y(ii,1)<.25
      TestVelocity(ii) = 0;
    else
      TestVelocity(ii)=Y(ii,1);
    end
  end
  sigN=zeros(1,length(Y(:,2)));
  for ii = 1:length(Y(:,2))
    if  (R^2*TestVelocity(ii)/(Y(ii,2)^3) > 32)%180)%if (Y(ii,1)/Y(ii,2) > 180)
      n = 0.166; m = 1200; CR4 = 1;
    else %(Y(ii,1)/Y(ii,2) > 70)
      n = 1; m = 40; CR4 = 1;
    %else
      %n = 0.42; m = 8.7; CR4 = 1;
    end
    sigN(ii) = 2*CR4*((2*n+1)/n)^n*m/(n+3)*(TestVelocity(ii)/Y(ii,2)).^n.*(R./Y(ii,2)).^2./Pr;
  end
    %Note: Stress not exact beyond transition to second regime
end
PressureNorm = exp(-T(:,1)/tconst);
strain = 1-Y(:,2)/h2o;

%
%=========================================================
% Check Constraints
max_strain = max(strain);
if (max_strain > 0.9)
  disp(['Failure! Strain exceeded maximal allowable  ',num2str(max_strain)])
  endwrite=1;
else
  endwrite=0;
end
%
%=========================================================
%Plotting Stress, Velocity of Outer Plate and Height of Foam with Time
if graph == 1
figure(1)
plot(T,sigN,T,PressureNorm)
title('Normalized Stress Applied to Building')
xlabel('Time (s)')
ylabel('Stress Normalized by Maximum Reflected Pressure (Pa/Pa)')

figure(2)
plot(T,Y(:,1))
title('Velocity Outer Steel Plate')
xlabel('Time (s)')
ylabel('Velocity (m/s)')
```

```
figure(3)
plot(T,Y(:,2))
title('Height of Foam')
xlabel('Time (s)')
ylabel('Heigth Specimen (m)')

end
%
%=========================================================
% Display Results
disp(fname)
disp(['Strain  ', num2str(strain(end))])
disp(['R = ', num2str(R,'%7.3E\n')])
disp('h1  h2o  W_Tot_Norm_Equiv  W_Core_Norm_Face  Max_Stress_Norm_Pmax
Max_Stress_Norm_Standard')
disp([num2str(h1,'%7.3E\n'); num2str(h2o,'%7.3E\n'); num2str(WT_Norm,'%7.3E\n');
num2str(Wc_Wf,'%7.3E\n'); num2str(max(sigN),'%7.3E\n');
num2str((max(sigN)/.4626),'%7.3E\n')])
disp(' ')
%
%=========================================================
% Write Data
if (data ==1 && endwrite == 0)
   Output=[h1, h2o, WT_Norm, Wc_Wf, (max(sigN)), (max(sigN))/.4626];
   dlmwrite('NNFIIISingleh1h2.txt', Output,'delimiter', '\t','-append');
end
%
%=========================================================
% ODE Functions
function dy = odenewtonian(t,y,h1,row1,R,mu,Pr)
tconst = 1E-4;
% y(1)=V1; Velocity of outer plate
% y(2)=h2; Core Thickness
dy = zeros(2,1);   % a column vector
dy(1) = (1/(row1*h1))*(Pr*exp(-t/tconst)-1.5*mu*(y(1)/y(2))*(R/y(2))^2);
dy(2) = -y(1);

function dy = odeNNF(t,y,h1,row1,R,n,m,CR4,Pr)
tconst = 1E-4;
% y(1)=V1; Velocity of outer plate
% y(2)=h2; Core Thickness
dy = zeros(2,1);   % a column vector
if (R^2*y(1)/(y(2)^3) > 32)%180)
   if (y(1) < .25 && t > 1E-4)
      dy(1) = 0;
   else
     dy(1) = (1/(row1*h1))*(Pr*exp(-t/tconst)-
2*CR4*((2*n+1)/n)^n*m/(n+3)*(y(1)/y(2))^n*(R/y(2))^2);
```

```
  end
else
  n = 1; m = 40; CR4 = 1;
  dy(1) = (1/(row1*h1))*(Pr*exp(-t/tconst)-2*CR4*((2*n+1)/n)^n*m/(n+3)*(y(1)/y(2))^n*(R/y(2))^2);
  2*CR4*((2*n+1)/n)^n*m/(n+3)*(y(1)/y(2))^n*(R/y(2))^2);
end
dy(2) = -y(1);
```

A.2 Code for dual-core, fluid-filled design (Newtonian and non-Newtonian fluids)

```
function [] = BlastLoadingDualCore(varargin)
%=========================================================================
% Sample of How To Run Code:
% BlastLoadingDualCore()
% BlastLoadingDualCore('write','on','radius', R, 'core_thickness_2', h2, 'core_thickness_4', h4,
%'plate_thickness_1', h1, 'plate_thickness_3', h3,'method', 'glycerol')
%=========================================================================
%=========================================================================
% Description: Code is designed to perform a parametric study for a dual-layer core composite
%plate with two face plate layers  for a blast plate-resistant building armor. This code can be used
%to study the effects of various parameters.
%=========================================================================
%Assumptions: Based on assumption of time constant for overpressure order 0.1 ms and the
%fluid stress governed by fluid only behavior since the stress is very high.
%=========================================================================
% Inputs:
%  varargin: variable inputs
%
% Outputs:
%   Max Stress on Building
%   Weight of Design
%=========================================================================
%Copyright Matthew A. Dawson 2007. All Rights Reserved.
%=========================================================================
close all

% displays error if odd number of inputs
if mod(nargin,2)==1
  error('Incorrect number of inputs');
end

% Examine pairs of inputs
m=length(varargin);
for i=1:2:m
  switch lower(varargin{i})
    case 'method'
      method=lower(varargin{i+1});
      if strcmp(method,'glycerol')==1
        method=1;
        fname = 'Glycerol (Newtonian Fluid)';
      elseif strcmp(method,'nnf')==1
        method=2;
```

```
            fname = 'Silica/EG 50 (Non-Newtonian Fluid)';
          elseif strcmp(method,'honey')==1
            method=3;
            fname = 'Honey (Newtonian Fluid)';
          else
            error('Method Not Recognized')
          end
        case 'max_time'
          max_time=varargin{i+1};
        case 'core_thickness_2'
          h2=varargin{i+1};
        case 'core_thickness_4'
          h4=varargin{i+1};
        case 'plate_thickness_1'
          h1=varargin{i+1};
        case 'plate_thickness_3'
          h3=varargin{i+1};
        case 'radius'
          R=varargin{i+1};
        case 'mass_tnt'
          W=varargin{i+1};
        case 'distance'
          D=varargin{i+1};
        case 'plot'
          graph=lower(varargin{i+1});
          if strcmp(graph,'on')==1
            graph=1;
          elseif strcmp(graph,'off')==1
            graph=0;
          else
            error('Graph command not recognized')
          end
        case 'write'
          writedata=lower(varargin{i+1});
          if strcmp(writedata,'on')==1
            data=1;
          elseif strcmp(writedata,'off')==1
            data=0;
          else
            error('Write command not recognized')
          end
    end
end
% Set Defaults
%Choose Design NFF,NNFF, or Standard
if exist('method','var')==0
    method=1;
    fname = 'Glycerol (Newtonian Fluid)';
```

```
end
%Max Time
if exist('max_time','var')==0
   tspan=[0,.002]; %Integration Time
else
   tspan=[0,max_time]; %Integration Time
end
%Thickness of Core Layer 2
if exist('h2','var')==0
   h2=0.01;
end
%Thickness of Core Layer 4
if exist('h4','var')==0
   h4=0.01;
end
%Thickness of Outer Plate Layer 1
if exist('h1','var')==0
   h1=0.005;
end
%Thickness of Outer Plate Layer 3
if exist('h3','var')==0
   h3=0.005;
end
%Radius
if exist('R','var')==0
   R=1;
end
%Plotting Command
if exist('graph','var')==0
   graph=0;
end
%Writing Command
if exist('data','var')==0
   data=0;
end
%{
%Specify Blast Mass TNT (kg)
if exist('W','var')==0
   W=230;
end
%Specify Distance (m)
if exist('D','var')==0
   D=2;
end
%}
%
%=========================================================================
%
```

```
%Material Parameters (All units SI standard: m, Pa, m/s, etc.)
%Outer Plate Layer (Steel)
row1=7800; row3 = 7800;
%Middle Fluid-Filled Foam Layer
h2o = h2;
h4o = h4;
if method ==1 %(@20C Glycerol = 1260kg/m3;1.49 Pas
    row2 = 1260; row4 = 1260; %Density
    mu = 1.49; %Viscosity
elseif method ==2 %(Silica/EG 50% NNF = 1500 kg/m3; ? Pas)
    row2 = 1500; row4 = 1500; %Density
    n = 0.166; %Power-Law Exponent
    m = 1200; %Power-Law Coefficient
    CR4 = 1; %Power-Law Empirical Constant
elseif method ==3 %(Honey @25C and 15.5% H2O content = 1450kg/m3 ; 13.8 Pas)
    row2 = 1450; row4 = 1450; %Density
    mu = 13.8; %Viscosity
end
%Weight Core Normalized by Weight Face sheets (kg/kg)
Wc_Wf = (row2*h2o+row4*h4o)/(row1*h1+row3*h3);
%Weight of Standard Design Assume 67.5 lbs/ft^2 = 330.25kg/m^2 as seen with sand steel design
WT_Norm = (row1*h1+row2*h2o+row3*h3+row4*h4)/(330.25);

%Blast Properties
tconst = 1E-4;
if exist('W','var')==0
  Pr = 1E8;
else
  if exist('D','var')==0
    D=2;
  end
  Z = D/(W^(1/3));
  Pa = 101.3E3;
  Ps = 1E3*(1772/(Z^3)-114/(Z^2)+108/Z);
  Pr = 2*Ps*(7*Pa+4*Ps)/(7*Pa+Ps);
  Disp('Peak Reflected Pressure Calculated from Input Blast Weight and Distance')
end
%
%=========================================================================
% Initialize and Solve ODE's
if (method == 1 || method == 3)
y0=[0 h2o 0 h4o]; %inital y values [V1o h2o V3o h4o]
options = []; %Dummy Vector for ODE45
[T,Y] = ode45(@odenewtonian,tspan,y0,options,h1,h3,row1,row3,R,mu,Pr);
elseif method == 2
y0=[0 h2o 0 h4o]; %inital y values [V1o h2o V3o h4o]
options = []; %Dummy Vector for ODE45
[T,Y] = ode45(@odeNNF,tspan,y0,options,h1,h3,row1,row3,R,n,m,CR4,Pr);
```

```
end
%
%=========================================================
% Calculate Results
if (method == 1 || method ==3)
  %Stress Normalized Exerted on Building, Depends only on h4 and V3
  sigN = 1.5*mu*(R^2)*(1./Y(:,4)).^3.*(Y(:,3))/(Pr);
elseif method == 2
  for ii = 1:length(Y(:,3))
    if Y(ii,3)<2
      TestVelocity(ii) = 0;
    else
      TestVelocity(ii)=Y(ii,3);
    end
  end
  sigN=zeros(1,length(Y(:,3)));
  for ii = 1:length(Y(:,3))
    if (TestVelocity(ii)/Y(ii,4) > 180)
      n = 0.166; m = 1200; CR4 = 1;
    else
      n = 1; m = 40; CR4 = 1;
    end
    sigN(ii) = 2*CR4*((2*n+1)/n)^n*m/(n+3)*(TestVelocity(ii)/Y(ii,4)).^n.*(R./Y(ii,4)).^2./Pr;
  end
end
PressureNorm = exp(-T(:,1)/tconst);
strain2 = 1-Y(:,2)/h2o;
strain4 = 1-Y(:,4)/h4o;
%
%=========================================================
% Check Constraints
max_strain = max(max(strain2),max(strain4));
if (max_strain > 0.9)
  disp(['Failure! Strain exceeded maximal allowable ',num2str(max_strain)])
  endwrite=1;
else
  endwrite=0;
end
%
%=========================================================
%Plotting Stress, Velocity of Outer Plate and Height of Foam with Time
if graph == 1
figure(1)
plot(T,sigN,T,PressureNorm)
title('Normalized Stress Applied to Building')
xlabel('Time (s)')
ylabel('Stress Normalized by Maximum Reflected Pressure (Pa/Pa)')
```

```
figure(2)
plot(T,Y(:,1),T,Y(:,3))
title('Velocity of Steel Plates')
xlabel('Time (s)')
ylabel('Velocity (m/s)')

figure(3)
plot(T,Y(:,2),T,Y(:,4))
title('Heights of Foam Layers')
xlabel('Time (s)')
ylabel('Heigth Specimen (m)')
end

%
%=========================================================================
% Display Results
disp(fname)
disp(['Strain   ', num2str(strain4(end))])
disp(['R = ', num2str(R,'%7.3E\n')])
disp('h1  h2o  h3   h4o     W_Tot_Norm_Equiv  W_Core_Norm_Face
Max_Stress_Norm_Pmax  Max_Stress_Norm_Standard')
disp([num2str(h1,'%7.3E\n'); num2str(h2o,'%7.3E\n'); num2str(h3,'%7.3E\n');
num2str(h4o,'%7.3E\n'); num2str(WT_Norm,'%7.3E\n'); num2str(Wc_Wf,'%7.3E\n');
num2str(max(sigN),'%7.3E\n'); num2str((max(sigN)/.4999),'%7.3E\n')])
disp(' ')
%=========================================================================
% Write Data
if (data ==1 && endwrite == 0)
  Output=[h1, h2o, h3, h4o, WT_Norm, Wc_Wf, (max(sigN)), (max(sigN))/.4999];
  dlmwrite('GlycerolDoubleh2vsh4.txt', Output,'delimiter', '\t','-append');
end
%
%=========================================================================
% ODE Functions
function dy = odenewtonian(t,y,h1,h3,row1,row3,R,mu,Pr)
tconst = 1E-4;
% y(1)=V1; Velocity of outer plate
% y(2)=h2; Core Thickness
dy = zeros(4,1);   % a column vector
dy(1) = (1/(row1*h1))*(Pr*exp(-t/tconst)-1.5*mu*((y(1)-y(3))/y(2))*(R/y(2))^2);
dy(2) = y(3)-y(1);
dy(3) = (1/(row3*h3))*(Pr*exp(-t/tconst)-1.5*mu*(y(3)/y(4))*(R/y(4))^2);
dy(4) = -y(3);

function dy = odeNNF(t,y,h1,h3,row1,row3,R,n,m,CR4,Pr)
tconst = 1E-4;
% y(1)=V1; Velocity of outer plate
% y(2)=h2; Core Thickness
```

```
dy = zeros(4,1);    % a column vector
if (y(1)/y(2) > 180)
   dy(1) = (1/(row1*h1))*(Pr*exp(-t/tconst)-2*CR4*((2*n+1)/n)^n*m/(n+3)*((y(1)-
y(3))/y(2))^n*(R/y(2))^2);
else
   n = 1; m = 40; CR4 = 1;
   dy(1) = (1/(row1*h1))*(Pr*exp(-t/tconst)-2*CR4*((2*n+1)/n)^n*m/(n+3)*((y(1)-
y(3))/y(2))^n*(R/y(2))^2);
end
dy(2) = y(3)-y(1);
if (y(3)/y(4) > 180)
   dy(3) = (1/(row3*h3))*(Pr*exp(-t/tconst)-2*CR4*((2*n+1)/n)^n*m/(n+3)*(y(3)/y(4))^n*(R/y(4))^2);
else
   n = 1; m = 40; CR4 = 1;
   dy(3) = (1/(row3*h3))*(Pr*exp(-t/tconst)-2*CR4*((2*n+1)/n)^n*m/(n+3)*(y(3)/y(4))^n*(R/y(4))^2);
end
dy(4) = -y(3);
```

A.3 Code for single-core, Fleck Deshpande design (Newtonian and non-Newtonian fluids)

```
function [] = BlastLoadingSingleCoreHC(varargin)
%=========================================================================
% Sample of How To Run Code:
% BlastLoadingSingleCoreHC()
%=========================================================================
% Description: Code is designed to perform a parametric study for a single-layer solid, foam core
%composite plate with one face plate layer for a blast plate-resistant building %armor. This code
%can be used to study the effects of various parameters.
%=========================================================================
%Assumptions: Based on assumption of time constant for overpressure order 0.1 ms.
%Function for Compression of outer plate with fluid filled foam core against infinitely rigid wall
%=========================================================================
clear all
tspan=[0,.003]; %Integration Time
y0=[0 0.1]; %inital y values [V1o h2o]
options = [];
h1 = 0.02; %Face plate thickness
Pr = 1E8; %Peak reflected pressure
row1=7800; %Density outer face plate
sigysteel = 300E6; %Steel yield stress
h20 = 0.1; %Core Thickness
reldeno = .11; %Initial relative density
row20 = 7800*reldeno; %Steel density core
[T,Y] = ode45(@odefun,tspan,y0,options,h1,row1,h20,Pr,sigysteel,reldeno);
sigN = .3*(reldeno./(Y(:,2)./h20)).^1.5*sigysteel/1E8;

figure(1)
plot(T,sigN)
title('Normalized Stress Applied to Building')
xlabel('Time (s)')
ylabel('Stress Normalized by Maximum Reflected Pressure (Pa/Pa)')

figure(2)
plot(T,Y(:,1))
title('Velocity Outer Steel Plate')
xlabel('Time (s)')
ylabel('Velocity (m/s)')

figure(3)
plot(T,Y(:,2))
title('Height of Foam')
xlabel('Time (s)')
ylabel('Heigth Specimen (m)')
```

```
weight = row1*h1+h20*row20;
strain = 1-min(Y(:,2))/h20;
if (strain > 0.5)
   disp(['Failure! Strain exceeded maximal allowable  ',num2str(strain)])
end

%Display Results
disp(['Core Thickness   ', num2str(h20)])
disp(['Weight   ', num2str(weight)])
disp(['Normalized Stress   ', num2str(max(sigN))])
disp(num2str(h20))
disp(num2str(weight))
disp(num2str(max(sigN)))

function dy = odefun(t,y,h1,row1,h20,Pr,sigysteel,reldeno)
tconst = 1E-4;
dy = zeros(2,1);    % a column vector
dy(1) = (1/(row1*h1))*(Pr*exp(-t/tconst)-.3*(reldeno/(y(2)/h20)).^1.5*sigysteel);
dy(2) = -y(1);
```

Appendix II: Suppliers and Distributors

ADINA R&D Company
Phone: (617) 926-5199
Address: 71 Elton Avenue, Watertown, MA 02472, USA.
Materials: ADINA finite element analysis software.

Cordek
Phone: 44 (0) 1403-799600
Address: Stane St, Slinfold, Horsham, RH13 0SZ, United Kingdom.
Materials: High-density polystyrene.

Farnell Leeds
Phone: 01 830-9277
Address: Units 4-5 Gofton Court Jamestown Road, Finglas, Dublin, Ireland.
Materials: ABS.

FEI Company
Phone: (503) 726-7500
Address: 5350 NE Dawson Creek Drive, Hillsboro, Oregon 97124 USA.
Materials: Scanning electron microscope (XL30 FEG ESEM).

Fisher Scientific
Phone: (770) 614-1090
Address: 2775 Horizon Ridge Ct, Suwanee, GA 30024.
Materials: Sorvall Legend Mach 1.6 Centrifuge.

Foamex
Phone: (800) 776-3626
Address: 1000 Columbia Avenue, Linwood, PA 19061.
Materials: Polyester-based, open-cell, polyurethane foam.

Fuso Chemical Company
Phone: (06) 6203-4771
Address: 3-10, Koraibashi 4-chome,Chuo-ku, Osaka-shi, Osaka, Japan.
Materials: Spherical silica nanoparticles.

Instron Corporation
Phone: (800) 877-6674
Address: 825 University Ave., Norwood, MA 02062-2643.
Materials: Dynatup drop-tower 9200 Series, Instron Model 1321.

McMaster-Carr Supply Co.
Phone: (609) 689-3000
Address: 200 New Canton Way, Robbinsville, NJ 08691.
Materials: General Supplies: Clamps, Glassware, Hammers, Rubber Stoppers, Thermometers, Tubes, etc.

Mettler-Toledo, Inc.
Phone: (800) 638-8547
Address: 1900 Polaris Parkway, Columbus, OH, 43240.
Materials: Electronic Balance.

Minerals Technology
Phone: (212) 878-1800
Address: 405 Lexington Ave., New York, NY 10174.
Materials: Precipitated calcium carbonate nanoparticles (Opcarb).

Mitutoyo
Phone: (630) 820-9666
Address: 965 Corporate Blvd., Aurora, IL 60502.
Materials: Digital Caliper (CD-6" CSX).

New Dimension Industries
Phone: (800) 251-7462
Address: 220 Anderson Avenue, Moonachie, NJ 07074.
Materials: Polyester-based, open-cell polyurethane foam.

Revolutionary Science
Phone: (651) 257-0633
Address: 13229 Saint Croix Ave., Lindstrom, Minnesota 55045.
Materials: Incufridge (RS-IF-202).

Scion Corporation
Phone: (301) 695-7870
Address: 82 Wormans Mill Ct, Frederick, MD 21701.
Materials: Scion Image analysis software.

Stable Microsystems
Phone: 44 (0)1483-427345
Address: Vienna Court, Lammas Road, Godalming, Surrey GU7 1YL, UK.
Materials: Texture Analyzer (TA XT Plus).

TA Instruments
Phone: (302) 427-4000
Address: 109 Lukens Drive, New Castle, DE 19720.
Materials: Controlled stress rheometer (ARG 2000).

Titan Tool Supply Co.
Phone: (716) 873-9907
Address: 68 Comet Ave., Buffalo, NY 14216.
Materials: Traveling microscope.

VWR International
Phone: (800) 932-5000
Address: 1310 Goshen Parkway, West Chester, PA 19380.
Materials: Ethylene Glycol, Glycerol, Digital Vortex Mixer.